A GEOPHYSICAL SURVEY OF ACTIVE VOLCANISM IN THE CENTRAL AND SOUTHERN ANDES

A Dissertation

Presented to the Faculty of the Graduate School

of Cornell University

In Partial Fulfillment of the Requirements for the Degree of

Doctor of Philosophy

by

Jennifer Ann Jay

May 2014

A GEOPHYSICAL SURVEY OF ACTIVE VOLCANISM IN THE CENTRAL AND SOUTHERN ANDES

Jennifer Ann Jay, Ph. D.

Cornell University 2014

The subduction of the Nazca plate beneath the South American plate results in great earthquakes and active volcanism along the Andean margin. The Central Volcanic Zone (CVZ) between 15°S and 28°S and the Southern Volcanic Zone (SVZ) between 33°S and 46°S are separated by a zone of flat slab subduction and differ significantly in the manifestation of current volcanic activity. The CVZ has been considered less hazardous due to the few number of historical volcanic eruptions compared to the SVZ, yet it contains the largest mid-crustal magma body on Earth and erupted at least 10,000 km^3 of ignimbrite in the Late Miocene (10-1 Ma). In this dissertation, I use InSAR (interferometric synthetic aperture radar), thermal remote sensing, and seismology to investigate active volcanism in the Central and Southern Andes. InSAR and thermal remote sensing provide synoptic coverage along the volcanic arc, and seismic experiments allow further examination of selected volcanoes. I establish the first catalog of seismicity at Uturuncu volcano in Bolivia, where InSAR has observed continuous uplift since 1992, and find an unusually high seismicity rate for a Pleistocene volcano as well as swarm activity and triggered earthquakes. I then conduct a survey using satellite thermal infrared data to detect thermal hotspots related to volcanic activity throughout the CVZ and SVZ. I find hotspots at many volcanoes that had not previously been documented, with the CVZ containing more volcanoes with hotspots than the SVZ. One of the most thermally active volcanoes in the SVZ, Cordón Caulle volcano, experienced a large rhyodacitic eruption from 2011-2012. I

use InSAR and petrology to model the pre-eruptive conditions at depth and co-eruptive processes and find that a large, long-lived crustal magma reservoir must be present beneath Cordón Caulle. Finally, I carry out an InSAR survey of volcanoes in southern Peru, completing a regional study of volcano deformation in the CVZ and allowing for a comprehensive comparative analysis between the CVZ and SVZ.

BIOGRAPHICAL SKETCH

Jennifer was born the second of two children on May 12, 1985 (Mothers Day) in sunny Newport Beach, California. She grew up in Huntington Beach, otherwise known as Surf City, USA. Throughout her childhood, she enjoyed reading, drawing, watching I Love Lucy re-runs, going to Disneyland, and doing gymnastics. In high school, she discovered her love of math, science, foreign languages, and sports.

In 2003, Jennifer moved one hour north of her hometown to Los Angeles to attend her father's alma mater, UCLA, for her undergraduate education. Her time at UCLA was occupied by gymnastics club, foreign travel, and of course attending classes. While at UCLA, she pursued a double major in Geophysics/Space Physics and Spanish. During her last semester at UCLA, Jennifer studied abroad in Santiago, Chile, where she took classes at the Pontifical Catholic University of Chile. The highlight of this experience was traveling to Patagonia, the Atacama Desert, and the volcanoes of the Lakes region.

Upon returning to the States, Jennifer decided to apply to graduate school at Cornell University to work with Matt Pritchard on Andean volcanology. The promise of field work every six months made the position sound particularly appealing. Despite getting stuck in a blizzard in Philadelphia while trying to attend the prospective student day, Jennifer was eventually able to visit Cornell where she was greeted by friendly graduate students and faculty and cold weather. During this visit, she decided to commit to spending the next 5 years of her life in Ithaca.
Jennifer has thoroughly enjoyed her time at Cornell. She has been fortunate to be able

to travel to Chile, Bolivia, Argentina, Alaska, Germany, and Japan for field work, classes, and conferences. She will miss the Cambodian food and Fat Boy scones at the Ithaca Farmers Market, hiking the gorge trails, running at the Cornell Plantations, but most of all she will miss the people of Snee Hall. Jennifer is looking forward to the next phase of her journey – working as a postdoctoral research fellow at the Smithsonian National Museum of Natural History in Washington, DC and starting a family with her husband Kendrick.

ACKNOWLEDGMENTS

I would not be sitting here today writing this dissertation if it weren't for the support of many family, friends, advisors, colleagues, and collaborators to whom I am eternally grateful. I would first like to thank my thesis advisor, Matt Pritchard. Thank you for taking a chance on a student with no prior research experience and for always taking the time to talk to me no matter how busy your schedule was. I feel so fortunate to have had the opportunity to travel to Chile and Bolivia; I will always have fond memories of my time in the field. Thank you for having confidence in me and encouraging me to step outside my comfort zone in scientific research, giving oral presentations in Spanish, and organizing field work and team meetings. I would also like to thank my minor committee members, Suzanne Kay and Phil Nicholson. Sue, your input has challenged me to look at Andean volcanism from not just a geophysical standpoint but also reconciling my observations with geochemistry. Phil, your thought-provoking questions during my oral exams have made me think about the Earth in the broader context of the solar system.

The support and camaraderie of my fellow graduate students in Snee Hall over the past 5 years has been overwhelming. Scott Henderson, I could not have asked for a better lab mate, field partner, travel buddy, and friend. Thank you for listening to my complaints about research problems, Delta Airlines, and life in general and for bearing with my ever-spreading mess in the lab. I would also like to thank Andrew Melkonian – you introduced me to the power of gawk and were always so willing to help out with any computer-related issues. To all other members of the Pritchard-

Lohman group – Holly, Chelsea, Francisco, Phil, Bill, Veronica, Julie, and Mike – thank you for making Friday early morning group meetings so lively and entertaining.

I would also like to acknowledge members of the seismology group – Diego, Anastasija, Patrick, and CC. I extend a special thanks to CC for helping me download seismic data, patiently answering all my questions related to seismology, teaching me Chinese, and most of all for your loyal friendship. I also thank Felipe Aron for always asking stimulating questions and for being a great swimming buddy. Rachel and Anastasija, your friendship has been invaluable to me; I would not have made it this far without all the good times we shared during knitting nights.

I would like to acknowledge the work of my co-authors in Chapter 2 on Uturuncu seismicity: Matthew E. Pritchard, Michael E. West, Douglas Christensen, Matthew Haney, Estela Minaya, Mayel Sunagua, Stephen R. McNutt, and Mario Zabala. The project would not have been possible without the help of the Bolivian Servicio de Areas Protegidas (especially the staff at the Reserva Eduardo Avaroa), the residents of Quetena Chico and Quetena Grande, and the staff of the Observatorio San Calixto. Seismic instruments were provided by Program for Array Seismic Studies of the Continental Lithosphere (PASSCAL). I thank Diego Martínez, David Cassis Chuquisea, Luís Galván, Tom Fournier, Lloyd Carothers, Anna Bellesiles, Branden Christensen, Scott Henderson, and the Servicio Nacional de Geología y Técnico de Minas for assistance in the field. We also thank Zach Chartrand, Christopher Bruton, Nicole Button, and Bekah Tsigonis for help in earthquake picking and location. This work was supported by NASA (National Aeronautics and Space Administration) grant NNX08AT02G issued through the Science Mission Directorate's Earth Science

Division and NSF (National Science Foundation) grant 0908281 which is part of the PLUTONS project (plutons.science.oregonstate.edu). The ambient noise tomography in this chapter was processed and analyzed by co-author Matthew Haney.

For the ASTER hotspot project (Chapter 3), I would like to acknowledge the work of my co-authors: Mark Welch, Matthew Pritchard, Peter Mares, Marissa Mnich, Andrew Melkonian, Felipe Aguilera, José Antonio Naranjo, Mayel Sunagua, and Jorge Clavero. I thank Geological Society of London editor D. Pyle, reviewers R. Wright and S. Murphy, and the ASTER Science Team for helpful feedback. This project was supported by NASA grant NNX08AT02G issued through the Science Mission Directorate's Earth Science Division. J. Clavero was supported by Fondecyt projects.

The Cordón Caulle project (Chapter 4) was greatly enhanced by the petrological analysis carried out by co-authors Fidel Costa and Jason Herrin. Other co-authors include Matthew Pritchard, Luis Lara, and Bradley Singer. Fidel thanks J. Cabato for help during the SIMS analysis, B. Scaillet for the thermodynamic calculations of the composition of the fluid phase, and L. Mastin for discussion about magma compressibility. ALOS data were provided by JAXA with access provided from the Alaska Satellite Facility and NASA. Envisat SAR imagery was acquired as a Category 1 research project from the European Space Agency. This work was partly supported by NASA grant NNX12AO31G issued through the Science Mission Directorate's Earth Science Division.

The InSAR survey of volcanoes in Peru (Chapter 5) benefitted from input from Orlando Macedo, Victor Aguilar, José Luis Torres Aguilar, and Felipe Aron. Orlando

and José Luis supplied earthquake locations and focal mechanisms derived from seismic data, and Felipe supplied co-seismic Coulomb stress models.

Finally, I acknowledge my NASA Earth and Space Science Fellowship (award number NNX10AQ76H) for providing three years of financial support for my research, living, and travel expenses.

TABLE OF CONTENTS

CHAPTER 1

INTRODUCTION

1.1 INTRODUCTION

The Andean mountain range of South America is one of the longest and highest continental mountain ranges on Earth. Active subduction of the oceanic Nazca and Antarctic plates beneath the continental South America plate results in great earthquakes and volcanism along the margin. The Andean volcanic belt contains nearly 200 Holocene volcanoes and is divided into four main segments – from north to south, these are the Northern (NVZ), Central (CVZ), Southern (SVZ), and Austral (AVZ) Volcanic Zones. The NVZ, CVZ, and SVZ are separated by regions of flat slab subduction, where the shallow subduction of the Nazca plate beneath the South America plate does not allow sufficient mineral devolatilization and flux melting of the mantle wedge to cause volcanism (Kay et al. 2005). The AVZ is separated from the SVZ near the Chile Triple Junction, where the collision of the Chile Ridge with the South America plate alters the depth of dehydration melting and causes a gap in the volcanic arc (Ramos and Kay 1992). Understanding the magmatic processes at play during all stages of the eruptive cycle is important for predicting the timing, size, style, and duration of volcanic eruptions. Accurate eruption forecasting is necessary for saving lives and preserving property in populated areas surrounding active volcanoes, as well as efficiently re-routing global air traffic.

In this dissertation, I will focus on the CVZ and SVZ of Peru, Bolivia, Chile, and Argentina. One major theme of this work is the comparison of activity between these two zones. The CVZ is home to 68 Holocene volcanoes, eight of which have erupted over the past 100 years. Though recent eruptive activity is relatively low, the late Miocene (10-1 Ma) saw the eruption of at least 10,000 km^3 of dacitic ignimbrite, forming the Altiplano-Puna Volcanic Complex in the middle of the CVZ (de Silva 1989). On the other hand, the SVZ contains 65 Holocene volcanoes of which 18 have erupted over the past 100 years. In addition to having more eruptions, the volcanoes of the SVZ also differ from their CVZ counterparts in magma composition; in general they tend to be more basaltic due to the thinner crust of the southern Andes (Kay et al. 2005).

Another theme of this work is the relationship between earthquakes and volcanic activity. Charles Darwin noted a significant increase in the number of volcanic eruptions in the SVZ following the 1835 Concepción earthquake and suggested an "intimate connection" between volcanism and earthquakes (Darwin, 1840). This connection has been a topic of active research, and evidence for a triggering relationship between large earthquakes and volcanic activity is growing (e.g., Linde and Sacks 1998; Walter and Amelung 2007; Eggert and Walter 2009; Watt et al. 2009). Here, I will examine not only triggered eruptions but also triggered volcano seismicity, deformation, and thermal hotspots. Although no large eruptions occurred immediately after the 27 February 2010 Mw 8.8 Maule earthquake, I will show that other volcanic processes were triggered by the earthquake.

Owing to their remote setting and limited accessibility, the current activity of many of the volcanoes in the CVZ and SVZ is not well known. Remote sensing techniques using data collected by satellites allow us to image all areas of the Earth from space. In this dissertation, I use both space-based remote sensing and ground-based monitoring techniques to characterize volcanic activity in the CVZ and SVZ. Specifically, I use ground-based seismic data to characterize local volcano seismicity, satellite thermal infrared data to detect high-temperature "hotspot" anomalies, and satellite interferometric synthetic aperture radar (InSAR) to measure ground deformation (see Appendix A3 for more details about the InSAR method).

In Chapter 2, I examine the seismicity associated with Uturuncu volcano in the CVZ (Jay et al. 2012). Uturuncu is a particularly worthy target for this study due to the fact that a circular region 70 km in diameter and centered on the volcano has been continuously uplifting at a rate of about 1 cm/yr since 1992 (Pritchard and Simons 2004), however there is evidence that uplift has recently ceased (see Section 1.3). Furthermore, Uturuncu is located in the middle of the Altiplano-Puna Volcanic Complex and is sitting above an expansive mid-crustal zone of partial melt. I find that Uturuncu exhibits relatively high rates of seismicity for a Pleistocene volcano, with earthquakes often occurring in swarms (clustered in time and space) which can be triggered by large regional earthquakes. The ambient noise tomography processing and analysis was carried out by co-author Matthew Haney.

In Chapter 3, I use thermal infrared data from the ASTER (Advanced Spaceborne Thermal Emission and Reflection Radiometer) instrument to survey the thermal activity of all Holocene volcanoes in the CVZ, SVZ, and AVZ (Jay et al.

2013). I show that the high spatial resolution of ASTER allows for the detection of many previously undocumented thermal hotspots. Thermal activity does not seem to be affected by large earthquakes, however the observations are limited due to infrequent data acquisitions. I find that, although the temperature of hotspots in the SVZ is generally higher due to eruptions, there are more volcanoes with hotspots in the CVZ.

In Chapter 4, I combine InSAR and petrology to examine the magmatic processes before and during the 2011-2012 eruption of Cordón Caulle volcano in the SVZ (Jay et al. 2014, in review). This eruption is particularly unique because of its large size, silicic composition, and the fact that it occurred 15 months after the Maule earthquake. I use InSAR to measure ground deformation before and during the eruption, and I model this deformation to infer magma source depths, geometries, and volume changes. Combining InSAR modeling with petrological analysis of the erupted products, I show that the magmatic plumbing system beneath Cordón Caulle is laterally extensive and consists of multiple interconnected reservoirs that were active during various time periods in the eruptive cycle.

In Chapter 5, I undertake an InSAR survey of all 16 Holocene volcanoes in southern Peru, the northernmost section of the CVZ. While previous InSAR studies of the region all end in 2002 or earlier, this survey spans 1995 to 2013. The deformation and eruptive behavior of these volcanoes differs from their CVZ neighbors to the south, suggesting a fundamental difference in the nature of these volcanic systems. I find multiple deformation episodes at volcanoes that are related to moderately sized earthquakes and earthquake swarms, but no deformation that is clearly related to

magmatic activity. I suggest that the open nature of some of these Peruvian volcanic systems does not allow for sufficient pressurization that would be required for magmatic deformation to be observed.

In summary, this dissertation combines seismology, thermal remote sensing, and InSAR to understand volcanic processes in the CVZ and SVZ. Though the SVZ is home to a greater number of historical eruptions, I find that many volcanoes in the CVZ are also "active" in that they exhibit seismicity, deformation, and thermal hotspots. Uturuncu volcano in the CVZ is anomalous in that it displays all three – long-term uplift, persistent thermal hotspot anomalies, and high rates of background seismicity. However, Uturuncu has had no historical eruptions and appears to be in a metastable state. On the other hand, Cordón Caulle volcano in the SVZ had a large eruption in 2011 but an episodic deformation history. This work reveals that the relationship between deformation and eruptions is dependent on many factors. In the future, I plan to explore this relationship further by examining volcanic deformation episodes on a global scale.

1.2 CO-AUTHOR CONTRIBUTIONS

This dissertation has been greatly enhanced by the contributions of co-authors with expertise in other fields of geoscience. In Chapter 2 on Uturuncu seismicity, co-author Matthew Haney carried out the ambient noise tomography processing and analysis. The results of the ambient noise tomography complement the findings of the seismicity analysis and thus are included in the chapter and the published paper.

In Chapter 3 on volcanic thermal hotspots, co-author Felipe Aguilera provided in-situ measurements of fumarole temperatures that were valuable in comparing with

the temperatures observed by satellite thermal infrared data. His field-based knowledge of the thermal activity of volcanoes in Chile was very helpful for our analysis. Input from co-author José Antonio Naranjo regarding field observations was also extremely valuable, particularly at volcanoes in the Chilean SVZ.

In Chapter 4 on Cordón Caulle, co-authors Fidel Costa and Jason Herrin carried out the petrological analysis. The combination of InSAR and petrology in the study of a large silicic eruption makes this chapter unique and allows us to draw conclusions that otherwise would not have been clear.

In Chapter 5 on Peruvian volcanism, Orlando Macedo of the Instituto Geofísico del Perú (IGP) provided earthquake locations and focal mechanisms calculated using data from a local seismic network. These locations are generally more reliable than what can be found in the global earthquake catalogs, especially for the low magnitude events in seismic swarms.

1.3 UPDATE ON UTURUNCU

Since the writing of Chapter 2 in 2011, there have been multiple publications regarding Uturuncu volcano that complement my findings. InSAR time series analyses by Fialko and Pearse (2012) and Henderson and Pritchard (2013) show evidence for a moat of subsidence surrounding the uplift, however the physical mechanism responsible for the subsidence is still debated. More recently, data from continuous GPS stations suggest that the uplift may have abruptly ended in 2010 (Henderson et al. 2013). Petrological studies of Uturuncu's historical eruptions show a shallow pre-eruptive storage region for the dacite lavas at around 5-6 km below the surface (Muir et al. 2014), close to the depths of ongoing volcano-tectonic seismicity

(Jay et al. 2012) but a few km deeper than the low velocity zone imaged by ambient noise tomography (Section 2.6.6) and much shallower than the proposed deformation sources. Studies using seismic data from a network of 33 broadband stations are ongoing.

REFERENCES

Darwin, C. (1840). XLII.--On the Connexion of certain Volcanic Phenomena in South America; and on the Formation of Mountain Chains and Volcanos, as the Effect of the same Power by which Continents are elevated. *Transactions of the Geological Society of London*, *s2-5*(3), 601–631.

De Silva, S. L. (1989). Altiplano-Puna volcanic complex of the central Andes. *Geology*.

Eggert, S., & Walter, T. R. (2009). Volcanic activity before and after large tectonic earthquakes: Observations and statistical significance. *Tectonophysics*, *471*(1-2), 14–26.

Fialko, Y., & Pearse, J. (2012). Sombrero uplift above the Altiplano-Puna Magma Body: evidence of a ballooning mid-crustal diapir. *Science (New York, N.Y.)*, *338*(6104), 250–2.

Henderson, S. T., & Pritchard, M. E. (2013). Decadal volcanic deformation in the Central Andes Volcanic Zone revealed by InSAR time series. *Geochemistry Geophysics Geosystems*, *14*(5).

Henderson, S. T., Pritchard, M. E., & Elliott, J. (2013). Quantifying crustal response to deep active intrusions with geodesy-based finite element modeling. In *American Geophysical Union Fall Meeting* (p. V12B–07). San Francisco, CA.

Jay, J. A., Costa, F., Pritchard, M. E., Lara, L. E., Singer, B. S., & Herrin, J. (2014). Locating magma reservoirs using InSAR and petrology before and during the 2011-2012 Cordón Caulle silicic eruption. *Earth and Planetary Science Letters*, *395*, 254–266.

Jay, J. A., Pritchard, M. E., West, M. E., Christensen, D., Haney, M., Minaya, E., … Zabala, M. (2012). Shallow seismicity, triggered seismicity, and ambient noise tomography at the long-dormant Uturuncu Volcano, Bolivia. *Bulletin of Volcanology*, *74*, 817–837.

Jay, J. A., Welch, M., Pritchard, M. E., Mares, P. J., Mnich, M. E., Melkonian, A. K., … Clavero, J. (2013). Volcanic hotspots of the central and southern Andes as seen from space by ASTER and MODVOLC between the years 2000 and 2010. *Geological Society, London, Special Publications*, *380*(1), 161–185.

Kay, S. M., Mpodozis, C., & Ramos, V. A. (2005). Andes. In R. C. Selley, L. R. M. Cocks, & I. R. B. T.-E. of G. Plimer (Eds.), *Encyclopedia of Geology* (pp. 118–131). Oxford: Elsevier.

Linde, A., & Sacks, I. (1998). Triggering of volcanic eruptions. *Nature*, *395*(October), 1997–1999.

Muir, D. D., Blundy, J. D., Rust, a. C., & Hickey, J. (2014). Experimental Constraints on Dacite Pre-eruptive Magma Storage Conditions beneath Uturuncu Volcano. *Journal of Petrology*, *55*(4), 749–767.

Pritchard, M. E., & Simons, M. (2004). An InSAR-based survey of volcanic deformation in the central Andes. *Geochemistry Geophysics Geosystems*, *5*(2), 1–42.

Walter, T., & Amelung, F. (2007). Volcanic eruptions following M≥ 9 megathrust earthquakes: Implications for the Sumatra-Andaman volcanoes. *Geology*, *35*(6), 539.

Watt, S. F. L., Pyle, D. M., & Mather, T. a. (2009). The influence of great earthquakes on volcanic eruption rate along the Chilean subduction zone. *Earth and Planetary Science Letters*, *277*(3-4), 399–407.

CHAPTER 2

SHALLOW SEISMICITY, TRIGGERED SEISMICITY, AND AMBIENT NOISE TOMOGRAPHY AT THE LONG-DORMANT UTURUNCU VOLCANO, BOLIVIA[1]

2.0 ABSTRACT

Using a network of 15 seismometers around the inflating Uturuncu Volcano from April 2009 to 2010, we find an average rate of about three local volcano-tectonic earthquakes per day, and swarms of 5–60 events a few times per month with local magnitudes ranging from −1.2 to 3.7. The earthquake depths are near sea level, more than 10 km above the geodetically inferred inflation source and the Altiplano Puna Magma Body. The Mw 8.8 Maule earthquake on 27 February 2010 triggered hundreds of earthquakes at Uturuncu with the onset of the Love and Rayleigh waves and again with the passage of the X2/X3 overtone phases of Rayleigh waves. This is one of the first incidences in which triggering has been observed from multiple surface wave trains. The earthquakes are oriented NW–SE similar to the regional faults and lineaments. The b value of the catalog is 0.49, consistent with a tectonic origin of the earthquakes. We perform ambient noise tomography using Love wave cross-correlations to image a low-velocity zone at 1.9 to 3.9 km depth below the surface centered slightly north of the summit. The low velocities are perhaps related to the hydrothermal system and the low-velocity zone is spatially correlated with earthquake

---

[1] A version of this chapter was originally published as: Jay, J. A., Pritchard, M. E., West, M. E., Christensen, D., Haney, M., Minaya, E., … Zabala, M. (2012). Shallow seismicity, triggered seismicity, and ambient noise tomography at the long-dormant Uturuncu Volcano, Bolivia. Bulletin of Volcanology, 74, 817–837. doi:10.1007/s00445-011-0568-7. Reprinted with permission from Springer.

locations. The earthquake rate appears to vary with time—a seismic deployment from 1996 to 1997 reveals 1–5 earthquakes per day, whereas 60 events/day were seen during 5 days using one seismometer in 2003. However, differences in analysis methods and magnitudes of completeness do not allow direct comparison of these seismicity rates. The rate of seismic activity at Uturuncu is higher than at other well-monitored inflating volcanoes during periods of repose. The frequent swarms and triggered earthquakes suggest the hydrothermal system is metastable.

2.1 INTRODUTION

Uturuncu is a 6008-m-high Pleistocene dacite stratovolcano located in the Altiplano-Puna volcanic complex (APVC) of the central Andes in SW Bolivia (22°16′ S, 67°11′ W), southeast of the town of Quetena Chico. 39Ar/40Ar ages of the dacite lavas have shown that the volcano was active between 890 ka and 271 ka, with the lavas becoming younger and less extensive at higher elevations (Sparks et al. 2008). Although there are no recent eruptions, Uturuncu has been showing signs of unrest in recent years through surface deformation and fumarolic activity. Interferometric Synthetic Aperture Radar (InSAR) studies have discovered a region of uplift that covers an area of about 70 km in diameter with a central uplift rate of approximately 1 to 2 cm/year between 1992 and 2006 (Pritchard and Simons 2004; Sparks et al. 2008). The source of this deformation is at least 17 km deep below local relief, indicating a magmatic rather than hydrothermal cause, and suggesting that the deformation is a result of the intrusion of new magma into the Altiplano-Puna Magmatic Body (APMB) (Sparks et al. 2008). Also, two active sulfur-producing fumarole fields have been documented near the summit (e.g. Kussmaul et al. 1977; Sparks et al. 2008). In

May 2003 and May 2009, the temperature of these fumaroles was measured to be slightly below 80°C (Sunagua 2004; Sparks et al. 2008; J. Gottsmann, personal communication, 2011), which is nearly the boiling point of water at the elevation of Uturuncu.

These signs of activity have sparked interest in further studies of Uturuncu to investigate the depth and location of potential zones of partial melt and whether that melt is moving. This paper will focus on using local earthquake locations, rates, and magnitudes, the volcano's response to large regional and global earthquakes, and ambient noise tomography to probe the subsurface magma plumbing system.

2.2 BACKGROUND

Uturuncu is within the APVC, an area of volcanism which covers about 50,000 km^2 between 21° and 24°S in Bolivia, Argentina, and Chile (de Silva 1989). From about 17 to 10 Ma, activity in the APVC was dominated by the emplacement of small porphyritic stocks, domes, and ignimbrites in the far backarc (Kay and Coira 2009), and from 10 to 4 Ma, at least 10,000 km^3 of dacitic ignimbrite were erupted (de Silva 1989; de Silva and Gosnold 2007). These eruptions had extrusion rates of 0.004 to 0.012 km^3/year (de Silva and Gosnold 2007). This ignimbrite flare-up is associated with the creation of several large caldera complexes and composite volcanoes.

The APVC is underlain by the APMB, the largest known active continental crustal magma body (Chmielowski et al. 1999). The APMB was identified using seismic receiver functions as a zone of very low seismic velocities at a depth of ~20 km below local relief, with a vs<1.0 km/s and a thickness of ~1 km (Zandt et al.

2003). Another receiver function study, however, gives the thickness of the low velocity zone to be 10-20 km (Yuan et al. 2000). Zones of very high electrical conductivity have also been observed in the region beneath the APVC and are most likely caused by the existence of partial melts in the crust (Schilling et al. 1997). Electrical conductivity investigations of the APMB have quantified the percentage of interconnected partial melt to be at least 14-27 vol.% (Schilling et al. 1997; Schilling et al. 2006).

Although seismology has been used extensively to detect and characterize the APMB, very little research has been conducted regarding shallow seismicity at Uturuncu specifically or other volcanoes of the Central Andes (although see Hellweg 2000; Clavero et al. 2005). From 1 to 6 April 2003, Sparks et al. (2008) carried out a seismic reconnaissance study at Uturuncu, setting up a single vertical component portable seismic recording system at five different sites at different times. While this study gave some indication of background activity (average of 2.6 earthquakes per hour), the present study is the first robust study of seismicity at this volcano using multiple three-component seismometers.

2.3 METHODS

The persistent ground deformation and high rates of seismicity at Uturuncu revealed in 2003 motivated a more complete seismic study of the region. A temporary seismic network was deployed at Uturuncu from April 2009 to April 2010 and consisted of 15 stations surrounding the volcano, with the farthest station located about 25 km from the summit (Fig. 2.1). The network consisted of nine Mark Products L22 short-period and six Guralp CMG-40T intermediate-period three-component seismometers, and a

GPS clock at each station. Data were recorded with a Reftek 130 Datalogger at a sample rate of 50 samples/s. Seismic data were later displayed and analyzed using the Antelope software package. Also, we have re-analyzed data from the five broadband

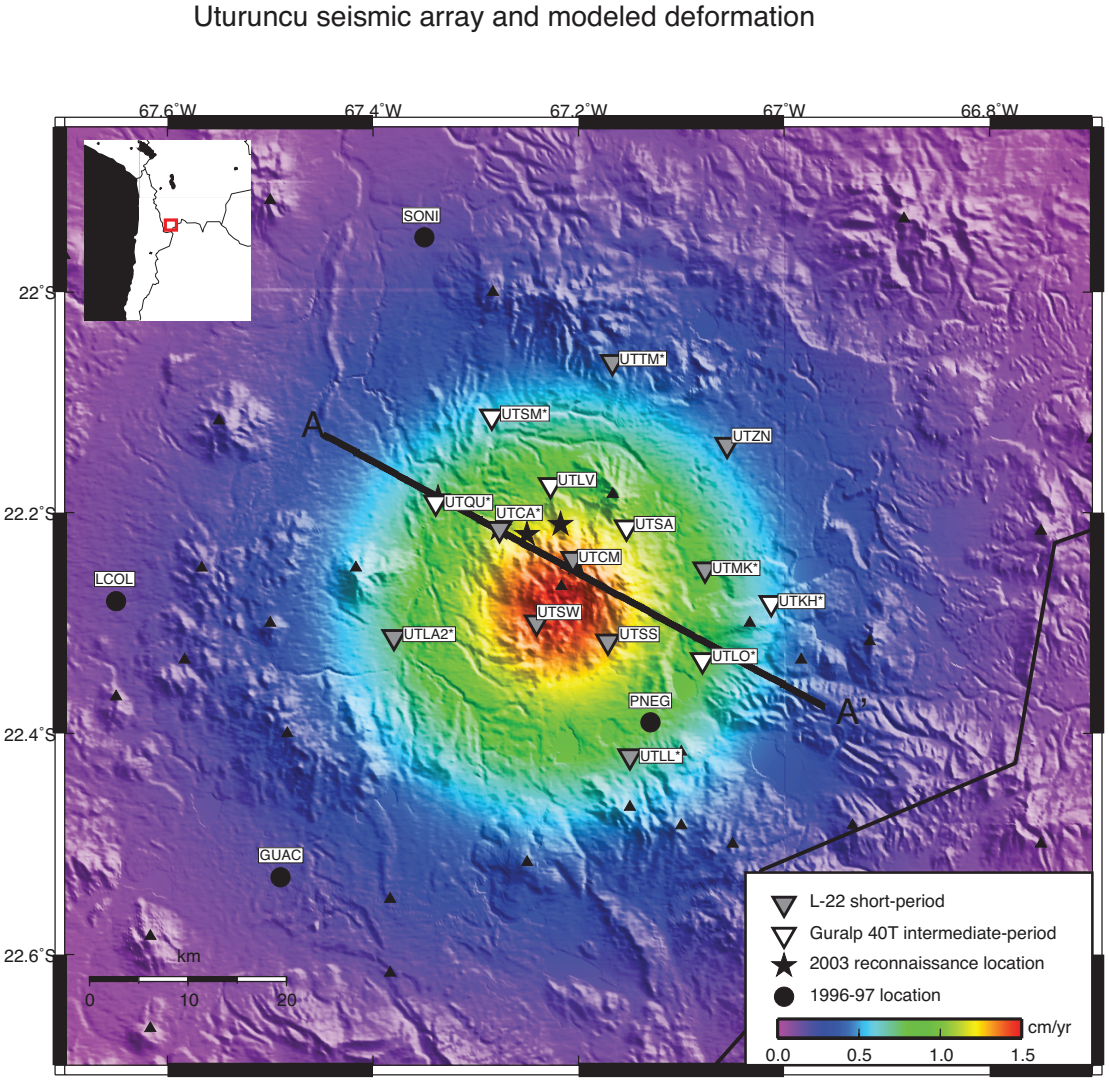

Figure 2.1 Location of seismic stations analyzed in this paper. Different types of instruments are shown with different symbols: inverted triangles are from 2009 to 2010 deployment, stars are from 2003, and circles are from 1996 to 1997. The modeled vertical ground uplift from the models of Pritchard and Simons (2004) is shown in color. Volcanoes from the de Silva and Francis database (1991) are shown as small triangles and the international border between Bolivia and Argentina as the solid line. A–A' profile for cross section in Fig. 2.6

stations ranging in distance from 15 to 76 km from the summit (Fig. 2.1) from the 1996-1997 APVC dataset (Chmielowski et al. 1999) to search for shallow earthquakes.

2.4 EARTHQUAKE LOCATIONS

We performed a manual review of the waveforms focusing on identifying various types of seismic events and locating local earthquakes. Virtually all of the events recorded are typical earthquakes, which volcano seismologists sometimes call volcano-tectionic VT events. These earthquakes demonstrate high-frequency content ranging up to 25 Hz, and clear P and S arrivals. A bandpass filter of 0.8–25 Hz was applied when the P and/or S arrivals could not be clearly distinguished from the noise. Hypocenters of events that had ten or more P and/or S phase picks were located using Antelope's location program genloc (Pavlis et al. 2004). Two different velocity models were used in the earthquake locations. In the first, the seismic velocity structure of the top 40 km was based on model A of Fig. 10 of Leidig and Zandt (2003), which incorporates a 1-km-thick low-velocity zone at 17 km depth. This shallow portion of the velocity model is based on receiver function analysis. Layers deeper than 40 km are based on Table 1 of Schurr et al. (2006). Here, we assume a vp/vs ratio of 1.75 (Table 1). A second velocity model of typical continental crust was also used to locate some of the earthquakes in the catalog. The difference in locations using the two different velocity models was less than typical errors in depth location (1-2 km, with the Leidig and Zandt velocity model giving deeper depths) and negligible differences in latitude and longitude.

Table 2.1: Velocity model used for earthquake location

Depth range (km)	v_p (km/s)	v_s (km/s)
Above 0.5	4.5	2.6
0.5-13	6.1	3.5
13-14	4.0	1.0
14-40	6.1	3.5
40-60	6.5	3.7
60-75	7.5	4.2
Below 75	8.2	4.7

Local Richter magnitudes were calculated based on the peak amplitude on horizontal components of the waveforms in a time window starting from the P arrival time and ending at two times the S-P time and correcting for the distance between earthquake and station. Traces were transformed to Wood-Anderson displacements prior to magnitude calculation.

2.5 AMBIENT NOISE TOMOGRAPHY

To further delineate the shallow crustal structure at Uturuncu, we apply ambient noise tomography (ANT) to the first 140 days of continuous recordings from the local network of 15 three-component seismometers. The fact that all the seismometers are three-component instruments means a multi-component version of ANT can be implemented (Lin et al. 2008). The main difference with conventional single-component ANT is that the temporal-normalization and spectral-whitening filters must be applied identically across all three components (N-S, E-W, and U-D) in order to preserve the relative amplitudes. By applying multi-component ANT to the Uturuncu seismic data, we are able to analyze cross-correlations between pairs of vertical components (ZZ), radial components (RR), transverse components (TT), and mixtures of vertical and radial components (ZR). Rayleigh waves propagating between stations

are captured on the ZZ, RR, and ZR correlations; Love waves appear on the TT correlations. Therefore, with multi-component ANT, we can analyze two independent modes of wave propagation. We do not analyze ZT or RT correlations since in an isotropic layered Earth model these components should be identically zero. In practice, they are not zero but have negligible amplitudes compared to the other correlations.

With 15 stations deployed at Uturuncu, there are 15 transverse and 30 vertical/radial channels. This yields 105 (=15 × 14/2) and 420 (=30 × 29/2 − 15) different cross-correlations for Love and Rayleigh waves, respectively. Note that the 15 cross-correlations between the vertical and radial component from the same seismometer are not used to analyze Rayleigh waves. In principle, the travel times for ANT picked from ZZ, RR, and ZR correlations between a station pair should be the same. However, with noisy data, the different correlations provide independent estimates of the same group travel time. For comparison, Masterlark et al. (2010) previously used multi-component ANT at Okmok Volcano, but since there were 9 single-component and 3 three-component seismometers, ANT could only be applied to the Rayleigh waves and not the Love waves.

Once the cross-correlations have been computed, we proceed with ANT as described in Masterlark et al. (2010) and summarized briefly here. Frequency–time analysis is applied to each cross-correlation, yielding a path-averaged dispersion curve for every station pair. All the path-averaged dispersion curves give a group travel time table as a function of station pair and frequency. At each frequency, 2D travel time tomography gives group velocity maps as a function of latitude and longitude. Finally, at each longitude and latitude point, the local dispersion curve is inverted for a depth

structure. In this manner, a 3D shear-wave velocity model is obtained. At Uturuncu, using the frequency band from 0.15 to 0.5 Hz, we are able to image the shear-wave velocity structure to depths of approximately 5 km. These depths reveal the shallow structure beneath the volcanic edifice and any small magma storage areas below the summit. ANT is not sensitive to the depths of the APMB. In a later section, we discuss how ambient noise methods can be extended to the 20 km depth of the APMB.

2.6 RESULTS

2.6.1 Seismicity

Earthquakes occur at an average rate of about three per day, and swarms of 5–60 events within a span of minutes to hours occur a few times per month (Fig. 2.2a). The extremely high rates of earthquakes at the end of February 2010 are due to events that were triggered by the 2010 Maule earthquake and will be discussed later. Local Richter magnitudes of the events range from about -1.2 to 3.7, with the swarm events generally demonstrating higher magnitudes than the non-swarm events (Fig. 2.2b). The largest non-triggered swarm occurred on 28 September 2009 and consisted of 60 locatable events over a time span of 28 h (Fig. 2.3). The waveforms of these events are high frequency and have clear P and S arrivals (Fig. 2.4). Most of these earthquakes are located close to the summit at depths near and above sea level (Fig. 2.5). While seismicity at Uturuncu is limited to shallow depths, geophysical studies have shown that partial melt in this region resides much deeper, at a depth of ~20 km below local relief (Zandt et al. 2003). Figure 2.6 shows a cross-sectional view of Uturuncu with earthquake depths, the brittle-ductile transition zone (inferred from heat flow studies,

see “Discussion” section), proposed magma body location (Zandt et al. 2003), and modeled deformation source locations (Pritchard and Simons 2004; Pearse and Fialko 2009). Seismic activity is predominantly located at depths of a few kilometers below and above sea level, about 17 km above any of the proposed magma

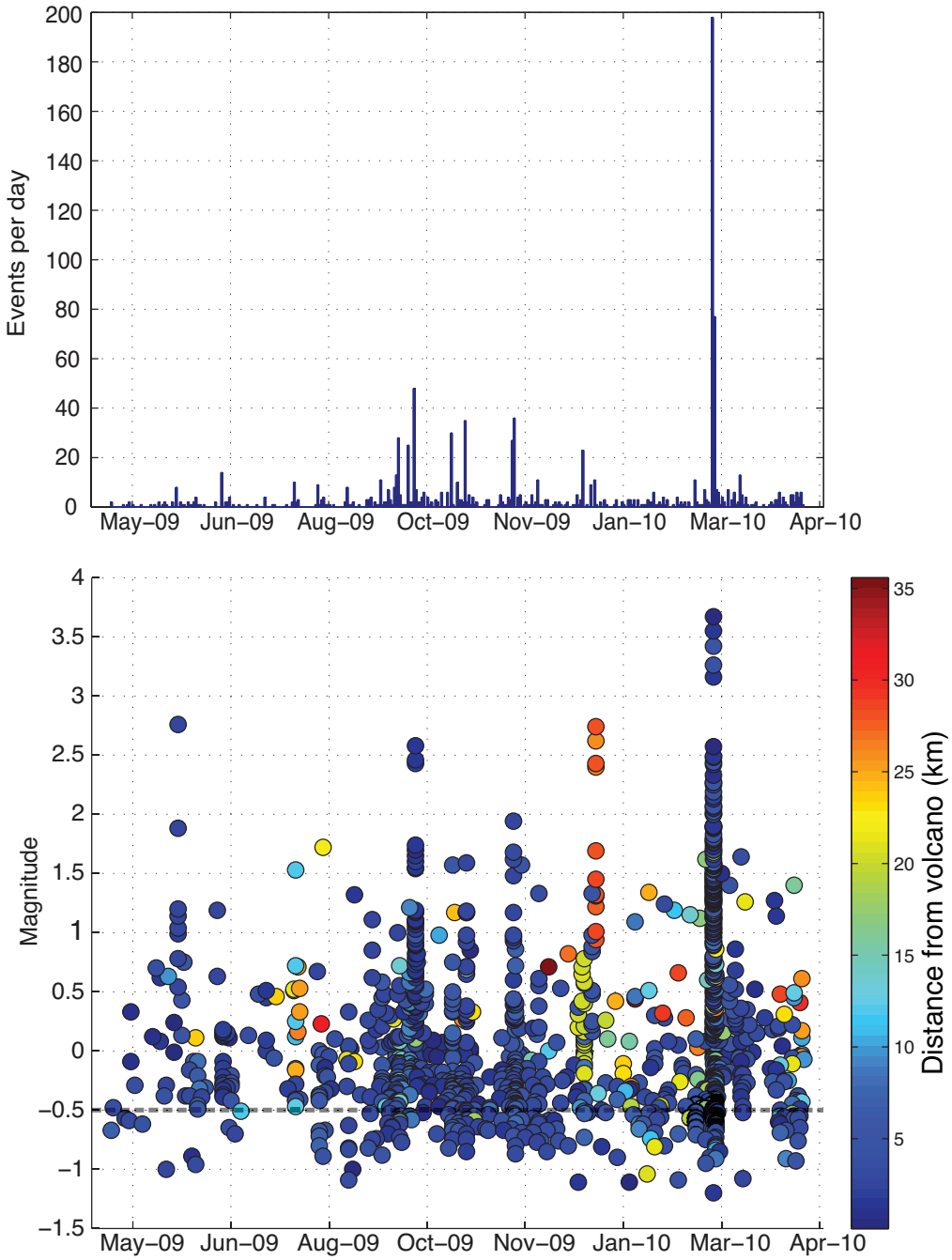

Figure 2.2: (Top) Histogram of the number of earthquakes per day within 50 km of Uturuncu Volcano from April 2009 to April 2010. (Bottom) Plot of the magnitudes of earthquakes as a function of time. Color indicates the distance (in kilometers) from the volcano. Gray dotted line represents magnitude of completeness of −0.51

accumulation regions. There are also earthquakes at deeper depths; these are probably mislocated earthquakes from the slab, which is at a depth of about 150 km beneath Uturuncu (Cahill and Isacks 1992). The error in location is likely caused by the small spatial footprint of the seismic network and the fact that the waveforms from some of the slab earthquakes were highly attenuated so that the S phase arrival could not be detected (see section 2.6.3).

We calculate b values using two different methods: a least squares fit to the frequency-magnitude distribution and a maximum likelihood estimate. Both calculations only include earthquakes that are within the network boundaries, giving a total of 1,138 events. A b value of 0.70 was calculated by fitting a least squares line to the cumulative magnitude histogram with a magnitude of completeness of -0.5. When we exclude the triggered events from the 2010 Maule earthquake (all events from 27 to 28 February 2010, discussed in detail below) from the b value calculation, we find a b value of 0.78 for the 863 earthquakes in the non-triggered catalog, with magnitudes of the catalog ranging from -1.1 to 2.8 and a magnitude of completeness of -0.5. Using the maximum likelihood estimate of the drop-off point in the frequency-magnitude distribution, we calculate a b value of 0.49 ± 0.02 for the complete catalog and a magnitude of completeness of -0.51 ± 0.06 (Fig. 2.7a), using bootstrapping for uncertainties. When we exclude the triggered events from the maximum likelihood b value calculation, we find a b value of 0.64 ± 0.04 (Fig. 2.7b), with magnitudes of the

catalog ranging from -1.1 to 2.8 and a magnitude of completeness of -0.37 ± 0.09. This analysis was performed using the earthquake catalog analysis software ZMAP (Wiemer 2001).

The least squares method of b value calculation gives equal weight to the few events of higher magnitude as the many events of lower magnitude. With the maximum likelihood method, we only consider data up to M 1.5 due to sparsity of

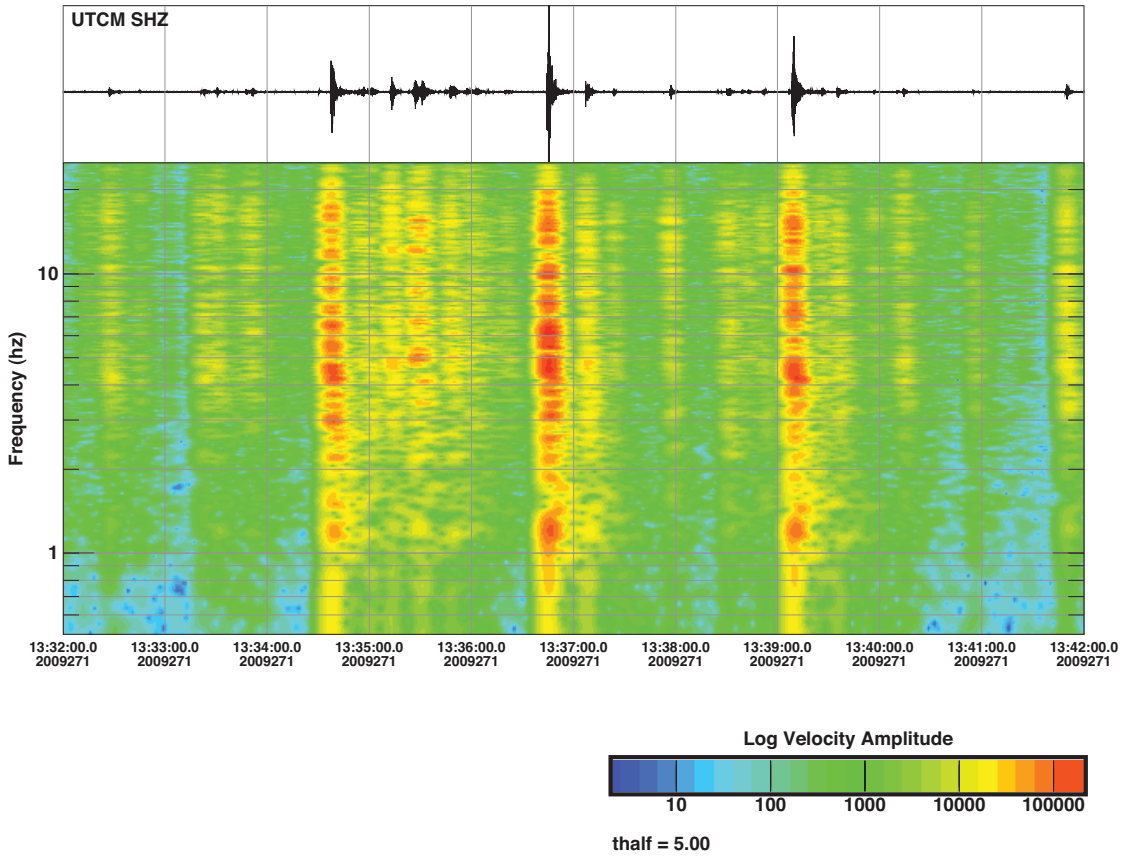

Figure 2.3: Seismogram and spectrogram from earthquake swarm from 28 Sep 2009 shown on station UTCM (short period). Instrument response has been removed. Location of this swarm can be found in Fig. 2.8, swarm #4. Locations of seismic stations are shown in Fig. 2.1

data above that magnitude. The difference in b values using these two methods is striking, but we find the maximum likelihood method to be more robust given the short time span of our dataset. The low b values of the complete catalog and the non-

triggered catalog are typical of tectonic processes (b=1) instead of closer to 2 as observed in other swarms where fluids are shown to be involved (e.g., Legrand et al 2010).

2.6.2 Volcano-tectonic earthquake swarms

Earthquake swarms differ from mainshock-aftershock sequences in that they do not exhibit a dominant mainshock followed by smaller aftershocks; rather, they consist of many events of similar size that are closely clustered in space and time (Benoit and McNutt 1996). The seismic data at Uturuncu suggest multiple swarm centers, with the most active center located just north of the summit (cluster 4 of Fig. 2.8). Swarms were identified as clusters of five or more earthquakes that have a temporal separation of less than 1 hour between each earthquake and spatial separation of less than 5 km. More than half of the Uturuncu earthquakes occur in swarms. Swarms have been identified in various tectonic settings, but they are especially common in volcanic and hydrothermal areas, such as Yellowstone, the Long Valley Caldera, and the Socorro Magma Body (e.g., Brantley et al. 2004; Stankova et al. 2008; Hill and Prejean 2005). Furthermore, like Uturuncu, these regions are known to be actively deforming.

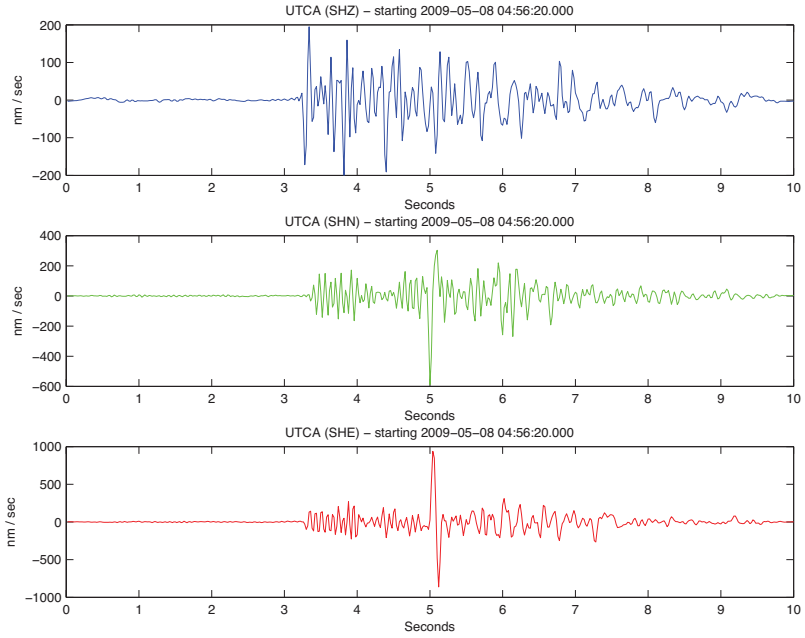

Figure 2.4: Typical waveforms for a shallow, local M -0.29 volcano-tectonic earthquake at Uturuncu shown on station UTCA (short- period). Instrument response has been removed. Locations of seismic stations are shown in Fig. 2.1. Vertical (SHZ), north-south (SHN), and east-west (SHE) components are shown.

2.6.3 Swarm triggered by the Maule earthquake

The Mw 8.8 Maule, Chile earthquake on 27 February 2010 triggered hundreds of local VT earthquakes at Uturuncu, which is located about 1,600 km from the epicenter. Rates of seismicity remained heightened for about 2 days following the earthquake before returning to normal background rates. The locations of the triggered events are similar to those of the non-triggered events (Fig. 2.9). High-pass filtering of the long period surface waves reveals that the first triggered events occurred with the onset of the minor-arc Love (G1) and Rayleigh (R1) waves (Fig. 2.10). The magnitude of the largest triggered earthquake is 3.7, which is also the largest magnitude event in the entire catalog. This earthquake is the second locatable triggered event and occurs with the onset of the Rayleigh wave. Triggered event waveforms are high frequency with

clear P and S arrivals (Fig. 2.11), similar to the non-triggered waveforms. Rates of triggered events reach up to one event per minute for about 1 h following G1/R1 arrivals. Triggered activity gradually declined following the passage of the R1 and G1 waves, however rates of triggered events increased again to a peak rate of two events per minute with the passage of the X2/X3 Rayleigh wave overtones, and this rate was sustained for about 20 min (Fig. 2.12). The X2/ X3 overtones are slightly higher in frequency than the G2/ G3 and R2/R3 waves, which do not appear to directly trigger seismicity, though they are lower in amplitude than the G2/G3 waves. The peak dynamic stresses associated with the passage of the surface waves were calculated using the method of Hill et al. (1993) and are shown in Table 2. The calculation was done using data from station UTKH, an intermediate-period station with a CMG-40 T sensor. A four-pole Butterworth low-pass filter of 0.01 Hz was necessary to examine the higher mode surface waves.

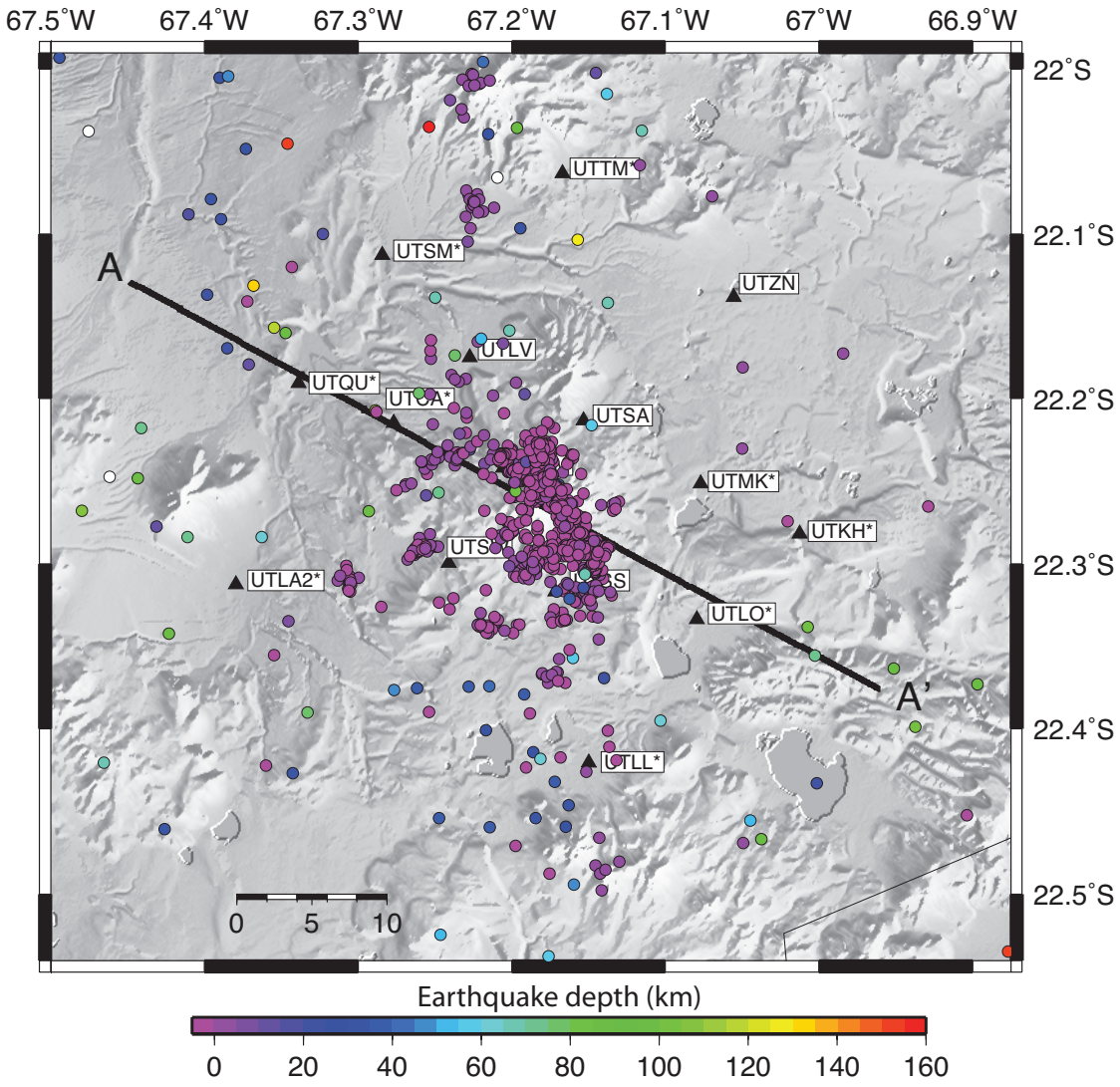

Figure 2.5: Locations of earthquakes from 2009 to 2010, with the earthquake depths relative to sea level shown in color. Data use hand-picked arrival times. The solid line shows the location of the profile in Fig. 2.6

2.6.3 Low-frequency regional events

Low-frequency events (2-3 Hz) lacking S waves are found throughout the dataset at an average rate of three per day. Though the locations of these events are poorly constrained, they are generally located outside of the station network and thus were not included in the catalog. There are 62 earthquakes with depths greater than 20 km

that are within the network and in the catalog. It is unclear whether the low-frequency content of these events is a result of a path effect or a source effect. We suspect that most of these events are regional slab earthquakes whose shear waves and high frequencies have been attenuated in the APMB. However, there are also regional slab earthquakes recorded by the network that do show distinct S-wave arrivals on all stations. An intermediary type of waveform shows highly attenuated S-wave arrivals that are only detected on the intermediate-period CMB-40T stations. This pattern of S-wave occurrence suggests that waves from various earthquakes undergo varying degrees of attenuation as they travel from their respective hypocenters to Uturuncu. A further study of this attenuation zone would be helpful in constraining the location and boundaries of the APMB and is planned. We do not rule out the possibility that some of the low-frequency events are occurring at deeper levels beneath Uturuncu, but further study is necessary to investigate this idea.

2.6.4 1996-1997 APVC array

From November 1996 to September 1997, Chmielowski et al. (1999) set up a seismic network, the APVC array, to record teleseismic earthquakes and local intermediate-depth events for receiver function analysis of the APMB. Five of the stations in the network (PNEG, LCOL, GUAC, CHAS, and SONI—Fig. 2.1) were located close enough to Uturuncu to potentially record seismicity from the volcano. Data from station PNEG, located 15 km SSE of Uturuncu, show a mean of about two local earthquakes per day from 10 November 1996 to 31 December 1996, determined by S-P times of 5 s or less. Most of these events cannot be located because they are

typically only recorded on PNEG, but an earthquake of unknown magnitude on 19 November 1996 was large enough to show up on four stations and is located roughly 3.5 km east of PNEG. There is also evidence in the larger footprint of the APVC array for another source of shallow seismicity away from Uturuncu ~14 km southeast of Laguna Colorada, or about 5-6 km south of station LCOL. This region demonstrated swarm-like activity from late December 1996 to early January 1997.

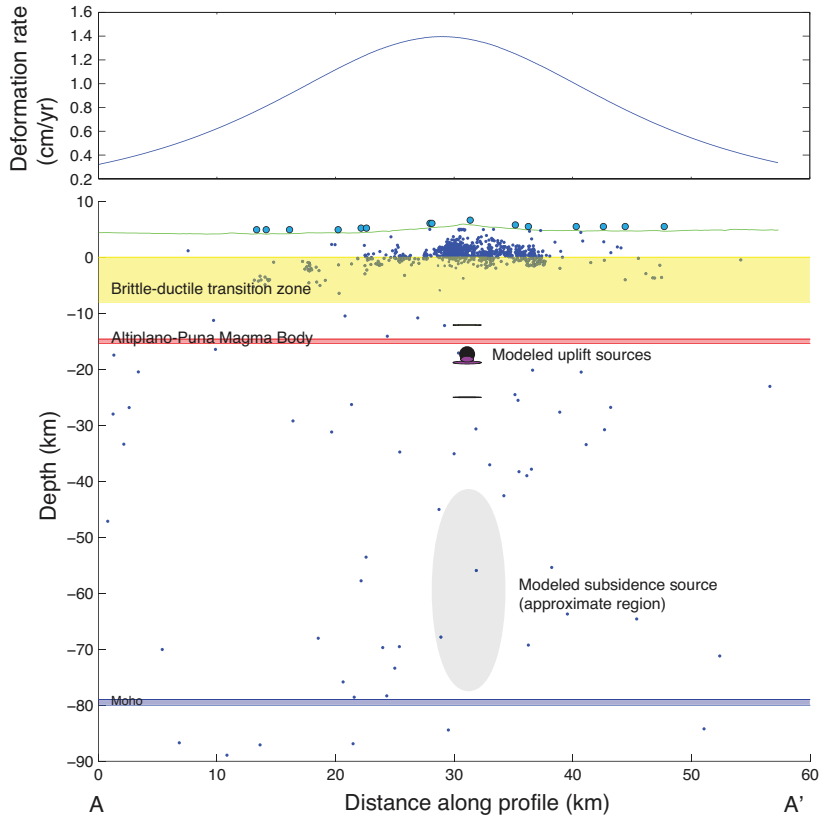

Figure 2.6: Cross section of earthquakes at Uturuncu from the profile shown in Fig. 2.5. Blue circles show the locations of seismometers, the depth of the APMB and Moho is from Zandt et al. (2003), the range of depths of the source of uplift is from Pritchard and Simons (2004), and the inferred depth range of the source of subsidence is estimated from Pearse and Fialko (2009) and unpublished work. The range of depths of the inferred brittle-ductile transition is discussed in the text. Deformation rate along profile (top) is from the model of Pritchard and Simons (2004) and shows vertical displacement. Green line shows topography

2.6.5 Time variability of seismicity rates

Direct comparison of seismicity rates from the 1996-1997 APVC array (Chmielowski et al. 1999), the 2003 (Sparks et al. 2008) reconnaissance study, and the 2009-2010 Andivolc array is difficult for multiple reasons. Differences in instrumentation, station locations, network durations, and data analysis techniques all contribute to very different magnitudes of completeness for each time period. The APVC array is more spread out and farther from the volcano, with the closest station being on the edge of the 2009-2010 array. Analysis of the APVC array was less thorough, and locations and magnitudes were generally not calculated. The 2003 reconnaissance study was carried out at locations close to the summit of the volcano, and the instruments were only deployed for 2-14 h at each station. Only 40 earthquakes were observed, locations could not be determined, and the method of magnitude calculation (coda duration) differed from the method used for the 2009-2010 dataset (amplitude based).

In spite of the difficulties, we attempt a search for temporal variations in an effort to determine if our 2009-2010 results are applicable across time as a background rate. We find an average rate of ~2 volcano-tectonic earthquakes per day from 1996 to 1997, and most of these are only recorded at one station of the array. In 2003, Sparks et al. (2008) found an average rate of 2.6 volcano-tectonic earthquakes per hour, which is equivalent to 62 earthquakes per day. This rate is much higher than rates measured in 1996-1997 and 2009-2010; this discrepancy is largely due to a lower magnitude of completeness for the 2003 dataset. To determine if seismicity rates of 2003 are comparable to rates in 2009-2010 when looking at just one station, we

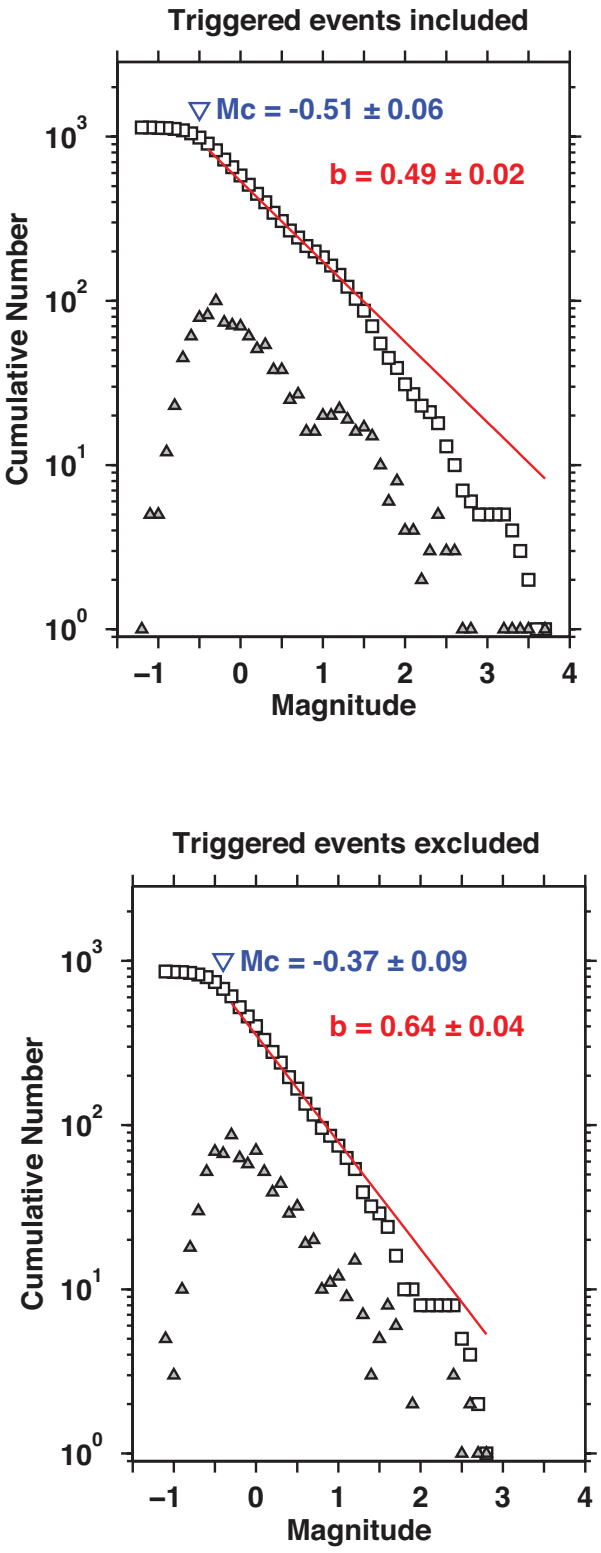

Figure 2.7: Magnitude–frequency histograms for calculating b values. Squares markers are cumulative and triangular markers are non- cumulative. (Top) All events included. (Bottom) Triggered events (all events from 27 to 28 February 2010) are excluded

examined 1 month of data from just the summit station (UTCM) and found an average rate of about seven to eight earthquakes per day, and >70 earthquakes in 1 h spanning the height of the 28 September 2009 swarm. One explanation for why the 2003 rates are so high is that during the 6 days of the seismic reconnaissance (1–6 April 2003), Uturuncu may have been in the midst of a swarm episode. The largest global earthquake that occurred during the 2003 deployment was a M 6.3 on 2 April 2003, located at the Mid-Atlantic Ridge, so we are confident that the high seismic activity detected in April 2003 was not a result of triggering due to the lack of great earthquakes during the time span of the deployment.

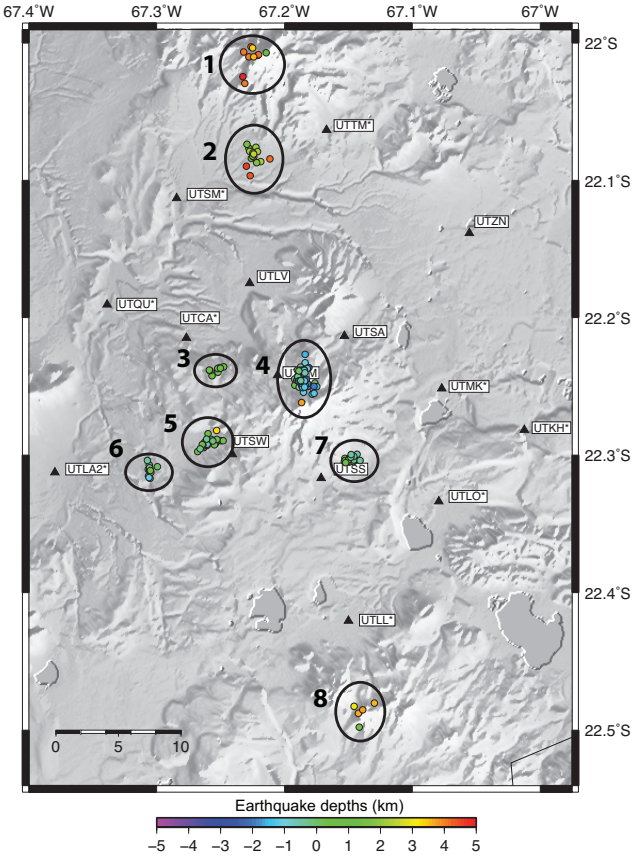

Figure 2.8: Locations of selected individual swarms in 2009: (1) 29 Dec, (2) 23 Dec, (3) 23 Dec, (4) 28 Sep, (5) 25 Sep, (6) 20 Sep, (7) 17 Oct, (8) 29–31 July. Swarms are defined in text

2.6.6 Ambient noise tomography

In Fig. 2.13, we show the envelopes of the cross-correlations at 0.3 Hz for all possible pairs of both Rayleigh and Love waves. The envelopes of the cross-correlations are plotted in Fig. 2.13 as a function of time and interstation distance, the distance between each station pair. The peak of each envelope is shown as a black circle. For the Love waves, the arrival time of the peak (the group travel time) is seen to depend almost linearly on the interstation distance. This is indicative of a direct, fundamental mode Love wave propagating between the stations. The best fitting line

to the moveout of the Love waves is related to the average Love wave velocity at a center frequency of 0.3 Hz. The deviations from this linear moveout are the 3D structure we attempt to image. The situation for Rayleigh waves is more complicated, as seen in Fig. 2.13b. Whereas the linear dependence of the group travel time on interstation distance for the Love waves is clear, the peaks for the Rayleigh wave do not display a clear linear moveout. This may be related to (a) an ambient noise wave field dominated by Love waves at Uturuncu or (b) a higher mode present in the Rayleigh waves that interferes with the fundamental mode, hindering the picking of arrival times. In either case, the Love waves present a superior opportunity for ANT than the Rayleigh waves. As a result, we have proceeded with Love wave ANT at Uturuncu. We note that our observation is at odds with studies which have found Rayleigh waves to be more reliably extracted from ambient noise than Love waves (e.g., Behr et al. 2011). However, a similar conclusion has been made by Lin et al. (2008), wherein the authors noted that ambient noise Love waves had a higher signal-to-noise ratio than Rayleigh waves in the western United States between 10- and 20-s period. Such observations of frequency bands with dominant Love waves implies that the Love waves do not arise as the result of mode-conversion of ambient noise Rayleigh waves. This raises the issue of how the interaction of the ocean and the solid Earth, the known mechanism of microseisms, produces shear forces that would result in mostly Love wave radiation in certain frequency bands. Shown in Fig. 2.14 are slices out of the 3D shear-wave velocity model derived from the Love waves. Notable is the prominent low-velocity zone (LVZ) at 1.9 km depth below the surface centered slightly to the north of the summit. The location of the LVZ to the north of the summit

overlaps spatially with the location of the most vigorous swarm activity observed at Uturuncu, suggesting a possible connection between the volcanic structure and regions of swarm seismicity. This LVZ persists to 3.9 km depth and may represent the final pathway for magma ascending from greater depths or a zone of hydrothermal alteration. Whether the present-day shallow low-velocity anomaly is indicative of fracturing, hydrothermal activity, or shallow magma storage will require more careful integration of the ANT results with earthquake and deformation data.

A denser network of 16 broadband stations (Guralp CMG-3 T sensors) was deployed at Uturuncu in April 2010, and 14 more were deployed in April 2011. Data from this network will be used in the future to image the deepstructure of Uturuncu down to the APMB using the microtremor method (Okada 2003).

2.7 DISCUSSION

2.7.1 Heat flow and the brittle-ductile transition zone

The majority of shallow earthquakes beneath Uturuncu are located at depths near or above sea level, which is about 5 km below the summit of Uturuncu. In order to determine whether the bottom of the seismicity is revealing the top of a magma chamber or is simply related to a reasonable regional heat flow, we calculate the depth of the brittle-ductile transition (BDT) based on heat flow. We hypothesize that deeper earthquakes are less abundant due to the shallow depth of the BDT beneath Uturuncu. A similar idea has been proposed at many other places around the world, where seismicity occurs primarily above the BDT (e.g., Hill 1992). We calculate the depth of the BDT based on heat flow density to determine if the BDT agrees with the depth of

seismicity and if the heat flow measurements are reasonable. The calculation will also have implications for the rheology of the subsurface beneath Uturuncu.

The first step in calculating the depth of the BDT is to determine the heat flow near Uturuncu. Although there have been no heat flow studies at Uturuncu, regional measurements from Springer and Forster (1998), Hamza et al. (2005), and Henry and Pollack (1988) were used to make a first-order estimate of the heat flow at Uturuncu. The nearest heat flow measurement was taken in Bolivia at Kolpani by Henry and Pollack (1988), and its value is 94 mW/m^2. In Table 1 of the paper, the coordinates are given as 21°18′S, 66°41′W, but Fig. 2.1 of the same paper plots this site at a location that appears to be further south. Furthermore, data provided by the Global Heat Flow Database of the International Heat Flow Commission website provided by the University of North Dakota (www.heatflow.und.edu) gives the coordinates of the Kolpani as -22.1856, -66.6833 and references this value as taken from Henry and Pollack (1988). Other nearby heat flow measurements in northern Chile at El Loa and

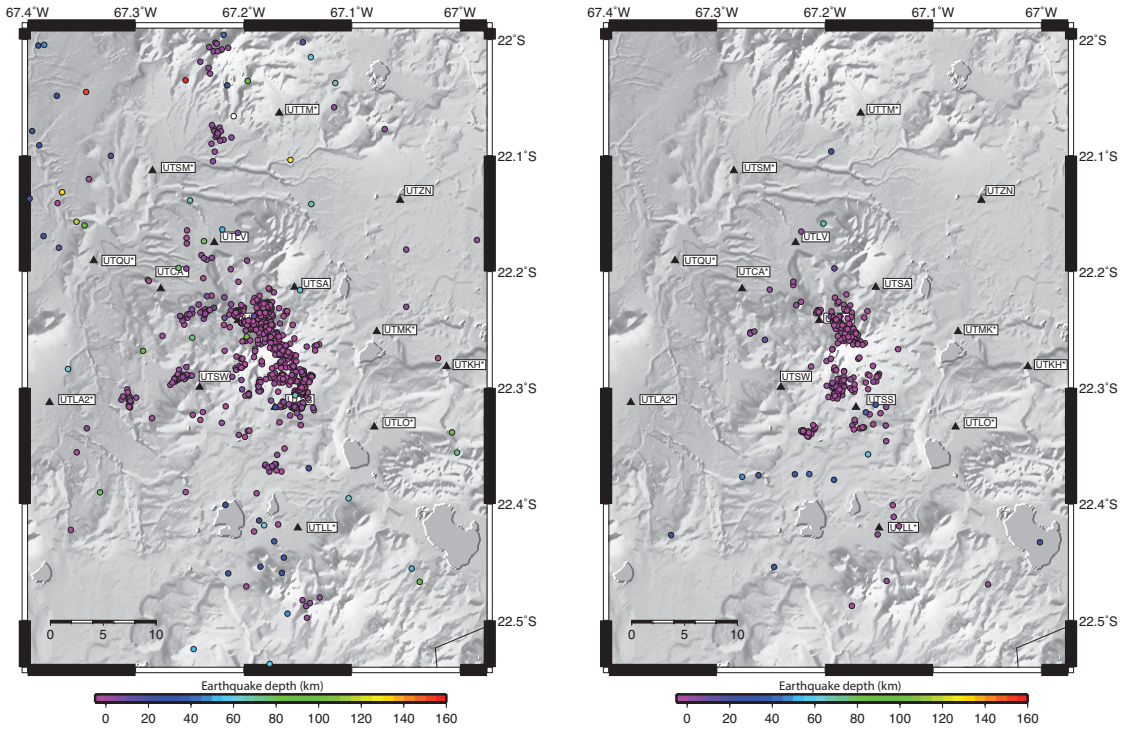

Figure 2.9: Seismicity maps of (left) non-triggered and (right) triggered events. Triggered events include all events from 28 Feb to 9 Mar 2010 and non-triggered events include all other data outside of that time span

Mansa Mina are 150 and 55 mW/m^2, respectively (Springer and Forster 1998). To the northeast in Bolivia, measurements are in the range of ~70–100 mW/m^2 (www.heatflow.und. edu). Figure 5 of Hamza et al. (2005) shows a heat flow map of the Central Andes that suggests that Uturuncu is located in an area of heat flow of up to 200 mW/m^2. For this reason, the BDT zone was calculated using values of heat flow of 100, 150, and 200 mW/m2 for geothermal gradient calculation. The BDT is then determined by calculating the intersection of the curve of maximum strength of frictional sliding vs. depth with the curve of maximum strength of plastic flow vs. depth. Maximum strength of frictional sliding was calculated using Byerlee's law, particularly Eq. 1a and b of Kirby and Kronenberg (1987),

$$\sigma_1 - \sigma_3 = 3.9\sigma_3$$

$$\sigma_1 - \sigma_3 = 218 + 2.1\sigma_3$$

And maximum strength of plastic flow was calculated using Eq. 5,

$$\sigma_1 - \sigma_3 = \left(\frac{\dot{\varepsilon}}{A}\right)^{1/n} \exp\left(\frac{H^*}{nRT}\right)$$

where $\sigma_1 - \sigma_3$ is the differential stress, $\dot{\varepsilon}$ is the strain rate, A is the material constant, n is a dimensionless constant for power law creep, H^* is the activation enthalpy, R is the gas constant, and T is the temperature.

The strain rate was determined from the deformation rate of 1 cm/year over an area of $\sim 10^2$ km^2 (10^{-14} s^{-1}), and creep parameters were taken from Table 1 of Ranalli and Murphy (1986). Using heat flow values of 100, 150, and 200 mW/m^2 and creep parameters for quartz diorite, the brittle– ductile transition occurs at depths of 8.5, 4.5, and 2.5 km below sea level, respectively. Using creep parameters for granite, the brittle-ductile transition occurs at 5.0, 2.2, and 0.8 km below sea level (Table 3). Many earthquakes at Uturuncu fall within these depth zones, but most occur above the shallowest calculation of 0.8 km (Fig. 2.6). This could imply a higher heat flow at Uturuncu than what was found in the literature, a weaker rheology of the shallow subsurface, or a combination of the two. Specifically, either the heat flow at Uturuncu is greater than 200 mW/m^2, the rheology is weaker than granite, or both. As seen in Fig. 2.6, earthquake depths increase with distance from the summit of Uturuncu, a trend that is consistent with higher heat flow at the summit than in the surrounding areas; however, it is also important to note that depth determinations become more unreliable at the edges of the network.

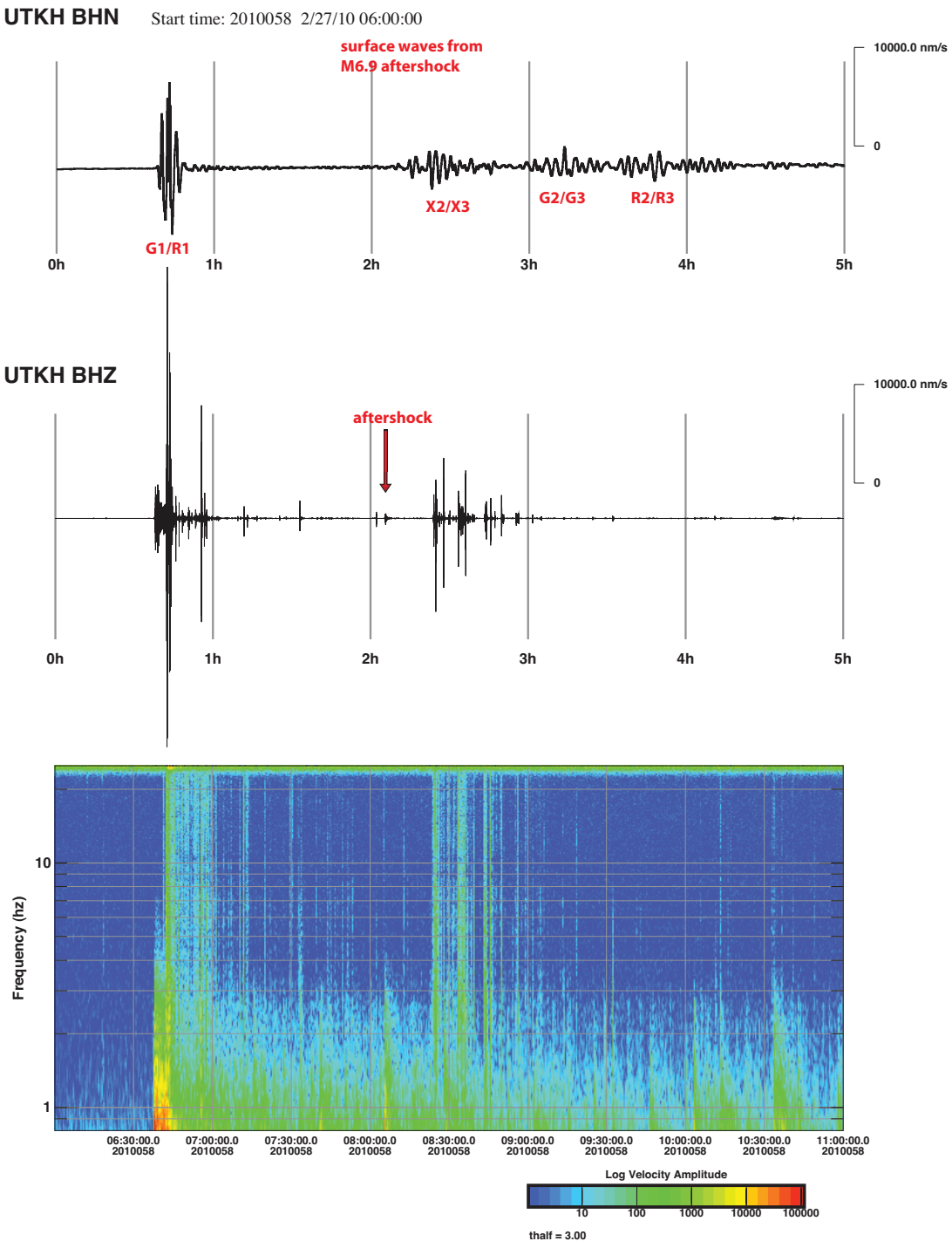

Figure 2.10: Earthquakes triggered by the Feb. 27, 2010 Mw 8.8 Maule, Chile earthquake. (Top) Low-pass filtered (fifth order Butterworth filter, 0–0.006 Hz) waveform showing different surface wave phase arrivals. (Middle) High pass filtered (fifth order Butterworth filter, 2– 25 Hz) waveform showing triggered local earthquakes and some aftershocks. Most unlabeled events are local earthquakes. Amplitude scale bar is in nanometer per second. (Bottom) Spectrogram showing high-frequency local earthquakes amidst long period surface wave energy from the Maule earthquake

2.7.2 Regional tectonics

There are four major transverse tectonic lineaments running NW-SE in the southern Altiplano to northern Puna (Viramonte et al. 1984). Volcanic centers tend to align with these lineaments, which reflect the structure of the basement layers. The northernmost lineament, the Lipez-Coranzuli lineament (also known as the Pastos Grandes-Cojina lineament) runs through Uturuncu (e.g., Lema and Choque 1996). The locations of volcano-tectonic earthquakes at Uturuncu are also oriented in a NW-SE trend, suggesting a relationship between the fault system at Uturuncu and the regional tectonics of the area. A NW-SE trending fault beneath Uturuncu may serve to localize stresses that are accumulating over the broad area of uplift (e.g., Sparks et al. 2008).

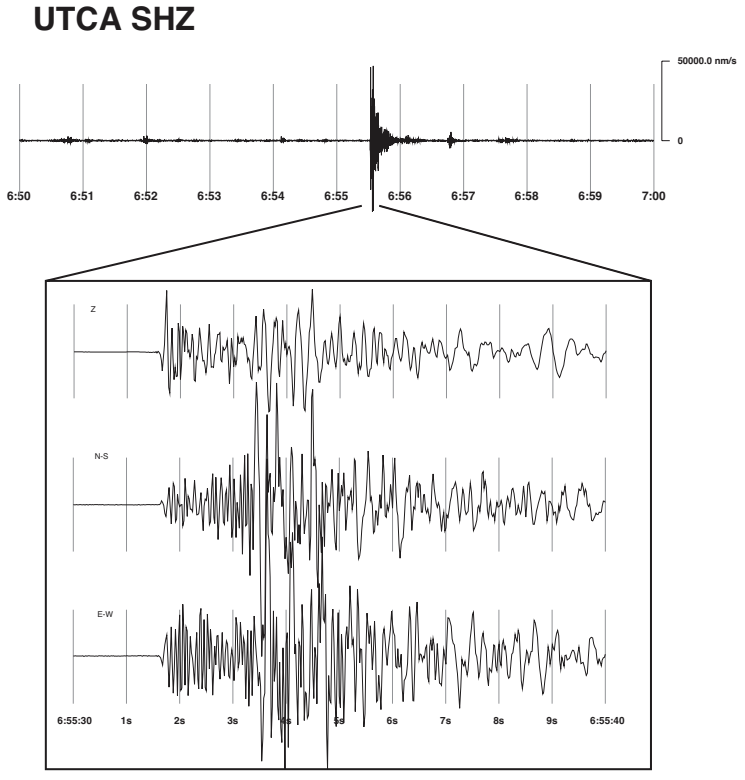

Figure 2.11: Examples of a triggered event waveform on station UTCA, a short-period sensor, at 6:55 am UT on 27 February 2010. Inset shows all three components

Earthquake swarms are common in volcanic regions, and proposed mechanisms for swarm generation usually involve initiation of activity by magmatic or other fluid processes (Hill 1997). We propose that swarms at Uturuncu are caused by magmatic processes related to the active inflation of the volcano, which in turn imposes stress on pre-existing faults in shallow regions beneath the volcano. This conclusion is consistent with the high-frequency, tectonic nature of the swarm waveforms, and a low b value of 0.49. However, the existence of swarms and triggered seismicity does indicate the involvement of magmatic and/or hydrothermal fluids in the generation of earthquakes, probably by changing effective stress by changes in pore pressure.

2.7.3 Response to large distant earthquakes

The triggering of seismicity at Uturuncu by the 2010 Maule earthquake is not an uncommon phenomenon; in fact seismic triggering by large distant earthquakes has recently been observed at many volcanic and geothermal regions around the world. For example, in 2002 the Mw 7.9 Denali Fault earthquake triggered earthquake swarms at volcanic and geothermal locations throughout the western United States at distances of up to 3,660 km from the epicenter (Prejean et al. 2004). In 2004, the Mw 9.0 Sumatra earthquake triggered a swarm at Mount Wrangell Volcano in Alaska, nearly 11,000 km away from the epicenter (West et al. 2005). The literature shows that triggered swarms usually begin with the arrival of the Love and Rayleigh waves, and in some cases there can also be a delayed response, such as a swarm that occurs hours after the large earthquake.

Table 2.2: Surface wave amplitudes of the 2010 Maule earthquake. Peak ground displacements are measured on station UTKH with a 4-pole Butterworth low-pass filter of 0.006 Hz. Love wave displacements are measured on the E–W component, Rayleigh on the Z component, and overtones on the N–S component. Peak velocities are the magnitudes of the peak velocity vectors

Arrival time (UTC)	Phase	Peak displacement (cm)	Peak velocity (cm/s)	Peak dynamic stress (kPa)
6:42	G1	0.8	0.93	93
6:43	R1	0.6	1.40	140
8:23	X2/X3	0.1	8.7x10-4	0.087
9:13	G2/G3	0.5	1.0x10-3	0.10
9:43	R2/R3	0.26	1.0x10-4	0.010

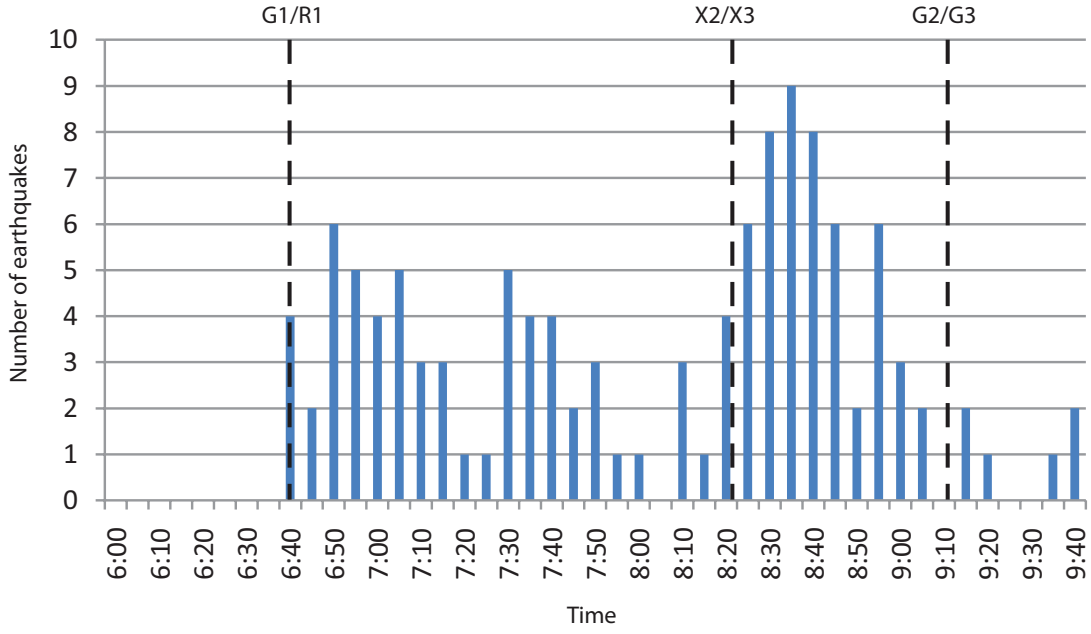

Figure 2.12: Histogram of triggered events from the Maule earthquake in 5-min bins. Dashed lines show arrival times of surface wave trains

Many models have been put forth regarding mechanisms for remotely triggered seismicity, involving frictional failure, non-magmatic crustal fluids, and crustal magma chambers. In order to explain the triggering mechanism at Uturuncu, we need to consider the following observations. First, Uturuncu is located outside of the near-field of the Maule earthquake, so dynamic stress changes are dominant and

static stress changes can be ignored. Second, triggered seismicity at Uturuncu demonstrates both immediate triggering in the surface wave train and delayed triggering which continued for 2 days following the Maule earthquake. Third, the triggered earthquakes are located in the same regions as the non-triggered earthquakes and have similar waveforms. Fourth, we know that Uturuncu is underlain by an inflating mid-crustal magma chamber and a shallow hydrothermal system which gives rise to sulfur-producing fumarolic fields at the summit. We consider models for remote triggering mechanisms that are consistent with all of these observations.

There are two plausible models that can explain the immediate triggering of seismicity at Uturuncu. The first requires changes in the state of the fault or friction across the fault surface and can directly explain triggering that is coincident with the passage of surface waves (Prejean et al. 2004). In this model, the earthquakes that occurred within the surface wave trains are a result of slip on local pre-existing faults directly triggered by favorably oriented dynamic stresses from the Maule surface waves. Though this model is attractive due to its simplicity, we do not have focal mechanisms for the triggered earthquakes to show that the faults are oriented favorably with respect to the dynamic stresses. The second model involves changes in pore fluid pressure as seismic waves perturb the hydrothermal system and redistribute pore pressure (Hill et al. 1993; West et al. 2005). The elevation of pore pressure reduces the strength of the fault rocks, leading to shear failure and triggered seismicity. The fact that the largest magnitude earthquake in the catalog was one of the first triggered events suggests that transient perturbation of the shallow crust by passing surface waves caused a greater amount of fault slip than is normally

accumulated due to the inflating mid-crustal magma chamber. This observation is consistent with both models.

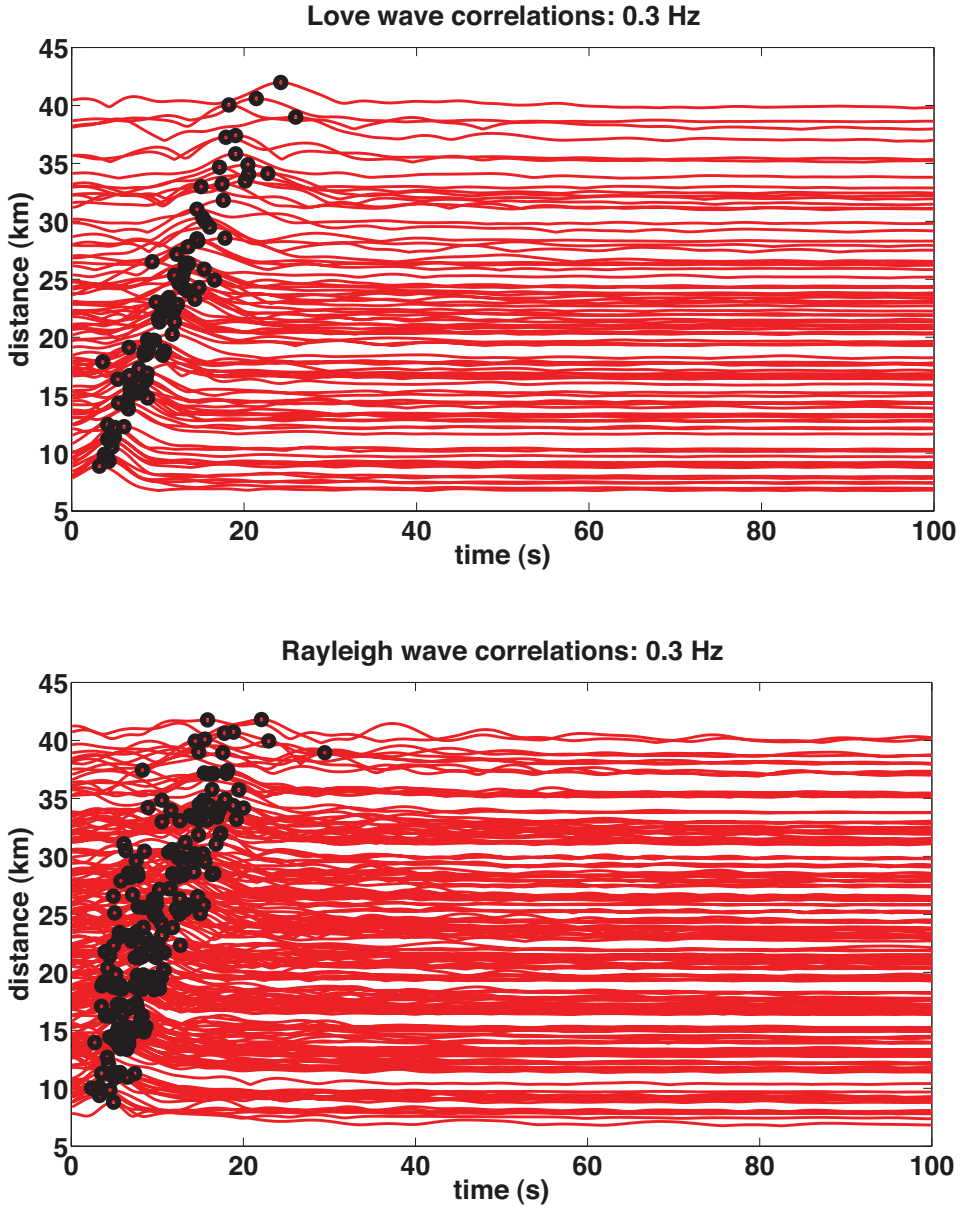

Figure 2.13: Envelopes of the ANT cross-correlations at 0.3 Hz for all possible pairs of both Rayleigh and Love waves, plotted as a function of time and interstation distance, the distance between each station pair. The peak of each envelope is shown as a black circle

Earthquakes that occurred after the passage of the surface waves but within 2 days of the Maule mainshock are triggered by dynamic stress changes that have been

converted into sustained stress changes (e.g. Husen et al. 2004; Prejean et al. 2004). This conversion can occur in a number of ways, and here, we suggest two plausible mechanisms at Uturuncu. The first involves the rupture of fluid seals in the hydrothermal system, leading to redistribution of pore pressure. This is similar to the immediate triggering mechanism, but with a delayed effect due to the response time for fluids to be transported. The second involves changes in the state of the mid-crustal magma chamber as the seismic waves pass through. In this model, the delayed triggering of seismicity is a secondary result of deformation that is triggered by internal pressure change of the magma chamber. Thus, delayed triggering can be attributed to the same process that generates background seismicity at Uturuncu -- pressure changes in the magma chamber cause uplift of the surface, exerting stress on shallow faults and resulting in swarms of volcano-tectonic earthquakes.

In order to assess the occurrence of triggered seismicity, we analyze waveforms from other large earthquakes that occurred during the time span of the network deployment. A review of other large global earthquakes shows that none of the 17 Mw > 7 earthquakes triggered significant activity at Uturuncu. The largest earthquake besides the Maule earthquake to occur during the deployment of this network was the Mw 8.1 Samoa Islands earthquake on 29 September 2009. The distance from Uturuncu to the Samoan earthquake is 10,800 km, and the peak amplitude of the Love waves (measured on the N–S component of station UTKH with the same filtering as described above) is 1.3×10^{-3} cm/s, greater than the amplitude of the X2/X3 overtone surface waves from the Maule earthquake but three orders of magnitude less than the amplitude of the Maule G1 waves. Nonetheless the triggered

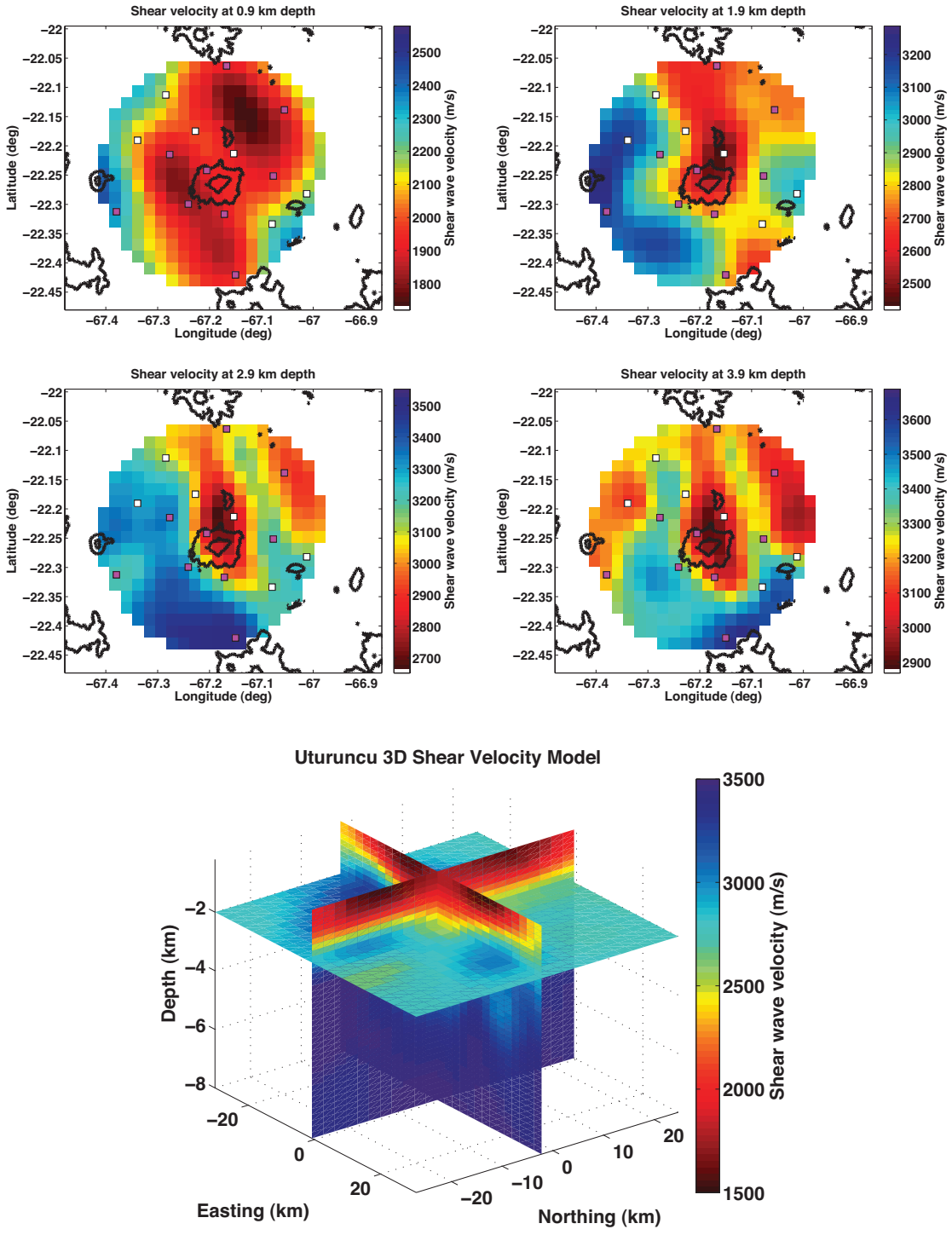

Figure 2.14: Ambient noise tomography results showing shear-wave velocities at various depths. Pink and white squares are seismic station locations for intermediate-period and short-period seismometers, respectively

earthquakes at Uturuncu seem unique in that triggering by the X2/X3 Rayleigh wave overtones has not been previously noted in the literature. If there is a threshold for triggering, it might depend on the previous history of the region since the X2/ X3 wave triggered earthquakes at Uturuncu but the Samoan earthquake did not. It is also important to note that the amplitude of the surface waves might not be the only criteria for triggering; the orientation or frequency content of the waves may also play a significant role in whether earthquakes are triggered. For the Maule earthquake, the Love waves are oriented predominantly E-W while in the Samoan case, they are oriented N-S. Interestingly, the Samoan earthquake occurred about 8 h after the last earthquake of the largest non-triggered swarm in the dataset, indicating that Uturuncu may have been in a relatively stable state since stresses had just recently been released during the swarm.

Table 2.3: Depth to the brittle-ductile transition zone. Various BDT depths (relative to sea level) assuming different rock types and heat flow values at Uturuncu

Rock type	Heat flow (mW/m^2)	BDT depth (km)
Quartz diorite	100	8.5
Quartz diorite	150	4.5
Quartz diorite	200	2.5
Granite	100	5.0
Granite	150	2.2
Granite	200	0.8

2.7.4 Global context

In order to place our findings at Uturuncu into a global context, we examine the literature for other deforming volcanoes that are being seismically monitored. Our goal is to determine if volcanic inflation is normally accompanied by seismicity, or if the high rate of seismic activity at Uturuncu is unusual for a volcano that has not erupted since 270 ka. Ideally, we would compare Uturuncu to other deforming dacitic

volcanoes in the Andes, but we are not aware of any that are seismically monitored. Instead, we focus our comparison on other volcanic systems that are similar to Uturuncu. Though some of the Cascades and Aleutian arc volcanoes differ in magma composition, they are relevant for comparison due to their location in a subduction zone setting. It is also important to compare Uturuncu to large caldera systems such as Yellowstone because although Uturuncu is currently a stratovolcano, it is located in a region surrounded by large calderas, the APVC. We also examine the literature concerning the Socorro Magma Body – though it differs in both composition and setting, it has striking similarities to the Altiplano-Puna Magma Body which underlies Uturuncu. In comparing Uturuncu to other arc volcanoes, calderas, and a mid-crustal magma body, we find that there is no simple relationship between magnitude of deformation, eruptive activity, and rates of seismicity (see Table 4).

In the Oregon Cascades, uplift of a broad region centered 5 km west of South Sister volcano has been going on since 1997, with uplift rates measured by InSAR of 3-5 cm/year from 1998 to 2001 and ~1.4 cm/year from 2004 to 2006 (Dzurisin et al. 2009). An earthquake swarm of 300 VT earthquakes with an average magnitude of ~1.9 occurred in this deforming region on 23-25 March 2004 (Venzke et al. 2002-2010). Besides this swarm, however, the Three Sisters region does not frequently exhibit swarms or high rates of seismicity; the average rate of activity is about 2-12 earthquakes per year since 2001 (Pacific Northwest Seismic Network (PNSN) website http://www. pnsn.org/SISTERS/sisters_decade.html). The magnitude of completeness is unknown for this catalog, but given the distribution of PNSN stations at Three Sisters (six stations within a 25 km radius), it is probably not significantly greater than

the magnitude of completeness at Uturuncu. The last eruption of South Sister volcano occurred at ~1.5 ka (Dzurisin et al. 2009). Uturuncu and South Sister are similar in that they both exhibit uplift rates on the order of cm/year despite long periods of dormancy, yet Uturuncu is significantly more seismically active.

Westdahl volcano in Alaska, whose last eruption was in 1992, exhibits active inflation and deflation with the eruption cycle (Lu et al. 2003), but less than 10 VT earthquakes are detected per year with a magnitude of completeness ranging from 0.6 to 0.9 (Dixon et al. 2006; 2008a; b; Dixon and Stihler 2009). Okmok volcano also exhibits deformation corresponding to the eruption cycle (Lu et al. 2010), yet higher seismicity rates of ~70–100 VT earthquakes per year (magnitude of completeness from 0.9 to 1.1), and up to 600 in 2008, the year of the most recent eruption (Dixon et al. 2006; 2008a; b; Dixon and Stihler 2009). For comparison, Uturuncu had 194 earthquakes of magnitude 0.9 or greater from 2009 to 2010, much greater than the average seismicity rate at Westdahl, but very similar to rates observed at Okmok. However, both Westdahl and Okmok are basaltic shield volcanoes, so their eruptive products are lower in viscosity than what is found at Uturuncu.

Mt. Peulik volcano, also located in Alaska, is an active Pleistocene stratovolcano. Peulik experienced an episode of inflation from 1996 to 1998, with uplift rates measured by InSAR reaching 17 cm/year (in the line-of-sight) from October 1996 to October 1997, followed by (and perhaps overlapping with) an earthquake swarm of greater than 400 earthquakes from May to October 1998 (Lu et al. 2002). However, from 2005 to 2008, the average rate of volcano-tectonic seismicity at Peulik was only 30 earthquakes per year with a magnitude of

completeness ranging from 0.8 to 1.3 (Dixon et al. 2006; 2008a; b; Dixon and Stihler 2009). For comparison, Uturuncu had 114 earthquakes of magnitude 1.3 or greater in 2009-2010. While Uturuncu and Peulik have both shown recent deformation, activity at Uturuncu in terms of seismicity and uplift is more steady and persistent. In comparing these deforming Aleutian arc volcanoes to Uturuncu, we find that although these volcanoes are actively erupting, the dormant Uturuncu Volcano is more seismically active than Westdahl and Peulik, and on par with Okmok.

Table 2.4: Seismicity at other deforming volcanic centers

Volcanic center	Last eruption	Deformation	Seismicity	Magnitude of completeness
Mammoth Mountain, Long Valley Caldera	50 ka	Uplift and subsidence (Hill et al. 2003)	~63 events/yr from 1978 to 2003 (VT swarms, LP and VLP events) (Hill and Prejean 2005)	1.2 to >2.5
Okmok	2008	Varies with eruption cycle	70-100 VT/yr (Dixon et al. 2006-2009)	0.9 to 1.1
Peulik	1814	Uplift 17 cm from 1996-1998 (Lu et al. 2002)	30 VT/yr from 2005-2008, swarm of 400 VT in 1998 (Dixon et al. 2006-2009; Lu et al. 2002)	0.8 to 1.3
Socorro Magma Body	N/A	Uplift 2-3 mm/yr (Fialko and Simons 2001)	At least 9 swarm episodes of hundreds of events since 1980 (Ibs-von Seht et al. 2008; Stankova et al. 2008; Ruhl et al. 2010)	-0.3 to 0
South Sister	1.5 ka	Uplift 3–5 cm/yr from 1998 to 2001 and ~1.4 cm/yr from 2004 to 2006 (Dzurisin et al. 2009)	2-12 VT/yr, swarm of 300 VT in 2004 (PNSN website; (Venzke et al. 2002-2010)	unavailable
Westdahl	1992	Varies with eruption cycle	< 10 VT/yr (Dixon et al. 2006-2009)	0.6 to 0.9
Yellowstone	70 ka	Uplift and subsidence	> 1000 VT/yr, large VT swarms (USGS Yellowstone Volcano Observatory)	1.1 to 1.5
Uturuncu	**270 ka**	**Uplift 1-2 cm/yr**	**> 1000 VT/yr, small VT swarms**	**-0.5**

Since Uturuncu is located in a region of large caldera complexes, we look at the activity of Yellowstone caldera for a rough comparison. The Yellowstone caldera

shows ongoing ground surface deformation, alternating between uplift and subsidence (Waite and Smith 2004; Smith et al. 2009). Seismicity is dominated by swarms of VT earthquakes, with the largest swarm in 1985 consisting of more than 3,000 events and the more recent Jan-Feb 2010 swarm consisting of 2,347 events (Husen et al. 2004; USGS Yellowstone Volcano Observatory). The magnitude of completeness for the Yellowstone catalog ranges from 1.1 to 1.5 between 1984 and 2003 (Farrell 2007). Yellowstone's last caldera-forming super-eruption occurred at 640 ka, but smaller eruptions have occurred as recently as 70 ka (Brantley et al. 2004). While Yellowstone is far more active in terms of the number of earthquakes and the rate and complex patterns of ground deformation than Uturuncu, the two systems are similar in having high seismic activity despite having very long periods of repose.

The Rio Grande Rift exhibits high rates of seismicity near Socorro, New Mexico, in a location known as the Socorro Seismic Anomaly (Sanford and Holmes 1962). This anomaly is located above the Socorro Magma Body, which is associated with steady crustal uplift of about 2 mm/year since 1912 (e.g., Pearse and Fialko 2010). Though the Socorro Magma Body differs in its mafic composition and extensional setting, we use it for comparison because of its similarities to the Altiplano-Puna Magma Body – both are sill-like bodies located at depths of ~20 km with low seismic velocities and thicknesses on the order of 100 m (Chmielowski et al. 1999; Sheetz and Schlue 1992) At least nine swarm episodes have been identified at the Socorro Seismic Anomaly since 1980 (Ibs-von Seht et al. 2008; Stankova et al. 2008; Ruhl et al. 2010). Swarms can last from days to months and can consist of up to 500 earthquakes (Ibs-von Seht et al. 2008). The most recent swarm occurred in August

2009 and consisted of 431 earthquakes in 26 days (Ruhl et al. 2010), with magnitudes and b values very similar to those found at Uturuncu. In Socorro, New Mexico, the depth of swarm activity is at depths of 6 to 7 km, about 12 km above the upper surface of the Socorro Magma Body (Stankova et al. 2008). The Uturuncu system is similar in that its seismicity is at a depth of about 15 km above the APMB; however swarms at Uturuncu are more frequent and shorter in duration with fewer events than swarms at Socorro.

This global comparison demonstrates the complexity of the relationship between deformation, eruptions, seismicity. Perhaps a more conclusive analysis could be achieved by taking into consideration the tectonic setting and magma composition of the volcanic systems. Such an approach is worthy of further attention and is planned.

2.8 CONCLUSIONS

Although Uturuncu has not erupted since 270 ka, multiple signs of activity have recently been discovered, including uplift of 1-2 cm/year, active sulfur fumaroles, and high rates of seismicity. These characteristics indicate that there are multiple levels of activity beneath Uturuncu. We propose that mid-crustal magma accumulation at ~20 km depth causes the broad uplift pattern, which in turn exerts stresses on pre-existing faults and a hydrothermal system at depths around sea level, generating VT earthquakes and earthquake swarms. The observed low b values are consistent with this interpretation and show no suggestion of fluid involvement. There are few low-frequency events and no episodes of volcanic tremor, hence no signs of shallow

accumulation of magma. We also document that seismicity at Uturuncu is susceptible to triggering by very large earthquakes, particularly the Mw 8.8 Maule, Chile earthquake of 27 February 2010, which triggered earthquake swarms with the R1/G1 and X2/X3 passages of surface waves and continued for 2 days. The fact that the X2/X3 waves triggered local earthquakes while the G2/R2 waves with higher amplitude (in velocity or displacement) did not suggests that the frequency content, and not just their amplitude is important for triggering. The immediate triggering response is a result of dynamic stress changes, and the delayed response is suggestive of a change in the state of either the hydrothermal system or the mid-crustal magma chamber.

Our calculation of the depth of the brittle-ductile transition zone agrees with the depth at which earthquakes occur at Uturuncu near sea level. We find that seismicity rates at Uturuncu have not varied significantly from 1996 to 97 to 2009-2010, but that the 5 days of observations in 2003 appear to correlate with a burst of activity only rivaled by the seismicity triggered by the 2010 Maule Chile earthquake. Yet, these time periods are difficult to compare due to variations in station locations, instrumentation, and data quality. We may be able to attribute the high seismicity rates measured in 2003 to a lower magnitude of completeness – it appears that most events from 2003 are smaller in magnitude than those from 2009-2010.

Ambient noise tomography results reveal a low-velocity zone at 1.9 to 3.9 km depth below the surface, but these low-velocity zones are neither well correlated nor uncorrelated with earthquake locations given the current accuracies of earthquake locations. The low-velocity zones and the fumarolic activity suggest the presence of a

shallow hydrothermal system beneath Uturuncu, although its link to the observed swarm behavior and remote triggering of seismicity is not yet well understood. Comparing Uturuncu to uplifting volcanic systems in North America that are seismically monitored (Yellowstone, South Sister, Alaskan volcanoes, Socorro), we find that swarms are very common, although the rates of swarm activity are very different in different places, probably due to tectonic setting and magma composition. In general, higher rates of seismicity and susceptibility to remote triggering of seismicity are associated with the presence of a hydrothermal or magmatic system and not necessarily with eruptive activity.

REFERENCES

Behr Y, Townend J, Bannister S, Savage MK (2011) Crustal shear wave tomography of the Taupo Volcanic Zone, New Zealand, via ambient noise correlation between multiple three-component networks. Geochem Geophys Geosyst 12:3

Benoit JP and McNutt SR (1996) Global volcanic earthquake swarm database 1979–1989. USGS Open-File Report 96–69

Brantley SR, Lowenstern JB, Christiansen RL, Smith RB, Heasler H, Waite G, Wicks C (2004) Tracking changes in Yellowstone's restless volcanic system. US Geol Survey http://pubs.usgs.gov/fs/ fs100-03. Accessed 31 March 2011

Cahill, T., & Isacks, B. L. (1992). Seismicity and shape of the subducted Nazca Plate. *Journal of Geophysical Research*, *97*(B12), 17503.

Chmielowski J, Zandt G, Haberland C (1999) The Central Andean Altiplano-Puna magma body. Geophys Res Lett 26:783–786

Clavero J, Soler V, Polanco E, Amigo A (2005) Preliminary seismic and diffuse CO2 flux characterization of active volcanoes from the central Andes of northern Chile. IASPEI abstract. Proceedings IASPEI General Assembly, Santiago, Chile.

de Silva SL (1989) Altiplano-Puna volcanic complex of the central Andes. Geol 17:1102–1106

de Silva SL, Gosnold WD (2007) Episodic construction of batholiths: insights from the spatiotemporal development of an ignimbrite flare-up. J Volcanol Geotherm Res 167:320–325

Dixon JP, Stihler SD (2009) Catalog of earthquake hypocenters at Alaskan volcanoes: January 1 through December 31, 2008. US Geol Surv Data Ser 467:86

Dixon JP, Stihler SD, Power JA, Tytgat G, Estes S, McNutt SR (2006) Catalog of Earthquake Hypocenters at Alaskan Volcanoes: January 1 through December 31, 2005. USGS Open-File Report 2006–1264

Dixon JP, Stihler SD, Power JA, Searcy C (2008a) Catalog of earthquake hypocenters at Alaskan volcanoes: January 1 through December 31, 2006. US Geol Surv Data Ser 326:79

Dixon JP, Stihler SD, Power JA (2008b) Catalog of earthquake hypocenters at Alaskan volcanoes: January 1 through December 31 2007. US Geol Surv Data Ser 367:82

Dzurisin D, Lisowski M, Wicks CW (2009) Continuing inflation at Three Sisters volcanic center, central Oregon Cascade Range, USA, from GPS, leveling, and InSAR observations. Bull Volcanol 71:1091–1110

Farrell JM (2007) Space-time seismicity and development of a geographical information system database with interactive graphics for the Yellowstone region. Dissertation, The University of Utah

Fialko Y, Simons M (2001) Evidence for on-going inflation of the Socorro magma body, New Mexico, from interferometric synthetic aperture radar imaging. Geophys Res Lett 28:3549–3552

Hamza VM, Dias F, Gomes A, Terceros Z (2005) Numerical and functional representations of regional heat flow in South America. Phys Earth Planet Inter 152:223–256

Hellweg M (2000) Physical models for the source of Lascar's harmonic tremor. J Volcanol Geotherm Res 101:183–198

Henry SG, Pollack HN (1988) Terrestrial heat flow above the Andean subduction zone in Bolivia and Peru. J Geophys Res 93 (B12):15,153–15,162

Hill DP (1977) A model for earthquake swarms. J Geophys Res 82 (8):1347-1352

Hill DP (1992) Temperatures at the base of the seismogenic crust beneath Long Valley Caldera, California, and the Phlegrean Fields Caldera, Italy. In: Gasparini P, Scarpa R, Aki K (eds) Volcanic Seismology. Springer, Berlin, pp 432–461

Hill DP, Prejean S (2005) Magmatic unrest beneath Mammoth Mountain, California. J Volcanol Geotherm Res 146:257–283

Hill DP, Reasenberg PA, Michael A et al (1993) Seismicity remotely triggered by the magnitude 7.3 Landers, California earthquake. Science 260:1617–1623

Hill DP, Langbein JO, Prejean S (2003) Relations between seismicity and deformation during unrest in Long Valley Caldera, California, from 1995 through 1999. J Volcanol Geotherm Res 127:175–193

Husen S, Wiemer S, Smith RB (2004) Remotely triggered seismicity in the Yellowstone National Park Region by the 2002 Mw 7.9 Denali Fault Earthquake, Alaska. Bull Seismol Soc Am 94(6B): S317–S331

Ibs-von Seht M, Plenefisch T, Klinge K (2008) Earthquake swarms in continental rifts—a comparison of selected cases in America, Africa, and Europe. Tectonophysics 452:66–77

Kay, S., & Coira, B. (2009). Shallowing and steepening subduction zones, continental lithospheric loss, magmatism, and crustalflow under the Central Andean Altiplano-Puna Plateau. *Geological Society of America Memoirs*, *204*, 229–259.

Kirby S, Kronenberg AK (1987) Rheology of the lithosphere: selected topics. Rev Geophys 25(6):1219–1244

Kussmaul S, Hormann PK, Ploskonka E, Subieta T (1977) Volcanism and structure of southwestern Bolivia. J Volcanol Geotherm Res 2:73–111. doi:10.1016/0377-0273(77)90016-6

Legrand D, Barrientos S, Bataille K, Cembrano J, Pavez A (2010) The fluid-driven tectonic swarm of Aysen Fjord, Chile (2007) associated with two earthquakes (Mw = 6.1 and Mw = .2) within the Liquiñe-Ofqui Fault Zone. Cont Shelf Res 31(3– 4):154–161

Leidig M, Zandt G (2003) Highly anisotropic crust in the APVC. J Geophys Res 108(B1):2014. doi:10.1029/2001JB000649

Lema JC, Choque N (1996) Carta Geológica Nacional. Servicio Nacional de Geología y Minería. SGB Serie I-CGB

Lin F, Moschetti MP, Ritzwoller MH (2008) Surface wave tomography of the western United States from ambient seismic noise: Rayleigh and Love wave phase velocity maps. Geophys J Int. doi:10.1111/j1365-246X.2008.03720.x

Lu Z, Wicks C, Dzurisin D, Power JA, Moran SC, Thatcher W (2002) Magmatic inflation at a dormant stratovolcano: 1996–1998 activity at Mount Peulik volcano, Alaska, revealed by satellite radar interferometry. J Geophys Res 17:2134

Lu Z, Masterlark T, Dzurisin D, Rykhus R, Wicks C (2003) Magma supply dynamics at Westdahl volcano, Alaska, modeled from satellite radar interferometry. J Geophys Res 108:2354

Lu Z, Dzurisin D, Biggs J, Wicks C, McNutt S (2010) Ground surface deformation patterns, magma supply, and magma storage at Okmok volcano, Alaska, from InSAR analysis: 1. Intereruption Deformation, 1997–2008. J Geophys Res 115:B00B02. doi:10.1029/2009JB006969

Masterlark T, Haney M, Dickinson H, Fournier T, Searcy C (2010) Rheologic and structural controls on the deformation of Okmok volcano, Alaska: FEMs, InSAR, and ambient noise tomography. J Geophys Res 115:B02409

Okada H (2003) The microtremor survey method, Translated by Koya Suto, Geophysical Monograph Series Vol 12. Society of Explora- tion Geophysicists, Tulsa

Pavlis GL, Vernon F, Harvey D, Quinlan D (2004) The generalized earthquake-location (GENLOC) package: an earthquake-location library. Comput Geosci 30:1079–1091

Pearse J, Fialko Y (2009) Modelling steady magmatic inflation at Uturuncu Volcano, Bolivia. American Geophysical Union, Fall Meeting 2009, abstract #G44A-05

Pearse J, Fialko Y (2010) Mechanics of active magmatic intraplating in the Rio Grande Rift near Socorro, New Mexico. J Geophys Res 115:B07413

Prejean SG, Hill DP, Brodsky EE, Hough SE, Johnston MJS, Malone SD, Oppenheimer DH, Pitt AM, Richards-Dinger KB (2004) Remotely triggered seismicity on the United States West Coast following the Mw 7.9 Denali fault earthquake. Bull Seismol Soc Am 94(6B):S348–S359

Pritchard ME, Simons M (2004) An InSAR-based survey of volcanic deformation in the central Andes. Geochem Geophys Geosyst 5:2.

Ramos, V. A., & Kay, S. M. (1992). Southern Patagonian plateau basalts and deformation: Backarc testimony of ridge collisions. *Tectonophysics*, *205*(1-3), 261–282.

Ranalli G, Murphy DC (1986) Rheological stratification of the lithosphere. Tectonophys 132:281–295

Ruhl C, Bilek SL, Stankova-Pursley J (2010) Relocation and characterization of the August 2009 microearthquake swarm above the Socorro magma body in the central Rio Grande Rift. Geophys Res Lett 37:L23304

Sanford AR, Holmes CR (1962) Microearthquakes near Socorro, New Mexico. J Geophys Res 67:4449–4459

Schilling FR, Partzsch GM, Brasse H, Schwarz G (1997) Partial melting below the magmatic arc in the central Andes deduced from geoelectromagnetic field experiments and laboratory data. Phys Earth Planet Inter 103:17–31

Schilling, F. R., Trumbull, R. B., Brasse, H., Haberland, C., Asch, G., Bruhn, D., … Vietor, T. (2006). Partial Melting in the Central Andean Crust: a Review of Geophysical, Petrophysical, and Petrologic Evidence. In O. Oncken, G. Chong, G. Franz, P. Giese, H.-J. Gotze, V. A. Ramos, … P. Wigger (Eds.), *The Andes: Active Subduction Orogeny* (pp. 459–474). Berlin.

Schurr B, Rietbrock A, Asch G, Kind R, Oncken O (2006) Evidence for lithospheric detachment in the central Andes from local earthquake tomography. Tectonophys 415:203–223

Sheetz KE, Schlue JW (1992) Inferences for the Socorro Magma Body from teleseismic receiver functions. Geophys Res Lett 19:1867–1870

Smith RB, Jordan M, Steinberger B, Puskas CM, Farrell J, Waite GP, Husen S, Chang W, O'Connell R (2009) Geodynamics of the Yellowstone hotspot and mantle plume:

Seismic and GPS imaging, kinematics, and mantle flow. J Volcanol Geotherm Res 188:26–56

Sparks RSJ, Folkes CB, Humphreys MCS, Barfod DN, Clavero J, Sunagua MC, McNutt SR, Pritchard ME (2008) Uturuncu Volcano, Bolivia: volcanic unrest due to mid-crustal magma intrusion. Amer J Sci 308:727–769

Springer M, Forster A (1998) Heat-flow density across the Central Andean subduction zone. Tectonophys 291:123–139

Stankova J, Bilek SL, Rowe CA, Aster RC (2008) Characteristics of the October 2005 Microearthquake Swarm and Reactiva- tion of Similar Event seismic swarms over decadal time periods near Socorro, New Mexico. Bull Seismol Soc Am 98 (1):93–105

Sunagua M (2004) Amenaza volcánica en la región del volcán Uturuncu–Provincia Sud Lípez del Departamento de Potosí. Dissertation, Universidad Autónoma Tomás Frías

Venzke E, Wunderman RW, McClelland L, Simkin T, Luhr JF, Siebert L, Mayberry G, and Sennert S (eds.) (2002–2010) Global volcanism, 1968 to the present. Smithsonian Institution, Global Volcanism Program Digital Information Series, GVP-4 (http:// www.volcano.si.edu/reports/)

Viramonte JG, Galliski MA, Araña Saavedra V, Aparicio A, García Cacho L, Martín Escorza C (1984) El finivolcanismo básico de la depresión de Arizaro, provincia de Salta, República Argentina. IX Congr Geol Argent 3:234–254

Waite GP, Smith RB (2004) Seismotectonics and stress field of the Yellowstone volcanic plateau from earthquake first-motions and other indicators. J Geophys Res 109:B02301. doi:10.1029/ 2003JB002675

West M, Sanchez JJ, McNutt SR (2005) Periodically triggered seismicity at Mount Wrangell, Alaska, after the Sumatra earthquake. Science 308:1144–1146

Wiemer S (2001) A software package to analyse seismicity: ZMAP. Seismol Res Lett 72(3):373–382

Yuan, X., Sobolev, S. V, Kind, R., Oncken, O., Bock, G., Asch, G., … Comte, D. (2000). Subduction and collision processes in the Central Andes constrained by converted seismic phases. *Nature*, *408*(6815), 958–61.

Zandt G, Leidig M, Chmielowski J, Baumont D, Yuan X (2003) Seismic detection and characterization of the Altiplano-Puna magma body, Central Andes. Pure Appl Geophys 160:789–807

CHAPTER 3

VOLCANIC HOTSPOTS OF THE CENTRAL AND SOUTHERN ANDES AS SEEN FROM SPACE BY ASTER AND MODVOLC BETWEEN THE YEARS 2000 AND 2010[2]

3.0 ABSTRACT

We examine 150 volcanoes and geothermal areas in the central, southern and austral Andes for thermal anomalies between the years 2000 and 2010 from two different spaceborne sensors: (1) those automatically detected by the MODVOLC algorithm from MODIS; and (2) manually identified hotspots in night-time images from ASTER (Advanced Spaceborne Thermal Emission and Reflection Radiometer). Based on previous work, we expected to find eight volcanoes displaying thermal anomalies (Ubinas, Villarrica, Copahue, Láscar, Llaima, Chaitén, Lonquimay and Chiliques). We document 35 volcanic areas with pixel-integrated temperatures of 4 up to more than 100 K above background in at least two images, and another 16 areas that have questionable hotspots with either smaller anomalies or a hotspot identified in only one image. Most of the thermal anomalies are related to known activity (i.e. lava and pyroclastic flows, growing lava domes, fumaroles, and lakes) while others are of unknown origin or reflect activity at volcanoes that were not thought to have surface activity. A handful of volcanoes exhibit temporal variations in the magnitude and location of their temperature anomalies that can be related to both documented and

---

[2] A version of this chapter was originally published as: Jay, J. A., Welch, M., Pritchard, M. E., Mares, P. J., Mnich, M. E., Melkonian, A. K., … Clavero, J. (2013). Volcanic hotspots of the central and southern Andes as seen from space by ASTER and MODVOLC between the years 2000 and 2010. Geological Society, London, Special Publications, 380(1), 161–185. doi:10.1144/SP380.1. Reprinted with permission from the Geological Society of London.

undocumented pulses of activity. Our survey reveals that low-amplitude volcanic hotspots detectable from space are more common than expected, based on lower spatial resolution data, and that these features could be more widely used to monitor changes in the activity of remote volcanoes. We find no evidence from ASTER or MODVOLC that the thermal anomalies were affected by six earthquakes with Mw above 7 in our study area from 2000 to 2010, although the observations may not have been optimal to detect such anomalies.

3.1 INTRODUCTION

At several volcanoes around the world, thermal anomalies have been observed from space prior to, during and after eruptions (e.g. Matthews et al. 1997; Dehn et al. 2000, 2002; Pieri & Abrams 2005; Carter & Ramsey 2009), after remote earthquakes (e.g. Harris & Ripepe 2007; Delle Donne et al. 2010) and related to 'background' volcanic activity, such as geothermal heating of lakes (e.g. Trunk & Bernard 2008). Given its synoptic coverage, spaceborne data are useful for surveying many potentially active volcanoes in remote areas on a regular basis. Of the 150 volcanoes and geothermal areas in the region, currently about 15 (all of which are in Chile) are regularly monitored from the ground (e.g. SERNAGEOMIN Observatorio Volcanológico de Los Andes del Sur). We have used infrared satellite images from the ASTER (on the Terra satellite) and MODIS (on the Terra and Aqua satellites) instruments to survey these potentially active volcanoes and geothermal areas across three different volcanic arcs: the central, southern and austral Andes (e.g. de Silva & Francis 1991; González-Ferrán 1995; Stern 2004), which extend over Chile, Peru, Argentina and Bolivia (-16 to -55S: Fig. 3.1). Although datasets from other satellites such as Landsat Thematic

Mapper (TM) and Enhanced Thematic Mapper Plus (ETM+), Advanced Very High Resolution Radiometer (AVHRR) and Geostationary Operational Environmental Satellite (GOES) are also available and have been used in our study area (e.g. Denniss et al. 1998; Dehn et al. 2002; Calder et al. 2004), analysis of these datasets is beyond the scope of our project. Our survey begins with the start of night-time data acquisition by ASTER and MODIS (early 2000), and ends on 22 February 2010. We end our survey 5 days before the Mw 8.8 Maule earthquake so as not to include potential seismically triggered thermal responses in our analysis; any activity triggered by the Maule earthquake will be analyzed in a future study.

To date, eight thermal anomalies have been documented at the volcanoes of these arcs, with four of them being persistent for multiple years (Láscar, Copahue, Villarrica and Llaima: e.g. Oppenheimer et al. 1993; Calder et al. 2004; Trunk & Bernard 2008; Proyecto Observación Visual Volcán Villarrica), three others appearing for only a few months (Ubinas, Lonquimay and Chiliques: e.g. Oppenheimer 1991; Venzke et al. 2002-2011; Pieri & Abrams 2004) and a hotspot at Chaitén Volcano beginning after its eruption began in May 2008 (e.g. SERNAGEOMIN 2010). Before embarking on this study, we suspected that several more volcanoes had thermal anomalies as there are about 40 persistently active fumarolic areas known in these arcs (e.g. de Silva & Francis 1991; González-Ferrán 1995; Venzke et al. 2002-2011; Tassi et al. 2010) and previous work has shown that some remote volcanoes in these arcs that were thought to be dormant have undergone surface deformation during our study period (e.g. Pritchard & Simons 2004; Fournier et al. 2010). One motivation for this study is therefore to determine which of the potentially active volcanoes in these

volcanic arcs show signs of thermal activity and whether additional volcanoes need to be added to the list of those considered potentially active. Because many of the volcanoes in the southern and austral Andes are permanently snow-covered, our current knowledge of thermal activity at these volcanoes is incomplete. Another motivation for our work is to better understand the causes of the thermal anomalies by assessing whether satellite thermal remote sensing can detect changes in the temperatures at these volcanoes in conjunction with eruptions or nearby large earthquakes (i.e. Mw > 7 threshold). During our study period, nine different volcanoes had documented eruptions and there were six earthquakes with Mw > 7 within our study area (Fig 3.1a).

3.2 METHODS

The primary dataset used in this study are images taken by ASTER (Advanced Spaceborne Thermal Emission and Reflection Radiometer), a multispectral instrument that includes five bands in the thermal infrared (TIR) (e.g. Pieri & Abrams 2004). We use the Surface Kinetic Temperature Product (AST08), which is a 90 m/pixel georeferenced map of pixel-integrated temperatures derived from the multiple bands using the temperature-emissivity separation (TES) method (Gillespie et al. 1998). The advantage of using the ASTER Product 8 data over the raw radiance data is that the TES algorithm removes reflected sky irradiance, calculates the emissivity of each pixel (which varies depending on land cover type) and solves for the temperature to an accuracy of +1.5 K (Gillespie et al. 1998). Although more than 10 years of data are available (ASTER was launched on the Terra satellite in 1999), night-time images of each volcano are acquired infrequently. For example, Chiliques Volcano has 122

cloud-free images over the last 10 years, while some other volcanoes have only one or two (Tables 1 & 2).

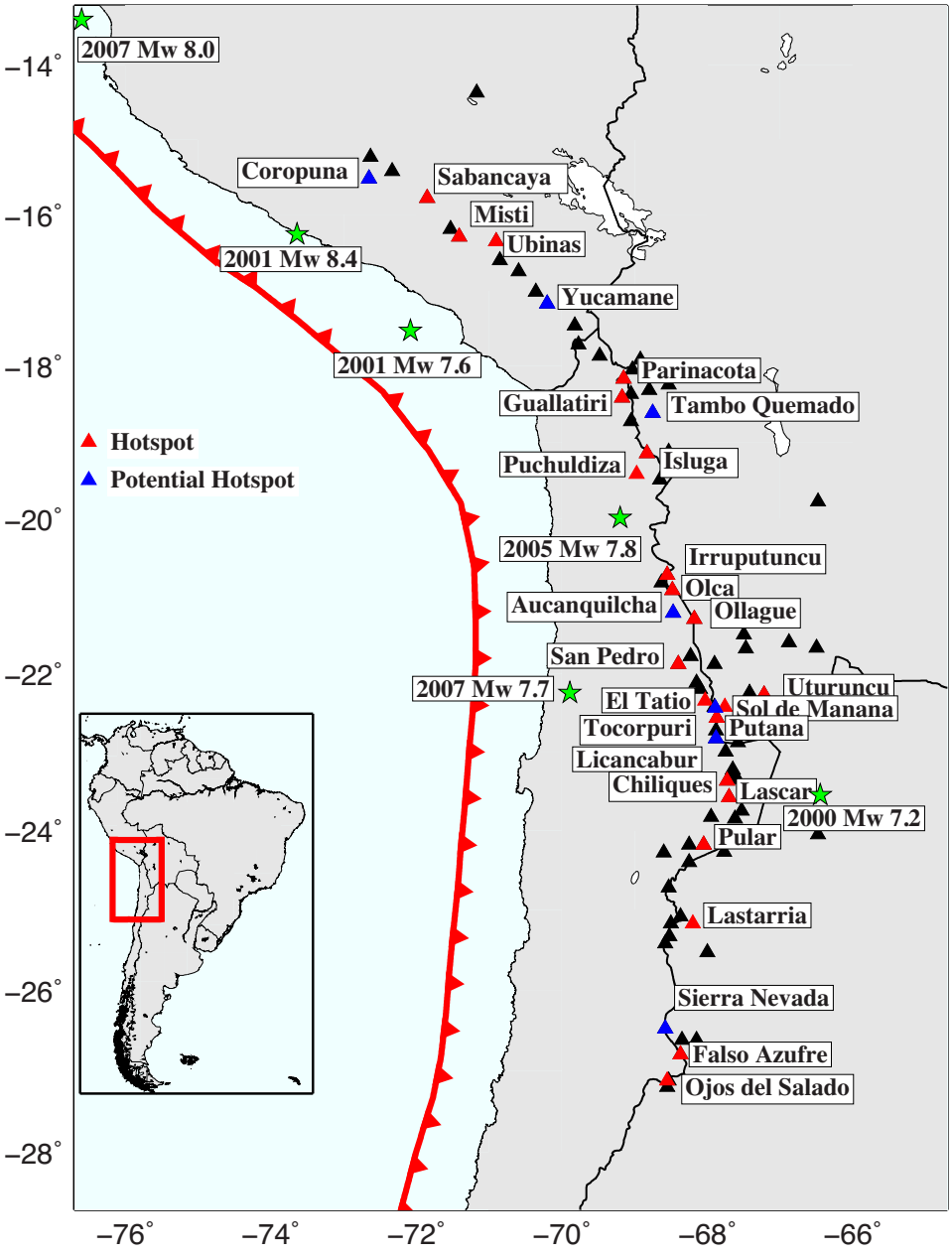

Figure 3.1a Reference map of hotspots and potential hotspots from: (a) central Andes volcanic arc. No hotspots were found in the austral Andes. Other volcanoes from the Smithsonian Institution database (Siebert & Simkin 2002–2012) are shown as black triangles. Epicentres of earthquakes from the USGS PDE catalogue between 1 January 2000 and 22 February 2010 with Mw > 7 are plotted as stars.

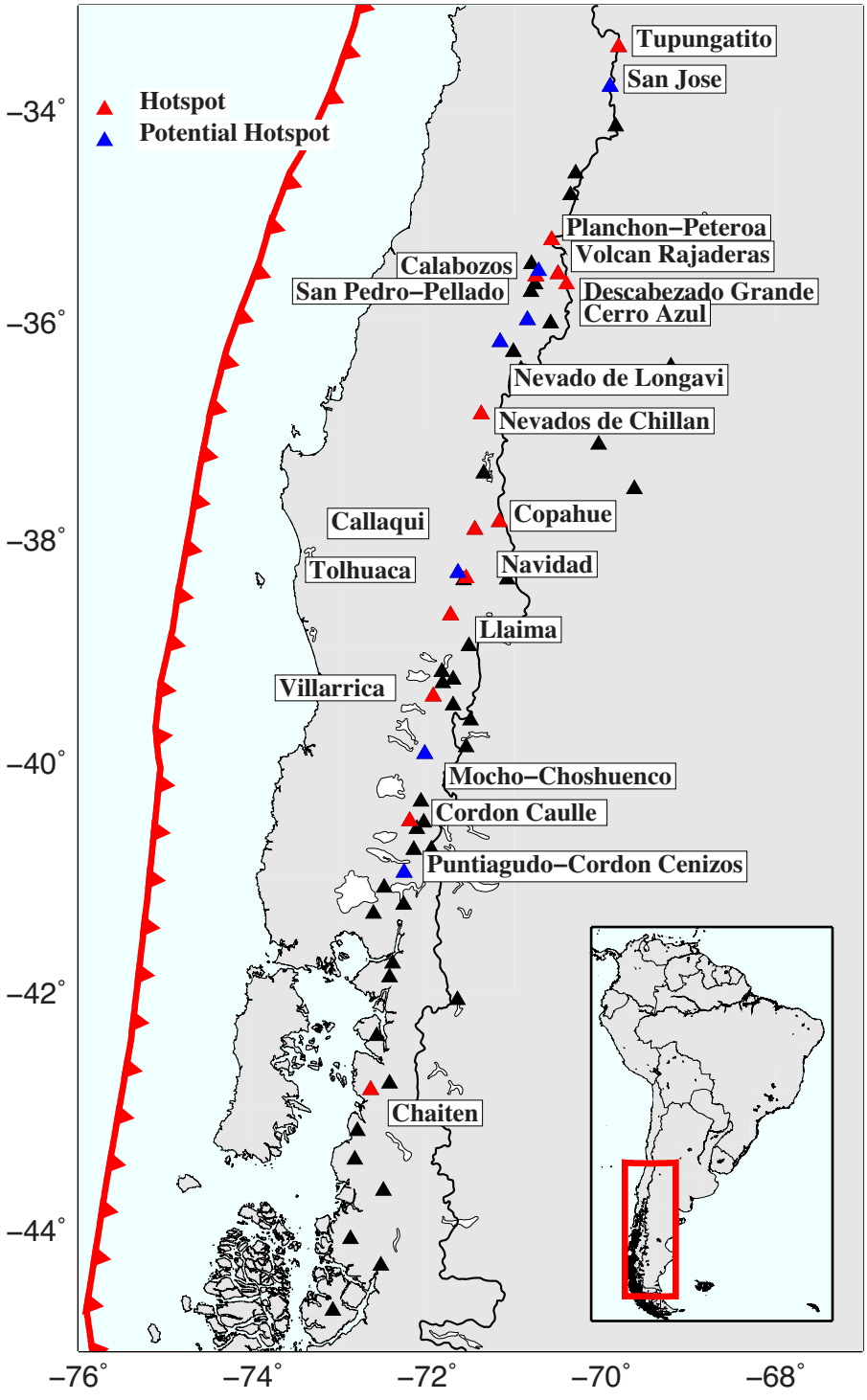

Figure 3.1b Reference map of hotspots and potential hotspots from: (b) southern Andes volcanic arc. No hotspots were found in the austral Andes. Other volcanoes from the Smithsonian Institution database (Siebert & Simkin 2002–2012) are shown as black triangles. Epicentres of earthquakes from the USGS PDE catalogue between 1 January 2000 and 22 February 2010 with Mw > 7 are plotted as stars.

We selected ASTER images that covered the volcanoes of the central, southern and austral Andes listed in the Smithsonian Global Volcanism Program database (Siebert & Simkin 2002-2012), with some additional targets from other compilations of potentially active volcanoes and geothermal areas (de Silva & Francis 1991; González-Ferrán 1995; Aguilera 2008; Tassi et al. 2010). We used a combination of web-based tools (the NASA Reverb ECHO, the USGS Global Visualization Viewer and the USGS Warehouse Inventory Search Tool) to search and order night-time AST08 images that covered the volcanoes.

Once the images were acquired, they were analyzed using the ENVI image-processing software package. The volcano of interest was identified by comparing the ASTER images to Google Earth optical imagery and matching up obvious features (e.g. cold mountain tops, and warmer valleys and lakes). Scenes in which clouds obscured the volcano of interest could not be used in this study. We found that cloud-free images of the volcanoes of the central Andes are plentiful because of the arid climate (e.g. Harris et al. 2000), while the more humid southern Andes have a greater abundance of clouds (e.g. Calder et al. 2004).

Since most of the volcanoes appear dark (cold) in the thermal imagery owing to their relatively high elevation and, sometimes, their snow cover, we zoomed in on the summit and applied a 2% linear contrast stretch to better distinguish pixel intensity at each volcano. We focused our search within 10km of the coordinates of each potentially active volcano given by Simkin & Siebert (2002–2012) so that hotspots unrelated to the volcanoes would not be detected by our methodology. To determine an approximate temperature anomaly at each potential hotspot, several east-west and

north-south profiles were manually made over suspected hotspots to determine the peak and background temperatures (Fig. 3.2). If a pixel was at least 4 K warmer than the perceived trend of background temperatures throughout the profile, the volcano would be marked as having at least a 'potential' hotspot (Tables 1 & 2). The temperature threshold was chosen because it is greater than the 1.5 K precision of the TES algorithm (Gillespie et al. 1998) and the intrinsic scatter of background temperatures we observed from looking at the large number of volcanoes in our survey.

When a hotspot was detected, we found the location of the pixel corresponding to the peak in a profile of temperatures made across the hotspot. We then visually compared the ASTER pixel- integrated temperature to Google Earth images to ascertain whether the warm pixel could have been caused by some topographical feature or obvious compositional change that could be determined from the optical imagery. Some of the anomalies were caused by geographical features such as lakes, snow-free mountain faces or areas of different rock composition with different thermal inertias (Fig. 3.3). For some volcanoes, it was not apparent whether the anomaly was due to volcanic activity or was caused by some other process (e.g. fire or single-event upsets) (Table 2). Any volcano with only a single pixel hotspot in one ASTER scene was marked as not having a hotspot, as these pixels were unrealistically hot and probably due to single-event upsets or fires rather than volcanic activity. 'Potential' hotspots would turn into 'definite' hotspots if the hotspot was found to be present in more than one scene, in the same location and not obviously due to geographical features; otherwise they would be labelled as 'questionable'.

Table 3.1 List of 35 volcanoes from the central and southern Andes with hotspots listed from north to south. Table 2 has 15 additional potential hotspots that merit further study. See Supplemental Table 1 for all data examined for each volcano. [1]A range of temperatures indicates temporal variability (see text);[2]de Silva & Francis (1991); [3]González-Ferrán (1995); [4]Siebert & Simkin (2002-); [5]Barragan et al., 1999; [6]Pieri & Abrams, 2004

Volcano Name	Country	Smithsonian Volcano #	# images with hotspot/ Total # cloud-free images	Mean temp above background	Potential cause of hotspot	Fig.
Central Volcanic Zone						
1) Sabancaya	Peru	1504-006	42/43	13	Fumaroles[2,3,4]	3.4a
2) Misti	Peru	1504-01	26/27	6	Lava dome, fumaroles[2,3,4]	3.4b
3) Ubinas	Peru	1504-02	18/19	12	Eruption/fumaroles[2,3,4]	3.4c
4) Huaynaputina	Peru	1504-03	5/17	7	?	3.4d
5) Guallatiri	Chile	1505-02	29/30	8	Fumaroles[2,3,4]	3.5
6) Isluga	Chile	1505-03	36/36	15	Fumaroles[2,3,4]	3.5
7) Puchuldiza	Chile	1505-032C	34/39	10	Hot spring[4]	3.4e
8) Irruputuncu	Bolivia	1505-04	41/41	9	Fumaroles[2,3,4]	3.5
9) Olca	Bolivia	1505-05	41/41	6	Fumaroles[2,3,4]	3.5
10) Ollagüe	Bolivia	1505-06	65/76	5	Fumaroles[2,3,4]	3.5
11) San Pedro	Chile	1505-07	48/48	5	Fumaroles[2,3]	3.4f
12) Uturuncu	Bolivia	1505-076A	27/27	15	Fumaroles[4]	3.5
13) El Tatio	Chile	1505-08A	56/56	10	Geysers[2,3,4]	3.5
14) Sol de Mañana	Bolivia	N/A	57/57	12	Geysers[2]	3.4g
15) Putana	Chile	1505-09	38/88	5	Fumaroles[2,3]	3.4h
16) Alítar	Chile	N/A	99/99	11	Fumaroles[3]	3.4i
17) Láscar	Chile	1505-10	75/75	30-100[1]	Eruption/fumaroles[2,3,4]	3.4j
18) Chiliques	Chile	1505-098	74/122	6	Lakes[4,6]	3.4k
19) Pular/Pajonales	Chile	1505-107	11/19	11	Sulfur deposits?	3.4l
20) Lastarria	Chile	1505-12	63/63	15	Fumaroles[2,3,4]	3.5
21) Falso Azufre	Chile/Argentina	1505-124	14/26	7	Sulfur deposits?	3.4m
22) Ojos del Salado	Chile/Argentina	1505-13	7/7	19	Fumaroles	3.5
Southern Volcanic Zone						
23) Tupungatito	Chile/Argentina	1507-01	28/28	33	Crater lake/fumaroles[3,4]	3.4n
24) Planchón-Peteroa	Chile	1507-04	25/26	30	Eruption/Crater lake/fumaroles[4]	3.4o
25) Calabozos/Volcan del Medio	Chile	1507-042	6/21	8	Hot springs[4]	3.4p
26) Descabezado Grande	Chile	1507-05	9/21	8	Fumaroles[3,4]	3.4q
27) Cerro Azul	Chile	1507-06	5/21	7	Fumaroles[6]	3.4r
28) Nevados de	Chile	1507-07	33/35	5-47[1]	Fumaroles[4]	3.8

Chillán						
29) Copahue	Chile/Argentina	1507-09	21/22	38	Crater lake/fumaroles[3,4]	3.2a, 3.4s
30) Callaqui	Chile	1507-091	20/23	8	Fumaroles[3,4]	3.2
32) Volcán Navidad	Chile	N/A	7/7	9	Thermal inertia of cinder cone?	3.4t
32) Llaima	Chile	1507-11	31/33	4-107[1]	Eruptions[3,4]	3.9
33) Villarrica	Chile	1507-12	29/33	5-80[1]	Lava lake, eruptions[3,4]	3.4u
34) Cordón Caulle/Puyehue	Chile	1507-15	6/6	15	Fumaroles and geysers[3,4]	3.4v
35) Chaitén	Chile	1508-41	6/14	4-100[1]	Lake? eruption[4]	3.10

Table 3.2 List of 15 volcanoes from the central and southern Andes with potential hotspots that merit further study. Table 1 has 36 more certain hotspots. See Supplemental Table 1 for all data examined for each volcano.
[1]These volcanoes do not have numbers in the Smithsonian database, but appear in González-Ferrán (1995). Coordinates for these volcanoes are in Supplemental Table 1.
[2]González-Ferrán (1995); [3]Siebert & Simkin (2002-); [4]de Silva & Francis (1991); [5]Morales et al., (1993); [6]Hildreth & Drake (1992)

Volcano Name	Smithsonian Volcano #	# images with potential hotspot/ Total # cloud-free images	Mean temperature above background	Potential cause of hotspot	Fig.
1) Coropuna	1504-003	1/10	6	Fumaroles[2,3]	A1.2.1a
2) Yucamane	1504-05	3/21	3	?	A1.2.1b
3) Parinacota	1505-012	28/36	6	Lack of snow cover, fumaroles[2,3]	A1.2.1c
4) Tambo Quemado	1505-021	1/21	6	Thermal inertia of lava dome	A1.2.1d
5) Aucanquilcha	1505-05A	9/42	4	Fumaroles[2,3,4]	A1.2.1e
6) Azufre	1505-061	6/48	4	?	A1.2.1f
7) Tocorpuri	N/A[1]	1/45	11	Lake? Sulfur deposits?	A1.2.1g
8) Licancabur	1505-092	13/48	3	Lake[2,3]	A1.2.1h
9) Sierra Nevada	1505-123	2/16	6	?	A1.2.1i
10) San José	1507-02	1/25	5	Fumaroles[3,4]	A1.2.1j
11) Volcán Rajaderas	N/A[1]	4/16	10	Nearby lake?	A1.2.1k
12) San Pedro-Pellado	1507-062	1/9	10	Fumaroles[3,4]	A1.2.1l
13) Nevado de Longavi	1507-063	1/1	4	Fumaroles[4]	A1.2.1m
14) Tolhuaca	1507-093	2/29	7	Fumaroles[3,4]	A1.2.1n
15) Mocho Choshuenco	1507-13	3/5	5	Lack of snow cover	3.3
16) Puntiagudo	1507-16	2/9	6	?	A1.2.1o

While the ASTER data have high spatial resolution (90 m/pixel) it has low temporal resolution, at best acquiring an image in our study area every few weeks over volcanoes for which data acquisitions have been requested. Conversely, the MODIS instrument on the Terra and Aqua satellites can detect hotspots on an approximately daily basis (assuming cloud-free images) but at a lower spatial resolution (from 1 km at nadir to about 2×5 km at the edge of the swath). We searched the MODIS hotspot Internet database created using the MODVOLC algorithm (e.g. Wright et al. 2004) for hotspots over our 150 volcanoes of interest during the same period as the ASTER observations (2000 – 2010). We entered the coordinates of each volcano into the interactive webpage and zoomed into an area 10 km wide. We then stepped through the 10 years of data with yearly increments to determine whether there are any hotspots at the volcano. Once hotspots were found, we included all of those detected in night-time images and daytime images that were not taken during the austral summer months (i.e. not November, December, January or February). We excluded these summer months because some of the hotspots in daytime images during summer are not due to internal processes – we found hotspots every year over certain areas only during summer. Because the MODVOLC detection threshold was set at a high level to avoid false positives (e.g. Wright et al. 2004), the algorithm will not detect the low levels of thermal activity at many of the volcanoes in our study area that might have been detectable in the raw MODIS data. Nonetheless, the MODVOLC-detected hotspots allow for a temporally dense and spatially comprehensive comparison with our manual ASTER search.

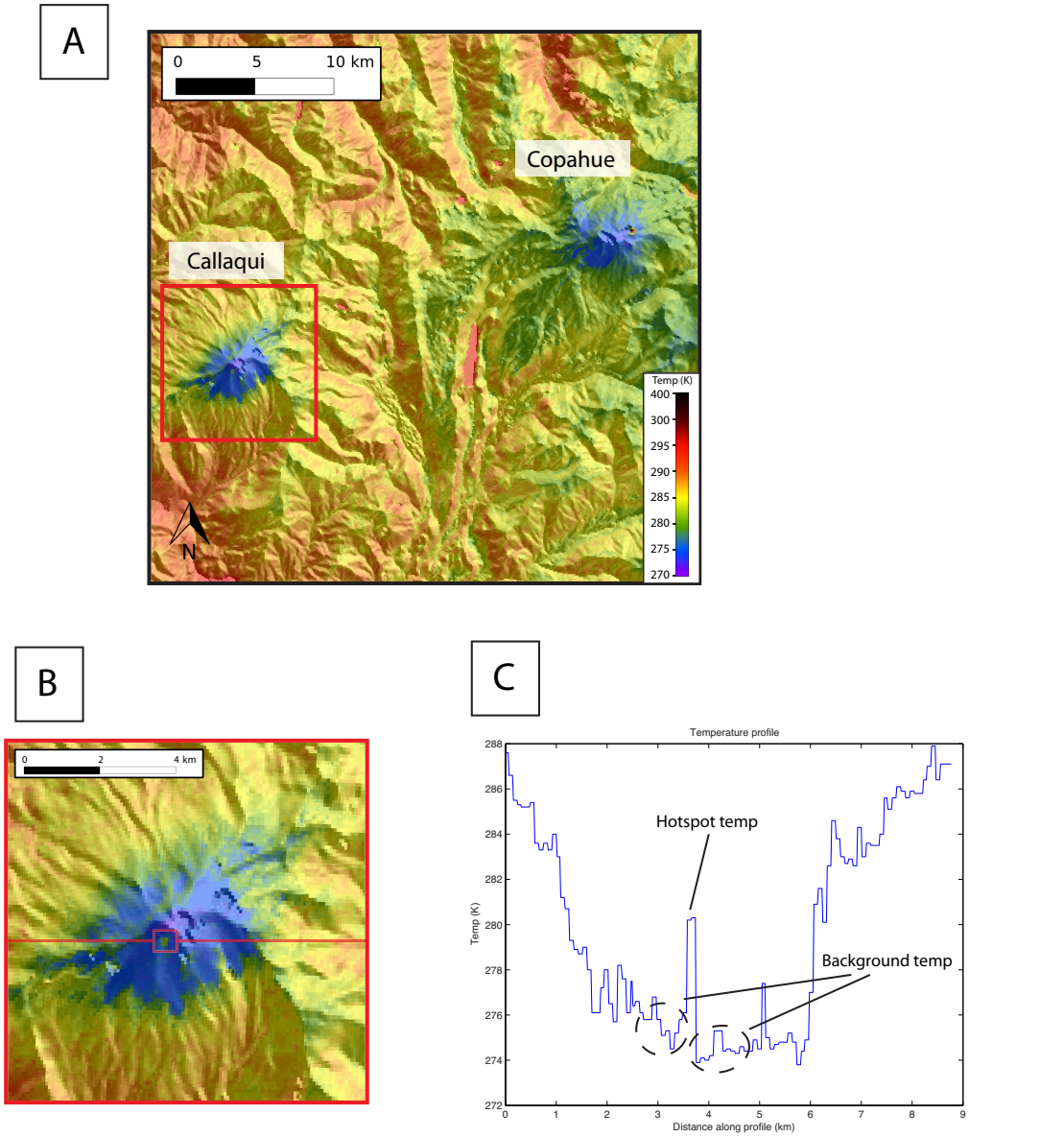

Figure 3.2 Example of plots used to evaluate hotspots. (a) Complete ASTER pixel-integrated temperature image from 1 December 2009. The box shows the location of the close-up image in (b) showing hotspots at Callaqui. The thermal anomaly at Copahue is also visible in this image and is labelled. (b) Zoom into the hotspot at Callaqui. The horizontal line shows the profile in (c). (c) Horizontal profile of temperatures; the hotspot is on the line in (b).

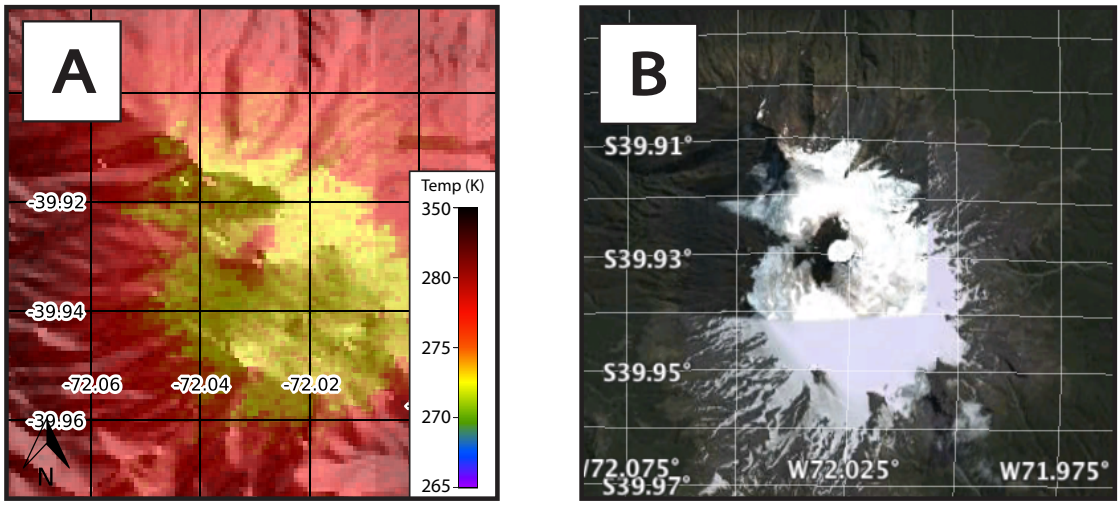

Figure 3.3 (a) Example of a potential hotspot for the Mocho-Choshuenco Volcano on 3 May 2006. The location of the hotspot coincides with the snow-free face of the volcano visible in (b) Google Earth imagery, most probably caused by high thermal inertia of the rock relative to snow-covered areas.

3.3 RESULTS

With ASTER, we find 51 volcanoes with either definite hotspots (35 volcanoes, Table 1) or questionable hotspots deserving further study (16 volcanoes, Table 2). Tables 1 and 2 contain the approximate temperature of each ASTER hotspot above the background temperature and the likely cause of the hotspot if known, as based on previous studies or reports from the Smithsonian Institution (Venzke et al. 2002-2011) (unless otherwise noted, all information on eruptive activity comes from these Smithsonian Institution reports). Images of all ASTER hotspots and potential hotspots are included in this paper. During an eruption, the target surface temperatures are often so high that the amount of radiance emitted by the eruptive products is greater than the upper sensitivity limit of the sensors' detectors, resulting in saturation. For the ASTER TIR bands, saturation occurs when the pixel-integrated temperature exceeds 360-380 K (Wright et al. 1999). For scenes in which saturation occurs, we record the

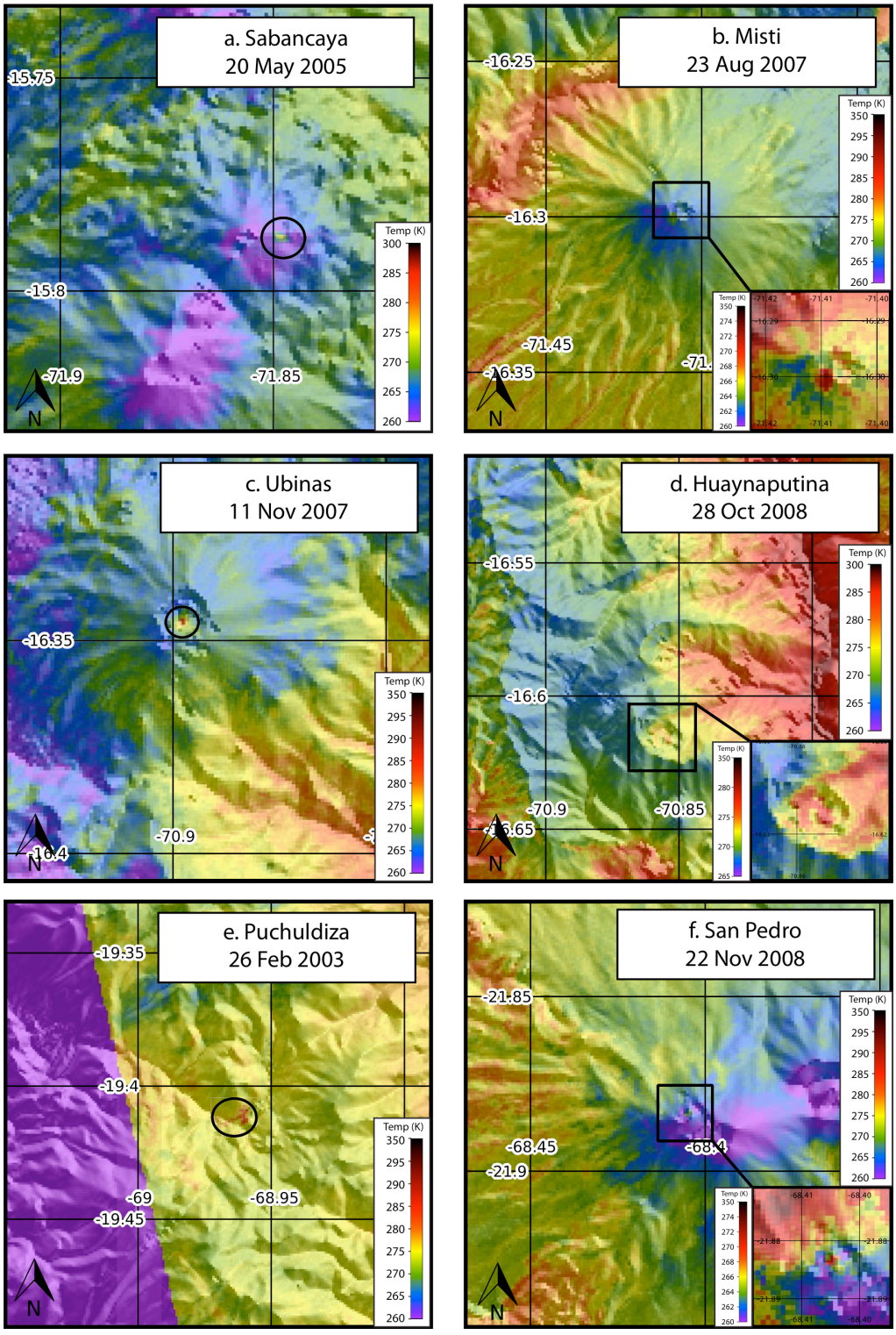

Figure 3.4 Close-up views of volcanoes with hotspots identified in ASTER pixel-integrated temperatures, with the color scale showing temperatures. Zoom-in boxes are provided for hotspots that are difficult to see in a volcano-wide image (with separate color-bar). See each image for dates.

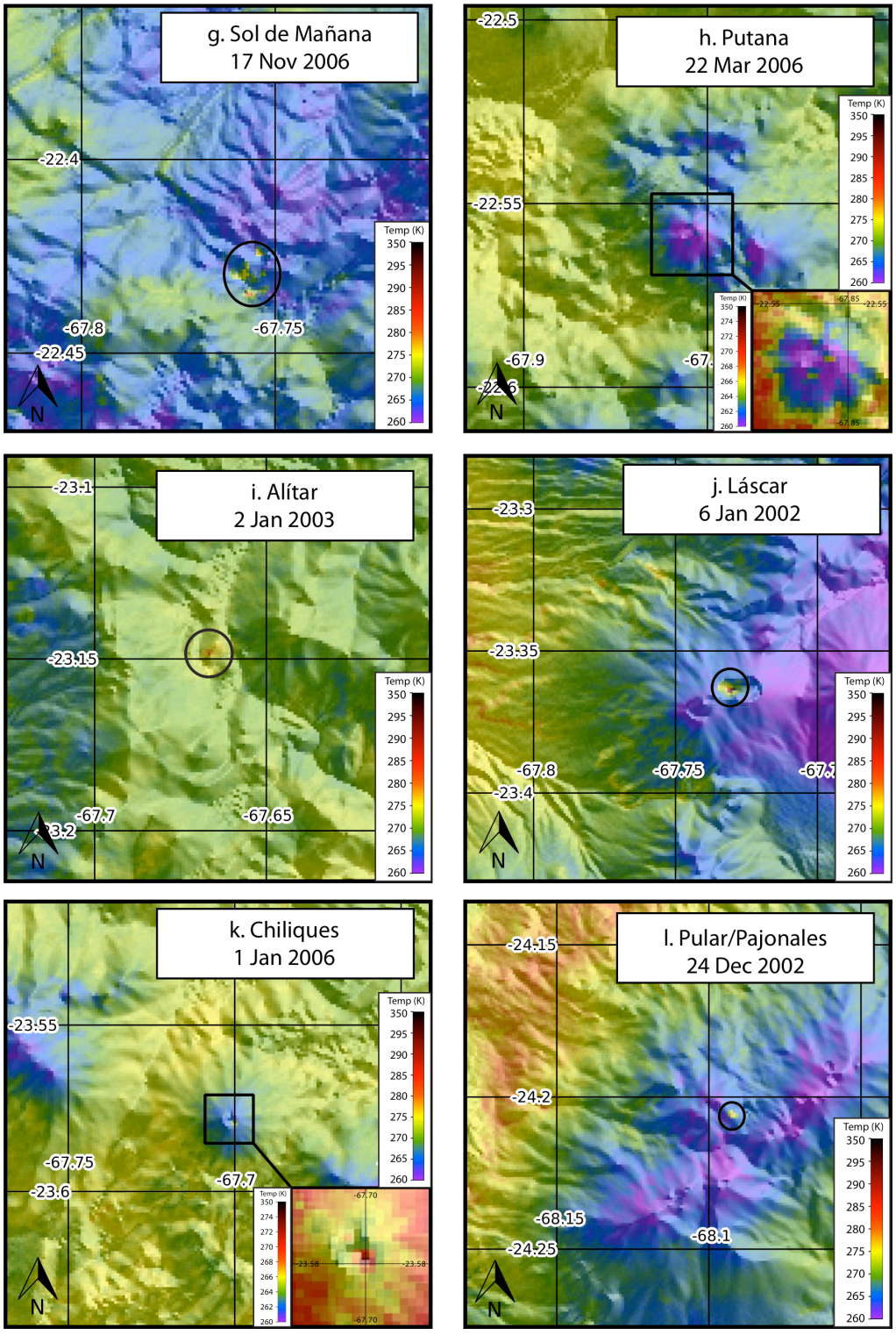

Figure 3.4 (cont.) Close-up views of volcanoes with hotspots identified in ASTER pixel-integrated temperatures, with the color scale showing temperatures. Zoom-in boxes are provided for hotspots that are difficult to see in a volcano-wide image (with separate color-bar). See each image for dates.

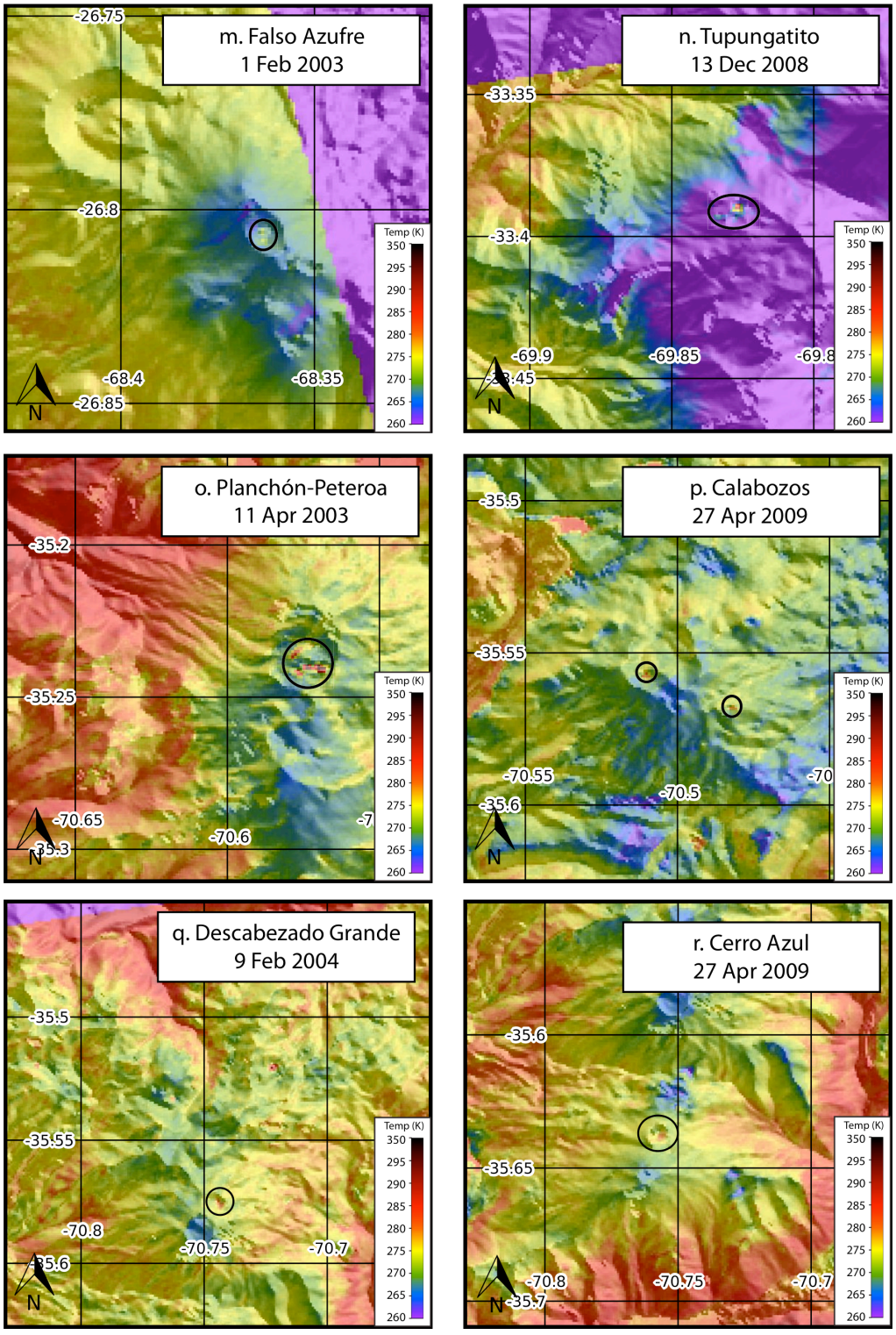

Figure 3.4 (cont.) Close-up views of volcanoes with hotspots identified in ASTER pixel-integrated temperatures, with the color scale showing temperatures. Zoom-in boxes are provided for hotspots that are difficult to see in a volcano-wide image (with separate color-bar). See each image for dates.

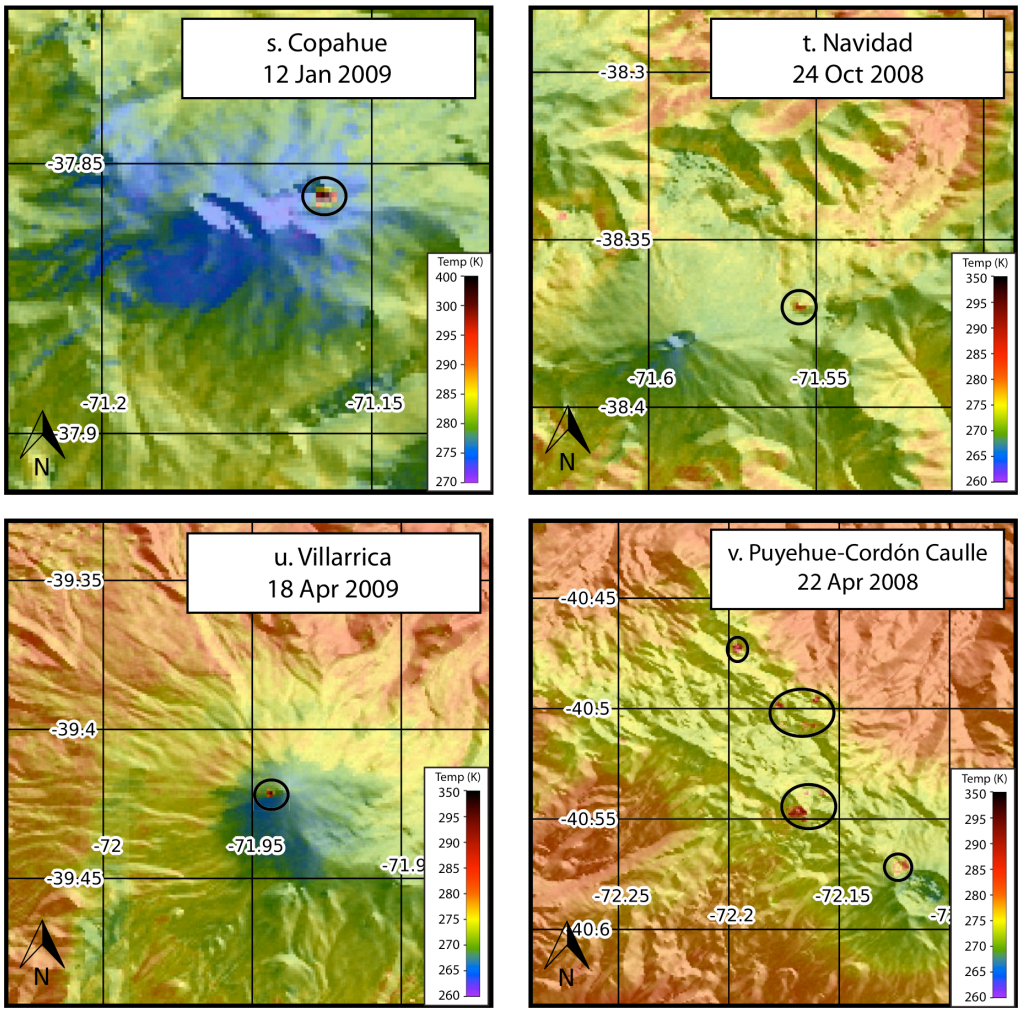

Figure 3.4 (cont.) Close-up views of volcanoes with hotspots identified in ASTER pixel-integrated temperatures, with the color scale showing temperatures. Zoom-in boxes are provided for hotspots that are difficult to see in a volcano-wide image (with separate color-bar). See each image for dates.

temperature of the hottest measurable pixel and make a note that other hotter pixels may be present but are outside of ASTER's dynamic range.

The majority of ASTER hotspots (80%) are related to known activity (Tables 1 & 2): 31 are related to persistently active fumaroles, hot springs or geothermal fields; five to geothermally heated lakes; one to an erupting lava lake; six to eruptions; and two to eruptive products, such as flows or lava domes. We could not find documented

evidence for the source of 10 of the hotspots, however. Given their magnitude and spatial extent, they appear to be similar to other known hotspots caused by fumaroles and hot springs. Even so, a number of these unidentified hotspots are likely to be related to non-volcanic processes, such as changes in thermal inertia between adjacent materials.

All eight volcanoes with eruptions during our study period have some hotspot either before, during or after the eruption: Sabancaya in 2003; Ubinas in 2006–2009; Láscar in 2004, 2005, 2006 and 2007; Nevados de Chillán in 2003 and 2008 (Naranjo & Lara 2004; Naranjo & Moreno 2009); Copahue in 2000 (Naranjo & Polanco 2004); Llaima in 2002, 2003, 2007 and 2008 – 2009; Villarrica in 2003-2004, 2004-2007, 2008 and 2009-2010; and Chaitén in 2008-2010 (Lara 2009). However, there are several volcanoes with known fumarolic activity that did not appear to have hotspots: Hualca Hualca, Calientes (just north of Yucamane in Peru), Tacora, Aguilucho cone at Azufre and Antofalla. Given the completeness of the temporal sampling (more than a dozen cloud-free images exist for each of them), we conclude that he fumaroles at these documented active volcanoes are too small spatially and/or thermally to be detectable by ASTER. In particular, we note that both Tacora and Aguilucho have permanently degassing areas with temperatures over the boiling point, yet these areas were not detected as hotspots in our search. This implies that the fumarolic fields are not large enough to produce a pixel-averaged temperature that is more than 4 K above background temperatures.

Our search using MODVOLC revealed hotspots at six volcanoes – Ubinas, Láscar, Villarrica, Llaima, Copahue and Chaitén – and we discuss these in the

following subsection. All volcanoes with hotspots detected by MODVOLC are observed to have ASTER hotspots, although ASTER observations are not always available at the time the MODVOLC hotspots were detected.

3.3.1 Comparison of remote and ground observations

The comparison of temperatures measured at a volcano on the ground with those measured by a satellite is not direct because the spaceborne observations average temperatures over an entire pixel (8100 m^2 for ASTER) composed of several sub-pixel regions of different temperatures. Ground observations are essential for disentangling the temperatures and spatial extents of these subpixel regions (e.g. Oppenheimer et al. 1993). We have compiled published measurements of the temperatures of fumaroles within our study in Table 3, but have left the determination of the spatial extent of the regions with the measured temperatures to future fieldwork. As expected, the ASTER measurements of temperature above background cannot simply be related to the maximum temperature observed on the ground. For example, the ASTER temperature above background at El Tatio and Lastarria are about the same but the maximum ground temperatures differ by hundreds of degrees (Table 3). At El Tatio, Uturuncu and other fumaroles, the ground temperatures are at the boiling point of water at these altitudes, while in other areas (i.e. Lastarria and Láscar) the ground temperatures are significantly higher. In a few cases (i.e. Lastarria, Uturuncu and Láscar) we can compare the repeat measurements of ground temperature with the ASTER observations. For Lastarria and Uturuncu, the ground and satellite observations are invariant over the time periods available, while Láscar exhibits much

variability that is consistent with the limited ground data available (see the sub-section ‘Láscar’ later and Fig. 3.6).

Figure 3.5 compares ground views of some fumarolically active volcanoes with an ASTER satellite view. For most documented fumaroles, the spatial extent of the ASTER hotspots are consistent with the known locations of activity; for example, the three hottest ASTER hotspots at Lastarria are situated within the largest fumarolic fields (Fig. 3.5h), with the smaller fourth fumarolic area (Aguilera et al. 2011) showing up as a more diffuse, lower intensity ASTER hotspot. Conversely, the magnitude and spatial extent of some of the ASTER hotspots are unexpected based on ground observations. The second, third and fourth hottest ASTER hotspots in the central Andes (Table 1) (i.e. Ojos del Salado (Fig. 3.5i), Uturuncu (Fig. 3.5f) and Isluga (Fig. 3.5b)) are also the most spatially extensive, but do not have the most prominent fumarolic vapour clouds on the ground. In fact, the fumarolic vapours at Ojos del Salado and Uturuncu are faint and only sometimes visible when standing right on top of the fumarolic field (Fig. 3.5i, f), while volcanoes with smaller ASTER hotspots have fumarolic clouds visible for tens of kilometres (e.g. Olca, Ollague, Irruputuncu: Fig. 3.5d, e, c). At Isluga and Irruputuncu, the largest fumarolic areas make up about one-half of the summit craters, which both have diameters of about 300 m. Based on the yellow color of the sulphur deposits at both volcanoes, the temperatures of the fumaroles are thought to be similar as the color of liquid sulphur changes from yellow to orange at a temperature of 406 K (e.g. Pieri et al. 1984; Naranjo 1985). However, the average size of the ASTER hotspot at Isluga over our study period (about 12 pixels) is significantly larger than at Irruputuncu (about four

pixels). At Isluga, the interpretation of a large area of elevated temperatures might be consistent with our field observation of fumaroles both in the summit crater and in an area located on the higher part of the southern flank at about 500 m down from the crater. Another interpretation is that the composition of Isluga's cinder cone crater (i.e. unconsolidated ash and pumice fall deposits) has different thermal properties to the lava domes and flows of Olca, Ollague and Irruputuncu.

The discrepancy between ground and ASTER observations is most probably related to some fumarolically active areas (i.e. Olca, Ollague and Irruputuncu) having very limited areas of high temperature, while hotspots (i.e. Uturuncu and Isluga) could have larger areas at lower temperatures. The dilution of a hotspot pixel temperature caused by subpixel-sized hotspot features is a common observation in thermal remote sensing of volcanoes (e.g. Pieri & Abrams 2005; Murphy et al. 2011). To test this hypothesis, we consider a subpixel hotspot region 400 m^2 in area with a temperature of 365 K surrounded by a background region with a temperature of 260 K, similar to the situation at Olca (Table 3). When averaging the hotspot temperature over a 90 × 90 m pixel, and assuming that the entire hotspot is within a single pixel, the temperature of that pixel would be 266 K, or 6 K above background. In another case, we consider a subpixel hotspot region 900 m^2 in area with a temperature of 350 K, similar to the situation at Uturuncu. While the hotspot at Uturuncu consists of more than one pixel, field observations indicate that only a fraction of each hotspot pixel is hotter than the background temperature. This calculation gives a pixel temperature of 270 K, or 10 K above background, for each hotspot pixel.

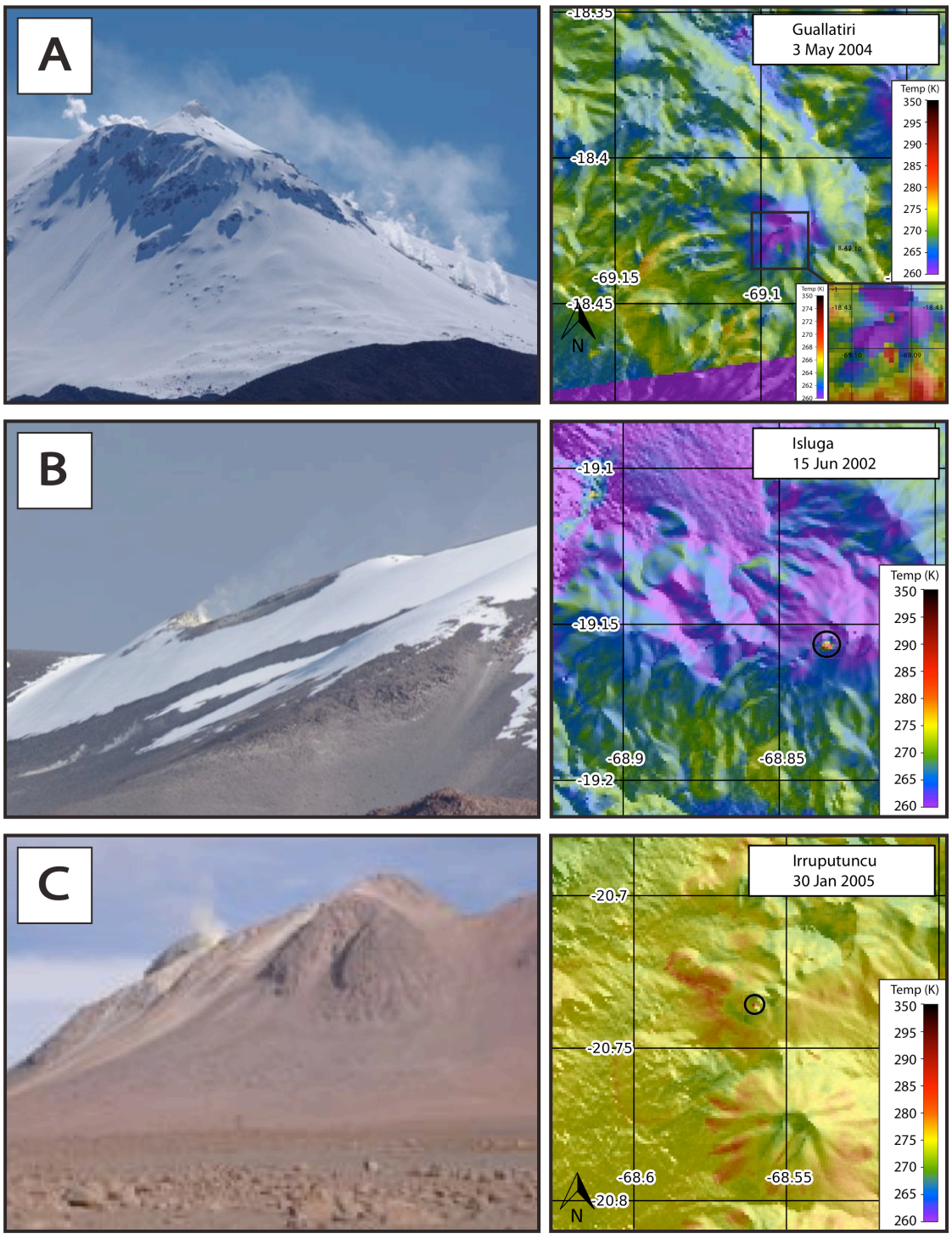

Figure 3.5 Comparison of ground and satellite views of selected hotspots for: (a)Guallatiri (ScottHenderson, March2012); (b) Isluga (Scott Henderson, March 2012); (c) Irruptuncu, SE side of Irruputuncu (Scott Henderson, October 2010)

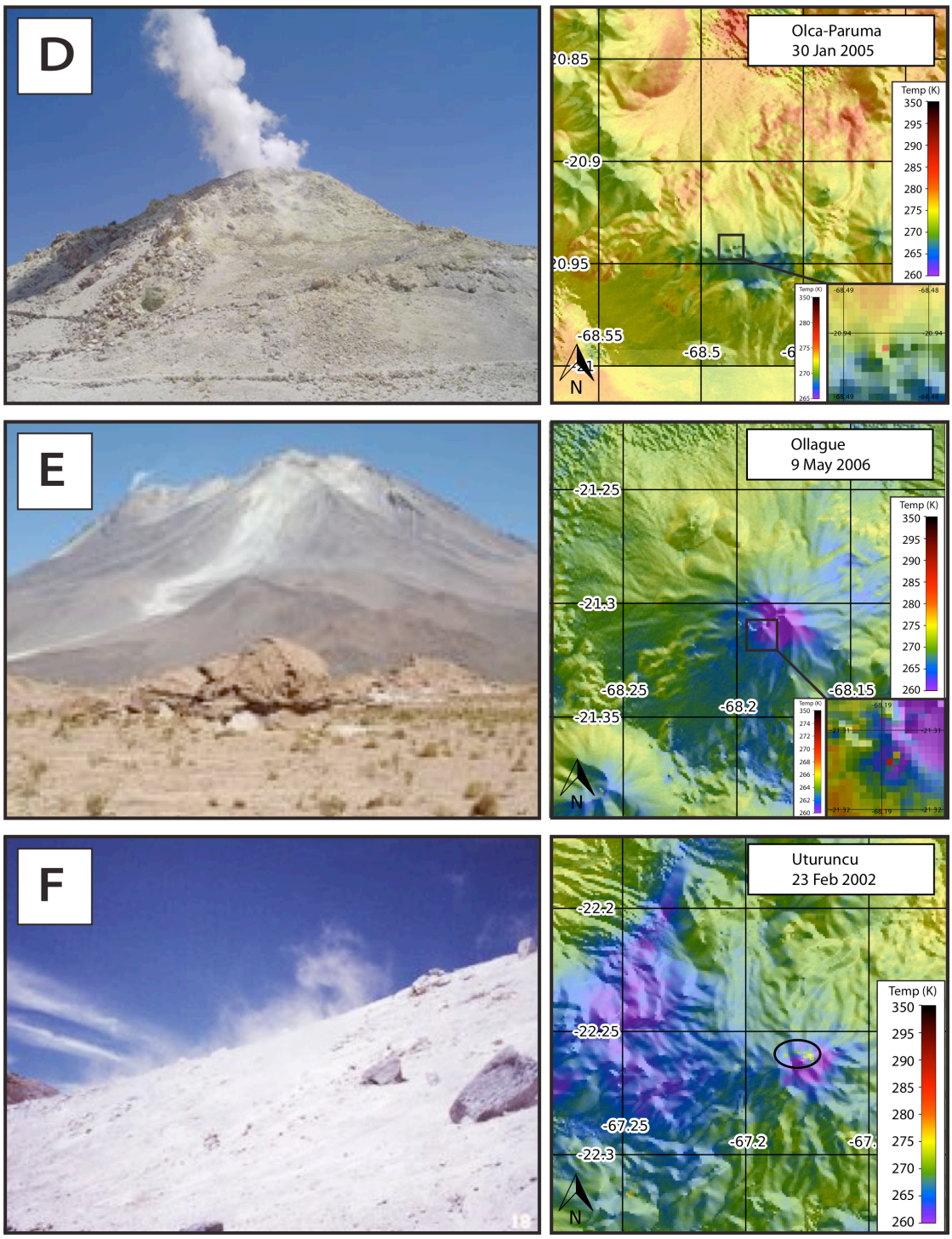

Figure 3.5 (cont.) Comparison of ground and satellite views of selected hotspots for: (d) Olca (Felipe Aguilera); (e) Ollague, SE side (Jennifer Jay, November 2010); (f) Uturuncu saddle between the two summits of Uturuncu Volcano as seen in April, 2003 (from Sunagua 2004)

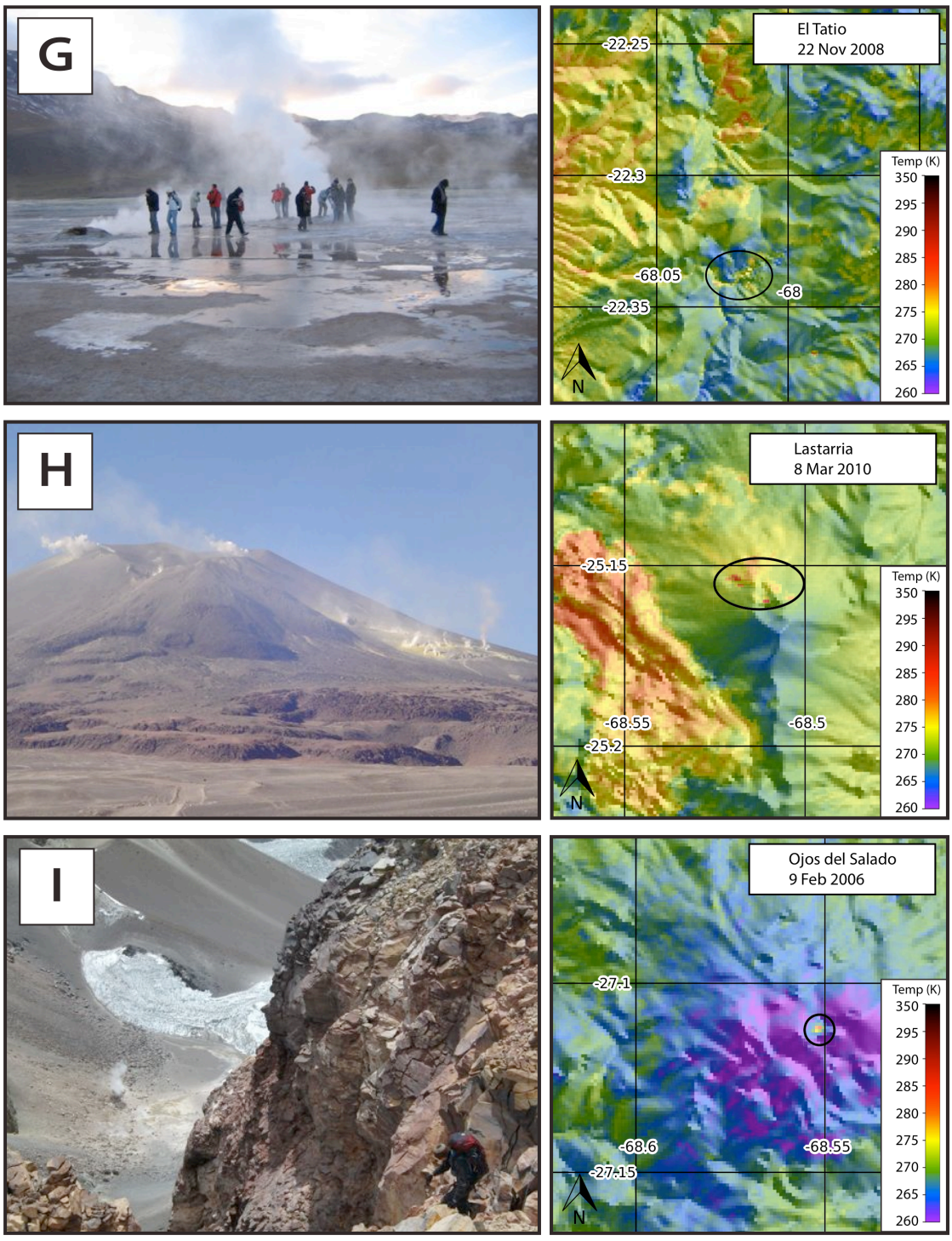

Figure 3.5 (cont.) Comparison of ground and satellite views of selected hotspots for: (g) El Tatio (Jennifer Jay, July 2007); (h) Lastarria Volcano, north side of the fumarolic areas (Felipe Aguilera); and (i) Ojos del Salado summit (Jonathan Kreiss-Tomkins, January 2011).

3.3.2 Temporal variability

Most of the hotspots have a roughly constant temperature above background on different dates within the uncertainty of our measurements (± 2-4 K) or too few observations to draw any conclusions about temporal variability. For five volcanoes, however, there are sufficient data and activity to discern some patterns in the temporal variability of hotspot temperature above background. In the next five subsections, we describe the potential significance of these time changes. However, we first describe four other volcanoes (Ubinas, Copahue, Isluga and Nevados de Chillán) that show plausible but ambiguous temporal variability. The observations at these four volcanoes are very few, but we find evidence that the temperature and/or spatial extent of the hotspots may vary with time.

Ubinas appears to have had a spike in thermal activity detected by MODIS during an eruptive cycle between May and December 2006 (Fig. 3.7a). There is one cloud-free ASTER scene of Ubinas during that timespan on 20 August 2006. The image shows a hotspot of 6 K above background and an ash plume drifting to the east. Hotspots before and after the eruption are generally higher in temperature but less spatially extensive (Fig. 3.7a).

The only MODVOLC hotspots detected at Copahue are in August 2000, related to the documented eruption during that time (Venzke et al. 2002-2011). ASTER images from March 2003 to January 2009 show variability from 15 to 48 K above background that are not simply related to seasonal temperature changes and might reflect variations of the internal heat flux. However, the ASTER temperature changes cannot be correlated with any known activity. Furthermore, the subsidence

Table 3.3 Comparison of selected ground measurements of fumarole surface temperatures (temperature, dates and references) with those measured at ASTER hotspots in this study

Volcano name	ASTER temp. (K)	Ground temp. (K)	Date of ground measurement	Source of ground temp. measurement
Misti	~269	> 523	1966;	Hantke & Parodi (1966)
		494	Dec. 1997;	Macedo et al. (2001);
		703	Sep. 2001;	Masías et al. (2010)
		461	Oct. 2009	
Tutupaca	N/A	> 473	1998?	Barragan et al. (1999)
Azufre	N/A	382 & 391	N/A	De Silva & Francis (1991)
Irruputuncu	~277	357-513	2007	Aguilera (2008)
Olca	~271	357-364	2007	Aguilera (2008)
El Tatio	~279	359;	N/A;	González-Ferrán (1995);
		316-364	2002-2004?	Tassi et al. (2005)
Uturuncu	~275	343-353	Oct. and Dec., 2002;	Sunagua (2004);
			April 2003;	Jo Gottsmann, personal
			April 2010	communication
Putana	~264	355-361	N/A	Tassi et al. (2011)
Alítar	~276	327-330	N/A	
Láscar	290-370	568-658;	Oct. 2002;	Venzke et al. (2002-2011),
		< 658;	Dec. 2004;	Tassi et al. (2009)
		345-523	Sept. 2006	
Lastarria	~279	566;	2002	Jorge Clavero, personal communication;
		354-681	2006-2009	Aguilera et al. (2011)
Copahue	311	408	2006?	Agusto et al. (2007)
Cordón Caulle	288	366	2004?	Sepúlveda et al. (2007)
Cerro Azul	275	318-348	1980's	Hildreth & Drake (1992)
Nevados de Chillán	266-320	330-361	22 January 2004	Venzke et al. (2002-2011)

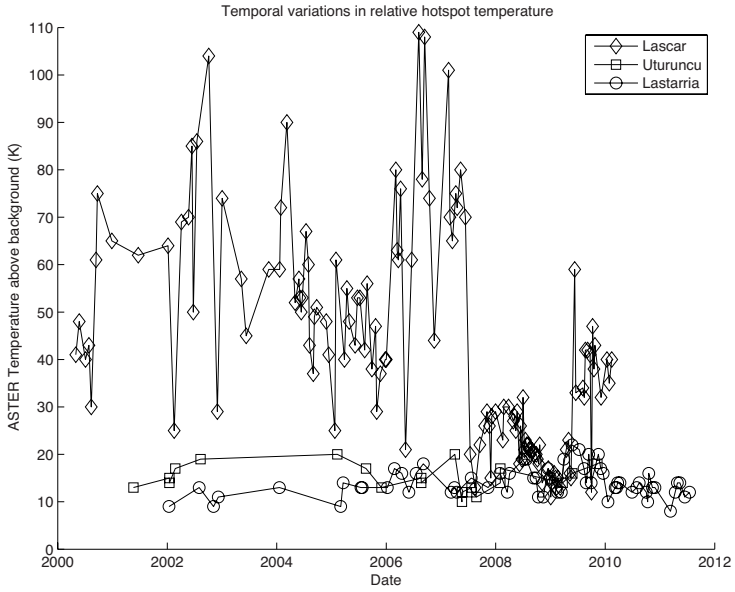

Figure 3.6 Temporal variations in relative hotspot temperatures at the Láscar, Uturuncu and Lastarria volcanoes. Note the large temperature variability at Láscar, and the relatively constant temperatures at Uturuncu and Lastarria.

rate observed by satellite InSAR (Interferometric Synthetic Aperture Radar) at Copahue has not shown any variability between 2002 and 2007 (Velez et al. 2011), which suggests temporally invariant activity during this time period.

There have been reports of an increase in fumarolic activity of Isluga Volcano in 2002-2003 (Céspedes et al. 2004). ASTER hotspot temperatures between 2001 and 2010 are 6-24 K above background, with the temperatures in the higher part of the range for most of the study period (2002 until about 2008). However, the number of observations is limited and there is a lot of scatter, so the evidence for a decrease in temperature after 2008 is not conclusive. MODVOLC hotspots were not detected at Isluga.

The ASTER hotspot at Nevados de Chillán is associated with normal hydrothermal activity and an elusive eruption in 2008. The normal hotspot temperature varies from 7 to 15 K above background; however, the temperature

reaches 25-47 K above background in five ASTER scenes from 14 March to 21 August 2008 (Fig. 3.8b). The shape of the hotspot also changes during this time period and resembles an eruption of lava. The timing of this eruption is consistent with the elusive eruption suggested by Naranjo & Moreno (2009) and the formation of a lava field called the Sebastián Volcano. Although the eruption seems to have ended by 12 January 2009, the lava flow still appears to be warmer than surrounding areas. There is one ASTER scene during the documented eruptive activity in August to September 2003 (Venzke et al. 2002-2011; Naranjo & Lara 2004); however, the hotspot shows no difference in location, shape or amplitude from the normal background activity. There were no hotspots detected by MODVOLC at Nevados de Chillán.

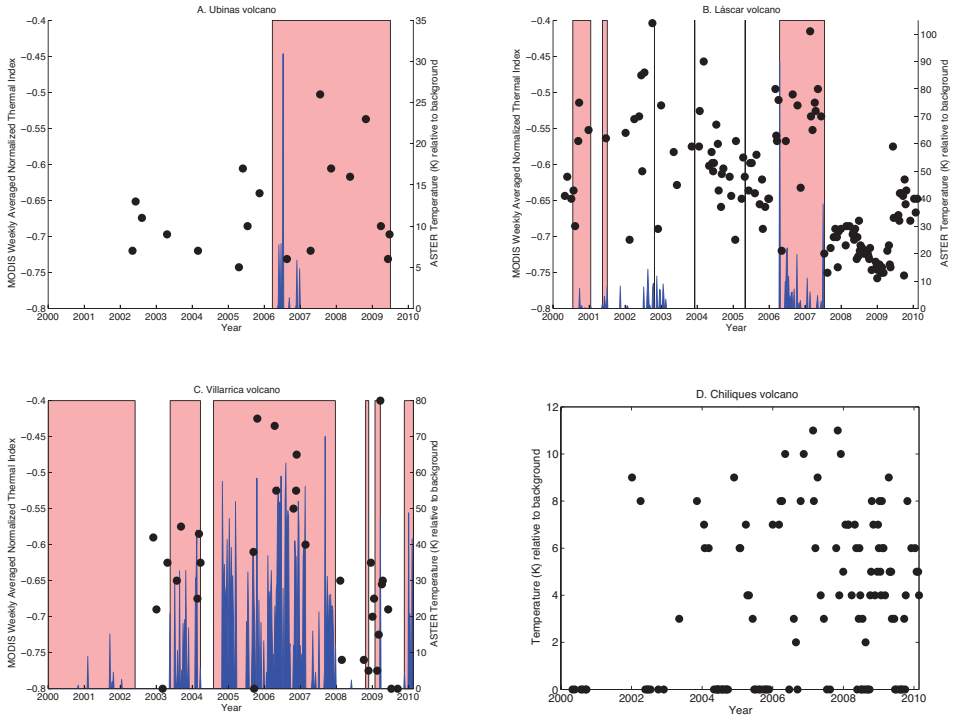

Figure 3.7 Time series of hotspot temperatures for: (a) Ubinas; (b) Láscar; (c) Villarrica; and (d) Chiliques. ASTER temperatures (black circles) are calculated relative to background. The Normalized Thermal Index (proxy for hotspot temperature) detected by MODIS (lower resolution than ASTER, but temporally more frequent) at each volcano calculated by the MODVOLC algorithm is shown as blue spikes (where available). Periods of known eruptive activity from Venzke et al. (2002–2011) are shown in pink.

3.3.3 Láscar

Thermal activity at Láscar, the most active volcano in the central Andes in historical times (Siebert & Simkin 2002-2012), has been documented for decades (e.g. Glaze et al. 1989; Oppenheimer et al. 1993; Harris et al. 1997; Matthews et al. 1997; Wooster & Rothery 1997; Denniss et al. 1998; Gar- deweg et al. 1998, Wooster 2001; Mather et al. 2004; Pavez et al. 2006). We observed a hotspot on this volcano for each of the

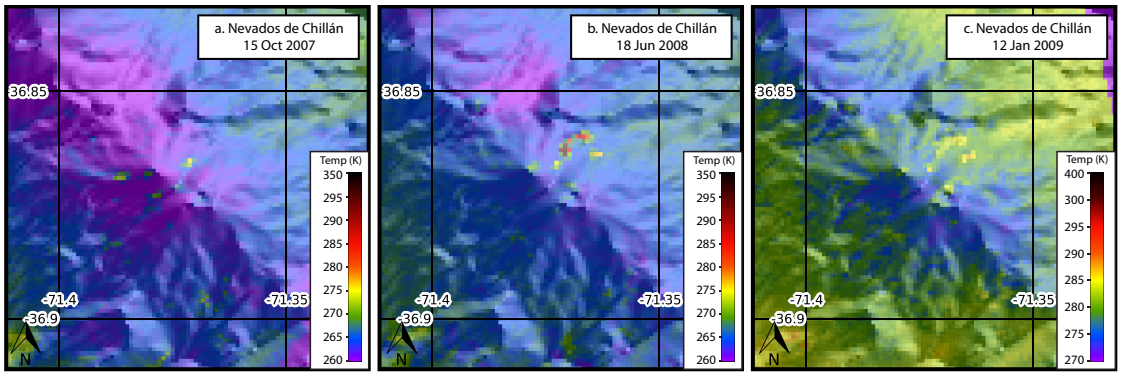

Figure 3.8 ASTER thermal images over Nevados de Chillán showing: (a) normal background hotspots; (b) hotspot related to an elusive eruption in 2008; and (c) a return to background activity in 2009. See each image for dates.

ASTER images we analyzed (Fig. 3.4). We plot the ASTER observed temperature above background in Figure 3.7b along with known eruptive activity from Venzke et al. (2002 – 2011) and the normalized thermal index from MODVOLC that is a proxy for the intensity of the MODIS hotspot. The temperature above background of the ASTER hotspot varied significantly over the 9 year period with a range of about 98 K, and MODVOLC recorded hotspots on many days between 2000 and 2007 (Fig. 3.7b). Ground temperature measurements taken in October 2002, December 2004 and September 2006 (Venzke et al. 2002 – 2011; Tassi et al. 2009) (Table 3) are consistent

with the ASTER observations in that the ASTER temperature in October 2002 was higher than in the other periods.

During the time period of satellite observations, significant eruptions at Láscar were reported in July 2000, May 2005 and April 2006 – July 2007. Smaller explosions were also documented in October 2002, May, July and August – October 2006, and, possibly, December 2003 and May 2001 (Clavero et al. 2006; Aguilera et al. 2006a, b). MODVOLC hotspots are associated with most of these eruptive episodes (Fig. 3.7b). However, not all eruptions have hotspots; for example, the explosions in December 2003 and May 2005 are not associated with MODVOLC hotspots, and there are MODVOLC hotspots in late 2001 and early 2002 without any documented eruptive activity.

The correlation between eruptive activity and the ASTER temperatures above background are less obvious than with the more frequent MODIS observations. There appears to be a multi-year timescale cycle of temperature change (Figs 3.6 & 7b). There is a temperature peak in 2002 followed by a decline to 2004 – 2006, then a temperature increase with the onset of the 2006 eruption and a sharp decline following the eruption. Temperatures remain low until 2009, when elevated temperatures are observed until the end of our study period. Previous work suggested a cyclic variation in temperature related to lava dome subsidence within the summit crater and eruptions up to the April 1993 eruption, but a more complex pattern between temperature and eruption since 1993 (Matthews et al. 1997). Observations of the summit crater suggest subsidence within the crater had occurred between March and December 2005, and that the crater floor remained at a low level until at least September 2006 (Venzke et

al. 2002 – 2011). The timing of the low level of the crater floor correlates with a period of stable but not anomalously low temperatures measured by ASTER. Ground observations made by one of us (F. Aguilera) in April and June, 2009, when ASTER temperatures are lowest, confirm that the crater floor was in a subsided state and that the inner crater walls had partially collapsed, reducing the area of fumarolic activity and, probably, the effective temperature observed by ASTER.

3.3.4 Chiliques

The first reported recent activity at Chiliques were two spatially distinct thermal anomalies observed in 2002 by ASTER (Pieri & Abrams 2004). No hotspot was observed in images from 2000 and the duration of the hotspot was less than 18 months (Pieri & Abrams 2004; Pritchard & Simons 2004). One hotspot at the summit is thought to be caused by geothermal heating of one or more crater lakes (Pieri & Abrams 2004); however, no field evidence of high temperature at the crater lakes has been reported so far. These lakes might stand out as thermal anomalies in the ASTER night-time scenes owing to the high thermal inertia of water compared to the surrounding rock (Fig. 3.4 k). The other hotspot is hypothesized to be related to fumarolic activity based on observations made during an airplane flyover by the Chilean Geological Survey (SERNAGEOMIN) (Pieri & Abrams 2004). However, such activity was not seen during an ascent to the summit by one of us (F. Aguilera) in November 2002. From 2000 to 2009, we find that the existence of the hotspot on Chiliques is variable in time; some images showing one or more hotspots (Fig. 3.4)

with temperatures up to 158 above background (Fig. 3.7d), while others show no anomaly. Most of the images with no hotspot are from the austral summer, but some are during other seasons. It is possible that the heat flux to the Chiliques fumaroles and lakes varies in time or that it is harder to detect the hotspots under certain conditions, such as warm ambient temperatures in summer. MODVOLC did not detect any hotspots at Chiliques.

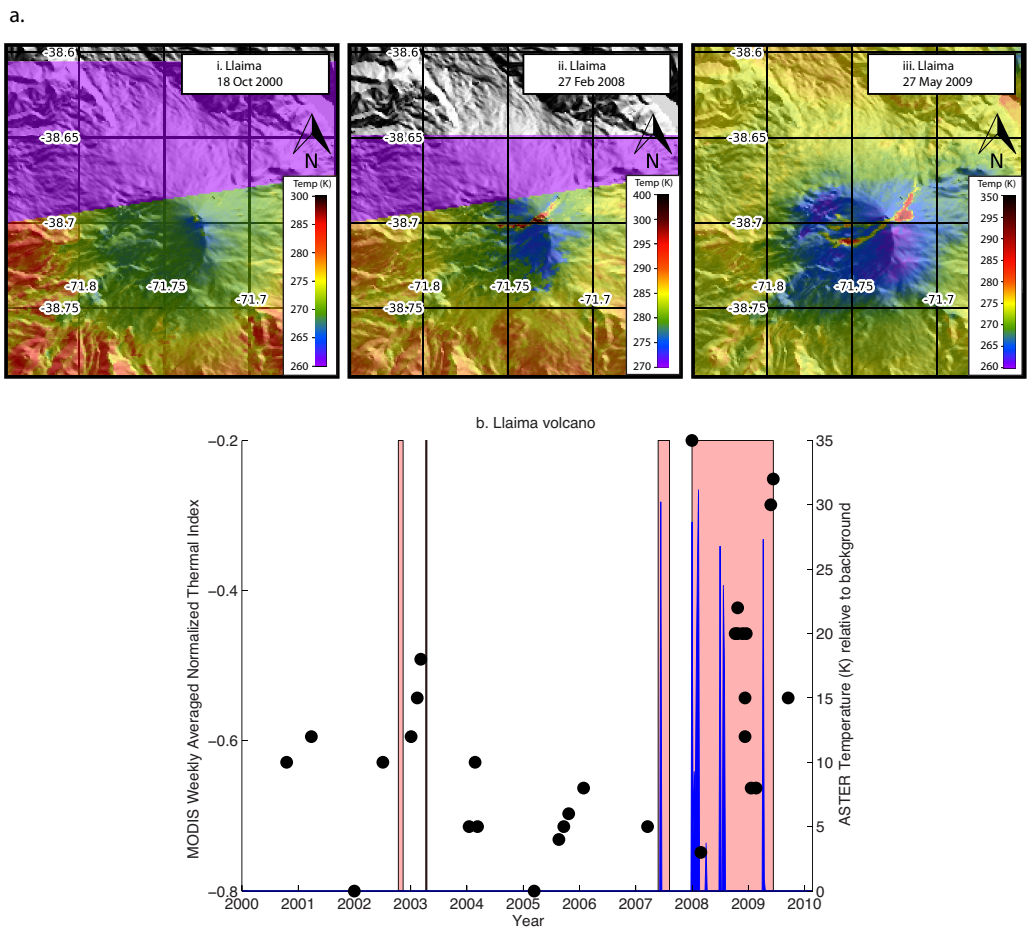

Figure 3.9 ASTER data showing the time variability of the hotspot at Llaima Volcano. (a) ASTER images: (i) image (18 October 2000) showing typical background thermal activity at Llaima near the summit; (ii) image (27 February 2008) showing hotspots due to the February 2008 eruptions; (iii) image (27 May 2009) showing hotpots due to lava flows from the April 2009 eruptions. (b) Plot of the temporal variability of Llaima hotspot temperatures recorded by ASTER and MODIS. See the Figure 3.6 caption for more details.

3.3.5 Llaima

Llaima is one of the most active volcanoes in Chile (e.g. Naranjo & Moreno 1991), with constant fumarolic activity (e.g. Muñoz 1983) and four eruptive periods during our observational interval (Fig. 3.9). We report 31 out of 33 cloud-free ASTER images as having a hotspot on Llaima with a temperature range from 4 to 107 K above background, with pixel saturation sometimes occurring. The highest temperatures were associated with lava flows from eruptions in January 2008 and April 2009, whose thermal signature lasted for months (Fig. 3.9b, c). 'Normal' fumarolic activity produced ASTER hotspots less than 15 K above background near the summit (Fig. 3.9), except for slightly higher temperatures between eruptions in 2002 and 2003. There is a suggestion that there were lower than average fumarolic temperatures in 2005 – early 2007 before thermal and eruptive activity increased in 2007 – 2009 (Naranjo et al. 2009). MODVOLC alerts occurred only during the main periods of eruptive activity in 2007–2009, but smaller eruptions in 2002 and 2003 did not register as hotpots in MODVOLC.

3.3.6 Chaitén

From February 2003 until April 2008, thermal activity at ChaiténVolcano seemed to be restricted to the moat between the rim of the summit crater and the dome in the centre (Fig. 3.10a), and is presumably related to small lakes. The hotspot temperature as measured by ASTER was 4 – 22 K above background. On 2 May 2008, Chaitén began its first historic eruption (Watt et al. 2009; Alfano et al. 2011), and both ASTER

and MODVOLC have recorded hotspots of the still ongoing activity (Fig. 3.10b–d). There is no evidence of precursory thermal activity before the 2 May eruption – an ASTER night-time image taken just a few weeks before the eruption (13 April) shows normal activity – and is consistent with the lack of other manifestations of precursory activity (ground deformation and seismicity) until a few days before the eruption (e.g. Lara 2009; Fournier et al. 2010; Wicks et al. 2011). The ASTER images show a

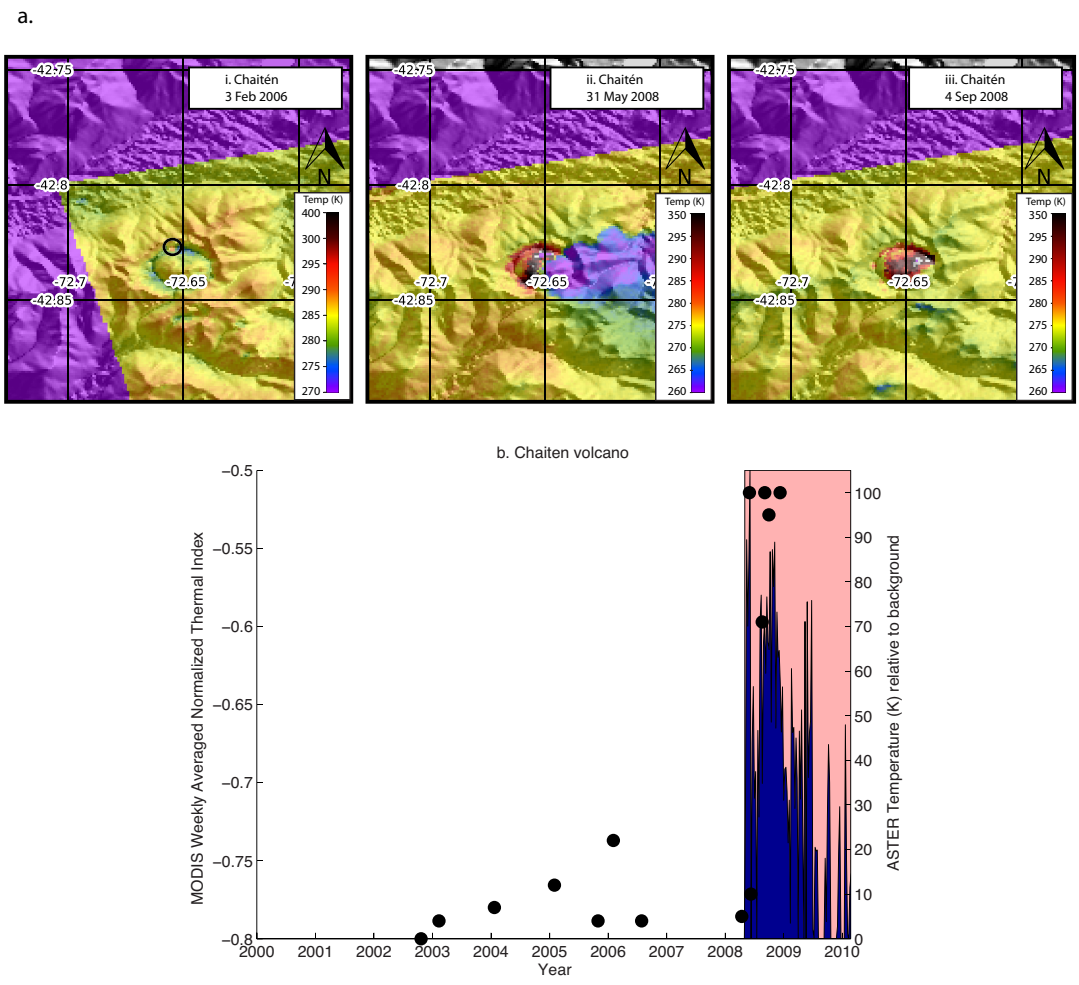

Figure 3.10 ASTER images showing the time variability of the hotspot at Chaitén Volcano. (a) ASTER images: (i) pre-eruptive image (3 February 2006) showing hotspots probably related to lakes; (ii) image (31 May 2008) taken after start of eruptive activity showing hot lava dome and a cool ash plume travelling from the crater to the east; (iii) image (4 September 2008) showing only the hot lava dome. (b) Plot of the temporal variability of the Chaitén hotspot temperatures recorded by ASTER and MODIS. See the Figure 3.6 caption for more details.

hotspot related to the growing lava dome (Fig. 3.8c), as well as cold areas related to ash and steam plumes that sometimes partially obscure the hot lava dome (Fig. 3.10b). Of the six cloud-free ASTER night-time images taken since the start of the eruption, four of them are saturated and show a temperature of about 373 K or approximately 100 K above background. The intensity of the MODVOLC normalized thermal index has declined between 2008 and 2010, a trend that is consistent with the fact that the growth rate of the rhyolite lava dome was fastest from June to September 2008 and then declined exponentially until ending in 2010 (Pallister et al. 2010). The thermal trend is not apparent in the ASTER data as the last available image is from December 2008.

3.4 DISCUSSION

We have found 23 hotspots and eight potential hotspots (31 total) at the 64 volcanoes and geothermal areas examined in the central Andes, and 13 hotspots and seven potential hotspots (20 total) at the 86 volcanoes and geothermal areas in the southern and austral Andes. While the percentage of volcanoes with hotspots is greater in the central Andes, the hotspots are hotter in the southern Andes, with seven different volcanoes having temperatures that exceeded 30 K above background compared to only one in the central Andes. The hotter hotspots in the southern Andes are consistent with the fact that this arc has historically had more eruptions than the central Andes (e.g. Siebert & Simkin 2002–2012) as the highest temperature hotspots occur during eruptive periods. In the southern Andes, magma composition is predominantly basalt to basaltic andesite and the crust is generally thinner than in the central Andes, where

crustal thickness reaches up to 70 km and andesite, dacite, and rhyolite compositions are dominant (Stern 2004). These factors may contribute to the higher eruptive activity in the southern Andes as well as the higher hotspot temperatures since basaltic lava (Llaima, Villarrica) is generally hotter than the more silicic products. Cerro Hudson in the southern Andes experienced one of the largest eruptions in the 20th century in 1991 (Siebert & Simkin 2002–2012) but did not have a hotspot; this is likely due to the fact that the timespan of our survey does not cover the historical eruptions and only four ASTER scenes were available (see Appendix A1.1).

Active volcanoes can manifest their activity in several different ways (e.g. seismic, thermal and ground deformation), and not all active volcanoes will exhibit all types of manifestations at the same time. For example, while at least 35 volcanoes in the central and southern Andes have thermal manifestations of activity detectable by satellite during the last decade, at least 16 volcanoes in the same areas have exhibited ground deformation observed by satellite InSAR since 2000. These lists of active volcanoes do not completely overlap. Three areas have had continuous deformation and thermal activity: Uturuncu (Pritchard & Simons 2004; Sparks et al. 2008), Copahue – the Navidad cone at Lonquimay (due to subsidence of the lava flow) – and Cordón Caulle (although the sign and magnitude of deformation at the latter seem to change with time) (Fournier et al. 2010; Jay et al. 2014). We consider volcanoes to be 'continuously deforming' if they exhibit deformation for the duration of our study period (2000 – 2010) and 'episodically deforming' if they exhibit at least one episode of deformation within this time period. Five others have had a continuous hotspot but probably episodic deformation based on the temporally limited SAR data acquisitions:

Putana (Henderson & Pritchard 2011), Láscar (Pavez et al. 2006), Lastarria (e.g. Froger et al. 2007; Ruch et al. 2009), Llaima and Chaitén (Fournier et al. 2010). Seven areas had deformation with no detected ASTER hotspot: Hualca Hualca (although deformation here ended in 1997, before ASTER was launched) (Pritchard & Simons 2004), Ticsani (although deformation here was probably short-lived and related to an earthquake swarm in October 2005) (Holtkamp et al. 2011), Cerro Overo (Henderson & Pritchard 2011), Lazufre (e.g. Pritchard & Simons 2004; Ruch et al. 2009), Cerro Blanco (although no cloud-free night-time images of this area have yet been acquired) (Pritchard & Simons 2004), Laguna del Maule and Cerro Hudson (Fournier et al. 2010). There are 28 hotspots and 16 questionable hotspots detected by ASTER with no observed deformation.

Recent studies have shown that thermal activity detected by MODVOLC at volcanoes can be affected by earthquakes (Harris & Ripepe 2007; Delle Donne et al. 2010). However, between 2000 and 2006, Delle Donne et al. (2010) did not find any MODVOLC thermal change at the volcanoes of our study area within 750 km of the earthquakes listed in the USGS PDE catalogue (completeness threshold about Mw 4.5). We expand upon the Delle Donne et al. (2010) study by investigating whether any of the six Mw > 7 earthquakes that occurred within our study area during our study period (stars in Fig. 3.1) had any effect upon any of the MODVOLC or ASTER hotspots (no distance threshold), including two earthquakes after their study ended in 2006. The specific earthquakes we examine are primarily on the shallow subduction interface unless otherwise noted: 12 May 2000 Mw 7.2 Chile earthquake (225km depth); 23 June 2001 Mw 8.4 Arequipa, Peru earthquake and aftershock on 7 July

2001; 13 June 2005 Mw 7.8 Tarapaca, Chile (115km depth); 15 August 2007 Mw 8.0 Pisco, Peru; and 14 November 2007 Mw 7.7 Tocopilla, Chile.

Because of the infrequent existence of cloud-free ASTER images, it is difficult to obtain temperatures shortly before and after an earthquake for most volcanoes. However, at Láscar, there is a reasonably good time series of observations, and it is known that ground deformation of a cooling pyroclastic flow there was enhanced by one of our selected earthquakes (Whelley et al. 2012). The temperature fluctuations from before and after each of the six earthquakes are not atypical of normal weekly to monthly fluctuations at Láscar, so we do not think that they can be tied to the earthquakes with certainty. We also note that, although Guallatiri experienced a shallow seismic swarm in response to the 2001 Arequipa earthquake (Glass pers. comm. 2011), we do not have ASTER data for this volcano prior to June 2002 so we cannot assess whether this increase in seismicity was accompanied by an increase in thermal activity.

We do not have a good explanation for the lack of any significant observed change to the volcanic hotspots in the central or southern Andes by large South American earthquakes, although we note two points that might be relevant. Delle Donne et al. (2010) concluded that most of the volcanoes that had a thermal response to earthquakes were erupting effusively, and there are only two or three volcanoes in our study area that fall into this category between 2000 and 2010 (Llaima, Villarrica and Chaitén). Secondly, it is possible that the thermal response at the volcanoes in this area is very short (of the order of days) or of low magnitude, and therefore difficult to observe by satellite. A short temperature anomaly at Misti Volcano, Peru, was

measured on the ground following the 2007 Pisco, Peru earthquake, but only lasted a few days (Masías et al. 2010). Another potential factor is that earthquakes affect the subvolcanic system but that these effects are not manifested immediately at the surface; for example, an increase in fluid movement in the subsurface rather than increased fumarolic activity at the surface.

3.5 CONCLUSIONS

Our survey of 150 volcanoes and geothermal areas in the central, southern and austral volcanic arcs of the Andes by ASTER night-time satellite thermal imagery has revealed 35 hotspots and 16 potential hotspots, while only eight of these had been previously reported. The hotspots have a number of origins including lava flows and domes, and geothermally heated lakes, but most can be related to known fumaroles or geothermal systems and have temperatures less than 30K above background. While the available data provide poor temporal coverage at most of the volcanoes, there are at least five examples of temporal variations in the temperature of the anomaly that can be correlated with known eruptive activity. However, we do not observe any significant change in thermal activity triggered by large earthquakes in South America but hypothesize that more frequent observations are required. While remote sensing already plays an important role in monitoring the remote volcanoes of this study area (e.g. MODVOLC, the Buenos Aires Volcanic Ash Advisory Center and satellite InSAR: Fournier et al. 2010), we find that high-resolution thermal imagery like that available from ASTER provides additional information about fumarolic activity and small-scale eruptions. For example, the number of volcanoes with hotspots, and the

size and temperature of some of those hotspots, are greater than would be expected based solely on ground or MODVOLC observations.

Though this study was not specifically designed to use thermal imagery as a tool for eruption forecasting, we find that, with improved temporal sampling of high resolution thermal infrared data and implementation of an automatic hotspot detection algorithm, this method might have potential for indicating which volcanic centers could erupt on short timescales.

REFERENCES

Aguilera, F. 2008. Origen y Naturaleza de los Fluidos en los Sistemas Volcánicos, Geotermales y Termales de Baja Entalpía de la Zona Volcánica Central (ZVC) Entre los 17o43′S y 25o10′S. Tesis, Doctoral 2008, Volume I. Andros Impresores, Santiago.

Aguilera, F., Viramonte, J., Medina, E., Guzmán, K., Becchio, R., Delgado, H. & Arnosio, M. 2006a. Eruptive activity from Lascar Volcano (2003 – 2005). 11th Chilean Geological Congress. Universidad Católica del Norte, Antofagasta, 397–400.

Aguilera, F., Viramonte, J., Medina, E., Guzmán, K., Becchio, R., Delgado, H. & Arnosio, M. 2006b. Recent eruptive activity from Lascar volcano 2006. 11th Chilean Geological Congress. Universidad Católica del Norte, Antofagasta, 393–396.

Aguilera, F., Carrizo, D. & Viramonte, J. 2007. Thermal monitoring of Lascar Volcano (northern Chile) based in remote sensing and field data. In: Demant, A. (ed.) Geosur 2007: An International Congress on the Geology and Geophysics of the Southern Hemisphere, Santiago de Chile, Actas, Volume 3. Centro de Extensio´ n Pontificia Universidad Católica de Chile, Santiago, 1997.

Aguilera, F., Tassi, F., Darrah, T., Moune, S. & Vaselli, O. 2011. Geochemical model of a magmatic – hydrothermal system at the Lastarria volcano, northern Chile. Bulletin of Volcanology, 74, 119 – 134.

Agusto, M., Tassi, F., Caselli, A., Vaselli, O., Tedesco, D. & Poreda, R. 2007. Chemical and isotopic features of thermal fluid discharges in the volcano – hydrothermal system of the Caviahue – Copahue volcanic complex (Argentina). (Abstract.) In: Geosur 2007: An International Congress on the Geology and Geophysics of the Southern Hemisphere, Santiago de Chile, Actas. Centro de Extensión Pontificia Universidad Católica de Chile, Santiago, 9.

Alfano, F., Bonadonna, C., Volentik, A. C. M., Connor, C. B., Watt, S. F. L., Pyle, D. M. & Connor, L. J. 2011. Tephra stratigraphy and eruptive volume of the May, 2008, Chaitén eruption, Chile. Bulletin of Volcanology, 73, 613–630.

Barragán, R. R. M., Arellano, G. V. M., Birkle, P., Portugal, M. E. & Diaz, H. G. 1999. Chemical description of spring waters from the Tutupaca and Rio Calientes (Peru) geothermal zones. International Journal of Energy Research, 23, 125–139.

Calder, E. S., Harris, A. J. L., Peña, P., Pilger, E., Flynn, L. P., Fuentealba, G. & Moreno, H. 2004. Combined thermal and seismic analysis of the Villarrica volcano lava lake, Chile. Revista Geológica de Chile, 31, 259–272.

Carter, A. J. & Ramsey, M. S. 2009. ASTER- and field- based observations at Bezymianny Volcano: Focus on the 11 May 2007 pyroclastic flow deposit. Remote Sensing of Environment, 113, 2142–2151.

Céspedes, L., Clavero, J. & Cayupi, J. 2004. Hazard management at Isluga volcano, Northern Chile: preliminary results. IAVCEI General Assembly, Pucón, Chile. Abstract 05a_107.

Clavero, J., Naranjo, J. A. & Cayupi, J. 2006. El ciclo eruptivo del 18 al 25 de Abril de 2006 del volcán Láscar, Andes Centrales (Abstract). 11th Chilean Geological Congress. Universidad Católica del Norte, Antofagasta, 435–438.

de Silva, S. & Francis, P. 1991. Volcanoes of the Central Andes, Volume 1. Springer, New York.

Dehn, J., Dean, K. & Engle, K. 2000. Thermal monitoring of North Pacific volcanoes from space. Geology, 28, 755–758.

Dehn, J., Dean, K., Engle, K. & Izbekov, P. 2002. Thermal precursors in satellite images of the 1999 eruption of Shishaldin Volcano. Bulletin of Volcanology, 64, 525–534.

Delle Donne, D., Harris, A. J. L., Ripepe, M. & Wright, R. 2010. Earthquake-induced thermal anomalies at active volcanoes. Geology, 38, 771–774.

Denniss, A. M., Harris, A. J. L., Rothery, D. A. & Francis, P. 1998. Satellite observations of the April 1993 eruption of Lascar volcano. International Journal of Remote Sensing, 19, 801–821.

Fournier, T. J., Pritchard, M. E. & Riddick, S. N. 2010. Duration, magnitude, and frequency of subaerial volcano deformation events: new results from Latin America using InSAR and a global synthesis. Geochemistry, Geophysics, Geosystems, 11, Q01003.

Froger, J.-L., Remy, D., Bonvalot, S. & Legrand, D. 2007. Two scales of inflation at Lastarria-Cordón del Azufre volcanic complex, central Andes, revealed from ASAR–ENVISAT interferometric data. Earth and Planetary Science Letters, 255, 148–163.

Gardeweg, M. C., Sparks, R. S. J. & Matthews, S. J. 1998. Evolution of Lascar Volcano, northern Chile. Journal of the Geological Society, 155, 89–104.

Gillespie, A., Rokugawa, S., Matsunaga, T., Cothern, J. S., Hook, S. & Kahle, A. B. 1998. A temperature and emissivity separation algorithm for advanced spaceborne Thermal Emission and Reflection Radiometer (ASTER) images. IEEE Transactions on Geoscience and Remote Sensing, 36, 1113 – 1126.

Glaze, L. S., Self, S., Francis, P. W. & Rothery, D. A. 1989. The 16 September 1986 eruption of Lascar volcano, north Chile – Satellite investigations. Bulletin of Volcanology, 51, 149–160.

González-Ferrán, O. 1995 Volcanes de Chile. Instituto Geografico Militar, Santiago.

Hantke, G. & Parodi, I. 1966. Catalogue of the Active Volcanoes And Solfatara Fields of Colombia, Ecuador and Peru (Catalogue of the Active Volcanoes of the World Part 19). International Association of Volcanology and Chemistry of the Earth's Interior (IAVCEI), Rome, 1–73.

Harris, A. J. L. & Ripepe, M. 2007. Regional earthquake as a trigger for enhanced volcanic activity: Evidence from MODIS thermal data. Geophysical Research Letters, 34, 1–6.

Harris, A. J. L., Butterworth, A. L., Carlton, R. W., Downey, I., Miller, P., Navarro, P. & Rothery, D. A. 1997. Low-cost volcano surveillance from space: case studies from Etna, Krafla, Cerro Negro, Fogo, Lascar and Erebus. Bulletin of Volcanology, 59, 49–64.

Harris, A., Flynn, L. P. et al. 2000. Real-time satellite monitoring of volcanic hot spots. In: Mouginis-Mark, P., Crisp, J. & Fink, J. (eds) Remote Sensing of Active Volcanism. American Geophysical Union, Geophysical Monograph, 116, 139–159.

Henderson, S. T. & Pritchard, M. E. 2011. Characterizing magmatic sources in the Central Andes Volcanic Zone with a regional InSAR time series survey. In: American Geophysical Union, Fall Meeting 2011. American Geophysical Union, Washington, DC, Abstract S34B-03.

Hildreth, W. & Drake, R. E. 1992. Volcán Quizapu, Chilean Andes. Bulletin of Volcanology, 54, 93–125.

Holtkamp, S. G., Pritchard, M. E. & Lohman, R. B. 2011. Earthquake swarms in South America. Geophysical Journal International, 187, 128–146.

Lara, L. E. 2009. The 2008 eruption of the Chaitén Volcano, Chile: a preliminary report. Andean Geology, 36, 125–129.

Macedo, O. D., Ramos, V. C. et al. 2001. Misti. Revista L.A.V.E., de la Asociación vulcanológique Européenne, 93.

Masías, P., Antayhua, Y. & Ramos, D. 2010. Monitoreo de las Fuentes termales y fumarolas del Volcán Misti (Arequipa) 2005 – 2010 (Abstract.) In: XV Congreso Peruano de Geología. Resúmenes Extendidos. Sociedad Geológica del Perú, Special Publications, 9, 1136 – 1139.

Mather, T. A., Tsanev, V. I., Pyle, D. M., McGonigle, A. J. S., Oppenheimer, C. & Allen, A. G. 2004. Characterization and evolution of tropospheric plumes from Lascar and Villarrica volcanoes, Chile. Journal of Geophysical Research, 109, D21303.

Matthews, S. J., Gardeweg, M. C. & Sparks, R. S. J. 1997. The 1984 to 1996 cyclic activity of Lascar Volcano, northern Chile: cycles of dome growth, dome subsidence, degassing and explosive eruptions. Bulletin of Volcanology, 59, 72–82.

Morales, J. R., Dinator, M. I., Llona, F. & Romo-Kroeger, C. 1993. Major components of aerosols emitted by the Lonquimay volcano, Chile. Journal of Radioanalytical and Nuclear Chemistry, 172, 181 – 192.

Muñoz, M. 1983. Eruption patterns of the Chilean volcanoes Villarrica, Llaima, and Tupungatito. Pure and Applied Geophysics, 121, 835–852.

Murphy, S. W., Filho, C. R. D. S. & Oppenheimer, C. 2011. Monitoring volcanic thermal anomalies from space: size matters. Journal of Volcanology and Geothermal Research, 203, 48 – 61.

Naranjo, J. A. 1985. Sulphur flows at Lastarria volcano in the North Chilean Andes. Nature, 313, 778–780.

Naranjo, J. A. & Lara, L. 2004. August – September 2003 small vulcanian eruption at the Nevados de Chillán Volcanic Complex, (36 50' S), southern Andes (Chile). Revista Geológica de Chile, 31, 359-366.

Naranjo, J. A. & Moreno, H. 1991. Actividad explosiva postglacial en el volcan Llaima, Andes del Sur (388 45′ S) [Abstract in English]. Revista Geológica de Chile, 18, 69–80.

Naranjo, J. A. & Moreno, H. 2009. Reciente erupción en el Complejo Volcánico Nevados de Chillán, Región del Biobío. (Abstract.) XII Congreso Geológico Chileno, Santiago, Actas, S3, 016.

Naranjo, J. A. & Polanco, E. 2004. The 2000 AD eruption of Copahue volcano, southern Andes. Revista Geológica de Chile, 31, 279–292.

Naranjo, J. A., Moreno, H., Peña, P. et al. 2009. Estilos eruptivos 2007–2008 del volcán Llaima, Andes del Sur. (Abstract.) XII Congreso Geolo´gico Chileo, Santiago, Actas, S3, 014.

Oppenheimer, C. 1991. Lava flow cooling estimated from Landsat Thematic Mapper infrared data: the Lonquimay eruption (Chile, 1989). Journal of Geophysical Research, 96, 21 865–21 878.

Oppenheimer, C., Francis, P. W., Rothery, D. A., Carlton, R. W. T. & Glaze, L. S. 1993. Infrared image analysis of volcanic thermal features – Lascar Volcano, Chile, 1984–1992. Journal of Geophysical Research, 98, 4269–4286.

Pavez, A., Remy, D., Bonvalot, S. & Diament, M. 2006. Insight into ground deformations at Lascar volcano (Chile) from SAR interferometry, photogrammetry and GPS data:

Implications on volcano dynamics and future. Remote Sensing of Environment, 100, 307–320.

Pallister, J. S., Diefenbach, A. K., Griswold, J., Munoz, J., Lara, L. E., Valenzuela, C., Burton, W. C. & Keeler, R. 2010. Volumes and eruption rates for the 2008–2009 Chaitén rhyolite lava dome. American Geophysical Union, Fall Meeting, 13 – 17, December 2010, San Francisco. AGU, Abstract V21D-2350.

Pieri, D. & Abrams, M. 2004. ASTER watches the world's volcanoes: a new paradigm for volcanological observations from orbit. Journal of Volcanology and Geothermal Research, 135, 13–28.

Pieri, D. & Abrams, M. 2005. ASTER observations of thermal anomalies preceding the April 2003 eruption of Chikurachki volcano, Kurile Islands, Russia. Remote Sensing of Environment, 99, 84–94.

Pieri, D. C., Baloga, S. & Nelson, R. 1984. Sulfur flows of Ra Patera, Io. Icarus, 780, 685–700.

Pritchard, M. E. & Simons, M. 2004. An InSAR-based survey of volcanic deformation in the central Andes. Geochemistry, Geophysics, Geosystems, 5, 1–42.

Ruch, J., Manconi, A. et al. 2009. Stress transfer in the Lazufre volcanic area, central Andes. Geophysical Research Letters, 36, 1–6.

Sepúlveda, F., Lahsen, A. & Powell, T. 2007. Gas geochemistry of the Cordón Caulle geothermal system, Southern Chile. Geothermics, 36, 389–420.

SERNAGEOMIN. 2010. Volcán Chaitén Informe Técnico, No. 115, 21 de Enero–05 de Febrero de 2010. http:// www.segemar.gov.ar/Chaitén/INFORME_115_21.01-05.02.10-1.pdf

Siebert, L. & Simkin, T. 2002 – 2012. Volcanoes of the World: An Illustrated Catalog of Holocene Volcanoes and Their Eruptions. Smithsonian Institution, Global Volcanism Program Digital Information Series, GVP-3. http://www.volcano.si.edu/world/

Sparks, R. S. J., Folkes, C. B. et al. 2008. Uturuncu volcano, Bolivia: Volcanic unrest due to mid-crustal magma intrusion. American Journal of Science, 308, 727 – 769.

Stern, C. 2004. Active Andean volcanism: its geologic and tectonic setting. Revista Geológica de Chile, 31, 161 – 206.

Sunagua, M. 2004. Amenaza Volcánica en la region del Volcán Uturuncu – Provincia Sud Lípez del Departamento de Potosí. Tesis de Grado, Universidad Autónoma Tomás Frías Potosí, Bolivia.

Tassi, F., Martinez, C., Vaselli, O., Capaccioni, B. & Viramonte, J. 2005. Light hydrocarbons as redox and temperature indicators in the geothermal field of El Tatio (northern Chile). Applied Geochemistry, 20, 2049 – 2062.

Tassi, F., Aguilera, F. et al. 2009. The magmatic- and hydrothermal-dominated fumarolic system at the Active Crater of Lascar volcano, northern Chile. Bulletin of Volcanology, 71, 171–183.

Tassi, F., Aguilera, F., Darrah, T., Vaselli, O., Capaccioni, B., Poreda, R. J. & Delgado Huertas, A. 2010. Fluid geochemistry of hydrothermal systems in the Arica-Parinacota, Tarapacá and Antofagasta regions (northern Chile). Journal of Volcanology and Geothermal Research, 192, 1–15.

Tassi, F., Aguilera, F., Vaselli, O., Darrah, T. & Medina, E. 2011. Gas discharges from four remote volcanoes in northern Chile (Putana, Olca, Irruputuncu and Alitar): a geochemical survey. Annals of Geophysics, 54, 121–136.

Trunk, L. & Bernard, A. 2008. Investigating crater lake warming using ASTER thermal imagery: case studies at Ruapehu, Poa´s, Kawah Ijen, and Copahue Volcanoes. Journal of Volcanology and Geothermal Research, 178, 259–270.

Velez, M. L., Euillades, P., Caselli, A., Blanco, M. & Díaz,J.M. 2011. Deformation of Copahue volcano: Inversion of InSAR data using a genetic algorithm. Journal of Volcanology and Geothermal Research, 202, 117–126.

Venzke, E., Wunderman, R. W., McClelland, L., Simkin, T., Luhr, J. F., Siebert, L., Mayberry, G. & Sennert, S. (eds). 2002 – 2011. Global Volcanism, 1968 to the Present. Smithsonian Institution, Global Volcanism Program Digital Information Series, GVP-4. http://www.volcano.si.edu/reports.

Watt, S. F. L., Pyle, D. M., Mather, T. A., Martin, R. S. & Matthews, N. E. 2009. Fallout and distribution of volcanic ash over Argentina following the May 2008 explosive eruption of Chaitén, Chile. Journal of Geophysical Research, 114, 1–11.

Whelley, P. L., Jay, J., Calder, E. S., Pritchard, M. E., Cassidy, N. J., Alcaraz, S. & Pavez, A. 2012. Post-depositional fracturing and subsidence of pumice flow deposits: Lascar Volcano, Chile. Bulletin of Volcanology, 74, 511–531.

Wicks, C., de la Llera, J. C., Lara, L. E. & Lowen- stern, J. 2011. The role of dyking and fault control in the rapid onset of eruption at Chaitén volcano, Chile. Nature, 478, 374–377.

Witter, J. B., Kress, V. C., Delmelle, P. & Stix, J. 2004. Volatile degassing, petrology, and magma dynamics of the Villarrica Lava Lake, Southern Chile. Journal of Volcanology and Geothermal Research, 134, 303–337.

Wooster, M. 2001. Long-term infrared surveillance of Lascar Volcano: contrasting activity cycles and cooling pyroclastics. Geophysical Research Letters, 28, 847–850.

Wooster, M. J. & Rothery, D. A. 1997. Thermal monitoring of Lascar Volcano, Chile, using infrared data from the along-track scanning radiometer: a 1992– 1995 time series. Bulletin of Volcanology, 58, 566 – 579.

Wright, R., Flynn, L. P., Garbeil, H., Harris, A. J. L. & Pilger, E. 2004. MODVOLC: near-real-time thermal monitoring of global volcanism. Journal of Volcanology and Geothermal Research, 135, 29–49.

Wright, R., Rothery, D. A., Blake, S., Harris, A. J. L. & Pieri, D. C. 1999. Simulating the response of the EOS Terra ASTER sensor to high-temperature volcanic targets. Geophysical Research Letters, 26, 1773 – 1776.

Wright, R., Garbeil, H. & Davies, A. G. 2010. Cooling rate of some active lavas determined using an orbital imaging spectrometer. Journal of Geophysical Research, 115, 1–14.

CHAPTER 4

LOCATING MAGMA RESERVOIRS USING INSAR AND PETROLOGY BEFORE AND DURING THE 2011-2012 CORDÓN CAULLE SILICIC ERUPTION[3]

4.0 ABSTRACT

We combine petrological and InSAR observations to probe the origin of deformation of Cordón Caulle volcano in Southern Chile before and during the 2011-2012 eruption. The erupted rhyodacite is crystal-poor and was stored at about 900° C with ca. 4 wt% H_2O and 220 ppm CO_2 in the melt, corresponding to a storage depth of about 6-7 km. In addition to a previously documented 2007-2008 deformation episode, we find three pre-eruptive deformation episodes: the first between 2008 and 2009 that covers ~400 km^2 with a maximum uplift of 18.5 cm, the second between February and March 2010 that covers ~20 km^2 with a maximum uplift of 10 cm, and the third between March and May 2011 that covers ~40 km^2 with a maximum uplift of 6 cm. Modeling of the 2008-2009 deformation episode suggests source depths of about 5-9 km, consistent with the petrologically determined magma storage depth. The sum of modeled source volume changes from 2007-2009 is about 12 times less than the observed erupted volume. Our calculation of magma compressibility shows that there must have been a significant volume of pre-existing magma in the reservoir to account for this difference. Co-eruptive subsidence shows evidence for three

[3] A version of this chapter was originally published as: Jay, J. A., Costa, F., Pritchard, M. E., Lara, L. E., Singer, B. S., & Herrin, J. (2014). Locating magma reservoirs using InSAR and petrology before and during the 2011-2012 Cordón Caulle silicic eruption. *Earth and Planetary Science Letters*, *395*, 254–266. Reprinted with permission from Earth and Planetary Science Letters.

distinct magma sources, and pre-eruptive inflation is seen at two of the three sources. Modeled deformation sources are located 2-10 km from the 2011-12 eruptive vent and coincide with the vents from previous historical eruptions (1921-22, 1960) and with the neighboring Puyehue volcano. This implies the existence of an interconnected magma plumbing system that allows for pressure transfer and which covers an area of at least 20 km^2. Thus, the deformation and geochemical characteristics of Cordón Caulle resemble that of a large silicic caldera system. The presence of a mafic crystal clot demonstrates the existence of basaltic melts in the silicic reservoir, but we find that the mafic magmas reached the reservoir at least several hundred years before eruption. Therefore, if the pre-eruptive deformation was caused by replenishment to a shallow reservoir, the new magma was silicic and similar to the pre-existing magma, and/or there was no interaction between the two. We find that pre-eruptive deformation can occur in pulses and reach its peak years before eruption, and thus lack of deformation does not necessarily imply that eruption is not imminent.

4.1 INTRODUCTION

Volcanic surface deformation measurements allow us to infer magmatic processes at depth, potentially providing information about the timing and size of an imminent eruption as well as about the subsurface reservoirs (e.g., Dvorak and Dzurisin, 1997; Lu et al., 2003). Combination of geophysical observations and geochemical data would allow us to make more robust interpretations of the physical processes involved during all stages of the eruption (e.g., Masterlark and Lu, 2004). However, particularly in the case of large silicic eruptions, we are rarely able to combine

geophysics and geochemistry, primarily limited by the fact that the two datasets are seldom available for a given eruption.

The 2011-2012 eruption of Cordón Caulle volcano in southern Chile provides a unique opportunity to study the deformation behavior of a silicic volcanic system before and during a large rhyodacite eruption. Petrological and geochemical studies of the erupted products provide independent information about magma storage areas and processes that may have led to eruption. In addition, the fact that the eruption occurred within 520 km and 16 months of the 2010 Mw 8.8 Maule earthquake sheds light on the long-debated yet poorly understood question of how and under what circumstances volcanic eruptions can be triggered by large distant earthquakes (e.g., Linde and Sacks, 1998; Walter and Amelung, 2007).

Puyehue-Cordón Caulle (-40.59^{o} S, -72.117^{o} W) is an active volcanic complex in the Andean Southern Volcanic Zone (Fig. 1). Explosive to effusive rhyodacitic eruptions of Cordón Caulle occurred in 1920-21, 1960, and 2011-12, all of about the same size (0.5-0.8 km^{3}) and of silicic composition (this work; Singer et al., 2008; Smithsonian Institution). Because of the strong evidence that the 1960 eruption was triggered by the Mw 9.5 Chilean earthquake, having occurred only two days after the earthquake (e.g., Barrientos, 1994; Lara et al., 2004), one might also expect a triggering relationship between the 4 June 2011 eruption and the 27 February 2010 Mw 8.8 Maule earthquake. However, the response time of over one year makes any such relationship unclear (e.g., Bonali et al., 2013).

The Puyehue-Cordón Caulle Complex overlies a mostly crystalline basement dissected by large fault systems, particularly the NW-striking set well developed in the

forearc sliver, and the NNE-striking branch of the Liquiñe-Ofqui Fault Zone (Fig. 1c) (Lara et al., 2004; Lara et al., 2006b). The upper part of the complex is formed by a graben, which hosts a corridor of Holocene domes and some of the most active hot springs in the Southern Andes. These high temperature pools, fumaroles and geysers are underlain by a large geothermal system (e.g., Sepulveda et al., 2004). Holocene basalt erupts exclusively through a large central vent complex to the SE (Puyehue volcano), whereas rhyodacite erupts across the entire SE-NW length of the lineament, including both Puyehue and Cordón Caulle (Fig. 1c).

The most recent Cordón Caulle eruption started on 4 June 2011 after two months of increased seismicity (Silva Parejas et al., 2012). The explosive stage, which lasted about 27 hours, started with a 10-12 km column with pulses that reached up to 15 km high. About 0.25 km^3 of dense rock equivalent (DRE) of rhyodacitic tephra was erupted in this stage (Silva Parejas et al., 2012), which was waning until 15 June when the effusive phase began. The latter evacuated *ca*. 0.5 km^3 of rhyodacitic lava at more than 30 m^3/sec declining after the first month of eruption (Bertin et al., 2012; Tuffen et al., 2013). By March 2012, the lava effusion was over (although evolution of the flow field continued) and by June 2012 the ash emissions also ceased (Tuffen et al., 2013). In this study, we measure and analyze ground deformation at Cordón Caulle using satellite Interferometric Synthetic Aperture Radar (InSAR) in the four years preceding and spanning the 2011-2012 eruption. We combine the InSAR observations with petrological data in an attempt to understand whether the deformation provides clues to the magmatic processes that triggered the eruption.

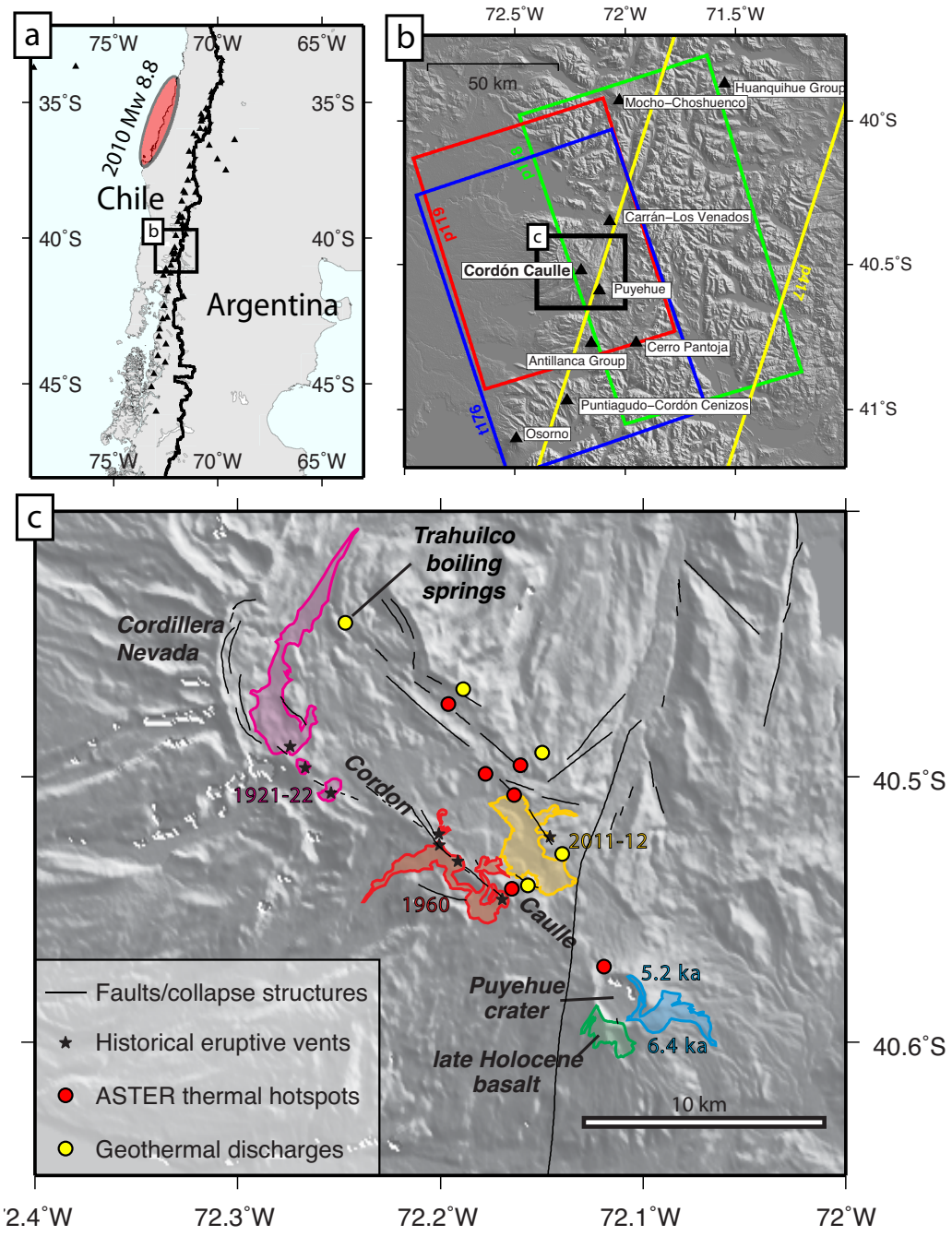

Figure 4.1 a) Map of the Andean Southern Volcanic Zone with Holocene volcanoes from the Smithsonian catalog shown as black triangles. Pink ellipse shows the approximate 2010 Mw 8.8 Maule earthquake rupture zone estimated from Lorito et al. (2011) and aftershock locations. b) Overview map showing the location of Cordón Caulle. Colored rectangles indicate outlines of ascending and descending ALOS and Envisat satellite paths. c) Zoom-in geologic map of the Puyehue-Cordón Caulle volcanic complex showing locations of eruptive vents and thermal features from Singer et al. (2008), Sepulveda et al. (2004), and Jay et al. (2013). See Singer et al. (2008) for more information about magma compositions.

4.2 METHODS

4.2.1 InSAR

Previous InSAR studies show that Cordón Caulle has undergone episodes of deformation since at least 1996 and has varied between subsidence and uplift in different locations of the volcanic complex (Fig. 4.2). Between 1996 and 1999, 8 cm of subsidence was observed in a pattern oriented along the strike of the Cordón Caulle fissure (Fig. 4.2a; Pritchard and Simons, 2004). In interferograms spanning 2003-2005 and 2004-2006, uplift rates of 1 cm/yr and 3 cm/yr were observed (Fournier et al., 2010). These uplift events occurred in the same location and with a similar spatial pattern as the 1996-1999 subsidence event. Between 2007 and 2008, the uplift retained a similar pattern but accelerated to nearly 20 cm/yr (Fig. 4.2b, Fournier et al., 2010). The patterns of the deformation episodes are not circular but rather elongated and irregular, probably related to the regional faults (e.g., Lara et al., 2006). Modeling of the 2007-2008 deformation using two inflating point sources put the sources at 7 and 4 km depth, and the cause of inflation was inferred to be either hydrothermal or magmatic (Fournier et al., 2010).

Here, we use L-band (23.6 cm wavelength) SAR data from the Japanese Space Agency (JAXA) ALOS satellite between January 2007 and March 2011 (pre-eruptive phase) and C-band (5.6 cm wavelength) data from the European Space Agency (ESA) Envisat satellite between February 2011 and March 2012 (pre-eruptive and co-eruptive phases). We use the ROI_PAC software (Rosen et al., 2004) to process all available data from ALOS ascending paths 118 and 119, descending path 417 and Envisat ascending track 176 beam 6 (Supplemental Fig. A2.1).

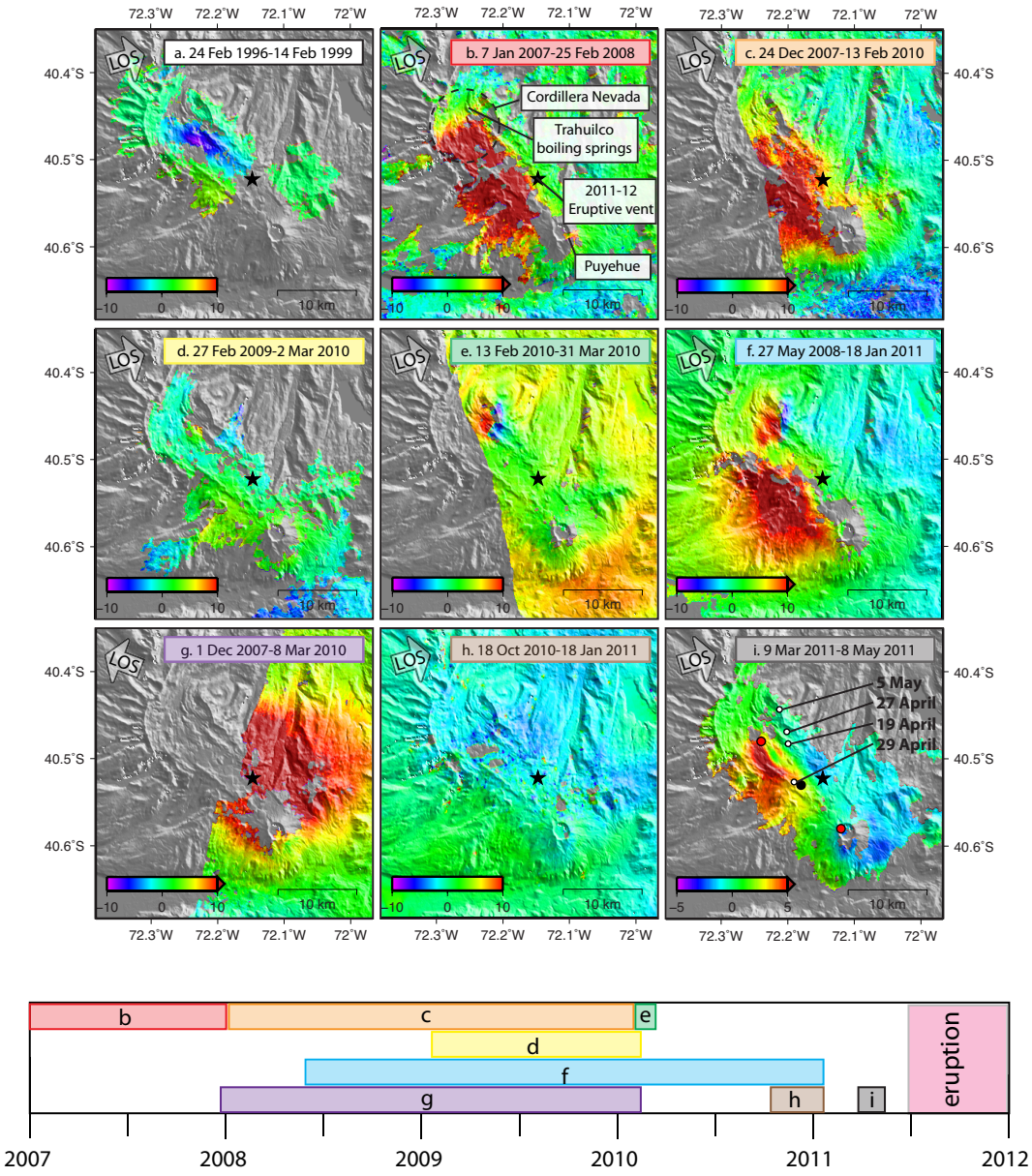

Figure 4.2 Individual pre-eruptive interferograms with colored labels corresponding to timespans represented in timeline. Line-of-sight (LOS) arrow shows look direction of satellite. Black star indicates location of the 2011-12 eruptive vent. i) white circles show locations of earthquakes reported by OVDAS (2011) that occurred during the time period of the interferogram (though hundreds of other earthquakes also occurred, their locations were not reported by OVDAS); black and red circles shows locations of modeled co-eruptive deflation sources (see Fig. 4.3 for more detail)

To reduce atmospheric noise in the pre-eruptive ALOS observations, we produce stacks of interferograms (perpendicular baselines < 2000 m) to use in our inversions for the 2007-2008 and 2008-2009 uplift episodes. We compute the stacks by summing the interferograms and dividing by the number of measurements in the stack for each pixel. This calculation assumes that the duration of the uplift event is completely spanned by all of the interferograms in the stack; we believe this is a valid assumption given that the amount of uplift is the same (within error) in each interferogram. This assumption implies that the duration of the uplift is no longer than the time span of the shortest interferogram, which spans 2 years and 6 days. For the 2007-2008 time period modeled by Fournier et al., (2010) there are only two coherent interferograms (path 119) that span only the time period before 25 Feb. 2008 (Fig. A2.1) and these have been stacked together for modeling.

We model the observed deformation using the following source types: point sources (e.g., Mogi, 1958), spheroids (Yang et al., 1988), tensile dislocations, and fault slip (Okada, 1992). Since little is known regarding the material properties of the subsurface at Cordón Caulle (i.e., seismic tomography has not been carried out to determine seismic velocities and therefore elastic moduli), we assume a homogeneous elastic half space in our modeling. Specifically, we use a Poisson's ratio of 0.25 and a shear modulus of 20 GPa. For the ALOS observations, we perform a joint inversion of interferograms from all three paths; using data from both ascending and descending paths provides better constraints on the deformation source characteristics because each path provides a different line-of-sight (LOS) displacement vector.

For the Envisat co-eruptive observations, we perform separate inversions using one or more point sources for each interferogram (13 in total), as deformation characteristics during the eruption are dynamic in pattern and magnitude. For interferograms with start dates of 7 June 2011 or later, we averaged the latitude, longitude, and depth of the source modeled from individual interferograms, because these interferograms had a similar best-fitting source location. We then re-ran the inversions with a fixed source location and solving only for volume change. We assume that the source location did not change after 7 June 2011 because the deformation after this date seem to be explained by a single reservoir that moves less than a few km (Fig. 4.3, section 3).

We use the inversion method of Fournier et al. (2010) to solve for the best-fitting source parameters using a Levenberg-Marquardt iterative least squares algorithm. Each inversion solves for the location, depth, and strength of the deformation source as well as a static offset and bilinear ramp to account for artifacts of the InSAR processing. The initial estimate for each inversion is determined through forward modeling.

4.2.2 Petrological Analyses

We studied two samples from the 2011-2012 eruption: a pumice from the fall deposits of 4 June 2011, and a lava flow sampled in 2011. Bulk-rock analyses were performed by X-Ray Fluorescence and ICP-MS. Backscattered electron images and quantitative mineral and glass analyses were obtained using a field emission gun electron microprobe (JEOL-JXA-8530F) at the Nanyang Technological University

(Singapore). Volatile and trace element analyses of glass inclusions in pyroxene were obtained at the Stanford-USGS SHRIMP-RG ion microprobe using the same instrument conditions, standardization, and corrections as detailed in Wright et al. (2012). More details about the instrument conditions for the petrological analysis are found in electronic appendix. The symbols used for mineral end members and compositional indicators plus representative analyses are found in Table 2.

4.3 RESULTS

4.3.1 Recent deformation episodes in Cordón Caulle and modeled sources

There are at least four episodes of pre-eruptive deformation between 2007-2011. Two discrete uplift episodes occur between 2007-2008 (Fig. 4.2b) and 2008-2009 (Fig. 4.2c, f, g) with different spatial extents, but both with maximum LOS displacement of about 20 cm/yr. This signal is oriented N-S and is broader in area than deformation observed before 2007 (Fornier et al., 2010). We find a third deformation episode in a 46-day interferogram spanning the 2010 Mw 8.8 Maule, Chile earthquake, on the eastern side of the Cordillera Nevada caldera with uplift of ~10 cm within the caldera and possible subsidence of ~10 cm on the eastern rim of the caldera (Fig. 4.2e). We observe no deformation with ALOS between 27 February 2009 and 5 March 2011. Between 9 March and 8 May 2011, we observe a fourth episode of deformation that consists of an irregular patch of uplift just south of Cordillera Nevada with a maximum LOS displacement of 6 cm (Fig. 4.2i).

Co-eruptive interferograms show the spatial and temporal evolution of the eruption. In most cases we are unable to determine the maximum displacement

because the center of deformation is incoherent (probably due to ash deposition), and our attempts at using pixel tracking and multiple aperture interferometry did not significantly improve spatial coverage. In an interferogram spanning 8 May to 7 June, we find a large lobe of subsidence centered beneath Cordillera Nevada with a maximum LOS subsidence of ~120 cm in coherent areas. This interferogram also shows a smaller lobe of subsidence near Puyehue volcano with a maximum LOS subsidence of about ~25 cm, and a lobe of apparent LOS uplift to the NE (Fig. 4.3a). Interferograms beginning on 7 June 2011 or later show one large lobe of subsidence centered beneath the eruptive vent and the same lobe of LOS increase to the NE (Fig. 4.3b-d).

In the following sections, we describe the model results for each of the different episodes of pre-eruptive and co-eruptive deformation.

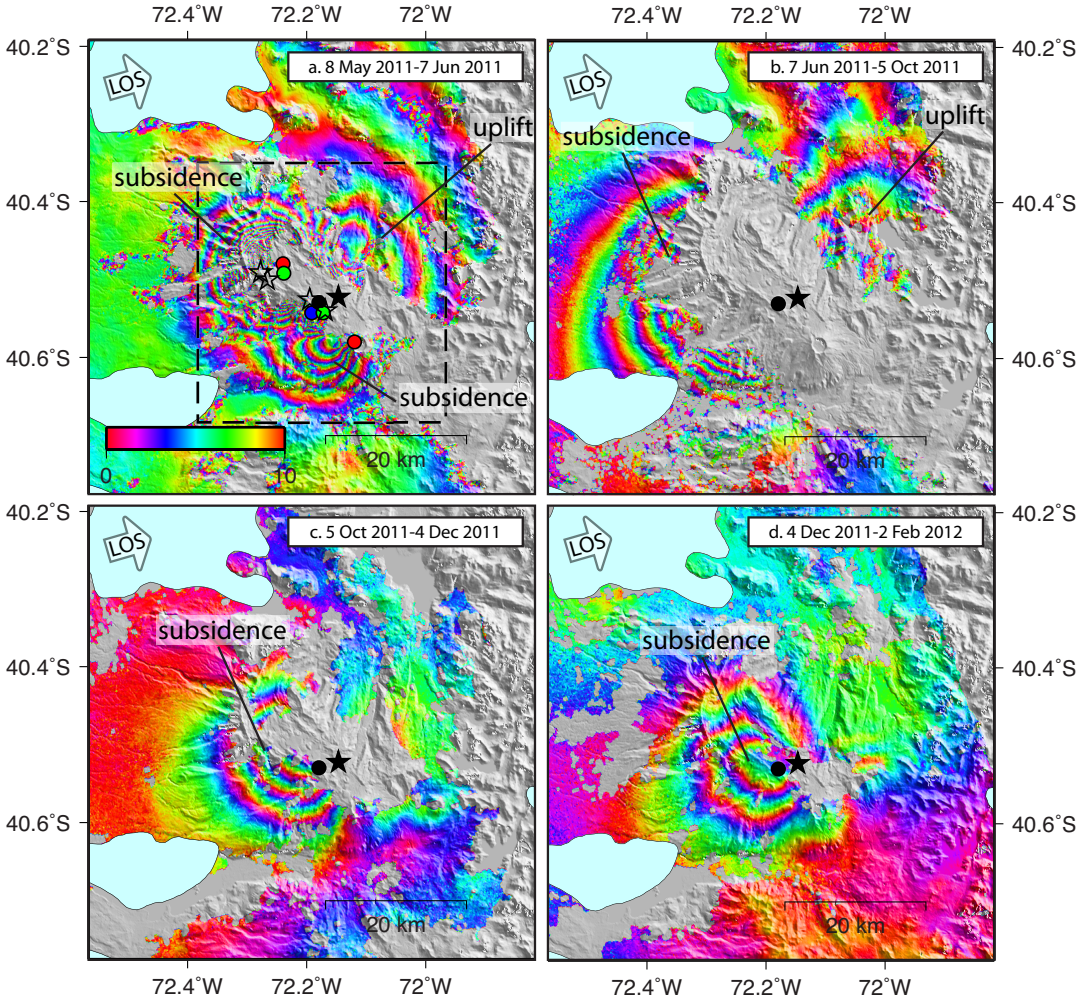

Figure 4.3 Unwrapped Envisat co-eruptive interferograms that have been rewrapped to a 10 cm deformation contour interval. Black star shows location of eruptive vent A) 8 May 2011 to 7 June 2011. Note two distinct lobes of subsidence. Red circles show locations of the two modeled deflation sources for this interferogram; green circles show locations of the two modeled inflation sources for the 2007-2008 uplift; blue circle shows location of the modeled inflation source for the 2008-2009 uplift; star outlines show locations of 1921-22 (NW) and 1960 (SE) paired eruptive vents; black dashed rectangle indicates boundaries of maps shown in Fig. 3; B) 7 June 2011 to 5 October 2011; C) 5 October 2011 to 4 December 2011; D) 4 December 2011 to 2 February 2012; black circle in b-d shows location of modeled deflation source for those interferograms

2007-2008 uplift

The results of our inversion are similar to the results of Fournier et al. (2010) but differ in depth and volume change due to the fact that we are stacking two interferograms

rather than using a single interferogram (Table 4.1; Fig. A2.2). The model results from this time period do not match the 2008-2009 uplift.

2008-2009 uplift

The results from our inversions for best-fitting point, spherical, and spheroidal deformation sources are reported in Table 4.1 and displayed in Fig. A2.3-2.7. Dislocation and fault slip models provide poor fits to the data and so are not considered. The source depth ranges from 5 to 9 km and the pressure change ranges from 2 to 30 MPa. Some of these pressure changes seem unlikely because they are higher than the yield strengths of rock (a few to tens of MPa; e.g., Touloukian et al., 1981) and thus would have induced dyking from the reservoir to the surface and eruption. Therefore we consider the models yielding pressure changes lower than the yield strength of rock as more realistic, although it is likely that viscoelastic effects also lower the pressure (e.g., Newman et al., 2001).

Though our simple models can reproduce the magnitude of deformation for individual paths reasonably well, we find that none of the source types described above adequately match the irregular shape of the deformation patterns and the difference in the amount of uplift between ascending and descending tracks. We suggest that either heterogeneities of the shallow subsurface may play a role in affecting the manifestation of deformation at the surface or the source geometry is more complex than a point source. The existence of an active geothermal system and a network of active faults in the region suggest vertical and lateral heterogeneities which can alter both the magnitude and spatial footprint of the surface deformation (e.g., Hautmann et al., 2010; Trasatti et al., 2003; Folch and Gottsmann, 2006).

However, there is no available seismic data at Cordón Caulle to resolve subsurface structure, thus limiting our ability to include more realistic rheological properties in our models.

Cordillera Nevada deformation (Feb.-Mar. 2010)

The Cordillera Nevada deformation event (Fig. 2e, f) only appears in interferograms that end after 13 February 2010 and begin before 31 March 2010, so we are confident that the deformation event occurred sometime between those two dates. Though many interferograms with 11 independent dates from p118 and p119 show uplift within the caldera and subsidence on the outer rim, one highly coherent interferogram from p118 spanning 24 December 2007 to 31 March 2010 shows only uplift, so whether or not the subsidence signal is real remains equivocal. The subsidence signal appears next to a topographic feature and could be due to atmospheric artifacts. The deformation is spatially correlated with a cluster of shallow seismicity located beneath the Cordillera Nevada caldera (Basualto et al., 2012), though heightened seismicity was not observed there until a year after the deformation event (February 2011). It is likely that the deformation event is temporally correlated with the 2010 Mw 8.8 Maule earthquake which ruptured 520 km to the north of the volcano, but the infrequency of the SAR acquisitions do not allow us to precisely pin down the timing of the deformation event. A Mw 5 event would be required in order to explain the observed deformation with fault slip, however no such event exists in the USGS National Earthquake Information Center (NEIC) catalog nor in the catalog of the Servicio Sismológico Universidad de Chile (SSUCH); in fact, there are no earthquakes in either catalog within 100 km of Cordón Caulle. Modeling of the Cordillera Nevada deformation with an inflating

point source gives a depth of 1.7 km below the surface with a volume change of 0.0014 km^3.

Early 2011 uplift

The deformation episode between 9 March and 8 May 2011 (Fig. 2i) coincides with a notable increase in seismicity reported by the Chilean Observatorio Volcanológico de los Andes del Sur (OVDAS). Earthquake swarms reported by OVDAS occurred on 19, 27, and 29 April, and 5 May, with magnitudes $M_L < 4$ and depths ranging from 3.5 to 5 km (SERNAGEOMIN/OVDAS Bulletin Numbers 11-16, 2011). The largest swarm during the interferogram time period occurred on 27 April, consisting of 140 earthquakes, the largest of which appears in global catalogs (USGS, ISC) with M_W 4.4 (M_L 3.9 in OVDAS report). The OVDAS locations for these earthquakes (plotted on Fig. 2i) cluster near the deformation and Cordillera Nevada. The best-fitting model for the uplift is a 12 km x 6 km rectangular sill at 4 km depth with a strike of 143°, a dip of 32° SW, and an opening of 4.5 cm (Supplemental Fig. S8), corresponding to a total volume change of 0.003 km^3 (12 km x 6 km x 4.5 cm). The residual contains significant deformation of +/- 2 cm LOS just south of Cordillera Nevada and is likely related to one or more of the earthquake swarms. Forward earthquake modeling of the residual gives a cumulative moment magnitude $M_W < 5$.

Table 4.1 InSAR inversion results covering all timespans. Asterisk* denotes the use of an interferogram stack rather than a single interferogram in the inversion.

Start Date	End Date	Source type	Longitude	Latitude	Depth (km)	Radius (km)	Semimajor axis (km)	Semiminor axis (km)	Length (km)	Width (km)	dV (km^3)	dP min (Pa)
7-Jan-07	25-Feb-08	Point 1	-72.24	-40.49	6.9						0.043	
		Point 2	-72.17	-40.54	3.8						0.016	
2007*	2008*	Point 1	-72.24	-40.49	2.8						0.009	
		Point 2	-72.18	-40.53	4.1						0.015	
2008*	2009*	Point	-72.19	-40.54	7.6						0.030	2.00E+07
2008*	2009*	Spheroid	-72.19	-40.54	8.7		0.25	0.18			0.000	3.00E+07
2008*	2009*	Sphere	-72.19	-40.54	5.8	4.9					0.040	2.00E+06
13-Feb-10	31-Mar-10	Point	-72.22	-40.55	1.7						0.001	
9-Mar-11	8-May-11	Sill	-72.23	-40.53	4				12	6	0.003	
8-May-11	7-Jun-11	Point 1	-72.24	-40.48	3.7						-0.086	
		Point 2	-72.12	-40.58	6.3						-0.046	
8-May-11	7-Jul-11	Point 1	-72.24	-40.48	3.8						-0.088	
		Point 2	-72.12	-40.58	6.1						-0.044	
7-Jun-11	7-Jul-11	Point	-72.18	-40.53	6						-0.120	
7-Jun-11	6-Aug-11	Point	-72.18	-40.53	6						-0.054	
7-Jun-11	5-Oct-11	Point	-72.18	-40.53	6						-0.300	
7-Jul-11	6-Aug-11	Point	-72.18	-40.53	6						-0.054	
6-Aug-11	5-Oct-11	Point	-72.18	-40.53	6						-0.049	
5-Oct-11	4-Dec-11	Point	-72.18	-40.53	6						-0.038	
5-Oct-11	3-Jan-12	Point	-72.18	-40.53	6						-0.048	
5-Oct-11	2-Feb-12	Point	-72.18	-40.53	6						-0.072	
5-Oct-11	3-Mar-12	Point	-72.18	-40.53	6						-0.077	
4-Dec-11	2-Feb-12	Point	-72.18	-40.53	6						-0.027	
4-Dec-11	3-Mar-12	Point	-72.18	-40.53	6						-0.025	

Co-eruptive deformation

In our modeling, interferograms that span the beginning of the eruption (8 May to 7 June and 8 May to 7 July) require two deflating point sources: one beneath Cordillera Nevada at 3.8 km depth and one beneath Puyehue at 6.1 km depth (Fig. 4.3a). All other interferograms require only one point source located near the eruptive vent at 6 km depth (Fig. 4.3b-d, Supplemental Fig. A2.9). The deflating point sources sufficiently account for the apparent LOS increase (labeled in Fig. 4.3 and red regions in Fig A2.9) in the NE due to the horizontal motions and shallow incidence angle of the satellite (39.1°-42.8° from perpendicular) – thus, an inflationary source is not necessary. The volume change rate of the modeled source was greatest during the early stages of the eruption, from 4 June to 7 July (Fig. 4.4). The cumulative volume change of the modeled source at depth is ~0.4 km^3, nearly equivalent to the 0.6-0.8 km^3 DRE output after accounting for magma compressibility (see Section 4.4.1).

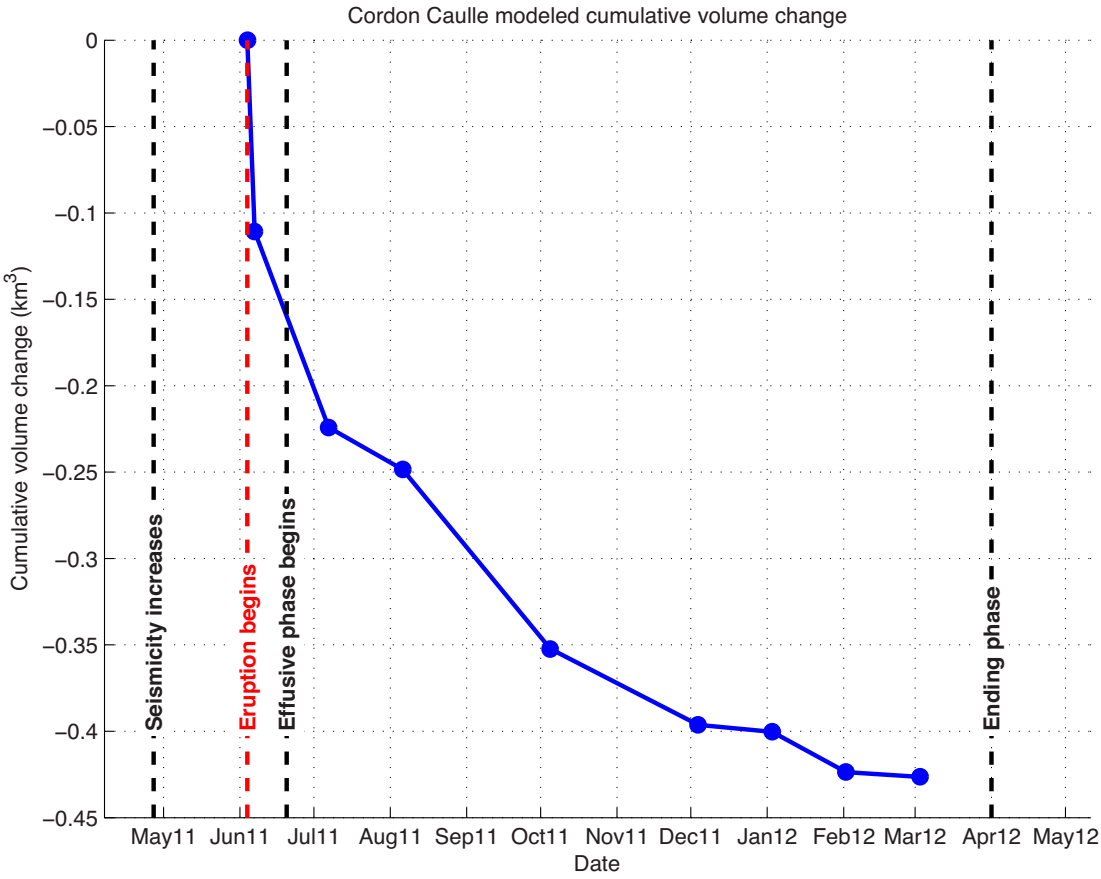

Figure 4.4 Cumulative co-eruptive volume decrease at depth from InSAR modeling. Volume changes for 13 temporally overlapping interferograms (Fig. S1) were modeled separately, then an inversion was carried out to solve for volume change rates between each time interval. For interferograms with 8 May as the start date, rates were calculated assuming that all volume change occurred starting on 4 June, the date of the eruption. Note the highest volume changes occurred within the first month of the eruption.

4.3.2 Petrological observations, magma pre-eruptive conditions, and reservoir processes

The 2011-2012 eruption produced tephra and lava flows of rhyodacitic composition that overlaps with those of the 1921-22 and 1960 events (Singer et al., 2008; Castro et al., 2013). The rocks are crystal poor, with less than 5 wt% of phenocrysts. Plagioclase (Pl) abundance dominates over clinopyroxene (Cpx) and orthopyroxene (Opx). Minor amounts of magnetite, ilmenite, pyrrhotite, and apatite are also found. Plagioclase

occurs as isolated phenocrysts but also commonly forming glomerocrysts with ortho and clinopyroxene (Fig. 4.5). Plagioclase shows oscillatory zoning and resorption surfaces but a narrow compositional range between An_{35} and An_{44} (mean at An_{38}; Table 4.2), except for one crystal that has core at about An_{88} (Fig. 4.5). Pyroxenes are either unzoned or may have a 20-30 μm-thick rim somewhat richer in Fe. They tend to be euhedral, although their interiors may show dissolution zones. Many Cpx crystals show small exsolution lamellae, which is probably the result of slow cooling in a crystal-rich zone or mushy zone of the Cordón Caulle reservoir (Fig. 4.5; Costa et al in prep). Fe-Ti oxides (magnetite and ilmenite) are unzoned and can be found in the matrix glass or in glomerocrysts.

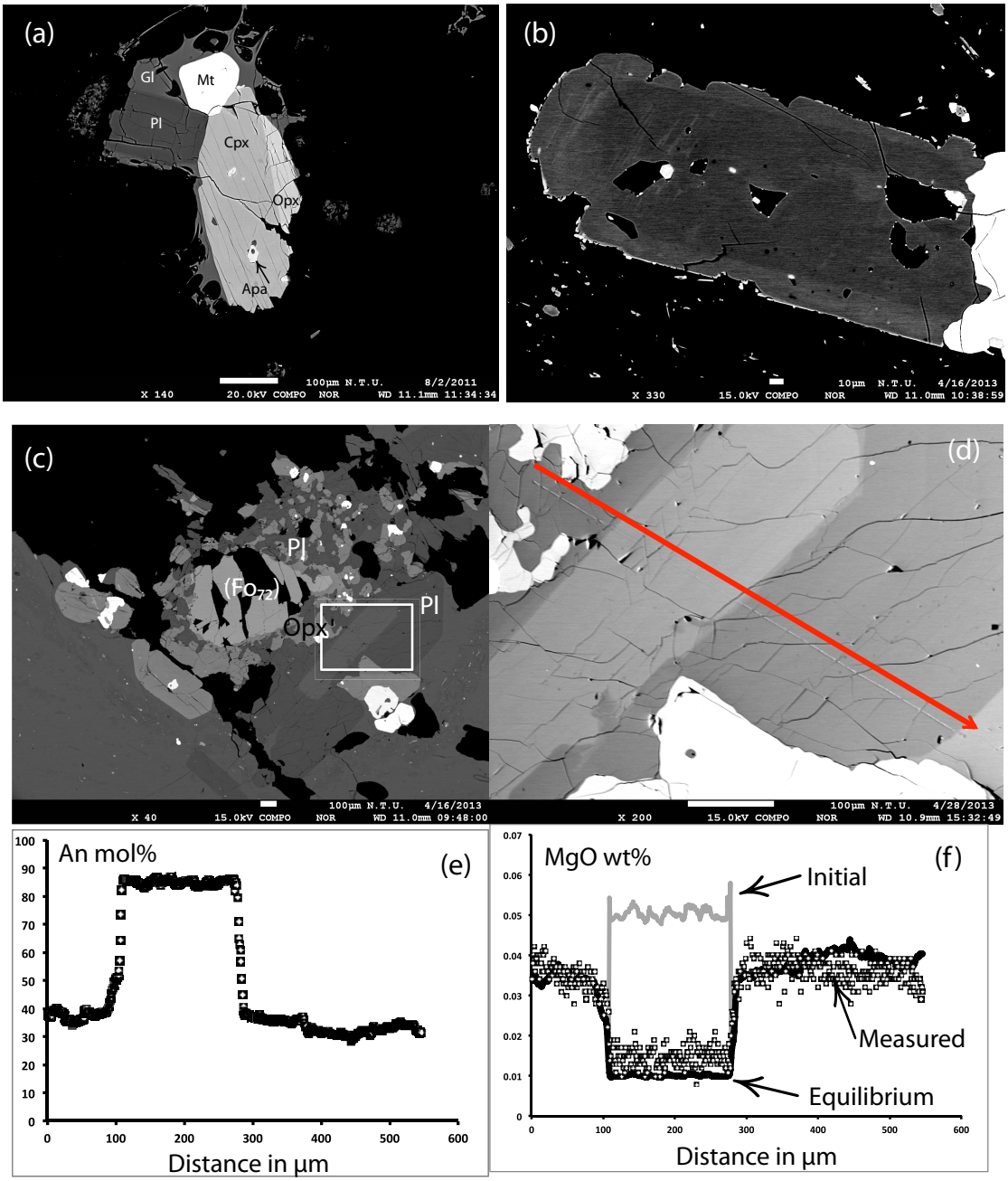

Figure 4.5 (a) Backscattered electron image (BSE) of glomerocryst containing the main minerals of the rhyodacite and matrix glass (Gl). Mineral symbols Cpx= Clinopyroxene, Opx = Orthopyroxene, Pl = Plagioclase, Mt = Magnetite. (b) BSE image of Cpx showing some exsolution lamellae suggesting that they might be derived from a slowly cooled part of the Caulle reservoir. (c) BSE image of olivine xenocryst with thick reaction corona made of Opx, Pl, and Cpx. Next to the reaction zone there is a large plagioclase crystal with a high-Ca core. Square marks the area shown in part (d). (d) BSE image of a detail of the plagioclase phenocryts shown in part (c) of the figure where the bright core rich in Ca can be clearly seen. Arrow marks the position of the electron microprobe traverse. (e) Anorthite profile across the plagioclase crystal showing the high Ca core that probably grew from a mafic melts in equilibrium with the olivine, surrounded by a Ca-poor rim in equilibrium with the dacite host, (f) profile of MgO concentration of the same

crystal. Note how the MgO profile is a mirror image of the An as can be expected during reequilibration by diffusion (e.g. Costa et al., 2003). The MgO initial refers to the concentration of the MgO in equilibrium with a mafic melt with 6 wt% MgO and at 1100° C that the crystal core may have grown from. The equilibrium profile is calculated after Costa et al. (2003), and it is in equilibrium with the dacite host (1.3 wt % MgO and 900° C). The equilibration of the core from the initial to the measured concentrations takes at least 200 years. This shows that mafic magmas have reached the upper part of the silicic reservoir below Caulle, but that this particular crystal clot did not intrude during the 3 last historical eruptions of the last 100 years and thus was not involved in triggering them.

One thin section also contains a crystal cluster made of an olivine crystal (Fo_{72}) with thick reaction rims of pyroxenes and plagioclase. The plagioclase has a core of An_{88} surrounded by thick rims of An_{55} to An_{40} (Fig. 4.5), with the abrupt shift in An content being followed by a change in the MgO concentration. The MgO in the core is lower than in the rims, suggesting that the whole crystal has been reequilibrated by diffusion with the rhyodacite host (e.g., Costa et al., 2003a; Costa et al., 2008). This crystal cluster shows that there is a mafic magma component reaching the silicic reservoir, either from below or from the surrounding wall rock (see Section 4.4.4). These petrological features are common to the products of the 1921-22 and 1960 eruptions (Costa et al., in prep). Glass inclusions in Cpx tend to have higher incompatible elements (e.g., Si, K) and lower compatibles (e.g., Fe, Ca, Mg) than the bulk-rock, but are still rhyodacitic. Ion-microprobe analyses of 6 glass inclusions in pyroxenes have water contents with a mean at 3.9 ± 0.7 wt % H_2O, about 220 ppm CO_2, and about 130 ppm SO_2 (Table 4.2). Their Sr is lower and Rb is higher than those of the bulk-rock in accord with their major element compositions being slightly more evolved (Table 4.2).

Table 4.2 Major elements compositions and pre-eruptive temperatures.
*** Calculated after solubility model of Moore (2008) for only water (lower pressure estimate) and the model of Papale et al (2006) for water and CO_2 (higher pressure)**
$ using a mean density of 2000 kg/m^3.
 # Using models of Ghiorso and Evans (2008) and Sauersaft et al. 2008 with respect to the NNO buffer
& Using thermodynamic modes of Scaillet and Pichavant (2003)

	WR (4-5 June)	**Glass inclusions (Mean; N=6)**	**std**
wt%			
SiO_2	69.4	72.1	0.52
TiO_2	1.01	0.42	0.01
Al_2O_3	14.0	13.66	0.06
FeO*	4.04	3.07	0.07
MnO	0.09	0.09	0.01
MgO	0.57	0.35	0.04
CaO	2.16	1.57	0.05
Na_2O	5.22	5.52	0.11
K_2O	2.76	2.94	0.10
P_2O_5	0.08		
Total	99.33	98.20	1.81
H_2O wt %		3.9	0.7
CO_2 ppm		221	44
Li ppm	30	48	2
Be ppm		2.9	0.3
B ppm		29.7	1.2
F ppm		808	115
S ppm		66	9
Cl ppm		1755	270
Rb ppm	69	79	7
Sr ppm	166	117	16
Mineral compositions			
Pl (An)	37.9		2.5
Cpx (Mg#)	62.4		1.9
Cpx (Wo)	37.4		4.5

Cpx (En)	39.0		2.0
Cpx (Fs)	23.6		2.8
Opx (Mg#)	56.5		2.0
Opx (Wo)	3.6		0.1
Opx (En)	54.4		1.9
Opx (Fs)	41.9		2.0
Pre-eruptive conditions			
T (^{o}C) #, n= 10	895		16
Log fO2%	-0.85		0.17
P (Mpa)*	100-140		
Depth km$	5-7		
Gas phase equilibrium composition (wt proportions)&			
H_2O	0.63		
H_2S	0.01		
CO_2	0.36		

Pre-eruptive conditions

Using the composition of touching pairs of Fe-Ti oxides we find temperatures ranging from 895 to 920 ^{o} C (± 20 ^{o}C) and oxygen fugacity close to the QFM (=quartz-fayalite-magnetite) oxygen reaction buffer (models of Sauerzaft et al., 2008; and Ghiorso and Evans, 2008). These are rather reduced conditions compared to other dacites and rhyodacites from subduction zones (e.g., Costa et al., 2004; Wright et al., 2012), but are consistent with the relatively low S contents and the presence of pyrrhotite in the rock. The pure water solubility model of Moore (2008) gives a minimum pressure for the storage of the rhyodacite of about 100 MPa, whereas incorporating the CO_2 concentration and using the H_2O-CO_2 solubility model of Papale et al. (2006) gives about 140 MPa. These observations are in agreement with

the phase equilibria study of Castro et al. (2013), although we obtain slightly higher total pressure. Using the thermodynamic solubility model of Scaillet and Pichavant (2003) we find that the coexisting fluid phase in equilibrium with the rhyodacite magma at these conditions would have about 0.4 wt% SO_2 in the fluid, and $\log fS_2 = -3.7$ bar. To calculate the depth of the magma reservoir from this pressure requires using the density of the crust. At Cordón Caulle we expect a silicic upper crust, with a density of about 2500 kg/m^3 which would give a depth of 4-6 km. However, the presence of a large hydrothermal system could lead to significantly lower crustal densities, and for a density of 2000 kg/m^3 we obtain a minimum depth of magma storage at 5-7 km.

4.4 DISCUSSION

4.4.1 Magma volume, excess gas, and compressibility from satellite and petrological data

A key question to understanding the driving mechanisms behind explosive eruptions is whether there is a volatile phase present in the magma reservoir prior to eruption. The presence of an exsolved volatile phase also plays a role in making the magma system compressible (melt + crystals + gas) which is important for relating the erupted volume of magma with the volume that may have been injected into the ground and caused surface deformation before the eruption (e.g., Johnson et al., 2000). We estimate the exsolved volatile content by comparing the amount of SO_2 that can be released by the erupted magma to the atmosphere with the actual amount of SO_2 measured from satellite (e.g., Devine et al., 1984; Scaillet et al., 2003; Costa et al.,

2003b). Though the principal volatile components in the magma are H_2O and CO_2, we use SO_2 as a tracer in our calculation because it is readily detectable from space. For this calculation, it is necessary to know the S content at depth (melt inclusions have a mean of 130 ppm of SO_2), the volume of erupted magma (0.6-0.8 km^3 of dense rock equivalent for the total Caulle eruption, e.g., Silva Parejas et al., 2012; Tuffen et al., 2013.), the amount of melt that can be degassed (the rhyodacite is crystal poor with about 95 wt% glass), and the amount of residual S in the interstitial melt. We could not get a sulfur analysis of the residual glass with the ion microprobe but its concentration was below the detection limit of the electron microprobe, which is 50 ppm S. Thus, we have assumed that about half of S was degassed from the melt which is probably an overestimate since Si-rich melt compositions tend to be less degassed (e.g., review of Scaillet et al. 2003). The results of the calculation show that the amount of SO_2 released by the eruption is about 140 kT SO_2, or about 1.5 times less than the mass of SO_2 estimated from space by the infrared atmospheric sounding interferometer (250 kT SO_2; Clarisee et al., 2013; Table 3). Note that this is probably a maximum estimate for the magma degassing because the satellite measurements were done at the beginning of the eruption, when only about 0.25 km^3 of magma had been erupted. The implication is that the magma reservoir of the 2011-2012 eruption was vapor saturated and contained excess gas, as is the case for many other silicic explosive eruptions (e.g., Costa et al., 2003b; Scaillet et al., 2003). The amount of exsolved gas in the reservoir can be calculated knowing that the SO_2 concentration in the gas phase was about 0.4 wt% (thermodynamic calculations using the model of Scaillet and Pichavant, 2003), and doing a mass balance to match the satellite data. We

find that the fluid phase contained 110 kT SO_2, 4 Mt of H_2O, and 2.2 Mt of CO_2, and represents about 1.5 wt% of the erupted magma (Table 4.3).

Magma compressibility and volume changes

The presence of an exsolved fluid phase in the Cordón Caulle magma reservoir has an influence on interpreting the relationship between volume changes at depth and the volume of erupted magma. Summing the modeled volume change from the two sources for the 2007-2008 uplift episode (0.02 ± 0.01 km^3) with the modeled volume change from the one source for the 2008-2009 uplift episode (0.03 ± 0.02 km^3) gives a total volume change of 0.05 ± 0.03 km^3. We neglect the March to May 2011 uplift as it only contributes a volume of 0.003 km^3. We assume that all of the deformation is caused by magma intrusion to derive an upper limit on the total volume change at depth associated with intrusion. The trade-off between source depth and volume change, as well as the assumption of source geometry, elastic homogeneity, and Poisson's ratio, all contribute to the uncertainty of the volume change (e.g., Newman et al., 2001, Lu et al., 2003, Pritchard and Simons, 2004;); however, having inverted for many different source geometries (see Appendix A2.1), we are confident that this value provides a reliable order-of-magnitude estimate and its depth is consistent with the petrological estimates. The total volume change value of 0.05 km^3 is about an order of magnitude less than the DRE volume of erupted material, 0.6-0.8 km^3 (Silva Parejas et al., 2012; Tuffen et al., 2013). Such a difference could be in part explained by the presence of a deformable fluid phase with a high compressibility (Table 3). The presence of exsolved volatiles in a saturated magma increases the compressibility

of the magma so that a given decrease in pressure leads to a greater expansion of the magma and thus a greater volume of erupted material at the surface.

We calculate the compressibility of the magma following the method of Huppert and Woods (2002), and then relate the pre-eruptive magma volume change at depth with the erupted volume using the mass balance equations of Mastin et al (2008) and Segall (2010) (see Appendix A2.2 for details). Using the value of 1.5 wt% fluid, we calculate a magma compressibility of 2.1 (± 0.4) x 10-10 Pa^{-1}, which is about twice that of a bubble-free system. Given this compressibility, the volume change at depth necessary to account for the observed erupted volume of 0.6-0.8 km^3 is 0.26 ± 0.06 km^3, which is about 5 times what we have obtained from InSAR models for pre-eruptive deformation (Table 3). We can also relate the modeled co-eruptive volume change to the erupted volume. Given our calculated compressibility of 2.1 (± 0.4) x 10-10 Pa^{-1}, our modeled cumulative volume change during the eruption (0.4 ± 0.1 km^3) is within error of the 0.26 ± 0.06 km^3 volume change at depth necessary to account for 0.6-0.8 km^3 of erupted material. This validates our calculation of magma compressibility and our method for determining exsolved volatile content assuming co-eruptive ground deformation is only caused by material leaving the chamber and erupting.

The calculations show that the InSAR-modeled volume change between 2007 and 2009 is insufficient to account for the observed volume of erupted material given magma compressibility. For systems such as Cordón Caulle that have not erupted for several decades and have had time to accumulate a volatile phase, volume changes inferred during the few years before eruption may only represent a fraction of the

volume that will be erupted. Since the erupted volume was greater than that estimated to have caused the 2007-2009 uplift, we conclude that the volume change inferred from InSAR modeling between 2007 and 2009 must have been augmented by volume from the existing reservoir (e.g., magma intruded before 1996, or during other time periods when there was no InSAR data from 1999 to 2003 or 2006 to 2007).

Table 4.3 Estimation of the volatile budget of the eruption necessary to determine magma compressibility
[1]estimated to be < 50 ppm (Scaillet et al., 2003); [2]using model of Scaillet and Pichavant (2003); [3]From Clarisse et al (2012); [4]Calculated to match the excess SO_2; [5]After Huppert and Woods (2002); [6]From Touloukian et al (1981); [7]Calculated from equation 5 of Mastin et al (2008)

Rocks	Value	Units
erupted volume (DRE)	800000000	m^3
rock density	2300	kg/m^3
mass of magma	1840	Mt
conc SO_2 g MI or exp undegassed glass /100	0.00013	
[1]conc SO_2 g degassed gl/100	0.00005	
Glass proportion	0.95	
Atmos petro melt degas SO_2	0.140	Mt
[2]conc g SO_2 in fluid	0.004	
pressure storage	140000000	Pa
R (gas constant)	8.31	J K/mol
T (temperature)	1173	K
[3] *volcanic gas satellite measurements*		
Atmos SO_2	0.25	Mt
Excess SO_2	0.11	Mt
[4]*Calculated Fluid phase*		
gas content	1.5	wt%
mass of fluid	27.6	Mt
SO_2 mass in fluid	0.110	Mt
Magma compressibility and mass balance		
density of ideal gas	259	kg/m^3
[5]density of bubble-bearing magma	2055	kg/m^3

compressibility of ideal gas	7.14E-09	Pa^{-1}
[6]compressibility of melt	1E-10	Pa^{-1}
[5]compressibility of bubble-bearing magma	2.06E-10	Pa^{-1}
volume change from InSAR	110000000	m^3
[7]calculated volume change	290000000	m^3

4.4.2 Magmatic versus hydrothermal pre-eruptive deformation sources

The range of modeled InSAR source depths for the 2007-2009 and that of the early 2011 uplift vary between 4-9 km and are consistent with the depth of a shallow rhyodacitic magma chamber at 5-7 km for the erupted materials. Therefore, we believe that the physical cause of the 2007-2009 and early 2011 deformation is likely to be magmatic. All these depths are greater than the 3 km depth of the hydrothermal system derived from gravity, chemical, and isotopic data (Sepulveda et al., 2005; Sepulveda et al., 2004). The physical cause of the 1996-1999 subsidence and the change from subsidence to uplift could be related to changes in the pressure state of the magmatic and/or hydrothermal systems as well as feedback between the two systems as suggested at Yellowstone (Dzurisin et al., 1994). It is also possible that there is not a simple depth transition between magmatic and hydrothermal sources such that there is a complex three-dimensional interaction of magmatic and hydrothermal fluids partially overlapping in depth.

In contrast, the shallow modeled depth (~2 km) of the source of the Cordillera Nevada deformation episode implies a hydrothermal cause. The Trahuilco springs, vigorous boiling springs located in the center of Cordillera Nevada (Sepulveda et al.,

2004), are fed by a shallow steam-heated aquifer and are the main outflow of the Cordón Caulle geothermal system. The activity of Trahuilco is believed to have migrated with time due to the existence of silica sinter craters near the active vent (Sepulveda et al., 2004).

4.4.3 Response to the Maule earthquake

The 27 February 2010 Mw 8.8 Maule earthquake likely triggered the short-lived, localized deformation at the dynamic geothermal system in Cordillera Nevada caldera in February-March 2010. We hypothesize that the physical shaking and the passage of the dynamic surface waves from the Maule earthquake caused the previously sealed hydrothermal system to develop fractures, allowing the migration of fluids into the observed region of uplift (e.g., Pritchard et al., 2013), although other mechanisms are possible (e.g., Hill and Prejean, 2007; Takada and Fukushima, 2013).

Although the Cordillera Nevada deformation may have been triggered by the Maule earthquake, our InSAR data show that Puyehue-Cordón Caulle did not exhibit any regional volcano-tectonic deformation in response to the earthquake that might have precipitated the eruption. Thus, although the 1960 Cordón Caulle eruption was likely triggered by the Mw 9.5 earthquake 240 km distant (e.g., Barrientos, 1994; Lara et al., 2004) the 2010 Mw 8.8 earthquake 520 km distant did not obviously trigger the eruption. The difference between the volcano response in 1960 and 2011 could be that the static stress change in 1960 was more than 100 times larger (e.g., Bonali et al., 2013); that dynamic stresses (from the passage of seismic body and surface waves)

were larger in 1960, triggering the eruption (e.g., Lara et al., 2004); or that the conditions within the magma chamber were different in 1960 and 2011.

4.4.4 Magmatic intrusions and eruption triggers

InSAR observations from 2007-2009 and early 2011 show inflation sources that are located either at the Cordillera Nevada (close to the 1921-22 vents) or close to the 1960 eruption vents, both far from the 2011 eruptive site, about 10 km NW and 2 km SW, respectively. The inflations are probably due to new magma intrusions of either mafic or silicic composition, although it is clear that no mafic magmas were erupted. The geochemical and petrological characteristics of the magmas erupted in 1921-22, 1960 and 2011-12 are nearly identical and suggest that they were derived from the same reservoir, probably a crystal-rich mush zone located between 4 and 7 km where rhyodacite segregation occurs (e.g., Bachmann and Bergantz, 2004). This implies that there is a well-developed and relatively large magma plumbing system with hydraulic connectivity (e.g. pressure transfer) that is at least 10 km to the NW and 2 km to the SW of the eruptive vent of 2011-12, and thus covers an area of at least 20 km^2 (Fig. 4.6).

We find very limited evidence of open-system processes in the mineral textures and zoning that are indicative of disequilibrium (e.g., Streck, 2008). For example, the Fe-Ti oxides do not show any evidence of chemical zoning as would be the case if the rhyodacite magma had been reheated right before eruption by a new influx of magma as has been reported in many other silicic arc magmas (e.g. Nakamura, 1995; Devine and Rutherford, 2003). We observe a crystal clot made of

Mg-rich olivine and high An plagioclase in the lava sample (Section 4.3.2; Fig. 4.5). This mineral assemblage is not in equilibrium with the host dacite and shows that despite the fact that Cordón Caulle has exclusively erupted rhyodacite magma in the last 100 years, mafic magmas of basaltic or basaltic andesite composition are able to reach the upper parts of the silicic reservoir. In fact, mafic intrusions into silicic magmas have occurred in the last 5,000 years at neighboring Puyehue volcano (Singer et al., 2008). We constrain the timing of the mafic intrusion by determining if the Mg content of the high An crystal core has been completely equilibrated by diffusion with the dacite melt (Costa et al., 2003a). Assuming that the high-An part originally grew from a melt with about 6 wt% MgO and a diffusion model for a 3D parallelepiped of the size of the plagioclase core at 900° C, we find that the minimum time that the crystal has resided in the dacite is at least 200 years. Thus, the intrusion occurred much prior to the eruption, and the mafic magma that was the source of the crystal clot was not a direct trigger of the eruption. However, it is still possible that magmatic intrusions reached the magma mush zone but did not erupt, and were overwhelmed by the large size of the mush zone. We conclude that if new magma was the cause of the deformation during 2007-2009, it did not mix with the pre-existing rhyodacitic reservoir and was not erupted during the 2011-2012 eruption. Instead, we hypothesize that the new magma in the 2007-2009 intrusions accumulated at the base of the reservoir and provided a heat source to rejuvenate the mush zone (Bachmann and Bergantz, 2004; Bachmann and Bergantz, 2008; Fig. 4.6).

Although we cannot be sure of the physical driver of the eruption, there was a clear increase in seismicity (as reported by OVDAS) and ground deformation in

March-May 2011 in between the volumetrically most important subsurface reservoir of the 2011 eruption and the eruptive vent (Fig. 4.2i). Earthquake locations do not show a simple spatial progression between the two locations, although an eastward migration is roughly observed (Basualto et al., 2012). We hypothesize that the deformation and seismicity is related to lateral and/or vertical transport of fluids (degassed volatiles and/or magma) toward the eruptive vent. Ground cracks could indicate that the eruption was fed by a dike (e.g., Castro et al., 2013), but the diagnostic pattern of dike opening deformation is not apparent in the first co-eruptive interferogram, although this region largely decorrelated because of the erupted ash (Fig. 4.3a). In fact, the pattern of uplift to the N-NE of the eruption suggests a component of horizontal deformation from the deflation source (section 4.3.1) and possibly a closing dike. Although we do not have a conclusive proximal trigger for the 2011-2012 eruption, the regional tectonics clearly played a role in the distribution of pre-eruptive and co-eruptive centers (Lara et al., 2006b), which are aligned along the west side of the Cordón Caulle graben (Fig. 4.3a), as well as the March-May 2011 deformation (Fig. 4.2i).

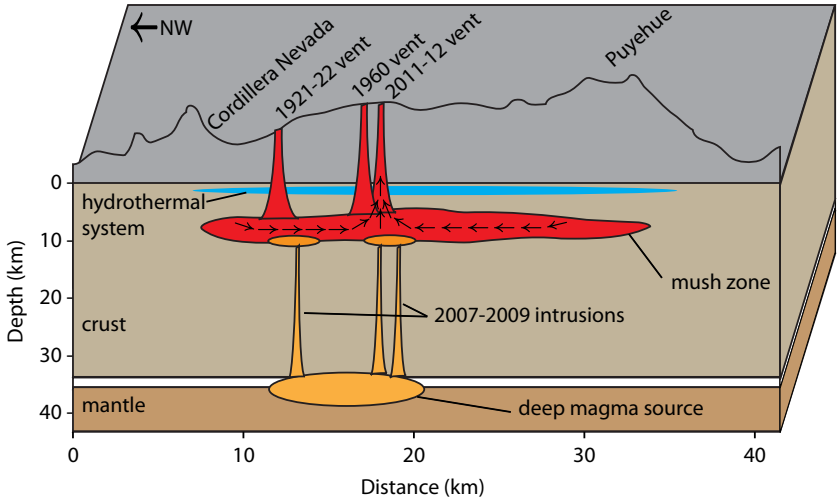

Figure 4.6 Cartoon cross-section showing a NW-SE topographic profile of Puyehue-Cordón Caulle, sites of the three last historical eruption, magma reservoir sizes and locations, and likely processes occurring at depth. We envision an extensive, long-lived crystal-rich zone at 4-7 km depth that has fed all three historical eruptions. Uplift between 2007- 2009 was probably caused by magma addition to the base of the crystal-rich zone.

4.4.5 Magma withdrawal areas and relation to Puyehue volcano

InSAR data spanning the first few days of the eruption show clear evidence for two distinct sources of deflation (Fig. 4.3a). The dominant source beneath Cordillera Nevada at ~4 km depth is near one of the sources of the 2007-2008 uplift, and the secondary source is located beneath Puyehue at ~6 km depth. The coherence between the locations of the inflation and deflation sources and their proximity to the 1921-22 and 1960 eruptive vents illustrates that there is a large magmatic plumbing system that covers at least 20 km^2. Hydraulic connection between the entire system and pressure transfer could explain how distant intrusions could lead to eruption 10 km away from the pressure source. The co-eruptive deflation below Puyehue is not matched by an inflation source but opens the possibility that magma from Puyheue also was mobilized by the eruption. The compositions of Puyehue and Cordón Caulle magmas

evolved separately over the past 300 ka, but both systems shifted to rhyolitic compositions in the past 20-30 ka, and <6 ka rhyodacites from Puyehue are compositionally similar to historical Cordón Caulle rhyodacites in SiO_2 content and trace element abundances and ratios (Singer et al. 2008). Thus, it is possible that the magma plumbing system that contains the rhyodacite extends laterally to the region below Puyehue volcano. In this scenario it seems that Puyehue and Cordón Caulle would share at least part of their plumbing system and implies a nearly continuous mush zone spanning from Cordillera Nevada to Puyehue, which are about 18 km apart (Fig. 4.6).

4.4.6 Global comparison

We are not aware of any other studies of volcanic deformation preceding large rhyodacitic eruptions of the volume studied here. While there are numerous studies of pre-eruptive deformation at basaltic systems in Alaska, Hawaii, Iceland, and elsewhere, (e.g., Dvorak and Dzurisin, 1997; Lu et al., 2003; Lu et al., 2010; Sigmundsson et al., 2010) and in the months before the May 1980 dacite eruption of Mt. St. Helens (e.g., Lipman et al., 1981), the nature of the deformation at Cordón Caulle is different in several respects. First, pre-eruptive deformation of Cordón Caulle is not localized to the volcanic edifice, but rather covers a broad region of about 400 km^2 including several eruptive vents, faults, and hydrothermal systems. Second, the peak deformation ocurred two years before the eruption, although increased seismicity in the days before eruption may indicate a second peak (e.g., Silva Parejas et al., 2012). This short run-up time has been compared to the 36 hours

of precursory seismicity (Lara, 2008) before the 2008 rhyolitic eruption at Chaitén volcano in Southern Chile (Castro et al., 2013), where fault-assisted diking allowed the rapid evacuation of rhyolitic material (Wicks et al., 2011). The 2011-2012 Cordón Caulle eruption does have a similarity to the build-up to the 2010 andesitic eruption of Eyjafjallajökull, Iceland – both had multiple pulses of uplift, two of which did not end in eruption within a year, and one that did (e.g., Pederson and Sigmundsson, 2006; Sigmundsson et al., 2010). These eruptions have implications for hazard assessment: volcanic deformation preceding eruptions can occur episodically at silicic andesitic to rhyolitic volcanoes, and a peak in deformation rate does not necessarily mean that an eruption is about to occur within a short time period, but increased vigilance is sometimes justified.

Chaitén and Cordón Caulle are also similar in that they had simultaneous effusive and explosive eruptions, perhaps caused by lava and pyroclasts undergoing different amounts of degassing as they ascend different paths within the dike feeding the eruption (Castro et al., 2013). Our results show that the 2011 eruption had multiple source zones separated by 10-15 km (depending on the eruptive phase) and are consistent with the model of Castro et al. (2013).

4.5 CONCLUSIONS

This study demonstrates the potential for using deformation to understand large silicic eruptions. Combining InSAR observations with petrological studies of the 2011-2012 eruption, we determine that the physical cause of the 2007-2009 uplift was likely an addition of magma to the a pre-existing shallow magma reservoir at 4-9 km depth which may have fed all three historical eruptions. The erupted magma was stored at

near liquidus conditions (900^{o} C, 4 wt% H_2O in the melt) and shows limited evidence of a thermal or chemical perturbation right before eruption, suggesting that the eruption was not simply triggered by a late major magma replenishment event.

We find that the inflation sources are located up to 10 km away from the 2011-12 eruptive vent and coincide with the 1921-22 and 1960 eruption sites. Some deflation also occurred below Puyehue volcano, which is about 8 km from the 2011-12 vent. These observations suggest that there is a well-developed magmatic system (probably a silicic crystal-rich mush zone) that allows for hydraulic connection and pressure transfer that spans at least 18 km in length and occupies an area of at least 20 km^2. Thus the plumbing system and deformation behavior of Cordón Caulle is similar to a large caldera system and probably controlled by the regional tectonic setting and fault systems.

REFERENCES

Bachmann, O., & Bergantz, G. (2004). On the Origin of Crystal-poor Rhyolites: Extracted from Batholithic Crystal Mushes. *Journal of Petrology*, *45*(8), 1565–1582.

Bachmann, O., & Bergantz, G. (2008). The Magma Reservoirs That Feed Supereruptions. *Elements*, *4*(1), 17–21.

Barrientos, S. E. (1994). Large thrust earthquakes and volcanic eruptions. *Pure and Applied Geophysics*, *142*(1), 173–224.

Basualto, D, Cardona, C, Franco, L, Gil, F, Valderrama, A, Hernández, E (2012). Mecanismos de Intrusión Relacionados con la Erupción del Complejo Volcánico Cordón Caulle – Chile Junio 4 de 2011, presented at XIII Congreso Geologico Chileno, Antofagasta, Chile.

Bertin, D.; Amigo, A.; Lara, L.E., Orozco, G.; Silva, C. 2012. Erupción del Cordón Caulle 2011-2012: evolución de la fase efusiva. In Congreso Geológicio Chileno No. 13, 545-547.

Bonali, F. L., Tibaldi, a., Corazzato, C., Tormey, D. R., & Lara, L. E. (2013). Quantifying the effect of large earthquakes in promoting eruptions due to stress changes on magma pathway: The Chile case. *Tectonophysics*, *583*, 54–67.

Castro, J. M., Schipper, C. I., Mueller, S. P., Militzer, a. S., Amigo, A., Parejas, C. S., & Jacob, D. (2013). Storage and eruption of near-liquidus rhyolite magma at Cordón Caulle, Chile. *Bulletin of Volcanology*, *75*(4), 702.

Clarisse L., D. Hurtmans, C. Clerbaux, J. Hadji-Lazaro, Y. Ngadi, and P.-F. Coheur (2012) Retrieval of sulphur dioxide from the infrared atmospheric sounding interferometer (IASI). Atmos. Meas. Tech., 5, 581–594.

Costa, F., Jay, J. A., Pritchard, M. E., Lara, L. E., Singer, B. S., & Herrin, J. (in prep). *Magmatic processes and time scales below a yet-to-be silicic caldera eruption*.

Costa, F., Chakraborty, S. and Dohmen, R. (2003a). Diffusion coupling between trace and major elements and a model for calculation of magma residence times using plagioclase. *Geochimica et Cosmochimica Acta* 67, 2189-2200.

Costa, F., Scaillet, B. and Gourgaud, A. (2003b). Massive atmospheric sulfur loading of the AD 1600 Huaynaputina eruption and implications for petrologic sulfur estimates. *Geophysical Research Letters* 30, 1068.

Costa, F., Scaillet, B. and Pichavant, M. (2004). Petrologic and experimental constraints on the pre-eruption conditions of Holocene dacite from Volcán San Pedro (36o S, Chilean

Andes) and the importance of sulfur in silicic subduction-related magmas. *Journal of Petrology* 45, 855-881.

Costa, F., Dohmen, R., and Chakraborty S. (2008) Time Scales of Magmatic Processes from Modeling the Zoning Patterns of Crystals. *Reviews in Mineralogy and Geochemistry* 69, 545-594.

Costa, F.; Lara, L. E.; Singer, B. S. (2011) Possible tectonic control on the origin and pre-eruptive conditions of the Cordón Caulle (Chile) 1921, 1960, and 2011 silicic eruptions, Abstract V33B-2626 presented at 2011 Fall Meeting, AGU, San Francisco, Calif., 5-9 Dec.

Devine JD, Rutherford MJ, Norton GE, Young SR (2003) Magma storage region processes inferred from geochemistry of Fe-Ti oxides in andesite magma, Soufrière Hills volcano, Montserrat, W.I. J Petrol 44:1375-1400

Dvorak, J., & Dzurisin, D. (1997). Volcano geodesy: The search for magma reservoirs and the formation of eruptive vents. *Reviews of Geophysics*, (97), 343–384.

Dzurisin, D., Yamashita, K., & Kleinman, J. (1994). Mechanisms of crustal uplift and subsidence at the Yellowstone caldera, Wyoming. *Bulletin of volcanology*, 261–270.

Folch, a., & Gottsmann, J. (2006). Faults and ground uplift at active calderas. Geological Society, London, Special Publications, 269(1), 109–120. doi:10.1144/GSL.SP.2006.269.01.07

Fournier, T. J., Pritchard, M. E., & Riddick, S. N. (2010). Duration, magnitude, and frequency of subaerial volcano deformation events: New results from Latin America using InSAR and a global synthesis. *Geochemistry Geophysics Geosystems*, *11*(1). doi:10.1029/2009GC002558

Ghiorso, M. S., & Evans, B. W. (2008). Thermodynamics of rhomohedral oxide solid solutions and a revision of the Fe-Ti two-oxide geothermometer and oxygen barometer. *American Journal of Science*, *308*(9), 957–1039.

Devine, J., H. Sigurdsson, A. N. Davis, and S. Self, (1984) Estimates of sulfur and chlorine yield to the atmosphere from volcanic eruptions and potential climatic effects, J. Geophys. Res., 89, 6309–6325.

Hautmann, S., Gottsmann, J., Sparks, R. S. J., Mattioli, G. S., Sacks, I. S., & Strutt, M. H. (2010). Effect of mechanical heterogeneity in arc crust on volcano deformation with application to Soufrière Hills Volcano, Montserrat, West Indies. *Journal of Geophysical Research*, *115*(B9), B09203.

Hill, D. & Prejean, S. Dynamic triggering. in Treatise on Geophysics, (Kanamori, H., ed), 258–288. Elsevier, Amsterdam, (2007).

Huppert, H. E., & Woods, A. W. (2002). The role of volatiles in magma chamber dynamics. *Nature*, *420*(6915), 493–5.

Jay, J., Welch, M., Pritchard, M., Mares, P., Mnich, M., Melkonian, A., Aguilera, F., et al. (2013). Volcanic hotspots of the central and southern Andes as seen from space by ASTER and MODVOLC between the years 2000-2011. *Geological Society, London, Special Publications*, *380*.

Johnson, D., Sigmundsson, F., & Delaney, P. (2000). Comment on "Volume of magma accumulation or withdrawal estimated from surface uplift or subsidence, with application to the 1960 collapse of Kīlauea volcano" by P.T. Delaney and D.F. McTigue. *Bulletin of Volcanology*, 491–493.

Lara, L.E., Naranjo, J. a., & Moreno, H. (2004). Rhyodacitic fissure eruption in Southern Andes (Cordón Caulle; 40.5°S) after the 1960 (Mw:9.5) Chilean earthquake: a structural interpretation. *Journal of Volcanology and Geothermal Research*, *138*(1-2), 127–138.

Lara, L.E., Moreno, H., Naranjo, J. a., Matthews, S., & Pérez de Arce, C. (2006a). Magmatic evolution of the Puyehue–Cordón Caulle Volcanic Complex (40° S), Southern Andean Volcanic Zone: From shield to unusual rhyolitic fissure volcanism. *Journal of Volcanology and Geothermal Research*, *157*(4), 343–366.

Lara, L. E. (2008). The 2008 eruption of the Chaitén Volcano, Chile: a preliminary report. Andean Geology, 36(1), 125–129.

Lara, Luis E., Lavenu, A., Cembrano, J., & Rodríguez, C. (2006b). Structural controls of volcanism in transversal chains: Resheared faults and neotectonics in the Cordón Caulle–Puyehue area (40.5°S), Southern Andes. *Journal of Volcanology and Geothermal Research*, *158*(1-2), 70–86.

Linde, A., & Sacks, I. (1998). Triggering of volcanic eruptions. *Nature*, *395*(October), 1997–1999.

Lipman P.W., Moore J.G., Swanson D.A., 1981, Bulging of the north flank before the May 18 eruption; geodetic data, in Lipman P., Mullineaux D.R., eds., The 1980 eruptions of Mount St. Helens, Washington: U.S. Geological Survey Professional Paper 1250, p. 143–155

Lorito, S., Romano, F., Atzori, S., Tong, X., Avallone, a., McCloskey, J., Cocco, M., et al. (2011). Limited overlap between the seismic gap and coseismic slip of the great 2010 Chile earthquake. *Nature Geoscience*, *4*(3), 173–177.

Lu, Z., Masterlark, T., Dzurisin, D., Rykhus, R., & Wicks, C. (2003). Magma supply dynamics at Westdahl volcano, Alaska, modeled from satellite radar interferometry. *Journal of Geophysical Research*, *108*(B7), 2354.

Lu, Z., Dzurisin, D., Biggs, J., Wicks, C., & McNutt, S. (2010). Ground surface deformation patterns, magma supply, and magma storage at Okmok volcano, Alaska, from InSAR analysis: 1. Intereruption deformation, 1997–2008. *Journal of Geophysical Research*, *115*(August 2008), B00B02.

Masterlark, T., & Lu, Z. (2004). Transient volcano deformation sources imaged with interferometric synthetic aperture radar: Application to Seguam Island, Alaska. *Journal of Geophysical Research*, *109*(B1), B01401.

Mastin, L.G.; Roeloffs, E.; Beeler, N.M.; & Quick, J.E. (2008) Constraints on the Size, Overpressure, and Volatile Content of the Mount St. Helens Magma System from Geodetic and Dome-Growth Measurements During the 2004–2006+ Eruption. In A Volcano Rekindled: The Renewed Eruption of Mount St. Helens, 2004–2006 Edited by David R. Sherrod, William E. Scott, and Peter H. Stauffer U.S. Geological Survey Professional Paper 1750,

Mogi, K. (1958), Relations between the eruptions of various volcanoes and the deformations of the ground surface around them, Bull. Earthquake Res. Inst. Univ. Tokyo, 36, 99–134.

Moore, G. (2008). Interpreting H2O and CO2 Contents in Melt Inclusions: Constraints from Solubility Experiments and Modeling. *Reviews in Mineralogy and Geochemistry*, *69*(1), 333–362.

Nakamura M (1995) Continuous mixing of crystal mush and replenished magma in the on going Unzen eruption. Geology 23:807-810.

Newman, A.V., Dixon, T.H., Ofoegbu, G., Dixon, J.E. (2001) Geodetic and seismic constraints on recent activity at Long Valley caldera, California: evidence for viscoelastic rheology. J. Volcanol. Geotherm. Res. 105, 183–206.

Okada, Y. (1992). Internal deformation due to shear and tensile faults in a half-space. *Bulletin of the Seismological Society of America*, *82*(2), 1018–1040.

Papale P, Moretti R, Barbato D (2006) The compositional dependence of the saturation surface of H2O + CO2 fluids in silicate melts. Chemical Geology 229, 78-95.

Pedersen, R., & Sigmundsson, F. (2006) Temporal development of the 1999 intrusive episode in the Eyjafjallajökull volcano, Iceland, derived from InSAR images. *Bulletin of volcanology*, **68**, 377-393.

Pritchard, M. E., & Simons, M. (2004a). An InSAR-based survey of volcanic deformation in the southern Andes. *Geophysical Research Letters*, *31*(15), 1–4.

Pritchard, M. E., & Simons, M. (2004b). An InSAR-based survey of volcanic deformation in the central Andes. *Geochemistry Geophysics Geosystems*, *5*(2), 1–42.

Pritchard, M. E., Jay, J. A., Aron, F., Henderson, S. T., & Lara, L. E. (2013). Subsidence at southern Andes volcanoes induced by the 2010 Maule, Chile earthquake. *Nature Geoscience*, *6*(8), 632–636.

Rosen P, Hensley S, Peltzer G, Simons M (2004) Updated repeat orbit interferometry package released. Eos Trans AGU 85:47

Sauerzapf, U., Lattard, D., Burchard, M., Engelmann, R., 2008. The titanomagnetite-ilmenite equilibrium: new experimental data and thermo-oxybarometric applica- tion to the crystallization of basic to intermediate rocks. Journal of Petrology 49, 1161–1185.

Scaillet, B. & Pichavant, M. (2003). Experimental constraints on volatile abundances in arc magmas and their implications for degassing processes. In: Oppenheimer, C., Pyle, D. M. & Barclay, J. (eds), Volcanic Degassing. Geological Society, London, Special Publications, 213, 23-52.

Scaillet, B., Luhr, J. F. & Carroll, M. R. (2003) Petrological and volcanological constraints on volcanic sulfur emissions to the atmosphere, AGU Geoph. Monograph 139, 11–40.

Segall, P. Earthquake and Volcano Deformation (2010). Princeton University Press.

Sepúlveda, F., Dorsch, K., Lahsen, A., Bender, S., & Palacios, C. (2004). Chemical and isotopic composition of geothermal discharges from the Puyehue-Cordón Caulle area (40.5°S), Southern Chile. *Geothermics*, *33*(5), 655–673.

Sepúlveda, F., Lahsen, A., Bonvalot, S., Cembrano, J., Alvarado, A., & Letelier, P. (2005). Morpho-structural evolution of the Cordón Caulle geothermal region, Southern Volcanic Zone, Chile: Insights from gravity and 40Ar/39Ar dating. *Journal of Volcanology and Geothermal Research*, *148*(1-2), 165–189.

Sigmundsson, F., Hreinsdóttir, S., Hooper, A., Arnadóttir, T., Pedersen, R., Roberts, M. J., Oskarsson, N., et al. (2010). Intrusion triggering of the 2010 Eyjafjallajökull explosive eruption. *Nature*, *468*(7322), 426–30.

Silva Parejas C, Lara LE, Bertin D, Amigo A, Orozco G (2012) The 2011–2012 eruption of Cordón Caulle volcano (Southern Andes): evolution, crisis management and current hazards. EGU General Assembly 2012, Vienna, Austria, 22–27 April 2012. p. 9382

Singer, B. S., Jicha, B. R., Harper, M. a., Naranjo, J. a., Lara, L. E., & Moreno-Roa, H. (2008). Eruptive history, geochronology, and magmatic evolution of the Puyehue-Cordón Caulle volcanic complex, Chile. *Geological Society of America Bulletin*, *120*(5-6), 599–618.

Streck MJ (2008) Mineral textures and zoning as evidence for open system processes. Rev Mineral Geochem 69:595-622

Takada, Y., & Fukushima, Y. (2013). Volcanic subsidence triggered by the 2011 Tohoku earthquake in Japan. *Nature Geoscience*, *6*(8), 637–641.

Touloukian, Y.S.; Judd, W.R.; & Roy, R.F, Eds. (1981) *Physical Properties of Rocks and Minerals Vol. 1* McGraw Hill, New York.

Trasatti, E., Giunchi, C., & Bonafede, M. (2003). Effects of topography and rheological layering on ground deformation in volcanic regions. *Journal of Volcanology and Geothermal Research*, *122*, 89–110.

Tuffen, H., M. R. James, J. M. Castro and C. I. Schipper, (2013) Exceptional mobility of an advancing rhyolitic obsidian flow at Cordón Caulle volcano in Chile, Nature communications, 4:2709.

Walter, T., & Amelung, F. (2007). Volcanic eruptions following M≥ 9 megathrust earthquakes: Implications for the Sumatra-Andaman volcanoes. *Geology*, *35*(6), 539.

Wicks, C., De la Llera, J. C., Lara, L. E., & Lowenstern, J. (2011). The role of dyking and fault control in the rapid onset of eruption at Chaitén volcano, Chile. *Nature*, *478*(7369), 374–7.

Wright, H.M., Bacon, C.R., Vazquez, J.A., and Sisson, T.W. (2012) Sixty thousand years of magmatic volatile history before the caldera-forming eruption of Mount Mazama, Crater Lake, Oregon. Contributions to Mineralogy and Petrology, 164 1027-1052.

Yang, X., Davis, P., & Dieterich, J. (1988). Deformation from inflation of a dipping finite prolate spheroid in an elastic half-space as a model for volcanic stressing. *Journal of Geophysical Research*, *93*(B5), 4249–4257.

CHAPTER 5

VOLCANO-TECTONIC INTERACTIONS AT PERUVIAN VOLCANOES REVEALED BY INSAR

5.0 ABSTRACT

An InSAR survey of all 16 Holocene volcanoes in the Andean Central Volcanic Zone of Peru reveals previously undocumented surface deformation that is accompanied by seismic activity. Our survey utilizes SAR data spanning from 1995 to the present from the ERS-1, ERS-2, and Envisat satellites, as well as selected data from the TerraSAR-X satellite. We find that earthquakes and earthquake swarms near Sabancaya volcano (15.78S, 71.85W) in late 2002, February 2013, and July 2013 have been accompanied by surface deformation. InSAR modeling suggests that faulting from the observed seismic moment can account for nearly all of the observed deformation and thus we have not yet found clear evidence for recent magma intrusion. All of the deformation episodes between 2002 and 2013 are spatially distinct from the inflation seen near Sabancaya from 1992 to 1997.

In addition to the activity at Sabancaya, we also observe deformation in the region between Ticsani (16.755S, 70.595W) and Tutupaca (17.025S, 70.358W) volcanoes. An earthquake swarm in 2005 produced surface deformation centered northwest of the volcano and was accompanied by north-south elongated subsidence to the southeast. We investigate a possible relationship between the seismicity and the subsidence and find that the swarm generates a stress field which may encourage the opening of fractures oriented parallel to both the elongation of the subsidence signal and the trend of regional faults. We hypothesize that the Ticsani swarm triggered the

subsidence to the southeast by allowing migration of hydrological fluids through subsurface cracks.

A noteworthy null result of our InSAR survey is the lack of deformation associated with magmatic activity. We find no deformation at Ubinas volcano (16.355S, 70.903W), one of the most active volcanoes in Peru, even during its 2006 eruption. The lack of magmatic deformation suggests that magma reservoirs at Peruvian volcanoes do not experience significant reservoir pressurization.

5.1 INTRODUCTION

The Andean Central Volcanic Zone (CVZ) between 15°S and 28°S contains 69 active volcanoes in parts of Peru, Bolivia, Chile, and Argentina. The Holocene volcanic arc in Peru contains 16 active volcanoes and comprises the northernmost section of the CVZ between 15°S and 18°S (Table 5.1). The CVZ abruptly ends north of 15°S due to the Peruvian flat slab subduction between 3°S and 15°S, where active volcanism has been absent for the last 3-4 My (Kay et al. 2005). In this study, we focus our InSAR survey only on the Peruvian section of the CVZ (Figure 5.1), as other portions have been studied previously (Henderson et al. 2013; Pritchard et al. 2014).

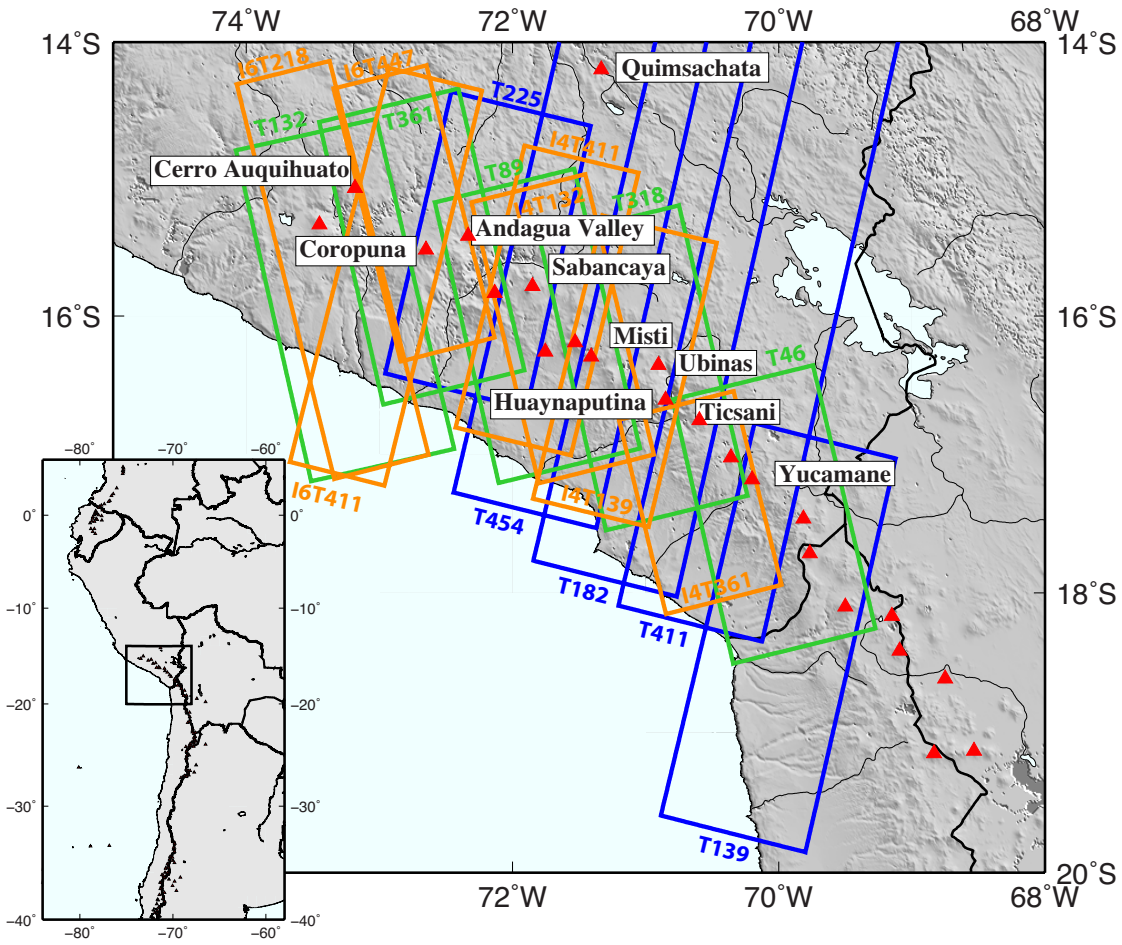

Figure 5.1 Map of southern Peru showing satellite tracks of SAR data coverage. Blue rectangles indicate ERS and Envisat Beam 2 descending tracks, green rectangles show ERS and Envisat Beam 2 ascending tracks, and orange rectangles show Envisat Beams 4 and 6 descending and ascending tracks. Red triangles show the locations of Holocene volcanoes from the Smithsonian database.

The 16 Holocene volcanoes of Peru are predominantly andesitic in composition, though compositions vary from rhyolite to basaltic andesite (see Table 5.1 and references therein). The compositions of the Peruvian volcanoes do not differ significantly from neighboring CVZ volcanoes in Chile, Bolivia, and Argentina (Smithsonian Institution 2014). Of the nine volcanoes whose last eruptions are known, seven erupted sometime within the past 600 years and three within the past century (Sabancaya, El Misti, and Ubinas; Smithsonian Institution 2014). The largest

historical eruption in South America was the VEI 6 eruption of Huaynaputina volcano in the year 1600 (De Silva and Zielinski 1998; Thouret et al. 1999). In the rest of the CVZ, five volcanoes (Guallatiri, Isluga, Irruputuncu, San Pedro, and Lascar) erupted within the past century (Smithsonian Institution 2014) but the total number of Holocene volcanoes in that region is 53, more than three times the number in Peru. The high occurrence of eruptions in Peru relative to the rest of the CVZ provides motivation for this InSAR survey. We investigate whether this difference in eruptive activity is accompanied by a difference in deformation style. We then consider what our observations can reveal regarding volcanic system characteristics and magma storage depths in the crust.

Previous InSAR surveys covering Peru have been carried out, but all end in 2002 or earlier (Pritchard and Simons 2002; Pritchard 2003; Pritchard and Simons 2004) or begin after 2007 and end in 2011 (Morales Rivera and Amelung 2013). The earlier studies document one deforming volcano in Peru: Hualca Hualca volcano, a late Pliocene to early Pleistocene stratovolcano just north of the younger Sabancaya and Ampato stratovolcanoes in the same complex (Smithsonian Institution 2014). Hualca Hualca was found to be uplifting at a rate of about 2 cm/year in the satellite line-of-sight (LOS), but this uplift appears to have ended in 1997 (Pritchard and Simons 2004). The later study of Morales Rivera and Amelung (2013) uses L-band ALOS data and finds a region 7 km SE of Cerro Auquihuato that has been uplifting since at least 2007 and was ongoing as of the last data acquisition in 2011.

InSAR has also detected deformation related to an earthquake swarm near Ticsani volcano in late 2005 (Holtkamp et al. 2011). We will further explore the nature and causes of the deformation episodes related to this swarm.

Table 5.1 Holocene volcanoes in Peru from north to south. Information is taken from the Smithsonian Institution Global Volcanism Program unless otherwise noted.
[1]Carlier and Carlotto 1990; [2]Smithsonian Institution; [3]Venturelli et al. 1978 ; [4]Sorensen and Holm 2008 ; [5]Delacour et al. 2007; [6]Gerbe and Thouret 2004; [7]Thouret et al. 2001; [8]Rivera et al. 2014; [9]De Silva and Zielinski 1998; [10]Thouret et al. 1999; [11]Byrdina et al. 2013; [12]Rivera and Mariño 2004

	Volcano name	Volcano type	Last eruption	Lat	Lon	Composition of most recent eruption
1	Quimsachata	Lava dome	4450 BCE	-14.2	-71.33	Rhyolite[1]
2	Cerro Auquihuato	Cinder cone	Unknown	-15.07	-73.18	No Data
3	Sara Sara	Stratovolcano	Unknown	-15.33	-73.45	Andesite / Basaltic Andesite[2]
4	Coropuna	Stratovolcano	Unknown	-15.52	-72.65	Andesite[3]
5	Andahua-Orcopampa	Cinder cones	1490 CE	-15.42	-72.33	Basaltic trachyandesite / Trachyandesite / Trachyte[4,5]
6	Huambo	Volcanic field	700 BCE	-15.83	-72.13	Andesite / Basaltic andesite[5]
7	Sabancaya	Stratovolcano	2003 CE	-15.78	-71.85	Dacite / Andesite[6]
8	Nevado Chachani	Stratovolcano	Unknown	-16.191	-71.53	Andesite / Basaltic Andesite[2]
9	Cerro Nicholson	Cinder cone	Unknown	-16.258	-71.753	Basalt[5]
10	El Misti	Stratovolcano	1985 CE	-16.294	-71.409	Rhyolite / Dacite / Andesite[7]
11	Ubinas	Stratovolcano	2013 CE	-16.355	-70.903	Dacite / Andesite[8]
12	Huaynaputina	Stratovolcano	1600 CE	-16.608	-70.85	Dacite[9,10]
13	Ticsani	Lava domes	1800 CE	-16.755	-70.595	Dacite / Andesite[11]
14	Tutupaca	Stratovolcano	Unknown	-17.025	-70.358	Andesite / Basaltic Andesite[2]
15	Yucamane	Stratovolcano	1902 CE	-17.18	-70.2	Andesite / Basaltic Andesite[12]
16	Nevados Casiri	Stratovolcano	Unknown	-17.47	-69.813	Trachyte / Trachyandesite[2]

5.2 METHODS

We use all available SAR data from the European Space Agency's (ESA) ERS-1, ERS-2, and Envisat satellites between the years 1995 to 2011. Due to the recent earthquake activity at Sabancaya volcano, we also use selected data from the German Aerospace Center's (DLR) TerraSAR-X satellite between January 2012 and January 2014 to image deformation that spans the time period of the increase in seismicity. We process data from the satellite tracks listed in Table 5.1 and displayed in Figure

5.1. SAR data from the Envisat and ERS satellites are C-band (5.6 cm wavelength), while data from TerraSAR-X are X-band (3.1 cm wavelength).

Table 5.2 InSAR data used in this study. D=descending orbit; A=ascending orbit. [1]Orbit number, in TerraSAR-X nomenclature

Satellite	Swath	Track	Orbit	Timespan	Volcanoes
ERS	N/A	225	D	1995-2003	Sabancaya, Coropuna, Andagua Valley
ERS	N/A	454	D	1995-2003	Sabancya, Misti, Cerro Nicholson
ERS	N/A	182	D	1995-2003	Misti, Ubinas, Huaynaputina, Ticsani
ERS	N/A	411	D	1995-2010	Ticsani
ERS	N/A	132	A	1996-2003	Sara Sara
ERS	N/A	318	A	2004-2006	Ticsani
Envisat	2	225	D	2002-2010	Sabancaya, Coropuna, Andagua Valley
Envisat	2	454	D	2002-2010	Sabancaya, Misti
Envisat	2	182	D	2002-2009	Misti, Ubinas, Huaynaputina, Ticsani
Envisat	2	411	D	2002-2010	Ticsani
Envisat	2	139	D	2002-2006	Taapaca, Tacora, Nevados Casiri
Envisat	2	361	A	2005-2006	Coropuna, Andagua Valley?
Envisat	2	89	A	2004-2006	Sabancaya, Huambo, Cerro Nicholson, Misti
Envisat	2	318	A	2004-2010	Misti, Ubinas, Huaynaputina, Ticsani, Tutupaca
Envisat	2	46	A	2005-2010	Taapaca, Tacora, Nevados Casiri, Yucamane
Envisat	4	411	D	2004-2006	Sabancaya
Envisat	4	139	D	2004-2010	Misti, Ubinas, Huaynaputina
Envisat	4	132	A	2004-2006	Sabancaya, Misti
Envisat	4	361	A	2004-2010	Ubinas, Huaynaputina, Ticsani, Tutupaca, Yucamane
Envisat	6	411	D	2005-2007	Coropuna
Envisat	6	218	A	2005	Sara Sara
Envisat	6	447	A	2005	Coropuna, Andagua Valley
TSX Stripmap	12	43[1]	A	2012-2014	Sabancaya

Interferograms are processed using the ROI_PAC software (Rosen et al. 2004). Modeling of the observed deformation at Sabancaya and Ticsani volcanoes is performed using the Neighborhood Algorithm (Sambridge 1999) to invert for an Okada dislocation of a fault plane (Okada 1992). Since little is known about the subsurface material properties at these volcanoes, we assume a homogeneous elastic half-space in the modeling. Specifically, we use a Poisson's ratio of 0.25 and a shear modulus of 20 GPa, typical values for shallow continental crust in volcanic regions (Trasatti et al., 2005). Each inversion solves for the location, depth, length, width, strike, dip, rake, and slip of the fault plane as well as a static offset and bilinear ramp

to account for artifacts of the InSAR processing, a standard procedure in InSAR modeling (e.g., Pritchard et al. 2002; Salichon et al. 2004).

Earthquake locations and focal mechanisms at Sabancaya volcano from 22 February to 31 July 2013 were calculated using data from a local seismic network. The network consists of three permanent stations and six temporary stations (see Figure 5.4 for locations) operated by the Instituto Geofísico del Perú (IGP). Seismic data analysis was carried out by the IGP.

5.3 RESULTS AND DISCUSSION

We find two volcanic regions that have experienced deformation during the time period of our study: Sabancaya volcano and Ticsani volcano. We document a null result at Ubinas volcano, even during its recent eruption.

Sabancaya volcano (-71.85W, -15.78S) is a dacite to andesite stratovolcano with frequent small eruptions in the past few decades (Gerbe and Thouret 2004; Smithsonian Institution 2014). It is the youngest of three edifices in a volcanic complex that includes Hualca Hualca to the north and Ampato to the south (Figure 5.3). Shallow crustal earthquakes in the region around Sabancaya are historically infrequent, however since early 2013 seismicity has greatly increased – the USGS catalog reports 9 earthquakes in 2013 within 50 km of Sabancaya and with depths less than 30 km, while only 7 earthquakes total were reported between 1973 and 2012 (Figure 5.2). We find that the seismicity at Sabancaya causes surface displacements that are observed by InSAR. In the following sections, we describe deformation episodes related to the seismicity.

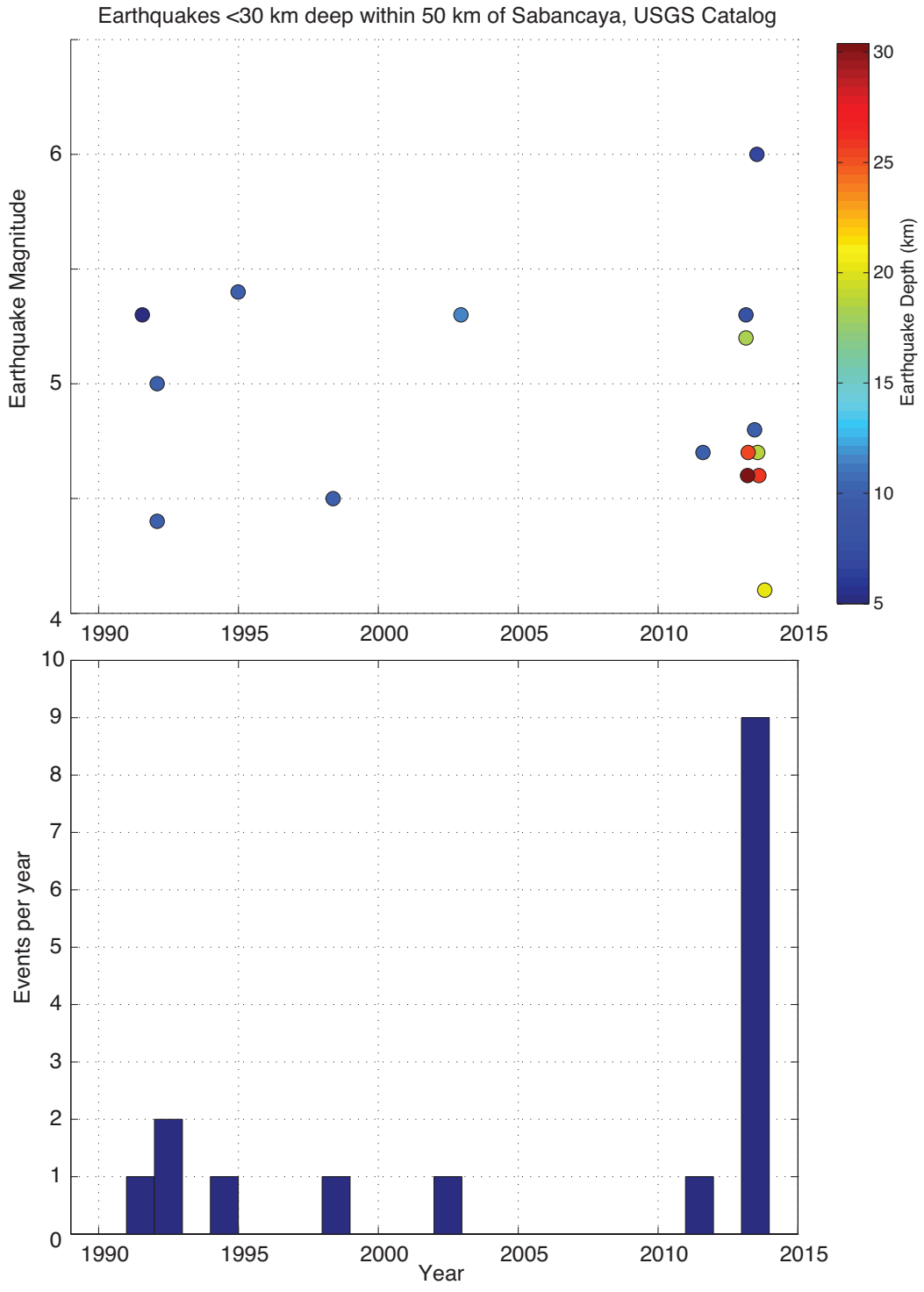

Figure 5.2 All earthquakes in the USGS PDE Catalog located within 50 km of Sabancaya volcano with depths less than 30 km. (Top) Plot showing earthquake magnitude vs. time, with the color of the circle corresponding to the earthquake depth. (Bottom) Histogram of the number of earthquakes per year. Note the dramatic increase in seismicity in 2013.

5.3.1 Sabancaya: Late 2002

An Envisat interferogram spanning 6 December 2002 to 12 September 2003 shows a region of subsidence about 20 km NW of the summit of Sabancaya with a maximum displacement of about 5 cm in the satellite line-of-sight (LOS) (Figure 5.3a). This lobe of subsidence is located just south of the Solarpampa fault, an east striking normal fault 14 km in length with a dip of 65° (Macharé et al. 2003). The deformation is likely related to a swarm of earthquakes that occurred on this fault on 13 December 2002, the largest of which was a Mw 5.3. InSAR modeling results give a cumulative moment magnitude of 5.8 and a depth of 12.2 km for this earthquake swarm (Table 5.3, Figure 5.5). The focal mechanism and depth derived from InSAR are similar to that of the Global CMT catalog, but the dip is significantly steeper - 68° from InSAR compared to 46° from Global CMT. The dip from InSAR modeling more closely agrees with field measurements of the Solarpampa fault, which indicate a dip of 65° (Macharé et al. 2003). The magnitude from InSAR modeling (Mw 5.8) is larger than the CMT magnitude (Mw 5.3); this can partially be reconciled by the fact that the there were three additional Mw > 4 earthquakes that occurred on 13 December 2002 in the same region with depths of 33 km (USGS catalog). However, the sum of the seismic moments from all catalogued earthquakes in the swarm does not add up to Mw 5.8. We conclude that either the InSAR model provides an unreliable magnitude due to noise in the interferogram, or additional slip may have occurred aseismically.

Motion across the Solarpampa fault is also seen in at least 5 interferograms, including one spanning 25 December 2002 to 18 April 2007 seen in Figure 5.3b. This interferogram shows LOS uplift of 4 cm in the region north of the fault, consistent

with uplift of the footwall of this normal fault. We suggest that this displacement may indicate slow slip or creep across the Solarpampa fault.

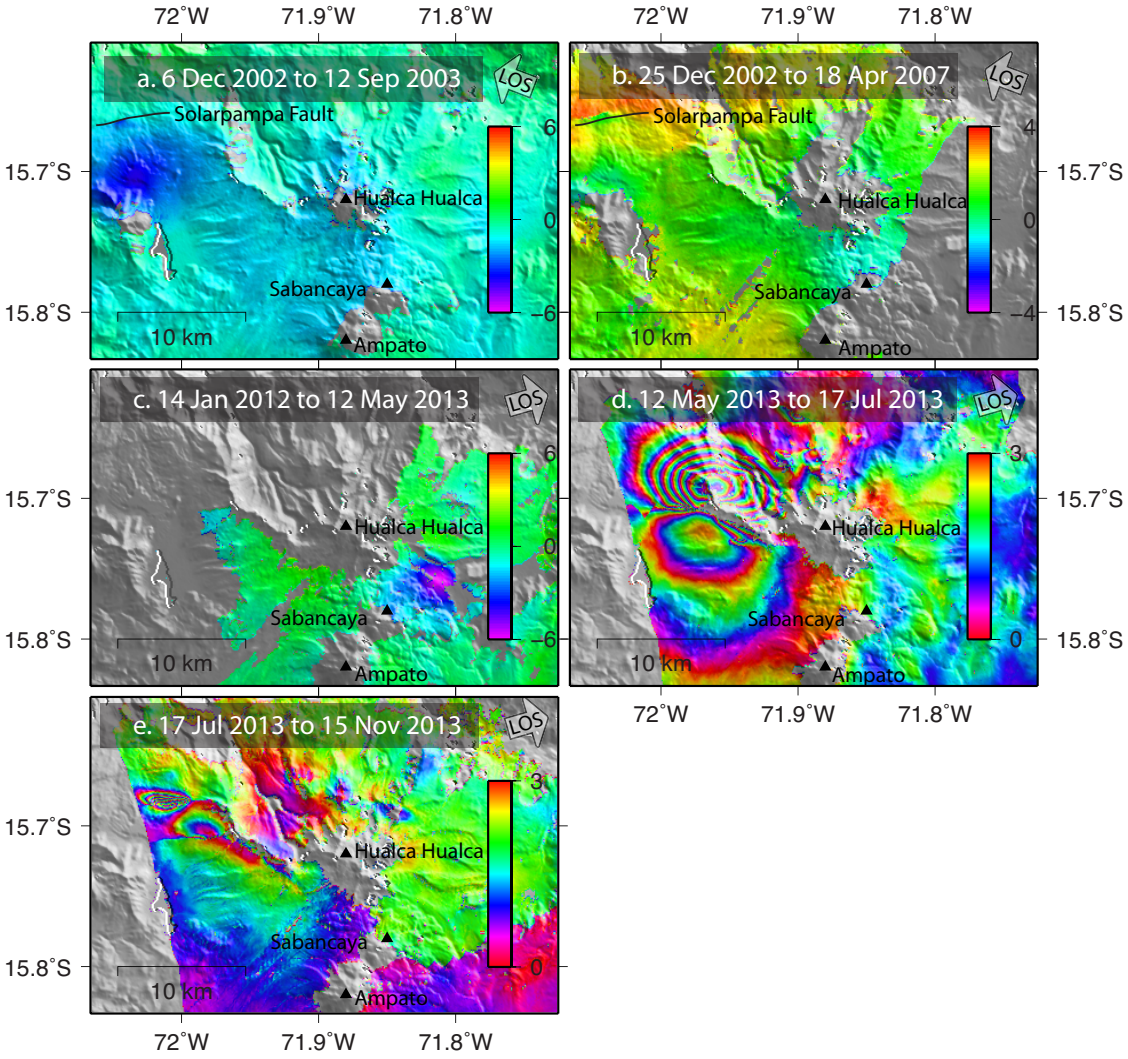

Figure 5.3 Interferograms showing line-of-sight deformation (cm) at Sabancaya volcano between 2002 and 2013. a) Unwrapped ERS interferogram from track 454 showing subsidence related to the Mw 5.3 earthquake on 13 December 2002; b) Unwrapped Envisat interferogram from track 225 beam 2 showing possible creep across the Solarpampa fault; c) unwrapped TerraSAR-X interferogram showing deformation related to the earthquake swarm in late February 2013; d) wrapped TerraSAR-X interferogram showing deformation related to the Mw 5.9 earthquake on 17 July 2013; e) wrapped TerraSAR-X interferogram showing deformation related to aftershock activity following the 17 July earthquake.

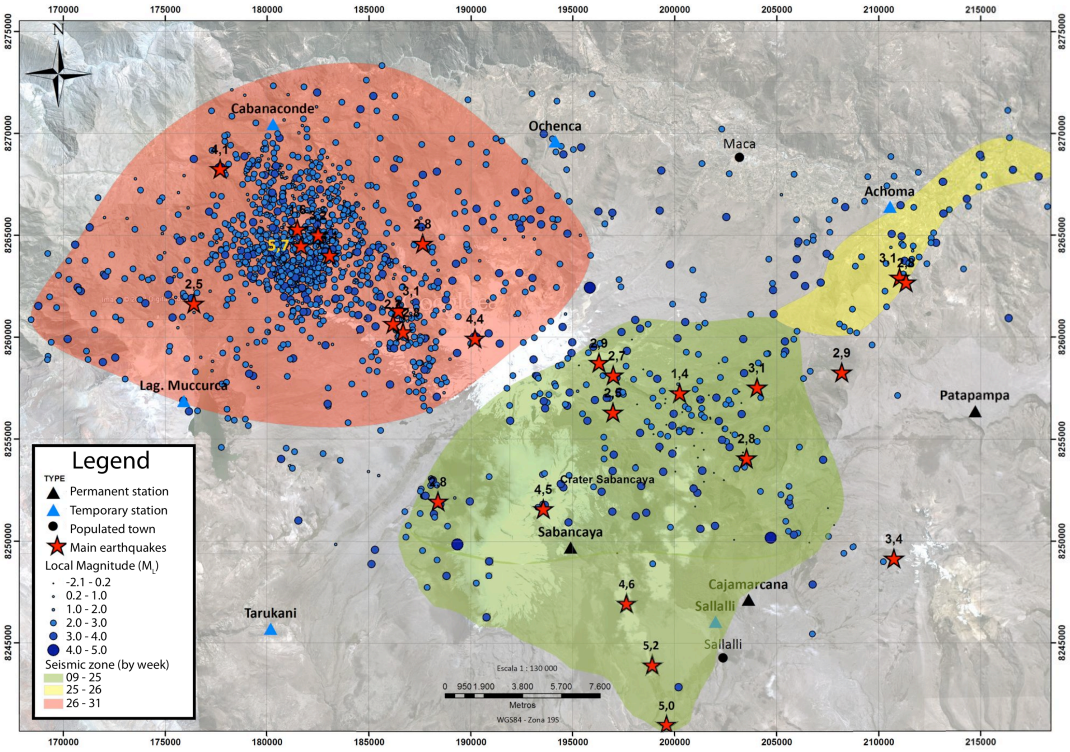

Figure 5.4 2013 seismicity map near Sabancaya volcano with locations calculated using a local network. Colored regions indicate temporal migration of seismicity from the south (green) to the northeast (yellow) to the northwest (red). Map provided by Orlando Macedo at the Instituto Geofísico del Perú (IGP)

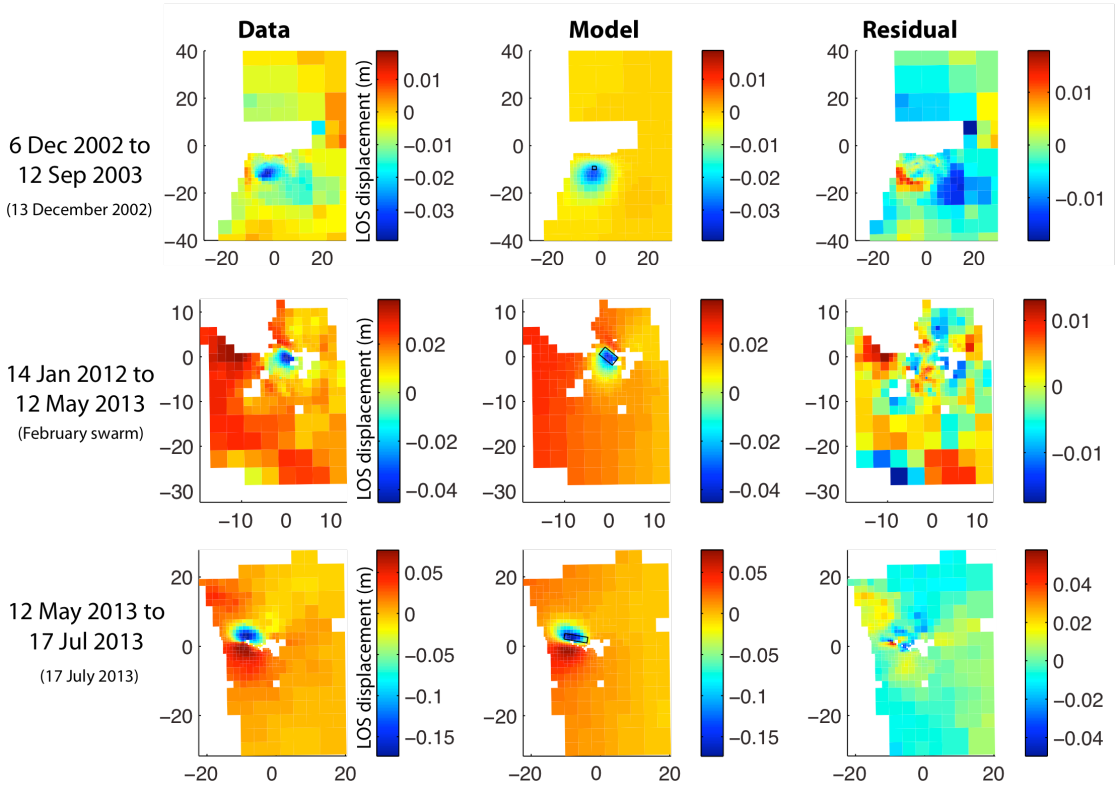

Figure 5.5 Sabancaya earthquake modeling results for (top) the Mw 5.3 13 December 2002 earthquake, (middle) the February 2013 earthquake swarm, and (bottom) the Mw 5.9 17 July 2013 earthquake.

5.3.2 Sabancaya: Early 2013

An earthquake swarm occurred near Sabancaya in late February 2013. The largest events in the swarm occurred on 22-23 February 2013 consisting of three volcano-tectonic (VT) earthquakes on 22 February with local magnitudes 4.6, 5.2, and 5.0 and one VT earthquake on 23 February with local magnitude 4.5 (Figure 5.4). These four earthquakes were all shallow, with depths less than 8 km. A TerraSAR-X interferogram that spans 14 January 2012 to 12 May 2013 shows a region of subsidence of 6 cm maximum LOS in the region of the swarm (Figure 5.3c), about 5 km NE of the summit of Sabancaya. Modeling of this interferogram gives a cumulative moment magnitude of Mw 5.5 and a depth of 4.1 km (Figure 5.5, Table

5.3). Focal mechanisms derived from the InSAR modeling are similar to both the Global CMT focal mechanism and focal mechanisms derived from the local Peruvian seismic network (Figure 5.6).

From 22 February to 16 June 2013, the seismicity was predominantly located to the NE and SE of Sabancaya (Figure 5.4, green region). Focal mechanisms for earthquakes during this time period (including the late February swarm earthquakes) show that the earthquakes mainly occurred on N-S striking thrust faults. From 17 to 30 June 2013, the earthquakes were situated more toward the NE, in a zone known as the Sepina lineament zone (Figure 5.4, yellow region). The focal mechanisms of these earthquakes also show reverse faulting but with predominantly NW-SE orientations.

5.3.3 Sabancaya: Mid 2013

On 17 July 2013, a Mw 5.9 earthquake occurred at 7 km depth about 15 km NW of Sabancaya (Figure 5.4). A TerraSAR-X interferogram spanning 12 May 2013 to 17 July 2013 shows a large lobe of subsidence of 16 cm LOS and a lobe of uplift of 6 cm LOS (Figure 5.3d). An interferogram spanning 17 July 2013 to 15 November 2013 shows at least two distinct pulses of deformation in the same region as the 17 July 2013 earthquake, presumably related to aftershock activity (Figure 5.3e). Modeling of the 12 May to 17 July 2013 interferogram gives a moment magnitude of Mw 5.8 and a depth of 3.5 km (Table 5.3). In this case, the InSAR focal mechanism is consistent with the focal mechanism calculated from the local seismic network (Figure 5.6). No deformation is observed at Sabancaya in a TerraSAR-X interferogram that spans 15 November 2013 to 20 January 2014.

		InSAR	GCMT	Local
6 Dec 2002 to 12 Sep 2003 (13 December 2002)	**Depth (km)**	12.2	15.0	N/A
	Mw	5.8	5.3	N/A
	Focal Mechanism		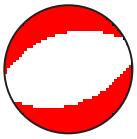	N/A
14 Jan 2012 to 12 May 2013 (February swarm)	**Depth (km)**	4.1	27.5, 20.4, 15.9, N/A	5, 8, 7, 5
	Mw	5.5	5.0, 5.3, 5.4, N/A	4.7, 5.2, 4.9, 4.6
	Focal Mechanism		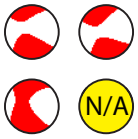	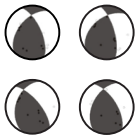
12 May 2013 to 17 Jul 2013 (17 July 2013)	**Depth (km)**	3.5	12	8
	Mw	5.8	6.0	5.9
	Focal Mechanism		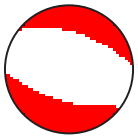	

Figure 5.6 Comparison of depths, magnitudes, and focal mechanisms for the three Sabancaya earthquake sequences calculated by InSAR modeling, the Global CMT, and local seismic networks. InSAR modeling for the February swarm calculates one solution for all swarm events since the interferogram spans the duration of the swarm.

From 1 to 31 July 2013, seismicity migrated toward the NW (Figure 5.4, red region), and focal mechanisms show normal faulting with approximately E-W orientations.

Table 5.3 Sabancaya modeling results

Parameter	13 Dec 2002 earthquake	Feb 2013 swarm	17 Jul 2013 earthquake
Mw	5.8	5.5	5.8
Length	1.7 km	3.8 km	6.7 km
Width	4.0 km	6.0 km	3.5 km
Depth	12.2 km	4.1 km	3.5 km
Strike	90	130	280
Dip	68°	69°	62°
Rake	125	59	58
Slip	2.8 m	0.3 m	0.9 m

In summary, we find that all deformation near Sabancaya observed by InSAR is related to earthquakes and faulting. The deformation episodes that occurred in late 2002, February 2013, and July 2013 are all clearly related to earthquake swarms that were recorded seismically. InSAR modeling shows that these deformation episodes can be fully accounted for by faulting; thus we find no clear evidence for magmatic activity or increased eruptive hazard at Sabancaya. Rather, we conclude that the deformation is purely tectonic, resulting predominantly from fault slip on extensional structures. This conclusion is consistent with previous field studies that show that recent and active deformation in the region results from normal faulting on several faults whose kinematics show N-S striking extension (Sebrier et al. 1985; Macharé et al. 2003).

5.3.4 Ticsani

We observe two deformation episodes near Ticsani volcano in late 2005 that were previously documented by Holtkamp et al. (2011) and Gonzalez et al. (2006). Using ERS data from track 318 and Envisat data from tracks 411 beam 2, 318 beam 2, and

361 beam 4, we determine that these two episodes must have occurred sometime between 29 June 2005 and 22 November 2005. The first deformation episode is centered about 7 km NW of Ticsani volcano and consists of a large lobe of subsidence with ~8 cm displacement in the line-of-sight (LOS) adjacent to a smaller lobe of uplift with ~6 cm LOS displacement. The second deformation episode is centered about 17 km SE of Ticsani and consists of a N-S oriented elliptical subsidence pattern with ~6 cm LOS displacement (Figure 5.7). The two episodes appear to have occurred simultaneously – all interferograms that contain the first episode also contain the second episode and vice versa.

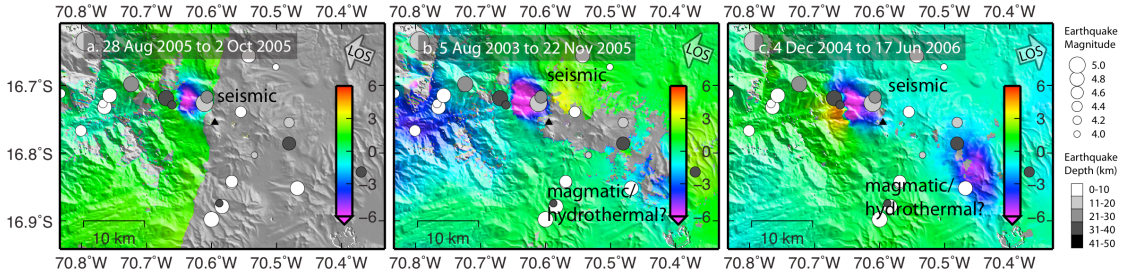

Figure 5.7 Ticsani interferograms showing LOS deformation (cm) associated with the earthquake swarm in late 2005. Panels (b) and (c) also show the subsidence to the southeast. White circles represent all earthquakes in the USGS PDE catalog with depths less than 50 km that occurred in 2005 (all happen to have occurred between 25 July and 20 October), with the size of the circle corresponding to magnitude and the shading corresponding to depth.

The first episode is most likely related to an earthquake swarm that occurred near Ticsani in late 2005 (USGS PDE, Holtkamp et al. 2011). There were 31 earthquakes within 50 km of Ticsani with depths less than 50 km in 2005 in the USGS PDE catalog, and all of these occurred between 25 July and 20 October (Figure 5.7). The magnitudes range from 4.0 to 5.3, and the cumulative moment magnitude of all 31 earthquakes is Mw 5.7. Modeling by Holtkamp et al. (2011) showed that this deformation episode could be explained by a Mw 5.7 normal faulting event with a

strike of 339° and a dip of 62°. Therefore, the InSAR-observed deformation can be fully explained by the seismic moment from the earthquake swarm and there is no evidence for aseismic fault slip.

The second deformation episode does not resemble a faulting event due to its symmetrical shape and the fact that only subsidence is observed with no uplift. However, the temporal overlap of the two episodes suggests a possible relationship between them. We hypothesize that the earthquake swarm (first episode) imposed stresses on subsurface faults and cracks in the vicinity of the observed subsidence (second episode) and allowed previously trapped fluids to escape the hydrothermal system. A similar phenomenon has been observed at volcanoes in southern Chile following the 2010 Maule earthquake (Pritchard et al. 2013).

In order to test this hypothesis, we calculate the static normal stress change on optimally oriented extensional structures imposed by the earthquake swarm at 5 km depth. We use the model of Holtkamp et al. (2011) as our input and calculate the orientation and magnitude of static stress change in the region of the observed subsidence. We find that the static normal stress change is oriented predominantly in the NW-SE direction, which is parallel to the semi-major axis of the elliptical subsidence pattern and to the mapped faults in the area (Figure 5.8). This implies that the seismic swarm caused a region of SW-NE tension in the subsidence region. This calculation supports the hypothesis that pre-existing cracks were opened by the seismic swarm, allowing hydrothermal fluids to flow and resulting in ground subsidence.

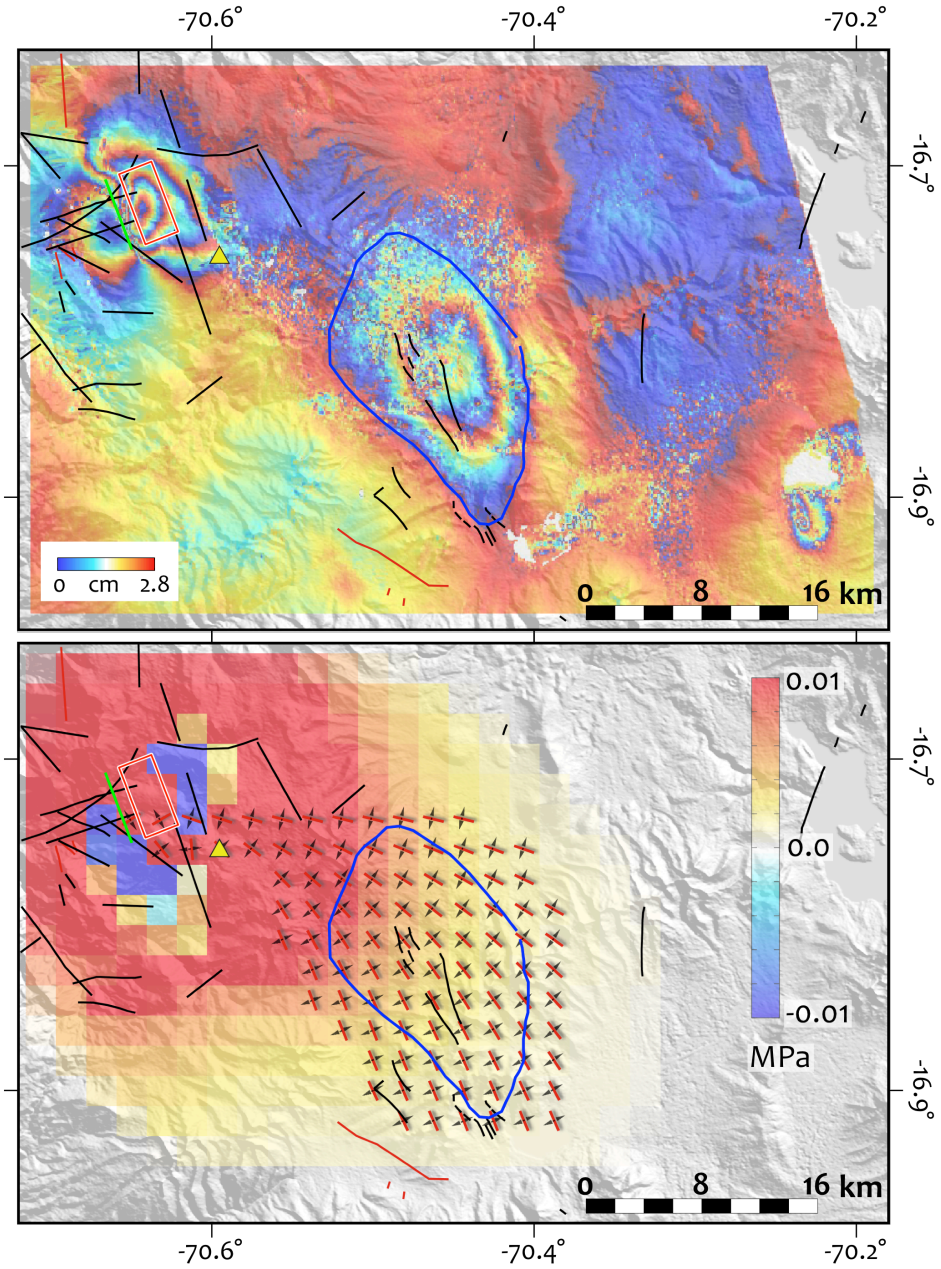

Figure 5.8 (Top) Wrapped Envisat interferogram (track 361 beam 4, 4 December 2004 to 17 June 2006) showing deformation related to the Ticsani earthquake swarm. Red lines represent normal faults and black lines represent faults with undetermined kinematics (INGEMMET 1975; Lavallée et al. 2009). (Bottom) Static normal stress change (MPa) on optimally oriented extensional structures imposed by the earthquake swarm at 5 km depth. Red lines show orientation of extensional structures and black arrows show direction of extension.

However, there are a couple of observations that contradict this hypothesis. First, the magnitude of the static stress change is less than 0.01 MPa. In Chile, the volcanoes that subsided due to the Maule earthquake experienced static stress changes that were ~10^2 times greater in magnitude than what we observe at Ticsani (Pritchard et al. 2013). Whether such low static stress changes are sufficient to trigger subsidence is questionable; however dynamic stress changes related to the passage of transient seismic waves could also be significant. Second, the location of the subsidence to the southeast of Ticsani is not in agreement with the known location of the hydrothermal system, which extends westward from the summit of Ticsani (Byrdina et al. 2013). There are no known springs or fumaroles in the region of subsidence; the closest springs are located just west of Toro Bravo lake, which is 5 km SE of Ticsani and 12 km NW of the center of subsidence.

We offer alternative hypotheses to reconcile these discrepancies. One possibility is that the subsidence is the direct expression of the earthquake swarm. The fact that no uplift is observed requires the dip of the normal fault plane to be extremely low, no more than about 30°. Even with a dip of 30°, the best-fitting model for an Okada dislocation provides a poor fit to the data (Figure 5.9). We therefore consider this scenario to be improbable. Another possibility is that the subsidence was indeed related to subsurface fluid flow, but not necessarily related to the hydrothermal system of Ticsani. The triggered response of surface streamflow and groundwater levels due to earthquakes is well documented in the literature and is usually attributed to enhanced hydraulic conductivity, increased fluid pressure, or release of water from

storage (e.g., Muir-Woods and King 1993; Montgomery and Manga 2003; Brodsky et al. 2003; Manga et al. 2003). We suggest that any combination of these processes was responsible for the subsidence at Ticsani.

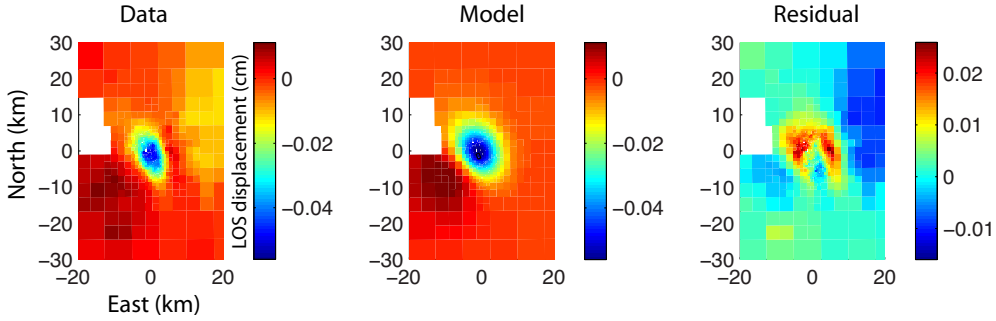

Figure 5.9 Resampled interferogram (data, 4 December 2004 to 17 June 2006), modeled interferogram (model), and residual assuming an Okada dislocation with a 30° dip for the subsidence pattern SE of Ticsani volcano. We dismiss the possibility that the subsidence is the surface expression of an earthquake because of the low dip required by the model and the poor fit to the data.

5.3.5 Null results

Two of the 16 volcanoes had eruptions during the timespan of our study: Sabancaya and Ubinas. Though we do document deformation episodes at Sabancaya (section 5.3.1 to 5.3.3), we find no deformation associated with its minor ash eruptions in 2000 and 2003. However, it has been suggested that the broad 1992-1997 uplift centered on Hualca Hualca was related to the 1990-1998 explosive activity at Sabancaya (Pritchard and Simons 2002; Pritchard and Simons 2004a; Gerbe and Thouret 2004).

Ubinas volcano is historically the most active volcano in Peru, with >20 degassing and ashfall episodes since AD 1550 (Thouret et al. 2005). The most recent eruption has been ongoing since at least September 2013 and consists of phreatic explosions, gas-and-ash emissions, and lava flows (Smithsonian Institution). Prior to this most recent eruptive episode, Ubinas underwent an andesitic VEI 2 eruption that

lasted from 27 March 2006 to December 2009 (Rivera et al. 2014). High-temperature thermal hotspots related to the eruptive activity were observed with satellite data from both the MODIS and ASTER instruments in 2006 (Jay et al. 2013). Petrological examination of the 2006-2009 erupted products suggest that the eruption was triggered by the ascent of a batch of hot mafic magma from a deep chamber at 16-19 km depth to a shallow chamber at 4-8 km depth (Rivera et al. 2014).

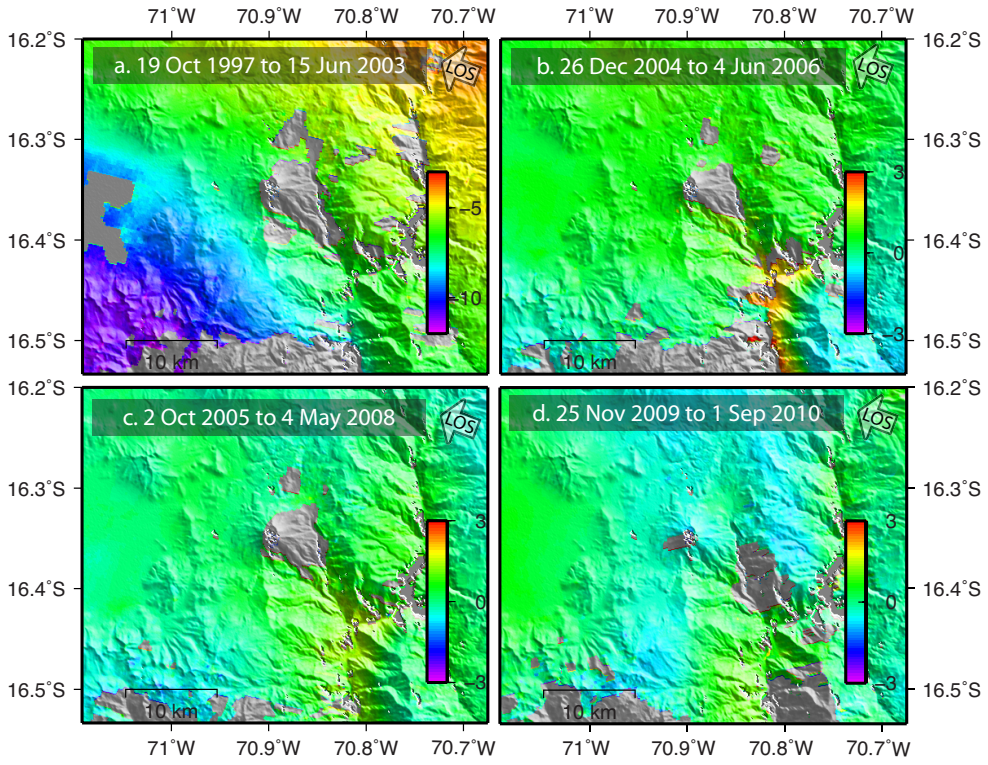

Figure 5.10 Unwrapped interferograms over Ubinas volcano showing LOS deformation (cm). a) ERS interferogram (track 182, 19 October 1997 to 15 June 2003) showing no deformation at Ubinas volcano prior to the 2006 eruption. The long wavelength SW-NE signal is related to deformation from the 23 June 2001 Mw 8.4 Peru earthquake. b) Envisat interferogram (track 182 beam 2, 26 December 2004 to 4 June 2006) showing no deformation in the 1+ year leading up to the eruption and during the first few months of the eruption which began on 27 March 2006. c) Envisat interferogram (track 182 beam 2, 2 October 2005 to 4 May 2008) showing no deformation at Ubinas volcano associated with the 2006-2009 eruptive period. d) Envisat interferogram (track 318 beam 2, 25 November 2009 to 1 September 2010) showing no deformation at Ubinas volcano following the 2006-2009 eruptive period.

We find no deformation at Ubinas volcano before, during, or after the 2006-2009 eruptive period (Figure 5.10). If the eruption was indeed triggered by a shallow

mafic intrusion as suggested by Rivera et al. (2014), the intrusion either 1) occurred before ERS observations began in 1995, 2) caused short-lived transient deformation that was elastically recovered before a second SAR observation occurred; 3) was so small that it did not produce significant ground deformation that could be detected by InSAR (perhaps due to small source volume changes and/or shallow source depths), or 4) did not produce deformation due to the open nature of the Ubinas volcanic system. In fact, open volcanic systems such as Popocatépetl and Colima in Mexico and Merapi in Indonesia do not show inflation prior to their frequent eruptions, presumably due to the fact that pressurization is limited by the open nature of their conduits (Chaussard et al. 2013). Ubinas appears to display a similar behavior – frequent small VEI 2-3 eruptions occur with a recurrence of four to seven eruptions per 100 years (Rivera et al. 2014), and continuous fumarolic activity is evidenced by a persistent satellite thermal hotspot in the summit crater (Jay et al. 2013).

We do not find deformation near Cerro Auquihuato that was documented by Morales Rivera and Amelung (2013), however our data coverage is sparse in that region.

5.3.6 Arc Comparison

Accounting for the 1992-1997 uplift at Hualca Hualca (Pritchard and Simons 2004) and the 2007-2011 uplift at Cerro Auquihuato (Morales Rivera and Amelung 2013), only two volcanoes in Peru show deformation that could potentially be magmatic compared to eight in the rest of the CVZ (Table 5.4; Henderson and Pritchard 2013; Pritchard et al. 2014). However, considering the total number of potentially active

volcanoes in Peru and the rest of the CVZ, the proportion of volcanoes that have demonstrated magmatic deformation is approximately equal throughout the CVZ (13-15%). On the other hand, 44% of the potentially active volcanoes in Peru have erupted in historical times, compared to only 15% in the rest of the CVZ.

Differences in magmatism and tectonics between the northern and southern CVZ have been suggested by previous studies. The onset of volcanism north of 17° S appears to have been more recent than in the south, as evidenced by the relative lack of older volcanic edifices in the north and possibly caused by the oblique subduction of the Nazca Ridge allowing the northward migration of volcanism (de Silva and Francis 1990). An extensional stress regime is highly developed in the northern CVZ, as evidenced by E-W trending recent and active normal faults (Sebrier et al. 1985). Though large silicic caldera systems are not as prevalent in the northern CVZ (de Silva and Francis 1990) as they are in the south (e.g., de Silva 1989; Kay and Coira 2009), a seismically-imaged low velocity zone associated with the presence of partial melt in the mid-crust is seen both in the north (Ma and Clayton 2014) and in the south (e.g., Zandt et al. 2003) with different spatial dimensions.

Extending the comparison to the south, we see that the proportion of volcanoes that have exhibited magmatic deformation is lower in the SVZ than in the CVZ, but the proportion of volcanoes that have recently erupted is about the same in the SVZ as in the Peruvian CVZ (Table 5.4; Smithsonian Institution 2014; Pritchard and Simons 2004b; Fournier et al. 2010; Pritchard et al. 2013). Recent eruptions within the past century in the SVZ are quite large (1932 Cerro Azul/Quizapu and 1991 Cerro Hudson

VEI 5; 2008 Chaitén and 2011 Cordón Caulle VEI 4) compared to the recent small VEI 1-3 eruptions at Sabancaya, El Misti, and Ubinas (Smithsonian Institution 2014).

Table 5.4 Comparison of volcanic activity between the CVZ of Peru, the CVZ of Chile and Bolivia, and the SVZ. [1]Smithsonian Institution 2014; [2]Henderson and Pritchard 2013; [3]Pritchard et al. 2014; [4]Pritchard and Simons 2004b; [5]Fournier et al. 2010; [6]Pavez et al. 2006; [7]Bathke et al. 2011

	No. of potentially active volcanoes[1]	No./proportion of known magmatically deforming volcanoes[2,3,4,5,6,7]	No./proportion of historically active volcanoes[1] (since 1500 CE)
CVZ - Peru	16	2 / 0.13	7 / 0.44
CVZ – Chile/Bolivia	53	8 / 0.15	8 / 0.15
SVZ	66	6 / 0.09	28 / 0.42

5.4 CONCLUSIONS

Our InSAR survey of volcanoes in Peru finds deformation related to earthquakes and earthquake swarms at Sabancaya and Ticsani, but no deformation that is clearly associated with magmatic activity. Although a greater proportion of volcanoes have erupted in the past 100 years in Peru than in the rest of the CVZ, the number of volcanoes that have deformed magmatically is not proportionally higher in Peru. On one hand, the 1600 eruption of Huaynaputina provides historical evidence that very large eruptions are indeed possible in this region. However, on the other hand, the low occurrence of magmatic deformation in Peru despite relatively frequent eruptions suggests that the magmatic plumbing systems beneath some of these volcanoes (Misti, Sabancaya, Ubinas) do not currently allow for the accumulation of large pressurizations.

REFERENCES

Bathke, H., Shirzaei, M., & Walter, T. R. (2011). Inflation and deflation at the steep-sided Llaima stratovolcano (Chile) detected by using InSAR. *Geophysical Research Letters*, *38*(10).

Brodsky, E. E., Roeloffs, E., Woodcock, D., Gall, I., & Manga, M. (2003). A mechanism for sustained groundwater pressure changes induced by distant earthquakes. *Journal of Geophysical Research*, *108*(B8), 1–10.

Byrdina, S., Ramos, D., Vandemeulebrouck, J., Masias, P., Revil, a., Finizola, a., … Macedo, O. (2013). Influence of the regional topography on the remote emplacement of hydrothermal systems with examples of Ticsani and Ubinas volcanoes, Southern Peru. *Earth and Planetary Science Letters*, *365*, 152–164.

Carlier, G., & Carlotto, V. (1990). Evidence for the origin of a shoshonitic suite by mixing of peraluminous and ultrapotassic magmas: the Oroscocha and Quimsachata quaternary volcanoes, Sicuani province, southern Peru. In *Symposium international "Géodynamique andine": résumés des communications* (pp. 325–328). ORSTOM.

Chaussard, E., Amelung, F., & Aoki, Y. (2013). Characterization of open and closed volcanic systems in Indonesia and Mexico using InSAR time series. *Journal of Geophysical Research: Solid Earth*, *118*(8), 3957–3969.

Delacour, A., Gerbe, M., & Thouret, J. (2007). Magma evolution of Quaternary minor volcanic centres in southern Peru, Central Andes. *Bulletin of Volcanology*, 69: 581–608.

De Silva, S. L. (1989). Altiplano-Puna volcanic complex of the central Andes. *Geology*, *17*, 1102–1106.

De Silva, S. L., & Francis, P. W. (1990). Potentially active volcanoes of Peru - Observations using Landsat Thematic Mapper and Space Shuttle imagery. *Bulletin of Volcanology*, *52*(4), 286–301.

De Silva, S. L., & Zielinski, G. (1998). Global influence of the AD 1600 eruption of Huaynaputina, Peru. *Nature*, *393*(June), 455–458.

Fournier, T. J., Pritchard, M. E., & Riddick, S. N. (2010). Duration, magnitude, and frequency of subaerial volcano deformation events: New results from Latin America using InSAR and a global synthesis. *Geochemistry Geophysics Geosystems*, *11*(1).

Gerbe, M.-C., & Thouret, J.-C. (2004). Role of magma mixing in the petrogenesis of tephra erupted during the 1990-98 explosive activity of Nevado Sabancaya, southern Peru. *Bulletin of Volcanology*, *66*(6), 541–561.

Gonzáles, K., Froger, J., Rivera, M., & Audin, L. (2006). Deformación co-sísmica producida por el sismo Mb=5.4 del 01 de Octubre de 2005 (Carumas-Moquegua), detectada por interferometría radar - InSAR. In *XIII Congreso Peruano de Geolgía* (Vol. 2005, pp. 488–489).

Henderson, S. T., & Pritchard, M. E. (2013). Decadal volcanic deformation in the Central Andes Volcanic Zone revealed by InSAR time series. *Geochemistry Geophysics Geosystems*, *14*(5).

Holtkamp, S. G., Pritchard, M. E., & Lohman, R. B. (2011). Earthquake swarms in South America. *Geophysical Journal International*, *187*(1), 128–146.

INGEMMET. (1975a). *Mapa Geológico del Cuadrángulo de Huaitire*. Retrieved from http://www.ingemmet.gob.pe/publicaciones/serie_a/mapas/34-v.jpg

INGEMMET. (1975b). *Mapa Geológico del Cuadrángulo de Omate*. Retrieved from http://www.ingemmet.gob.pe/publicaciones/serie_a/mapas/34-u.jpg

Jay, J. A., Pritchard, M. E., Aron, F., Delgado, F., Macedo, O., & Aguilar, V. (2013). Volcano-tectonic interactions at Sabancaya and other Peruvian volcanoes revealed by InSAR and seismicity. In *American Geophysical Union Fall Meeting* (p. V51E–2735). San Francisco, CA.

Jay, J. A., Welch, M., Pritchard, M. E., Mares, P. J., Mnich, M. E., Melkonian, A. K., … Clavero, J. (2013). Volcanic hotspots of the central and southern Andes as seen from space by ASTER and MODVOLC between the years 2000 and 2010. *Geological Society, London, Special Publications*, *380*(1), 161–185.

Kay, S., & Coira, B. (2009). Shallowing and steepening subduction zones, continental lithospheric loss, magmatism, and crustalflow under the Central Andean Altiplano-Puna Plateau. *Geological Society of America Memoirs*, *204*, 229–259.

Kay, S. M., Mpodozis, C., & Ramos, V. A. (2005). Andes. In R. C. Selley, L. R. M. Cocks, & I. R. B. T.-E. of G. Plimer (Eds.), *Encyclopedia of Geology* (pp. 118–131). Oxford: Elsevier.

Lavallée, Y., de Silva, S. L., Salas, G., & Byrnes, J. M. (2009). Structural control on volcanism at the Ubinas, Huaynaputina, and Ticsani Volcanic Group (UHTVG), southern Peru. *Journal of Volcanology and Geothermal Research*, *186*(3-4), 253–264.

Ma, Y., & Clayton, R. W. (2014). The crust and uppermost mantle structure of Southern Peru from ambient noise and earthquake surface wave analysis. *Earth and Planetary Science Letters*, *395*, 61–70.

Macharé, J., Fenton, C. H., Machette, M. N., Lavenu, A., Costa, C., & Dart, R. L. (2003). Database and Map of Quaternary Faults and Folds in Perú and its Offshore Region. *USGS Open-File Report 03-451*.

Manga, M. (2003). Response of streamflow to multiple earthquakes. *Geophysical Research Letters*, *30*(5), 1214.

Montgomery, D. R., & Manga, M. (2003). Streamflow and water well responses to earthquakes. *Science (New York, N.Y.)*, *300*(5628), 2047–9.

Morales Rivera, A. M., & Amelung, F. (2013). Volcano deformation and modeling in the Andean Volcanic Belt from InSAR time-series. In *American Geophysical Union Fall Meeting* (p. G31A–0958). San Francisco, CA.

Muir-Wood, R., & King, G. C. P. (1993). Hydrological signatures of earthquake strain. *Journal of Geophysical Research*, *98*(B12), 22035.

Okada, Y. (1992). Internal deformation due to shear and tensile faults in a half-space. *Bulletin of the Seismological Society of America*, *82*(2), 1018–1040.

Pavez, A., Remy, D., Bonvalot, S., & Diament, M. (2006). Insight into ground deformations at Lascar volcano (Chile) from SAR interferometry, photogrammetry and GPS data: Implications on volcano dynamics and future. *Remote Sensing of Environment*, *100*, 307–320.

Pritchard, M. E. (2003). *Recent crustal deformation in west- central South America*. California Institute of Technology.

Pritchard, M. E., Henderson, S. T., Jay, J. A., Soler, V., Krzesni, D. A., Button, N. E., … Clavero, J. (2014). Reconnaissance earthquake studies at nine volcanic areas of the central Andes with coincident satellite thermal and InSAR observations.

Pritchard, M. E., & Simons, M. (2002). A satellite geodetic survey of large-scale deformation of volcanic centres in the central Andes. *Nature*, *418*(6894), 167–71.

Pritchard, M., Simons, M., Rosen, P., Hensley, S., & Webb, F. (2002). Co-seismic slip from the 1995 July 30 Mw= 8.1 Antofagasta, Chile, earthquake as constrained by InSAR and GPS observations. *Geophysical Journal International*, *150*, 362–376.

Pritchard, M. E., & Simons, M. (2004a). An InSAR-based survey of volcanic deformation in the central Andes. *Geochemistry Geophysics Geosystems*, *5*(2), 1–42.

Pritchard, M. E., & Simons, M. (2004b). An InSAR-based survey of volcanic deformation in the southern Andes. *Geophysical Research Letters*, *31*(15), 1–4.

Rivera, M., & Mariño, J. (2004). Volcán Yucamane (Sur del Perú): Geología, Petrología y Evaluación Preliminar de las Amenazas Volcánicas. *Boletín de La Sociedad Geológica Del Perú*, *98*, 7–27.

Rivera, M., Thouret, J.-C., Samaniego, P., & Le Pennec, J.-L. (2014). The 2006–2009 activity of the Ubinas volcano (Peru): Petrology of the 2006 eruptive products and insights into genesis of andesite magmas, magma recharge and plumbing system. *Journal of Volcanology and Geothermal Research*, *270*, 122–141.

Rosen, P., Hensley, S., Peltzer, G., & Simons, M. (2004). Updated repeat orbit interferometry package released. *Eos Transactions AGU*, *85*(47).

Salichon, J., Lundgren, P., Delouis, B., & Giardini, D. (2004). Slip history of the 16 October 1999 Mw 7.1 Hector Mine earthquake (California) from the inversion of InSAR, GPS, and teleseismic data. *Bulletin of the Seismological Society of America*, *94*(6), 2015–2027.

Sambridge, M. (1999). Geophysical inversion with a neighbourhood algorithm-I. Searching a parameter space. *Geophysical Journal International*, *138*(2), 479–494.

Sebrier, M., Mercier, J. L., Megard, F., Laubacher, G., & Carey-Gailhardis, E. (1985). Quaternary normal and reverse faulting and the state of stress in the central Andes of south Peru. *Tectonics*, *4*(7), 739–780.

Silva, S. De, & Zielinski, G. (1998). Global influence of the AD 1600 eruption of Huaynaputina, Peru. *Nature*, *393*(June), 455–458.

Smithsonian Institution National Museum of Natural History Global Volcanism Program. (2014). Retrieved from http://www.volcano.si.edu

Sørensen, E., & Holm, P. (2008). Petrological inferences on the evolution of magmas erupted in the Andagua Valley, Peru (Central Volcanic Zone). *Journal of Volcanology and Geothermal Research*, *177*(2), 378–396.

Thouret, J., Davila, J., & Eissen, J. (1999). Largest explosive eruption in historical times in the Andes at Huaynaputina volcano, a.d. 1600, southern Peru. *Geology*.

Thouret, J., & Finizola, A. (2001). Geology of El Misti volcano near the city of Arequipa , Peru. *Geological Society of America Bulletin*, *113*, 1593–1610.

Trasatti, E., Giunchi, C., & Bonafede, M. (2005). Structural and rheological constraints on source depth and overpressure estimates at the Campi Flegrei caldera, Italy. *Journal of Volcanology and Geothermal Research*, *144*(1-4), 105–118.

Venturelli, G., Fragipane, M., Weibel, M., & Antiga, D. (1978). Trace element distribution in the cainozoic lavas of Nevado Coropuna and Andagua Valley, Central Andes of Southern Peru. *Bulletin of Volcanology*, *41*, 213–228.

Zandt, G., Leidig, M., Chmielowski, J., Baumont, D., & Yuan, X. (2003). Seismic Detection and Characterization of the Altiplano-Puna Magma Body, Central Andes. *Pure and Applied Geophysics*, *160*(3), 789–807.

APPENDIX A1

ASTER THERMAL HOTSPOT TEMPERATURES

A1.1 COMPLETE TABLE OF HOTSPOT TEMPERATURES, 2000-2010

Supplemental Table 1: A complete list of volcanoes examined with ASTER data. The list is organized by volcano from north to south following (where available) the volcano number (in the first column) from the Smithsonian Insitution database (Simkin and Siebert, 1994; Siebert & Simkin, 2002-). For volcanoes not in the database, we show the latitude and longitude from Gonzalez-Ferran (1995). The date of each cloud-free ASTER scene is listed in the second column followed by whether the image has a hotspot (marked with a Y), no hotspot (N), or a questionable hotspot (?), the approximate hottest temperature of the hotspot from the Product 8 Pixel Integrated Temperature, and the temperature of the hotspot relative to background as determined by a profile. An asterisk * next to the hotspot temperature signifies the scene is saturated. See text for discussion of the criteria used to determine if the image has a hotspot or a questionable hotspot. When an individual image has multiple hotspots, these are separated by a /.

Volcano SI # or Lat/Lon	Date of ASTER image	Hotspot?	Hottest Pixel (K)	Relative Temperature (K)
1) Coropuna				
1504-003	7/24/2002	N		
	3/1/2005	N		
	7/23/2005	N		
	2/16/2006	N		
	10/30/2006	N		
	1/18/2007	Y	269	6
	6/11/2007	N		
	8/7/2007	N		
	12/4/2007	N		
	7/31/2008	N		
2) Hualca Hualca				
-15.70S				
-71.88W				
	8/28/2003	N		
	7/29/2004	N		
	3/17/2005	N		
	4/27/2005	N		
	6/5/2005	N		
	6/14/2005	N		
	8/1/2005	N		
	8/24/2005	N		
	9/25/2005	N		
	10/20/2005	N		

	11/21/2005	N		
	3/4/2006	N		
	7/10/2006	N		
	10/7/2006	N		
	11/15/2006	N		
	2/19/2007	N		
	4/24/2007	N		
	5/19/2007	N		
	6/27/2007	N		
	7/13/2007	N		
	8/23/2007	N		
	9/15/2007	N		
	11/18/2007	N		
	3/9/2008	N		
	5/28/2008	N		
	6/13/2008	N		
	6/29/2008	N		
	8/16/2008	N		
	11/20/2008	N		
	1/23/2009	N		
	5/15/2009	N		
	5/31/2009	N		
	6/16/2009	N		
	7/2/2009	N		
	8/3/2009	N		
	8/19/2009	N		
	9/4/2009	N		
	10/6/2009	N		
	2/11/2010	N		
3) Sabancaya				
1504-006	8/28/2003	N		
	7/29/2004	Y	271	10
	3/17/2005	Y	276	11
	4/27/2005	Y	264	9
	5/20/2005	Y	274	14
	6/5/2005	Y	277	14
	6/14/2005	Y	273	13
	8/1/2005	Y	276	12
	8/24/2005	Y	274	15
	9/25/2005	Y	269	8
	10/20/2005	Y	271	6
	11/21/2005	Y	271	7
	3/4/2006	Y	272	12
	7/10/2006	Y	275	13
	10/7/2006	Y	274	10
	11/15/2006	Y	276	10
	2/19/2007	Y	274	16
	4/24/2007	Y	277	15
	5/19/2007	Y	274	17
	6/27/2007	Y	275	18
	7/13/2007	Y	269	10
	8/23/2007	Y	277	11
	9/15/2007	Y	273	8
	11/18/2007	Y	275	11

	1/21/2008	Y	269	8
	3/9/2008	Y	279	19
	5/28/2008	Y	272	12
	6/13/2008	Y	269	11
	6/29/2008	Y	274	14
	8/16/2008	Y	277	15
	9/17/2008	Y	273	13
	11/20/2008	Y	277	12
	1/23/2009	Y	277	18
	5/15/2009	Y	275	20
	5/31/2009	Y	270	13
	6/16/2009	Y	269	15
	7/2/2009	Y	274	14
	8/3/2009	Y	276	19
	8/19/2009	Y	272	12
	9/4/2009	Y	274	13
	10/6/2009	Y	179	15
	11/7/2009	Y	273	11
	2/11/2010	Y	276	12
4) Chachani				
1504-007	8/28/2003	N		
	6/5/2005	N		
	6/14/2005	N		
	7/7/2005	N		
	8/1/2005	N		
	8/17/2005	N		
	9/25/2005	N		
	10/7/2006	N		
	2/19/2007	N		
	4/24/2007	N		
	5/19/2007	N		
	6/27/2007	N		
	7/13/2007	N		
	8/23/2007	N		
	11/27/2007	N		
	3/9/2008	N		
	5/28/2008	N		
	6/13/2008	N		
	6/29/2008	N		
	8/16/2008	N		
	11/20/2008	N		
	1/23/2009	N		
	5/31/2009	N		
	6/16/2009	N		
	7/2/2009	N		
	8/3/2009	N		
	9/4/2009	N		
5) Misti				
1504-01	6/6/2002	Y	275	8
	8/9/2002	Y	271	6
	8/28/2003	N		
	6/5/2005	Y	268	7
	7/7/2005	Y	267	6

	8/17/2005	Y	268	8
	9/25/2005	Y	272	9
	10/7/2006	Y	270	5
	2/19/2007	Y	263	4
	4/24/2007	Y	271	5
	6/27/2007	Y	268	5
	7/13/2007	Y	267	5
	8/23/2007	Y	266	5
	11/18/2007	Y	271	4
	11/27/2007	Y	269	4
	3/9/2008	Y	271	6
	5/28/2008	Y	267	6
	6/13/2008	Y	265	7
	6/29/2008	Y	267	5
	8/16/2008	Y	269	8
	11/20/2008	Y	272	7
	1/23/2009	Y	272	7
	5/31/2009	Y	267	6
	6/16/2009	Y	266	7
	7/2/2009	Y	268	6
	8/3/2009	Y	265	5
	9/4/2009	Y	267	5
6) Ubinas				
1504-02	5/5/2002	Y	276	7
	6/6/2002	Y	281	13
	8/9/2002	Y	279	11
	4/22/2003	Y	279	9
	2/29/2004	Y	275	7
	4/20/2005	Y	274	5
	5/29/2005	Y	278	17
	7/16/2005	Y	273	10
	11/14/2005	Y	284	14
	8/20/2006	Y	271	6
	4/17/2007	Y	277	7
	7/22/2007	Y	291	26
	11/11/2007	Y	283	17
	5/21/2008	Y	285	16
	10/28/2008	Y	293	23
	3/14/2009	N		
	3/30/2009	Y	277	10
	6/9/2009	Y	271	6
	6/25/2009	Y	271	9
7) Huaynaputina				
1504-03				
	6/6/2002	N		
	8/9/2002	Y	277	7
	2/29/2004	N		
	4/20/2005	N		
	5/29/2005	N		
	7/16/2005	N		
	8/20/2006	Y	275	9
	4/17/2007	N		
	7/22/2007	N		

	11/11/2007	N		
	5/21/2008	N		
	10/28/2008	Y	277	5
	3/5/2009	Y	275	9
	3/14/2009	Y	280	6
	3/30/2009	N		
	6/9/2009	N		
	6/25/2009	N		

8) Ticsani

1504-031	12/21/2001	N
	7/1/2002	N
	2/29/2004	N
	3/19/2005	N
	4/20/2005	N
	5/29/2005	N
	7/16/2005	N
	7/25/2005	N
	1/8/2006	N
	6/26/2006	N
	8/20/2006	N
	4/17/2007	N
	7/6/2007	N
	7/22/2007	N
	11/11/2007	N
	5/21/2008	N
	9/26/2008	N
	10/28/2008	N
	3/14/2009	N
	3/30/2009	N
	6/9/2009	N
	6/25/2009	N

9) Tutupaca

1504-04		
	12/21/2001	N
	7/1/2002	N
	3/19/2005	N
	7/16/2005	N
	7/25/2005	N
	1/8/2006	N
	6/26/2006	N
	8/20/2006	N
	4/17/2007	N
	7/6/2007	N
	11/11/2007	N
	5/21/2008	N
	7/24/2008	N
	9/26/2008	N
	10/28/2008	N
	11/13/2008	N
	12/15/2008	N
	2/17/2009	N
	3/14/2009	N
	3/30/2009	N

	6/9/2009	N		
	6/25/2009	N		
	7/11/2009	N		
	8/12/2009	N		
	8/28/2009	N		
	10/15/2009	N		
	10/31/2009	N		
	12/2/2009	N		

10) Calientes
-17.17S
-70.18W

	12/21/2001	N		
	3/19/2005	N		
	7/25/2005	N		
	1/8/2006	N		
	6/26/2006	N		
	7/6/2007	N		
	7/24/2008	N		
	9/26/2008	N		
	11/13/2008	N		
	2/17/2009	N		
	3/14/2009	N		
	3/30/2009	N		
	7/11/2009	N		
	8/12/2009	N		
	8/28/2009	N		
	10/15/2009	N		
	10/31/2009	N		
	12/2/2009	N		

11) Yucamane

1504-05	12/21/2001	N		
	7/1/2002	N		
	3/19/2005	?	272	3
	7/25/2005	N		
	1/8/2006	N		
	11/1/2006	N		
	6/26/2006	?		
	7/6/2007	?		
	6/22/2008	N		
	7/24/2008	N		
	9/26/2008	N		
	11/13/2008	N		
	2/17/2009	N		
	3/14/2009	N		
	3/30/2009	N		
	4/6/2009	N		
	8/12/2009	N		
	8/28/2009	N		
	10/15/2009	N		
	10/31/2009	?		
	12/2/2009	N		

12) Nevados Casiri

1504-06	12/24/2002	N		
	6/25/2003	N		
	7/25/2005	N		
	11/5/2005	N		
	2/18/2006	N		
	6/17/2006	N		
	8/13/2006	N		
	5/28/2007	N		
	10/10/2007	N		
	2/8/2008	N		
	5/5/2008	N		
	5/30/2008	N		
	6/22/2008	N		
	4/6/2009	N		
	7/11/2009	N		
13) Tacora				
1505-01	12/24/2002	N		
	12/24/2002	N		
	6/25/2003	N		
	7/25/2005	N		
	11/5/2005	N		
	2/18/2006	N		
	6/17/2006	N		
	8/13/2006	N		
	5/28/2007	N		
	10/10/2007	N		
	2/8/2008	N		
	5/5/2008	N		
	5/30/2008	N		
	6/22/2008	N		
14) Taapaca				
1505-011				
	9/19/2002	N		
	12/24/2002	N		
	5/26/2004	N		
	10/29/2005	N		
	11/5/2005	N		
	2/18/2006	N		
	6/17/2006	N		
	8/13/2006	N		
	12/3/2006	N		
	2/21/2007	N		
	5/28/2007	N		
	10/10/2007	N		
	10/19/2007	N		
	5/5/2008	N		
	5/30/2008	N		
	6/22/2008	N		
	4/6/2009	N		
	5/1/2009	N		
15) Parinacota				
1505-012	6/15/2002	Y	260	6

	9/19/2002	Y	265	5
	6/2/2003	Y	263	8
	11/9/2003	N		
	5/3/2004	Y	265	7
	1/30/2005	Y	266	4
	5/6/2005	N		
	7/9/2005	Y	263	9
	10/29/2005	N		
	2/18/2006	Y	267	6
	4/23/2006	Y	264	7
	8/29/2006	Y	264	6
	9/30/2006	Y	261	5
	12/3/2006	Y	266	6
	5/28/2007	N		
	10/19/2007	Y	265	4
	5/14/2008	N		
	7/1/2008	Y	261	9
	7/17/2008	Y	266	10
	8/2/2008	Y	258	6
	8/18/2008	Y	264	8
	10/5/2008	Y	262	4
	10/21/2008	Y	266	4
	12/8/2008	N		
	12/24/2008	N		
	5/1/2009	Y	265	10
	5/17/2009	Y	263	11
	6/18/2009	Y	262	8
	7/4/2009	Y	259	5
	8/5/2009	Y	263	7
	8/21/2009	Y	262	6
	9/6/2009	Y	262	4
	9/22/2009	Y	261	4
	10/8/2009	Y	266	5
	10/24/2009	N		
	2/13/2010	Y	266	4

16) Guallatiri

1505-02	6/15/2002	Y	260	5
	9/19/2002	N		
	6/2/2003	Y	265	9
	11/9/2003	Y	269	5
	5/3/2004	Y	268	11
	1/30/2005	Y	271	6
	7/9/2005	Y	264	11
	10/29/2005	Y	264	6
	2/18/2006	Y	269	6
	4/23/2006	Y	267	5
	8/29/2006	Y	267	10
	12/3/2006	Y	269	6
	2/21/2007	Y	268	5
	5/28/2007	Y	262	4
	10/19/2007	Y	264	5
	7/1/2008	Y	262	12
	7/17/2008	Y	265	8
	8/2/2008	Y	261	8

	8/18/2008	Y	263	9
	10/21/2008	Y	268	8
	5/1/2009	Y	265	9
	5/17/2009	Y	264	12
	6/18/2009	Y	262	12
	7/4/2009	Y	261	6
	8/5/2009	Y	263	11
	8/21/2009	Y	263	7
	9/6/2009	Y	264	7
	9/22/2009	Y	263	7
	10/8/2009	Y	265	6
	2/13/2010	Y	268	4

17) Tambo Quemado

1505-022	6/5/2001	N		
	12/30/2001	N		
	4/5/2002	N		
	7/26/2002	N		
	4/24/2003	N		
	6/2/2003	N		
	5/3/2004	N		
	1/30/2005	N		
	7/2/2005	N		
	2/27/2006	N		
	4/23/2006	Y	279	6
	7/21/2006	N		
	3/2/2007	N		
	7/8/2007	N		
	12/31/2007	N		
	4/21/2008	N		
	7/1/2008	N		
	9/12/2008	N		
	1/25/2009	N		
	6/11/2009	N		
	2/13/2010	N		
	6/5/2010	N		
	6/30/2010	N		
	4/21/2011	N		
	4/30/2011	N		
	5/7/2011	N		
	6/1/2011	N		

18) Arintica

1505-023	1/19/2001	N
	6/15/2002	N
	9/19/2002	N
	11/9/2003	N
	5/3/2004	N
	1/30/2005	N
	7/9/2005	N
	10/29/2005	N
	2/18/2006	N
	4/23/2006	N
	8/29/2006	N
	9/30/2006	N

12/3/2006	N		
2/21/2007	N		
5/28/2007	N		
10/19/2007	N		
5/14/2008	N		
7/1/2008	N		
7/17/2008	N		
8/2/2008	N		
8/18/2008	N		
10/5/2008	N		
10/21/2008	N		
11/22/2008	N		
4/15/2009	N		
5/1/2009	N		
5/17/2009	N		
6/18/2009	N		
7/4/2009	N		
8/5/2009	N		
8/21/2009	N		
9/6/2009	N		
9/22/2009	N		
10/8/2009	N		
2/13/2010	N		

19) Isluga
1505-03

8/24/2001	Y	273	10
6/15/2002	Y	284	22
6/2/2003	Y	285	23
11/9/2003	Y	292	24
5/3/2004	Y	287	22
7/9/2005	Y	284	23
10/29/2005	Y	280	13
4/7/2006	Y	283	15
5/9/2006	Y	278	13
8/29/2006	Y	281	15
9/30/2006	Y	275	11
11/17/2006	Y	284	15
2/21/2007	Y	281	15
4/10/2007	Y	271	13
7/15/2007	Y	275	11
10/19/2007	Y	274	14
5/14/2008	Y	271	9
7/1/2008	Y	279	21
7/17/2008	Y	280	17
8/2/2008	Y	280	21
8/18/2008	Y	277	13
10/5/2008	Y	266	9
10/21/2008	Y	282	17
11/22/2008	Y	281	14
1/9/2009	Y	281	13
1/25/2009	Y	282	13
5/1/2009	Y	277	11
5/17/2009	Y	277	14

	6/18/2009	Y	276	18
	7/4/2009	Y	271	13
	8/5/2009	Y	277	17
	8/21/2009	Y	273	10
	9/6/2009	Y	277	13
	9/22/2009	Y	272	8
	10/8/2009	Y	278	11
	2/13/2010	Y	280	10

20) Tata Sabaya

1505-032	6/5/2001	N
	8/24/2001	N
	4/5/2002	N
	7/26/2002	N
	12/1/2002	N
	4/24/2003	N
	5/10/2003	N
	6/2/2003	N
	1/23/2005	N
	4/29/2005	N
	7/2/2005	N
	10/22/2005	N
	2/27/2006	N
	4/7/2006	N
	4/16/2006	N
	7/21/2006	N
	11/17/2006	N
	3/2/2007	N
	2/17/2008	N
	4/21/2008	N
	5/23/2008	N
	7/10/2008	N
	7/26/2008	N
	8/11/2008	N
	8/27/2008	N
	9/12/2008	N
	9/28/2008	N
	11/15/2008	N
	12/1/2008	N
	12/17/2008	N
	1/9/2009	N
	1/18/2009	N
	1/25/2009	N
	4/24/2009	N
	5/10/2009	N
	6/11/2009	N
	6/27/2009	N
	7/29/2009	N
	8/14/2009	N
	9/15/2009	N
	10/1/2009	N
	10/17/2009	N

21) Puchuldiza

1505-032C	4/12/2002	Y	281	9
	5/14/2002	N		
	6/15/2002	Y	276	10
	2/26/2003	Y	285	12
	11/9/2003	Y	280	5
	5/3/2004	Y	275	11
	1/30/2005	Y	277	11
	7/9/2005	Y	277	11
	2/18/2006	N		
	5/9/2006	Y	277	9
	8/13/2006	Y	273	10
	8/29/2006	Y	276	9
	9/30/2006	Y	277	5
	12/3/2006	Y	281	11
	2/21/2007	Y	279	7
	4/10/2007	Y	274	8
	5/28/2007	Y	274	6
	7/15/2007	Y	276	11
	10/19/2007	N	275	12
	5/14/2008	Y	278	12
	5/30/2008	Y	276	9
	7/1/2008	Y	273	10
	7/17/2008	Y	276	10
	8/2/2008	Y	273	11
	8/18/2008	Y	274	10
	10/5/2008	Y	275	9
	10/21/2008	Y	278	10
	11/22/2008	Y	278	11
	5/1/2009	Y	274	12
	5/17/2009	Y	276	10
	6/18/2009	Y	272	9
	7/4/2009	Y	268	10
	8/5/2009	Y	274	10
	8/21/2009	Y	274	11
	9/6/2009	Y	275	10
	9/22/2009	Y	274	9
	10/8/2009	Y	276	9
	1/28/2010	N		
	2/13/2010	N		

22) Nuevo Mundo

1505-036	10/15/2005	N		
	11/2/2009	N		
	11/11/2009	N		

23) Irruputuncu

1505-04	4/12/2002	Y	279	8
	6/15/2002	Y	274	10
	9/19/2002	Y	276	9
	2/26/2003	Y	283	10
	11/9/2003	Y	280	7
	5/3/2004	Y	282	13
	1/30/2005	Y	285	11
	7/9/2005	Y	275	10
	10/29/2005	Y	274	8

	1/1/2006	Y	283	13
	2/18/2006	Y	282	11
	5/9/2006	Y	274	8
	8/29/2006	Y	276	10
	12/3/2006	Y	280	6
	2/21/2007	Y	279	9
	4/10/2007	Y	279	8
	5/28/2007	Y	271	6
	7/15/2007	Y	273	9
	10/19/2007	Y	280	10
	1/23/2008	Y	276	3
	5/14/2008	Y	272	7
	7/1/2008	Y	277	12
	7/17/2008	Y	276	9
	8/2/2008	Y	274	11
	8/18/2008	Y	270	5
	10/5/2008	Y	272	7
	10/21/2008	Y	279	10
	11/6/2008	Y	274	5
	11/22/2008	Y	283	12
	4/15/2009	Y	278	8
	5/1/2009	Y	278	8
	5/17/2009	Y	279	10
	6/18/2009	Y	273	9
	8/5/2009	Y	275	9
	8/21/2009	Y	272	8
	9/6/2009	Y	275	7
	9/22/2009	Y	274	8
	10/8/2009	Y	279	10
	1/12/2010	Y	281	8
	1/28/2010	Y	284	12
	2/13/2010	Y	283	6

24) Pampa Luxsar

1505-042	6/21/2001	N
	1/6/2002	N
	4/5/2002	N
	4/12/2002	N
	6/24/2002	N
	12/1/2002	N
	2/26/2003	N
	5/10/2003	N
	1/21/2004	N
	1/30/2005	N
	4/29/2005	N
	7/2/2005	N
	10/22/2005	N
	2/27/2006	N
	4/7/2006	N
	5/9/2006	N
	8/6/2006	N
	11/17/2006	N
	3/2/2007	N
	12/31/2007	N
	5/23/2008	N

	7/10/2008	N		
	7/26/2008	N		
	8/2/2008	N		
	8/11/2008	N		
	8/27/2008	N		
	9/12/2008	N		
	11/6/2008	N		
	11/15/2008	N		
	11/22/2008	N		
	12/1/2008	N		
	12/17/2008	N		
	1/9/2009	N		
	1/18/2009	N		
	2/3/2009	N		
	3/7/2009	N		
	4/24/2009	N		
	5/10/2009	N		
	6/11/2009	N		
	6/27/2009	N		
	7/29/2009	N		
	8/5/2009	N		
	8/14/2009	N		
	8/21/2009	N		
	9/6/2009	N		
	10/1/2009	N		
	10/8/2009	N		
	10/17/2009	N		
	12/4/2009	N		
	1/21/2010	N		
	1/28/2010	N		

25) Olca-Paruma

1505-05	4/12/2002	Y	271	4
	6/15/2002	Y	268	5
	9/19/2002	Y	268	4
	2/26/2003	Y	275	5
	11/9/2003	Y	273	6
	5/3/2004	Y	271	5
	1/30/2005	Y	275	5
	5/6/2005	Y	268	4
	7/9/2005	Y	267	6
	10/29/2005	Y	267	6
	1/1/2006	Y	273	8
	5/9/2006	Y	268	4
	8/29/2006	Y	274	4
	12/3/2006	Y	274	6
	2/21/2007	Y	272	7
	4/10/2007	?	272	3
	5/28/2007	?	267	3
	7/15/2007	Y	268	7
	10/19/2007	Y	272	6
	1/23/2008	Y	275	6
	5/14/2008	Y	265	4
	7/1/2008	Y	268	11
	7/17/2008	Y	268	5

8/2/2008	Y	267	5
8/18/2008	Y	267	4
10/5/2008	Y	267	7
10/21/2008	Y	272	8
11/6/2008	Y	270	6
11/22/2008	Y	272	7
4/15/2009	Y	275	8
5/1/2009	Y	272	5
5/17/2009	Y	272	5
6/18/2009	Y	267	7
8/5/2009	Y	269	11
8/21/2009	Y	266	5
9/6/2009	Y	269	5
9/22/2009	Y	267	4
10/8/2009	Y	271	5
1/12/2010	Y	275	6
1/28/2010	Y	275	7
2/13/2010	Y	278	7

26) Aucanquilcha
1505-05A

4/12/2002	?	265	4
6/15/2002	N		
2/26/2003	N		
11/9/2003	?	267	3
5/3/2004	N		
1/30/2005	?	265	3
5/6/2005	N		
7/9/2005	?	258	5
10/29/2005	N		
1/1/2006	N		
2/18/2006	N		
5/9/2006	N		
8/29/2006	N		
12/3/2006	N		
2/21/2007	?	261	3
4/10/2007	?	264	3
5/28/2007	N		
7/15/2007	N		
10/19/2007	N		
1/23/2008	N		
5/14/2008	N		
7/1/2008	?	259	3
7/17/2008	N		
8/2/2008	N		
8/18/2008	N		
10/5/2008	N		
10/21/2008	N		
11/6/2008	N		
11/22/2008	N		
12/24/2008	N		
4/15/2009	N		
5/1/2009	N		
5/17/2009	N		
6/18/2009	N		

7/4/2009	N		
8/5/2009	?	263	5
8/21/2009	N		
9/6/2009	N		
9/22/2009	N		
10/8/2009	N		
1/12/2010	N		
1/28/2010	?	262	4

27) Ollague
1505-06

6/21/2001	Y	262	6
1/6/2002	N		
4/5/2002	Y	273	4
4/12/2002	N		
6/15/2002	Y	267	6
6/24/2002	Y	268	5
12/1/2002	N		
2/26/2003	Y	273	3
5/10/2003	N		
11/9/2003	Y	273	5
1/21/2004	Y	274	5
5/3/2004	Y	270	5
1/30/2005	Y	275	4
4/29/2005	?	266	3
7/2/2005	?	266	2
7/9/2005	Y	269	6
10/22/2005	N		
10/29/2005	Y	270	6
1/1/2006	Y	274	4
3/22/2006	N		
4/7/2006	Y	271	6
5/9/2006	Y	270	7
8/6/2006	N		
8/29/2006	Y	270	7
11/17/2006	Y	275	6
2/21/2007	Y	273	4
3/2/2007	Y	275	4
4/10/2007	Y	271	4
7/15/2007	Y	267	7
10/19/2007	?	271	3
12/31/2007	Y	275	5
1/23/2008	N		
5/14/2008	Y	266	6
5/23/2008	Y	267	4
7/1/2008	Y	267	6
7/10/2008	Y	269	6
7/17/2008	Y	268	5
7/26/2008	Y	267	5
8/2/2008	Y	266	6
8/11/2008	Y	269	5
8/18/2008	Y	268	5
8/27/2008	Y	268	3
9/12/2008	Y	267	7
10/5/2008	Y	268	6

10/14/2008	Y	271	4
10/21/2008	Y	270	4
11/6/2008	N		
11/22/2008	Y	272	4
12/1/2008	Y	272	4
12/17/2008	N		
12/24/2008	?	269	3
1/9/2009	Y	273	5
1/25/2009	Y	275	7
2/3/2009	Y	272	4
4/15/2009	Y	273	7
4/24/2009	Y	267	3
5/1/2009	Y	274	9
5/10/2009	Y	268	5
5/17/2009	Y	269	3
6/11/2009	Y	268	4
6/18/2009	Y	268	7
6/27/2009	Y	265	4
7/4/2009	Y	267	8
8/5/2009	N		
8/14/2009	Y	269	5
8/21/2009	Y	268	7
9/6/2009	Y	268	4
9/15/2009	?	269	3
9/22/2009	Y	269	6
10/1/2009	?	268	3
10/8/2009	Y	272	6
10/17/2009	?	269	3
10/24/2009	?	271	3
12/4/2009	Y	274	4
1/12/2010	Y	275	5
1/28/2010	Y	273	5

28) Azufre
1505-061

1/6/2002	N		
4/12/2002	N		
6/15/2002	N		
2/26/2003	N		
11/9/2003	N		
1/21/2004	N		
5/3/2004	N		
1/30/2005	N		
5/6/2005	N		
7/9/2005	N		
10/29/2005	N		
1/1/2006	?	270	5
3/22/2006	N		
4/7/2006	N		
5/9/2006	?	262	4
8/29/2006	N		
10/16/2006	N		
2/21/2007	N		
4/10/2007	N		
7/15/2007	N		

10/19/2007	N		
1/23/2008	?	266	4
4/12/2008	N		
5/14/2008	N		
7/1/2008	N		
7/17/2008	N		
8/2/2008	N		
8/18/2008	N		
10/5/2008	N		
10/21/2008	N		
11/6/2008	?	265	3
11/22/2008	N		
12/8/2008	N		
12/24/2008	N		
1/9/2009	?	267	4
1/25/2009	?	269	4
4/15/2009	N		
5/1/2009	N		
5/17/2009	N		
6/18/2009	N		
7/4/2009	N		
8/5/2009	N		
8/21/2009	N		
9/6/2009	N		
9/22/2009	N		
10/8/2009	N		
10/24/2009	N		
1/12/2010	N		

29) San Pedro
1505-07

4/12/2002	Y	268	5
6/15/2002	Y	262	5
2/26/2003	Y	272	6
7/4/2003	Y	264	5
11/9/2003	Y	268	6
5/3/2004	Y	265	3
1/30/2005	Y	270	7
7/9/2005	Y	264	4
10/29/2005	Y	264	6
1/1/2006	Y	271	7
2/18/2006	Y	266	8
5/9/2006	Y	264	5
8/13/2006	?	262	2
8/29/2006	Y	264	5
10/16/2006	Y	267	4
12/3/2006	Y	272	7
2/21/2007	Y	269	7
4/10/2007	Y	267	3
5/28/2007	Y	261	3
7/15/2007	Y	262	6
10/19/2007	Y	268	4
1/23/2008	Y	270	7
4/12/2008	Y	269	4
5/14/2008	Y	262	4

5/30/2008	Y	260	4
7/1/2008	Y	264	6
7/17/2008	Y	264	4
8/2/2008	Y	261	3
8/18/2008	Y	261	3
10/5/2008	Y	263	6
10/21/2008	Y	267	7
11/6/2008	Y	267	5
11/22/2008	Y	270	8
12/8/2008	Y	273	8
12/24/2008	Y	269	6
4/15/2009	Y	270	6
5/1/2009	?	265	2
5/17/2009	Y	268	5
6/18/2009	Y	265	7
7/4/2009	Y	262	4
8/5/2009	Y	268	8
8/21/2009	Y	264	6
9/6/2009	Y	264	5
9/22/2009	Y	264	6
10/8/2009	Y	267	4
10/24/2009	Y	268	6
1/12/2010	Y	272	4
1/28/2010	Y	273	6

30) Paniri
-22.05S
-68.23W

1/6/2002	N
4/12/2002	N
6/15/2002	N
2/26/2003	N
11/9/2003	N
5/3/2004	N
1/30/2005	N
7/9/2005	N
10/29/2005	N
1/1/2006	N
5/9/2006	N
8/29/2006	N
10/16/2006	N
2/21/2007	N
7/15/2007	N
10/19/2007	N
1/23/2008	N
7/1/2008	N
10/5/2008	N
10/21/2008	N
1/25/2009	N
4/15/2009	N
6/18/2009	N
1/12/2010	N

31) Tocorpuri
-22.87S

-67.92W	6/21/2001	N		
	4/12/2002	Y	273	11
	6/24/2002	N		
	12/1/2002	N		
	5/10/2003	N		
	6/16/2005	N		
	7/2/2005	N		
	7/9/2005	N		
	10/22/2005	N		
	8/6/2006	N		
	8/29/2006	N		
	10/16/2006	N		
	11/17/2006	N		
	12/31/2007	N		
	5/14/2008	N		
	5/23/2008	N		
	6/15/2008	N		
	7/1/2008	N		
	7/10/2008	N		
	7/17/2008	N		
	7/26/2008	N		
	8/2/2008	N		
	8/11/2008	N		
	8/18/2008	N		
	8/27/2008	N		
	9/12/2008	N		
	9/28/2008	N		
	10/5/2008	N		
	10/14/2008	N		
	11/15/2008	N		
	12/1/2008	N		
	12/17/2008	N		
	5/10/2009	N		
	6/18/2009	N		
	6/27/2009	N		
	7/4/2009	N		
	7/29/2009	N		
	8/5/2009	N		
	8/14/2009	N		
	9/6/2009	N		
	9/15/2009	N		
	10/1/2009	N		
	10/17/2009	N		
	10/24/2009	N		
	12/4/2009	N		
32) Uturuncu				
1505-076A	5/20/2001	Y	268	13
	1/15/2002	Y	278	15
	1/15/2002	Y	278	14
	2/23/2002	Y	276	17
	8/11/2002	Y	277	19
	8/11/2002	Y	277	19
	2/8/2005	Y	279	20
	2/8/2005	Y	279	20

	8/19/2005	Y	275	17
	8/19/2005	Y	275	17
	11/30/2005	Y	281	13
	8/22/2006	Y	272	15
	8/22/2006	Y	272	14
	4/3/2007	Y	282	20
	4/3/2007	Y	283	20
	5/21/2007	Y	267	10
	5/21/2007	Y	269	12
	7/24/2007	Y	267	13
	7/24/2007	Y	267	12
	8/25/2007	Y	271	11
	8/25/2007	Y	271	11
	2/1/2008	Y	274	14
	2/1/2008	Y	274	17
	3/23/2009	Y	276	14
	3/23/2009	Y	277	14
	5/26/2009	Y	275	16
	11/9/2009	Y	279	18

33) El Tatio

1505-08=A	1/6/2002	Y	281	11
	4/12/2002	Y	282	9
	6/15/2002	Y	276	14
	6/24/2002	Y	273	11
	2/26/2003	Y	283	8
	11/9/2003	Y	282	11
	1/21/2004	Y	283	9
	5/3/2004	Y	279	13
	1/30/2005	Y	281	7
	4/29/2005	Y	277	11
	7/9/2005	Y	276	13
	10/22/2005	Y	278	12
	10/29/2005	Y	279	12
	3/6/2006	Y	285	8
	3/22/2006	Y	282	6
	4/7/2006	Y	282	9
	5/9/2006	Y	276	9
	8/29/2006	Y	278	11
	10/16/2006	Y	280	11
	11/17/2006	Y	284	12
	2/21/2007	Y	283	10
	3/2/2007	Y	286	8
	4/10/2007	Y	280	12
	7/15/2007	Y	274	11
	10/19/2007	Y	278	9
	1/23/2008	Y	284	7
	5/14/2008	Y	278	14
	6/15/2008	Y	276	15
	7/1/2008	Y	273	12
	7/17/2008	Y	276	12
	8/2/2008	Y	274	12
	8/18/2008	Y	275	12
	10/5/2008	Y	275	10
	10/21/2008	Y	279	10

	11/6/2008	Y	279	10
	11/22/2008	Y	280	10
	12/8/2008	Y	284	11
	12/24/2008	Y	276	7
	1/9/2009	Y	282	11
	1/25/2009	Y	283	9
	2/3/2009	Y	281	6
	4/15/2009	Y	284	9
	4/24/2009	Y	280	11
	5/1/2009	Y	280	11
	5/10/2009	Y	278	13
	5/17/2009	Y	280	13
	6/18/2009	Y	277	6
	7/4/2009	Y	271	12
	8/5/2009	Y	277	12
	8/21/2009	Y	274	12
	9/6/2009	Y	275	9
	9/22/2009	Y	278	14
	10/8/2009	Y	278	10
	10/24/2009	Y	279	11
	1/12/2010	Y	285	7
	1/28/2010	Y	285	8

34) Sol de Mañana

-22.43S	6/21/2001	Y	273	11
-67.76W	1/6/2002	Y	274	10
	4/5/2002	Y	282	15
	6/24/2002	Y	265	10
	12/1/2002	Y	278	13
	2/19/2003	Y	282	11
	2/26/2003	Y	273	6
	4/24/2003	Y	276	11
	5/10/2003	Y	276	16
	1/21/2004	Y	277	9
	1/23/2005	Y	277	7
	2/24/2005	Y	278	6
	4/29/2005	Y	277	16
	6/16/2005	Y	277	15
	7/2/2005	Y	275	15
	10/22/2005	Y	277	17
	1/10/2006	Y	276	8
	2/27/2006	Y	280	15
	3/6/2006	Y	282	11
	3/22/2006	Y	283	12
	4/7/2006	Y	280	12
	8/6/2006	Y	274	14
	10/16/2006	Y	277	15
	11/17/2006	Y	281	15
	3/2/2007	Y	283	13
	7/8/2007	Y	271	10
	12/31/2007	Y	281	14
	5/23/2008	Y	278	15
	6/15/2008	Y	275	18
	7/10/2008	Y	277	12
	7/26/2008	Y	272	14

	8/11/2008	Y	274	15
	8/27/2008	Y	280	13
	9/12/2008	Y	274	13
	9/28/2008	Y	277	15
	10/14/2008	Y	281	18
	11/15/2008	Y	278	13
	12/1/2008	Y	278	14
	12/17/2008	Y	280	15
	1/2/2009	Y	273	8
	1/9/2009	Y	275	7
	1/18/2009	Y	283	12
	1/25/2009	Y	280	15
	2/3/2009	Y	280	12
	2/19/2009	Y	282	11
	3/7/2009	Y	274	6
	4/24/2009	Y	272	10
	5/10/2009	Y	276	16
	6/27/2009	Y	275	12
	7/29/2009	Y	275	14
	8/14/2009	Y	277	17
	9/15/2009	Y	278	13
	10/1/2009	Y	276	11
	10/17/2009	Y	276	11
	12/4/2009	Y	281	14
	1/21/2010	Y	282	11
	2/22/2010	Y	270	8
35) Putana				
1505-09	6/21/2001	Y	258	8
	1/6/2002	N		
	4/5/2002	Y	266	6
	4/12/2002	Y	266	6
	6/24/2002	N		
	12/1/2002	N		
	1/2/2003	N		
	2/19/2003	N		
	2/26/2003	N		
	4/24/2003	N		
	5/10/2003	N		
	1/21/2004	N		
	5/3/2004	N		
	1/23/2005	Y	260	5
	1/30/2005	Y	266	5
	2/24/2005	N		
	4/29/2005	N		
	6/16/2005	N		
	7/2/2005	N		
	7/9/2005	Y	262	6
	10/22/2005	Y	261	5
	1/1/2006	N		
	1/10/2006	N		
	2/27/2006	N		
	3/6/2006	N		
	3/22/2006	Y	267	9
	4/7/2006	Y	265	4

5/9/2006	N		
8/6/2006	Y	262	4
8/29/2006	N		
10/16/2006	N		
11/17/2006	N		
3/2/2007	N		
4/10/2007	N		
12/31/2007	N		
1/23/2008	Y	263	5
2/17/2008	N		
5/14/2008	Y	259	5
5/23/2008	Y	263	4
6/15/2008	N		
7/1/2008	N		
7/10/2008	N		
7/17/2008	N		
7/26/2008	Y	261	5
8/2/2008	N		
8/11/2008	N		
8/18/2008	N		
8/27/2008	Y	264	4
9/12/2008	Y	261	4
9/28/2008	N		
10/5/2008	Y	259	5
10/14/2008	Y	267	4
10/21/2008	Y	264	4
11/6/2008	N		
11/15/2008	N		
11/22/2008	Y	266	6
12/1/2008	Y	265	4
12/17/2008	Y	266	5
12/24/2008	Y	266	4
1/2/2009	N		
1/9/2009	N		
1/18/2009	N		
1/25/2009	N		
2/3/2009	N		
2/19/2009	Y	266	5
3/7/2009	N		
4/24/2009	Y	264	5
5/10/2009	N		
6/11/2009	N		
6/18/2009	Y	261	4
6/27/2009	N		
7/4/2009	N		
7/29/2009	N		
8/5/2009	Y	265	5
8/14/2009	Y	263	4
8/21/2009	Y	260	5
9/6/2009	Y	263	4
9/15/2009	N		
9/22/2009	Y	261	4
10/1/2009	Y	263	4
10/8/2009	N		
10/17/2009	N		

	10/24/2009	Y	265	4
	12/4/2009	Y	269	5
	1/12/2010	Y	270	5
	1/21/2010	Y	271	5
	1/28/2010	Y	270	6
	2/22/2010	Y	267	4

36) Sairecabur

1505-091	7/27/2000	N
	10/15/2000	N
	10/15/2000	N
	6/21/2001	N
	4/5/2002	N
	6/15/2002	N
	10/5/2002	N
	10/5/2002	N
	12/1/2002	N
	2/19/2003	N
	5/10/2003	N
	11/9/2003	N
	1/21/2004	N
	5/3/2004	N
	6/4/2004	N
	8/7/2004	N
	9/8/2004	N
	12/13/2004	N
	12/13/2004	N
	4/29/2005	N
	6/7/2005	N
	6/23/2005	N
	6/23/2005	N
	7/9/2005	N
	8/26/2005	N
	9/27/2005	N
	10/22/2005	N
	3/6/2006	N
	3/6/2006	N
	8/6/2006	N
	10/16/2006	N
	11/17/2006	N
	11/17/2006	N
	6/13/2007	N
	6/13/2007	N
	10/19/2007	N
	6/15/2008	N
	10/5/2008	N
	10/14/2008	N
	10/21/2008	N
	11/22/2008	N
	11/22/2008	N
	12/17/2008	N
	1/9/2009	N
	6/11/2009	N
	10/1/2009	N

37) Licancabur

1505-092	9/13/2000	N		
	10/15/2000	?	265	2-3
	10/15/2000	?	266	3
	6/21/2001	N		
	4/5/2002	N		
	4/12/2002	N		
	6/15/2002	N		
	10/5/2002	Y	266	4
	10/5/2002	?	269	2-3
	12/1/2002	N		
	2/19/2003	N		
	5/10/2003	N		
	11/9/2003	N		
	1/21/2004	N		
	5/3/2004	?	260	2-4
	6/4/2004	N		
	8/7/2004	N		
	9/8/2004	?	261	3
	1/30/2005	N		
	4/29/2005	N		
	6/7/2005	N		
	6/23/2005	N		
	6/23/2005	N		
	7/9/2005	N		
	8/26/2005	Y	268	3
	9/27/2005	?	267	3
	3/6/2006	N		
	3/6/2006	N		
	4/7/2006	N		
	11/17/2006	?	264	2
	11/17/2006	N		
	3/2/2007	N		
	4/10/2007	?	266	4
	6/13/2007	N		
	6/13/2007	N		
	10/19/2007	N		
	3/27/2008	N		
	6/15/2008	N		
	10/14/2008	N		
	10/21/2008	N		
	11/22/2008	Y	266	3
	11/22/2008	Y	265	3
	12/17/2008	Y	268	3
	1/9/2009	N		
	3/7/2009	N		
	6/11/2009	N		
	6/18/2009	N		
	1/12/2010	N		

38) Guayaques

1505-093	5/1/2000	N		
	7/4/2000	N		
	9/22/2000	N		
	10/15/2000	N		

	12/27/2000	N
	6/21/2001	N
	4/5/2002	N
	5/23/2002	N
	6/24/2002	N
	10/5/2002	N
	4/24/2003	N
	6/11/2003	N
	1/21/2004	N
	5/28/2004	N
	6/13/2004	N
	7/15/2004	N
	9/1/2004	N
	12/13/2004	N
	1/23/2005	N
	3/28/2005	N
	4/13/2005	N
	4/29/2005	N
	6/7/2005	N
	8/26/2005	N
	9/20/2005	N
	10/22/2005	N
	11/23/2005	N
	2/27/2006	N
	3/6/2006	N
	3/15/2006	N
	4/7/2006	N
	6/19/2006	N
	8/6/2006	N
	11/17/2006	N
	3/2/2007	N
	6/6/2007	N
	6/13/2007	N
	11/29/2007	N
	2/17/2008	N
	6/8/2008	N
	6/15/2008	N
	8/11/2008	N
	10/14/2008	N
	12/1/2008	N
	12/17/2008	N
	1/2/2009	N
	1/9/2009	N
	6/11/2009	N
	1/21/2010	N

39) Purico Complex

1505-094	5/1/2000	N
	7/4/2000	N
	9/22/2000	N
	10/15/2000	N
	10/15/2000	N
	12/27/2000	N
	12/27/2000	N
	4/5/2002	N

	5/23/2002	N		
	6/24/2002	N		
	10/5/2002	N		
	10/5/2002	N		
	1/2/2003	N		
	6/11/2003	N		
	1/21/2004	N		
	5/3/2004	N		
	5/28/2004	N		
	6/13/2004	N		
	7/15/2004	N		
	12/13/2004	N		
	12/13/2004	N		
	3/28/2005	N		
	4/13/2005	N		
	4/29/2005	N		
	6/7/2005	N		
	6/7/2005	N		
	6/23/2005	N		
	6/23/2005	N		
	7/9/2005	N		
	8/26/2005	N		
	9/20/2005	N		
	9/27/2005	N		
	10/22/2005	N		
	10/22/2005	N		
	3/6/2006	N		
	3/6/2006	N		
	3/15/2006	N		
	4/7/2006	N		
	8/6/2006	N		
	11/17/2006	N		
	11/17/2006	N		
	3/2/2007	N		
	6/13/2007	N		
	6/13/2007	N		
	11/29/2007	N		
	8/11/2008	N		
	10/14/2008	N		
	10/14/2008	N		
	10/21/2008	N		
	11/22/2008	N		
	11/22/2008	N		
	12/1/2008	N		
	12/1/2008	N		
	12/17/2008	N		
	1/2/2009	N		
	1/9/2009	N		

40) Alítar
-23.15S
-67.63W

	5/1/2000	Y	273	7
	5/24/2000	Y	275	11
	7/4/2000	Y	275	15

7/27/2000	Y	270	7
9/13/2000	Y	274	12
9/22/2000	Y	275	14
10/15/2000	Y	277	11
12/27/2000	Y	279	12
6/21/2001	Y	271	10
4/5/2002	Y	281	12
5/23/2002	Y	270	10
10/5/2002	Y	280	14
12/1/2002	Y	280	13
1/2/2003	Y	280	8
5/10/2003	Y	276	12
6/11/2003	Y	270	9
7/29/2003	Y	272	9
8/30/2003	Y	273	9
1/21/2004	Y	283	12
3/9/2004	Y	280	14
5/28/2004	Y	271	9
6/13/2004	Y	271	10
6/20/2004	Y	275	9
7/15/2004	Y	274	9
7/31/2004	Y	273	12
9/1/2004	Y	278	11
12/13/2004	Y	281	10
3/28/2005	Y	282	11
4/13/2005	Y	278	10
4/29/2005	Y	272	8
6/7/2005	Y	277	13
6/16/2005	Y	274	10
6/23/2005	Y	274	14
8/26/2005	Y	276	14
9/20/2005	Y	274	11
10/22/2005	Y	275	11
11/23/2005	Y	278	12
2/27/2006	Y	280	9
3/6/2006	Y	283	11
3/15/2006	Y	282	11
3/22/2006	Y	282	10
4/7/2006	Y	279	11
5/9/2006	Y	275	9
6/19/2006	Y	275	13
8/6/2006	Y	276	12
9/14/2006	Y	276	11
10/16/2006	Y	278	13
11/17/2006	Y	280	12
3/2/2007	Y	282	10
3/18/2007	Y	280	9
5/12/2007	Y	275	12
6/6/2007	Y	275	10
6/13/2007	Y	277	12
8/16/2007	Y	274	9
11/4/2007	Y	274	9
11/29/2007	Y	279	11
12/6/2007	Y	278	12
12/31/2007	Y	282	12

	2/24/2008	Y	283	15
	3/20/2008	Y	280	10
	3/27/2008	Y	282	10
	4/28/2008	Y	274	10
	5/7/2008	Y	274	11
	5/23/2008	Y	277	12
	6/8/2008	Y	273	8
	6/15/2008	Y	268	9
	6/24/2008	Y	271	11
	7/10/2008	Y	271	6
	7/26/2008	Y	271	10
	8/2/2008	Y	272	12
	8/11/2008	Y	273	10
	8/27/2008	Y	278	12
	9/12/2008	Y	274	11
	9/28/2008	Y	273	10
	10/14/2008	Y	279	12
	11/6/2008	Y	276	10
	11/15/2008	Y	276	10
	11/22/2008	Y	280	14
	12/17/2008	Y	280	13
	1/2/2009	Y	281	8
	1/9/2009	Y	278	8
	1/25/2009	Y	282	11
	2/3/2009	Y	279	10
	4/24/2009	Y	278	13
	5/10/2009	Y	272	10
	6/11/2009	Y	275	10
	6/27/2009	Y	273	10
	7/4/2009	Y	270	9
	7/29/2009	Y	271	10
	8/5/2009	Y	276	12
	8/14/2009	Y	274	11
	8/21/2009	Y	272	10
	10/1/2009	Y	275	10
	10/17/2009	Y	274	9
	12/4/2009	Y	281	13
	1/12/2010	Y	283	12
	1/21/2010	Y	284	12
	1/28/2010	Y	283	13
	2/22/2010	Y	281	11

41) Colachi

1505-095	5/1/2000	N
	7/4/2000	N
	7/27/2000	N
	9/22/2000	N
	12/27/2000	N
	6/21/2001	N
	1/6/2002	N
	4/5/2002	N
	6/24/2002	N
	7/17/2002	N
	10/5/2002	N
	1/2/2003	N

	6/11/2003	N
	1/21/2004	N
	5/28/2004	N
	6/4/2004	N
	7/15/2004	N
	9/1/2004	N
	9/24/2004	N
	1/23/2005	N
	1/30/2005	N
	3/28/2005	N
	4/13/2005	N
	4/29/2005	N
	6/7/2005	N
	8/10/2005	N
	9/20/2005	N
	10/22/2005	N
	11/23/2005	N
	1/1/2006	N
	2/27/2006	N
	3/15/2006	N
	6/17/2006	N
	6/19/2006	N
	8/6/2006	N
	3/2/2007	N
	6/6/2007	N
	6/13/2007	N
	11/29/2007	N
	2/24/2008	N
	6/8/2008	N
	10/14/2008	N
	12/1/2008	N
	12/17/2008	N
	1/2/2009	N
	1/9/2009	N
	1/25/2009	N
	6/11/2009	N
	1/12/2010	N

42) Acamarachi

1505-096	5/1/2000	N
	7/4/2000	N
	7/27/2000	N
	9/22/2000	N
	12/27/2000	N
	6/21/2001	N
	1/6/2002	N
	4/5/2002	N
	6/24/2002	N
	7/17/2002	N
	10/5/2002	N
	12/1/2002	N
	1/2/2003	N
	3/7/2003	N
	4/24/2003	N
	6/11/2003	N

	1/21/2004	N		
	5/28/2004	N		
	6/13/2004	N		
	7/15/2004	N		
	9/1/2004	N		
	9/24/2004	N		
	11/27/2004	N		
	12/13/2004	N		
	3/28/2005	N		
	4/13/2005	N		
	4/29/2005	N		
	6/7/2005	N		
	6/23/2005	N		
	8/26/2005	N		
	9/20/2005	N		
	10/22/2005	N		
	11/23/2005	N		
	1/1/2006	N		
	3/6/2006	N		
	3/15/2006	N		
	4/7/2006	N		
	6/17/2006	N		
	6/19/2006	N		
	8/6/2006	N		
	11/17/2006	N		
	3/2/2007	N		
	5/12/2007	N		
	6/6/2007	N		
	6/13/2007	N		
	11/4/2007	N		
	11/29/2007	N		
	12/6/2007	N		
	2/24/2008	N		
	6/8/2008	N		
	8/11/2008	N		
	10/14/2008	N		
	11/6/2008	N		
	12/1/2008	N		
	12/17/2008	N		
	1/2/2009	N		
	1/9/2009	N		
	1/25/2009	N		
	6/11/2009	N		
	12/4/2009	N		
43) Chiliques				
1505-098	5/1/2000	N		
	5/24/2000	N		
	7/27/2000	N		
	8/12/2000	N		
	9/13/2000	N		
	9/22/2000	N		
	1/6/2002	Y	275	9
	4/5/2002	Y	272	8
	5/23/2002	N		

6/15/2002	N		
6/24/2002	N		
7/17/2002	N		
10/5/2002	N		
12/1/2002	N		
5/10/2003	?	265	3
11/9/2003	Y	274	8
1/21/2004	Y	274	7
1/28/2004	Y	275	6
3/9/2004	Y	273	6
5/3/2004	N		
5/28/2004	N		
6/4/2004	N		
6/13/2004	N		
6/20/2004	N		
7/15/2004	N		
7/31/2004	N		
8/7/2004	N		
9/1/2004	N		
9/8/2004	N		
9/24/2004	N		
11/27/2004	Y	272	9
1/23/2005	Y	273	6
1/30/2005	Y	270	6
3/28/2005	Y	275	7
4/13/2005	Y	268	4
4/29/2005	Y	262	4
6/7/2005	?	261	3
6/23/2005	N		
7/9/2005	N		
8/10/2005	N		
8/26/2005	N		
9/27/2005	N		
10/22/2005	N		
10/29/2005	N		
11/23/2005	N		
1/1/2006	Y	273	7
3/6/2006	Y	276	7
3/22/2006	Y	276	8
4/7/2006	Y	272	8
5/9/2006	Y	267	10
6/19/2006	N		
8/6/2006	?	263	3
8/29/2006	?	262	2
9/14/2006	N		
10/16/2006	Y	272	8
11/17/2006	Y	275	10
2/21/2007	Y	272	11
3/2/2007	Y	272	8
3/18/2007	Y	274	6
4/10/2007	Y	272	9
5/12/2007	?	265	4
6/13/2007	?	262	3
7/15/2007	N		
8/16/2007	N		

10/19/2007	Y	269	6
11/4/2007	Y	272	11
11/20/2007	Y	266	4
12/6/2007	Y	274	10
12/31/2007	Y	275	5
1/23/2008	Y	273	7
2/17/2008	Y	276	7
2/24/2008	Y	272	7
3/27/2008	Y	272	4
4/28/2008	Y	266	7
5/14/2008	Y	263	6
5/23/2008	N		
6/8/2008	?	261	3
6/15/2008	Y	258	6
6/24/2008	?	258	4
7/1/2008	N		
7/10/2008	N		
7/17/2008	?	260	3
8/2/2008	N		
8/18/2008	?	258	2
8/27/2008	N		
9/12/2008	N		
9/28/2008	N		
10/5/2008	Y	261	4
10/14/2008	Y	271	5
10/21/2008	Y	271	8
11/6/2008	Y	270	7
11/22/2008	Y	270	4
12/17/2008	Y	271	5
12/24/2008	Y	276	7
1/2/2009	Y	276	6
1/9/2009	Y	272	8
1/18/2009	Y	273	5
1/25/2009	Y	271	4
2/3/2009	Y	275	8
2/10/2009	Y	275	6
2/19/2009	Y	273	6
3/7/2009	Y	272	4
4/15/2009	Y	268	9
4/24/2009	Y	267	5
5/1/2009	Y	267	5
5/10/2009	Y	265	5
5/17/2009	?	266	3
6/11/2009	?	261	3
6/18/2009	N		
7/4/2009	N		
8/5/2009	N		
8/21/2009	N		
9/6/2009	N		
9/22/2009	?	260	3
10/1/2009	N		
10/8/2009	Y	267	4
10/24/2009	Y	270	8
12/4/2009	Y	274	6
1/12/2010	Y	276	6

	1/28/2010	Y	273	5
	2/13/2010	Y	277	5
	2/22/2010	Y	274	4
44) Láscar				
1505-10	5/1/2000	Y	326	
	7/4/2000	Y	328	69-71
	7/27/2000	Y	345	86
	9/22/2000	Y	301	48
	12/27/2000	Y	345	85-86
	12/27/2000	Y	369	103-106
	1/6/2002	Y	344	
	4/5/2002	Y	304	44
	5/23/2002	Y	324	60
	6/15/2002	Y	325	
	6/15/2002	Y	340	
	6/24/2002	Y	319	54-56
	7/17/2002	Y	290	32-33
	10/5/2002	Y	313	50-54
	10/5/2002	Y	327	67
	1/2/2003	Y	318	58
	6/11/2003	Y	303	43
	11/9/2003	Y	300	36
	1/21/2004	Y	310	47-49
	1/28/2004	Y	304	38
	5/3/2004	Y	309	49
	5/28/2004	Y	311	43
	6/4/2004	Y	294	
	6/4/2004	Y	327	
	6/13/2004	Y	309	39-43
	7/15/2004	Y	320	52-54
	7/15/2004	Y	308	8-10
	7/31/2004	Y	304	42
	8/7/2004	Y	313	54
	9/1/2004	Y	316	52-56
	9/8/2004	Y	293	38
	9/24/2004	Y	307	48
	11/27/2004	Y	289	31
	12/13/2004	Y	299	37
	1/23/2005	Y	301	
	1/30/2005	Y	350	78-80
	3/28/2005	Y	332	60-64
	4/13/2005	Y	329	59-62
	4/29/2005	Y	342	72-76
	6/7/2005	Y	322	56-58
	6/7/2005	Y	317	52-54
	6/23/2005	Y	370	104
	6/23/2005	Y	339	75
	8/10/2005	Y	352	87
	8/26/2005	Y	362	99-102
	8/26/2005	Y	338	68-71
	9/27/2005	Y	334	63-66
	10/22/2005	Y	340	73-76
	10/22/2005	Y	330	69-69
	10/29/2005	Y	278	20-22

	11/23/2005	Y	291	28
	1/1/2006	Y	280	18
	3/6/2006	Y	289	28
	3/15/2006	Y	294	23-26
	3/22/2006	Y	296	31-32
	4/7/2006	Y	283	20
	4/7/2006	Y	284	15-22
	5/9/2006	Y	283	21
	6/17/2006	Y	280	17
	8/6/2006	Y	279	17
	8/29/2006	Y	283	
	11/17/2006	Y	279	
	2/21/2007	Y	282	
	3/2/2007	Y	283	16
	3/18/2007	Y	326	63
	4/10/2007	Y	335	69
	5/12/2007	Y	282	17
	6/13/2007	Y	342	77
	7/15/2007	Y	306	45
	11/20/2007	Y	341	79
	11/29/2007	Y	313	54
	12/6/2007	Y	301	39
	2/17/2008	Y	309	50
	2/24/2008	Y	345	86
	8/11/2008	Y	313	55
	10/14/2008	Y	300	42
	10/14/2008	Y	327	67
	10/21/2008	Y	306	44
	11/22/2008	Y	305	43
	11/22/2008	Y	281	21
	12/1/2008	Y	316	56
	12/1/2008	Y	335	76
	12/17/2008	Y	367	104
	12/24/2008	Y	283	23
	1/2/2009	Y	307	48
	1/9/2009	Y	283	21
	1/25/2009	Y	279	16
	1/25/2009	Y	326	65

45) Cordón de Puntas Negras

1505-101	7/27/2000	N
	1/6/2002	N
	4/5/2002	N
	6/24/2002	N
	10/5/2002	N
	3/7/2003	N
	8/30/2003	N
	1/21/2004	N
	6/13/2004	N
	11/27/2004	N
	11/27/2004	N
	12/13/2004	N
	6/7/2005	N
	8/10/2005	N
	8/26/2005	N

	11/23/2005	N
	11/23/2005	N
	1/1/2006	N
	4/7/2006	N
	6/17/2006	N
	6/19/2006	N
	11/17/2006	N
	5/12/2007	N
	6/13/2007	N
	11/4/2007	N
	12/6/2007	N
	12/6/2007	N
	6/15/2008	N
	11/22/2008	N
	12/1/2008	N
	12/24/2008	N
	1/9/2009	N
	6/11/2009	N
	12/4/2009	N

46) Cerro Overo
-23.77S
-67.41W

	5/1/2000	N
	1/6/2002	N
	4/5/2002	N
	6/24/2002	N
	8/30/2003	N
	10/1/2003	N
	6/13/2004	N
	4/13/2005	N
	11/23/2005	N
	6/19/2006	N
	11/29/2007	N
	12/1/2008	N
	1/2/2009	N
	1/9/2009	N
	1/18/2009	N
	2/3/2009	N
	12/4/2009	N

47) Cerro Tujle

1505-103	4/28/2002	N
	6/15/2002	N
	8/18/2002	N
	12/24/2002	N
	11/9/2003	N
	7/9/2005	N
	8/10/2005	N
	10/29/2005	N
	1/1/2006	N
	2/2/2006	N
	2/18/2006	N
	5/9/2006	N
	8/13/2006	N

	2/21/2007	N		
	4/10/2007	N		
	5/12/2007	N		
	5/28/2007	N		
	7/15/2007	N		
	1/23/2008	N		
	3/27/2008	N		
	5/14/2008	N		
	5/30/2008	N		
	7/1/2008	N		
	7/17/2008	N		
	8/2/2008	N		
	8/18/2008	N		
	10/5/2008	N		
	10/21/2008	N		
	11/6/2008	N		
	11/22/2008	N		
	12/8/2008	N		
	12/24/2008	N		
	2/10/2009	N		
	4/15/2009	N		
	5/1/2009	N		
	5/17/2009	N		
	6/18/2009	N		
	7/4/2009	N		
	8/5/2009	N		
	8/21/2009	N		
	9/6/2009	N		
	9/22/2009	N		
	10/8/2009	N		
	10/24/2009	N		
	1/12/2010	N		
	1/28/2010	N		
	2/13/2010	N		
48) El Negrillar				
1505-106	4/28/2002	N		
	8/18/2002	N		
	4/6/2003	N		
	6/9/2003	N		
	5/26/2004	N		
	4/11/2005	N		
	7/25/2005	N		
	1/8/2006	N		
	2/18/2006	N		
	8/13/2006	N		
	3/9/2007	N		
	5/28/2007	N		
	3/11/2008	N		
	6/22/2008	N		
	4/6/2009	N		
	8/12/2009	N		
49) Pular/Pajonales				
1505-107	4/28/2002	Y	267	12

	8/18/2002	N		
	12/24/2002	Y	277	16
	4/6/2003	Y	275	14
	6/9/2003	N		
	12/11/2003	Y	274	13
	5/26/2004	N		
	4/11/2005	Y	257	5
	10/29/2005	N		
	2/18/2006	Y	273	13
	8/13/2006	N		
	2/21/2007	Y	273	14
	5/28/2007	N		
	10/10/2007	Y	265	9
	3/11/2008	N		
	5/30/2008	Y	262	7
	6/22/2008	N		
	4/6/2009	Y	269	8
	5/8/2009	Y	263	7

50) Socompa

1505-109	4/28/2002	N
	4/28/2002	N
	8/18/2002	N
	8/18/2002	N
	12/24/2002	N
	12/24/2002	N
	4/6/2003	N
	6/9/2003	N
	12/11/2003	N
	12/11/2003	N
	4/11/2005	N
	2/18/2006	N
	2/18/2006	N
	8/13/2006	N
	8/13/2006	N
	11/1/2006	N
	11/1/2006	N
	3/9/2007	N
	3/9/2007	N
	5/28/2007	N
	5/28/2007	N
	7/31/2007	N
	10/10/2007	N
	1/30/2008	N
	3/11/2008	N
	3/11/2008	N
	4/3/2008	N
	5/30/2008	N
	6/22/2008	N
	7/8/2008	N
	7/24/2008	N
	9/10/2008	N
	9/26/2008	N
	10/12/2008	N
	12/15/2008	N

	2/17/2009	N
	4/6/2009	N
	5/8/2009	N
	5/24/2009	N
	8/12/2009	N
	8/28/2009	N
	9/13/2009	N
	9/29/2009	N
	11/16/2009	N
	12/2/2009	N

51) Llullaillaco

1505-11	6/22/2002	N
	8/2/2002	N
	11/6/2002	N
	12/8/2002	N
	1/9/2003	N
	1/19/2004	N
	3/3/2005	N
	3/19/2005	N
	7/16/2005	N
	7/25/2005	N
	1/8/2006	N
	2/25/2006	N
	4/14/2006	N
	6/1/2006	N
	7/19/2006	N
	9/5/2006	N
	11/1/2006	N
	3/9/2007	N
	4/1/2007	N
	4/17/2007	N
	11/11/2007	N
	1/30/2008	N
	3/11/2008	N
	4/3/2008	N
	7/8/2008	N
	7/24/2008	N
	9/10/2008	N
	9/26/2008	N
	10/12/2008	N
	11/13/2008	N
	12/15/2008	N
	12/31/2008	N
	2/17/2009	N
	3/14/2009	N
	5/24/2009	N
	7/11/2009	N
	8/12/2009	N
	8/28/2009	N
	9/13/2009	N
	9/29/2009	N
	11/16/2009	N
	12/2/2009	N
	12/18/2009	N

	1/19/2010	N		
52) Escorial				
1505-112	8/2/2002	N		
	11/6/2002	N		
	6/9/2003	N		
	12/11/2003	N		
	1/19/2004	N		
	3/3/2005	N		
	1/8/2006	N		
	2/25/2006	N		
	4/14/2006	N		
	6/1/2006	N		
	9/5/2006	N		
	11/1/2006	N		
	10/10/2007	N		
	11/11/2007	N		
	1/30/2008	N		
	3/18/2008	N		
	4/3/2008	N		
	7/8/2008	N		
	7/24/2008	N		
	9/10/2008	N		
	9/26/2008	N		
	10/12/2008	N		
	11/13/2008	N		
	12/15/2008	N		
	2/17/2009	N		
	3/14/2009	N		
	3/30/2009	N		
	5/24/2009	N		
	7/11/2009	N		
	8/12/2009	N		
	8/28/2009	N		
	9/13/2009	N		
	9/29/2009	N		
	11/16/2009	N		
	12/2/2009	N		
	1/19/2010	N		
53) Lastarria				
1505-12	1/13/2002	Y	280	9
	8/2/2002	Y	270	13
	11/6/2002	Y	274	9
	12/8/2002	Y	277	11
	1/19/2004	Y	281	13
	3/3/2005	Y	280	9
	3/19/2005	Y	281	14
	7/16/2005	Y	267	13
	7/25/2005	Y	269	13
	1/8/2006	Y	283	13
	2/25/2006	Y	286	17
	4/14/2006	Y	280	16
	6/1/2006	Y	277	12
	7/19/2006	Y	281	16

	9/5/2006	Y	275	18
	3/9/2007	Y	282	12
	4/1/2007	Y	279	13
	4/17/2007	Y	283	12
	7/22/2007	Y	270	15
	11/11/2007	Y	274	13
	1/30/2008	Y	285	16
	3/18/2008	Y	283	12
	4/3/2008	Y	278	16
	7/8/2008	Y	275	19
	7/24/2008	Y	278	19
	9/10/2008	Y	275	15
	9/26/2008	Y	275	15
	10/12/2008	Y	276	11
	11/13/2008	Y	279	11
	12/15/2008	Y	284	17
	12/31/2008	Y	285	15
	2/17/2009	Y	280	12
	3/14/2009	Y	281	12
	3/30/2009	Y	286	19
	5/24/2009	Y	283	22
	7/11/2009	Y	276	21
	8/12/2009	Y	277	17
	8/28/2009	Y	278	14
	9/13/2009	Y	279	20
	9/29/2009	Y	276	14
	11/16/2009	Y	287	20
	12/2/2009	Y	286	17
	12/18/2009	Y	287	16
	1/19/2010	Y	279	10

54) Cordón del Azufre

1505-121	1/13/2002	N
	1/13/2002	N
	5/30/2002	N
	8/2/2002	N
	12/8/2002	N
	1/19/2004	N
	5/10/2004	N
	3/3/2005	N
	3/19/2005	N
	5/13/2005	N
	7/16/2005	N
	7/16/2005	N
	1/8/2006	N
	2/25/2006	N
	4/14/2006	N
	4/14/2006	N
	7/19/2006	N
	9/5/2006	N
	3/9/2007	N
	4/1/2007	N
	4/1/2007	N
	4/17/2007	N
	4/17/2007	N

	7/22/2007	N
	11/11/2007	N
	11/11/2007	N
	1/30/2008	N
	1/30/2008	N
	3/18/2008	N
	7/8/2008	N
	7/8/2008	N
	7/24/2008	N
	7/24/2008	N
	9/10/2008	N
	9/10/2008	N
	9/26/2008	N
	9/26/2008	N
	10/12/2008	N
	10/12/2008	N
	11/13/2008	N
	11/13/2008	N
	12/15/2008	N
	12/15/2008	N
	12/31/2008	N
	12/31/2008	N
	2/17/2009	N
	2/17/2009	N
	3/14/2009	N
	3/30/2009	N
	5/24/2009	N
	5/24/2009	N
	7/11/2009	N
	8/12/2009	N
	8/28/2009	N
	8/28/2009	N
	9/13/2009	N
	9/13/2009	N
	9/29/2009	N
	11/16/2009	N
	11/16/2009	N
	12/2/2009	N
	12/2/2009	N
	12/18/2009	N
	1/19/2010	N
	1/19/2010	N
55) Bayo		
1505-122	3/19/2005	N
	1/8/2006	N
	7/19/2006	N
	1/30/2008	N
	7/8/2008	N
	7/24/2008	N
	11/13/2008	N
	12/15/2008	N
	8/12/2009	N
	8/28/2009	N
	9/13/2009	N

	9/29/2009	N		
56) Antofalla				
-25.56S	6/28/2001	N		
-67.90W	4/28/2002	N		
	11/6/2002	N		
	12/24/2002	N		
	4/6/2003	N		
	12/11/2003	N		
	2/13/2004	N		
	5/26/2004	N		
	7/25/2005	N		
	11/5/2005	N		
	1/8/2006	N		
	2/18/2006	N		
	4/14/2006	N		
	8/13/2006	N		
	11/1/2006	N		
	3/9/2007	N		
	5/28/2007	N		
	7/31/2007	N		
	10/10/2007	N		
	1/30/2008	N		
	3/11/2008	N		
	7/8/2008	N		
	7/24/2008	N		
	11/13/2008	N		
	12/15/2008	N		
	4/6/2009	N		
	5/8/2009	N		
	7/11/2009	N		
	8/12/2009	N		
	8/28/2009	N		
	9/13/2009	N		
	9/29/2009	N		
57) Sierra Nevada				
1505-123	5/30/2002	N		
	12/8/2002	N		
	2/1/2003	N		
	3/10/2005	N		
	5/13/2005	N		
	9/18/2005	N		
	2/9/2006	?	266	4
	7/19/2006	N		
	11/8/2006	N		
	4/1/2007	N		
	11/11/2007	N		
	3/2/2008	N		
	12/31/2008	?	270	7
	3/5/2009	N		
	3/30/2009	N		
	1/19/2010	N		
58) Falso Azufre				

1505-124	2/7/2002	Y	268	8
	5/30/2002	?	252	2
	12/8/2002	Y	267	9
	2/1/2003	Y	272	4
	3/3/2005	Y	270	4
	3/10/2005	Y	266	5
	3/19/2005	Y	267	4
	5/13/2005	Y	263	7
	7/16/2005	N		
	9/11/2005	N		
	9/18/2005	N		
	2/9/2006	Y	274	8
	7/19/2006	N		
	11/8/2006	?	261	2
	4/1/2007	Y	264	4
	6/29/2007	Y	254	6
	9/1/2007	N		
	11/11/2007	?	258	3
	3/2/2008	Y	270	12
	12/31/2008	Y	266	5
	3/5/2009	?	269	3
	3/30/2009	Y	268	9
	1/19/2010	Y	268	7

59) Ojos del Salado

1505-13	2/1/2003	Y	275	20
	9/18/2005	Y	261	15
	2/9/2006	Y	282	22
	11/8/2006	Y	267	14
	4/1/2007	Y	269	16
	3/2/2008	Y	276	26
	3/5/2009	Y	278	23

60) El Solo

1505-131	2/2/2001	N
	2/1/2003	N
	3/7/2004	N
	7/7/2005	N
	8/17/2005	N
	9/18/2005	N
	9/25/2005	N
	10/11/2005	N
	1/31/2006	N
	2/9/2006	N
	11/8/2006	N
	6/27/2007	N
	7/13/2007	N
	11/27/2007	N
	1/5/2008	N
	1/21/2008	N
	3/2/2008	N
	8/16/2008	N
	11/4/2008	N
	11/20/2008	N
	1/7/2009	N

	1/23/2009	N
	2/8/2009	N
	2/24/2009	N
	3/5/2009	N
	8/3/2009	N
	9/20/2009	N
	10/22/2009	N
	11/23/2009	N
	12/9/2009	N

62) Cerro el Condor

1505-19	2/7/2002	N
	5/30/2002	N
	12/8/2002	N
	3/3/2005	N
	3/10/2005	N
	3/19/2005	N
	3/19/2005	N
	5/13/2005	N
	7/16/2005	N
	9/11/2005	N
	9/18/2005	N
	2/9/2006	N
	7/19/2006	N
	11/8/2006	N
	4/1/2007	N
	4/17/2007	N
	6/29/2007	N
	9/1/2007	N
	11/11/2007	N
	3/2/2008	N
	12/31/2008	N
	3/30/2009	N
	1/19/2010	N

63) Peinado

1505-20	2/7/2002	N
	5/30/2002	N
	12/8/2002	N
	3/3/2005	N
	3/10/2005	N
	3/19/2005	N
	5/13/2005	N
	7/16/2005	N
	9/11/2005	N
	7/19/2006	N
	4/1/2007	N
	4/26/2007	N
	6/29/2007	N
	9/1/2007	N
	11/11/2007	N
	12/31/2008	N
	3/30/2009	N
	1/19/2010	N

64) Tipas				
1505-22	2/1/2003	N		
	9/18/2005	N		
	1/31/2006	N		
	2/9/2006	N		
	11/8/2006	N		
	11/27/2007	N		
	3/2/2008	N		
	3/5/2009	N		
65) Tupungatito				
1507-01	12/19/2001	Y	290	30
	10/10/2002	Y	275	25
	1/23/2003	Y		30
	3/12/2003	Y		10-15
	11/12/2005	Y	285	32
	11/12/2005	Y	287	35
	3/27/2006	Y		25
	12/8/2006	Y	288	28
	5/10/2007	Y	285	30
	11/9/2007	Y	285	35
	1/12/2008	Y	295	30
	2/13/2008	Y	295	30
	7/22/2008	Y	280	35
	10/10/2008	Y	290	40
	10/26/2008	Y	288	38
	11/11/2008	Y	290	30
	12/13/2008	Y	290	35
	12/29/2008	Y	295	
	1/14/2009	Y	297	30
	3/3/2009	Y	295	25
	3/12/2009	Y	295	35
	3/19/2009	Y	295	30
	3/28/2009	Y	295	30
	4/20/2009	Y	295	32
	4/29/2009	Y	292	32
	5/6/2009	Y	292	35
	7/9/2009	Y	282	32
	8/10/2009	Y	284	34
66) Piuquenes				
-33.53S	12/19/2001	N		
-69.82W	10/10/2002	N		
	12/8/2006	N		
	5/10/2007	N		
	11/9/2007	N		
	7/22/2008	N		
	10/10/2008	N		
	10/26/2008	N		
	11/11/2008	N		
	12/13/2008	N		
	12/29/2008	N		
	3/12/2009	N		
	3/28/2009	N		
	4/20/2009	N		

	4/29/2009	N	
	5/6/2009	N	
	8/10/2009	N	
67) San Jose			
1507-02	10/10/2002	N	
	1/26/2004	N	
	1/26/2005	N	
	3/27/2006	N	
	4/3/2006	?	5
	12/8/2006	N	
	11/9/2007	N	
	1/12/2008	N	
	2/13/2008	N	
	7/22/2008	N	
	10/1/2008	N	
	10/10/2008	N	
	10/26/2008	N	
	11/2/2008	N	
	11/11/2008	N	
	11/18/2008	N	
	12/13/2008	N	
	12/29/2008	N	
	1/5/2009	N	
	1/14/2009	N	
	2/22/2009	N	
	3/3/2009	N	
	3/19/2009	N	
	4/20/2009	N	
	5/6/2009	N	
	7/9/2009	N	
	8/10/2009	N	
68) Maipo			
1507-021	10/10/2002	N	
	8/10/2003	N	
	1/26/2004	N	
	2/2/2004	N	
	5/8/2004	N	
	1/26/2005	N	
	3/27/2006	N	
	4/3/2006	N	
	3/14/2007	N	
	5/24/2007	N	
	1/12/2008	N	
	2/13/2008	N	
	7/22/2008	N	
	10/1/2008	N	
	10/26/2008	N	
	11/2/2008	N	
	11/11/2008	N	
	11/18/2008	N	
	12/13/2008	N	
	12/29/2008	N	
	1/5/2009	N	

	1/14/2009	N
	2/22/2009	N
	3/3/2009	N
	3/19/2009	N
	4/20/2009	N
	5/6/2009	N
	7/9/2009	N
	8/10/2009	N

69) Listado

-34.3S	10/10/2002	N
-69.93W	8/10/2003	N
	12/7/2003	N
	1/26/2005	N
	4/3/2006	N
	3/14/2007	N
	5/24/2007	N
	1/12/2008	N
	2/13/2008	N
	7/22/2008	N
	10/26/2008	N
	11/2/2008	N
	11/11/2008	N
	11/18/2008	N
	12/13/2008	N
	12/29/2008	N
	1/14/2009	N
	2/22/2009	N
	3/3/2009	N
	3/19/2009	N
	4/20/2009	N
	5/6/2009	N
	7/9/2009	N
	8/10/2009	N

70) Caldera del Atuel

1507-023	10/10/2002	N
	1/26/2005	N
	4/16/2005	N
	4/16/2005	N
	8/31/2005	N
	4/3/2006	N
	3/14/2007	N
	5/24/2007	N
	7/22/2008	N
	10/26/2008	N
	11/2/2008	N
	11/18/2008	N
	2/22/2009	N
	3/3/2009	N
	3/19/2009	N
	4/20/2009	N
	5/6/2009	N
	7/9/2009	N
	8/10/2009	N

71) Palomo				
1507-022	12/7/2003	N		
	1/26/2005	N		
	4/16/2005	N		
	4/16/2005	N		
	8/31/2005	N		
	2/14/2006	N		
	4/3/2006	N		
	3/16/2008	N		
	11/2/2008	N		
	2/22/2009	N		
	3/10/2009	N		
	7/16/2009	N		
72) Tinguiririca				
1507-03	12/7/2003	N		
	1/26/2005	N		
	4/16/2005	N		
	8/31/2005	N		
	2/14/2006	N		
	3/16/2008	N		
	2/22/2009	N		
	3/10/2009	N		
	7/16/2009	N		
73) Risco Plateado				
1507-024	4/24/2002	N		
	1/26/2005	N		
	4/3/2006	N		
	8/25/2006	N		
	3/16/2008	N		
	10/1/2008	N		
	11/2/2008	N		
	11/18/2008	N		
74) Alto del Padre				
-35S	2/9/2004	N		
-70.48W	3/5/2004	N		
	2/11/2005	N		
	4/6/2007	N		
	7/29/2008	N		
	4/27/2009	N		
75) Planchón-Peteroa				
1507-04	4/11/2003	Y	305	40
	5/6/2003	Y	305	38
	6/30/2003	Y	290	28
	10/20/2003	Y	295	32
	11/30/2003	Y	298	30
	1/8/2004	Y	305	35
	2/9/2004	Y		30
	3/5/2004	Y		30
	11/23/2004	Y	305	35
	2/4/2005	Y		35

	2/11/2005	Y		25
	4/9/2005	Y	300	30
	7/5/2005	Y	288	35
	3/11/2006	N		
	10/21/2006	Y	295	30
	2/26/2007	Y	298	25
	4/6/2007	Y	298	30
	1/3/2008	Y	290	20
	2/4/2008	Y	295	20
	3/23/2008	Y	294	24
	4/17/2008	Y	288	18
	7/29/2008	Y	285	25
	8/23/2008	Y	285	25
	4/27/2009	Y	300	30
	6/23/2009	Y	292	40
	7/25/2009	Y	292	35

76) Caldera del Colorado

-35.3S	10/20/2003	N
-70.53W	11/30/2003	N
	1/8/2004	N
	2/9/2004	N
	3/5/2004	N
	11/23/2004	N
	2/11/2005	N
	10/21/2006	N
	2/26/2007	N
	4/6/2007	N
	1/3/2008	N
	2/4/2008	N
	3/23/2008	N
	4/17/2008	N
	7/29/2008	N
	8/23/2008	N
	4/27/2009	N
	6/23/2009	N
	7/25/2009	N

77) Descabezado Chico

-35.52S	2/15/2003	N
-70.62W	5/6/2003	N
	11/30/2003	N
	2/9/2004	N
	3/5/2004	N
	2/4/2005	N
	2/11/2005	N
	4/9/2005	N
	7/5/2005	N
	10/21/2006	N
	10/28/2006	N
	4/6/2007	N
	6/9/2007	N
	2/4/2008	N
	3/23/2008	N
	4/17/2008	N

	7/29/2008	N		
	8/23/2008	N		
	4/27/2009	N		
	6/23/2009	N		
	7/25/2009	N		
78) Volcán la Palizada				
-35.53S	2/15/2003	N		
-70.82W	11/30/2003	N		
	2/9/2004	N		
	2/4/2005	N		
	10/21/2006	N		
	10/28/2006	N		
	4/6/2007	N		
	6/9/2007	N		
	2/4/2008	N		
	3/23/2008	N		
	4/17/2008	N		
	7/29/2008	N		
	8/23/2008	N		
	4/27/2009	N		
	6/23/2009	N		
	7/25/2009	N		
79) Volcán Rajaderas				
-35.53S	2/15/2003	N		
-70.72W	11/30/2003	N		
	2/9/2004	Y	284/287	14/15
	2/4/2005	Y	283/285	8/9
	10/21/2006	N		
	10/28/2006	N		
	4/6/2007	Y	278	8
	6/9/2007	N		
	2/4/2008	Y	286/290	7/12
	3/23/2008	?	280/284	8/12
	4/17/2008	N		
	7/29/2008	N		
	8/23/2008	N		
	4/27/2009	N		
	6/23/2009	N		
	7/25/2009	N		
80) Colorado				
-35.53S	2/15/2003	N		
-70.68W	11/30/2003	N		
	2/9/2004	N		
	2/4/2005	N		
	2/11/2005	N		
	10/21/2006	N		
	10/28/2006	N		
	6/9/2007	N		
	2/4/2008	N		
	3/23/2008	N		
	4/17/2008	N		
	7/29/2008	N		

	8/23/2008	N		
	4/27/2009	N		
	6/23/2009	N		
	7/25/2009	N		

81) Volcán Alto de las Mulas

-35.55S	2/15/2003	N		
-70.82W	11/30/2003	N		
	2/9/2004	N		
	2/4/2005	N		
	10/21/2006	N		
	10/28/2006	N		
	4/6/2007	N		
	6/9/2007	N		
	2/4/2008	N		
	3/23/2008	N		
	4/17/2008	N		
	7/29/2008	N		
	8/23/2008	N		
	4/27/2009	N		
	6/23/2009	N		
	7/25/2009	N		

82) Calabozos/Volcán del Medio

1507-042	2/15/2003	N		
	5/6/2003	N		
	11/30/2003	N		
	2/9/2004	Y	279	6
	3/5/2004	Y	281	9
	2/4/2005	Y	281	5
	4/9/2005	N		
	7/5/2005	N		
	3/11/2006	N		
	10/21/2006	N		
	10/28/2006	N		
	2/26/2007	N		
	4/6/2007	N		
	2/4/2008	N		
	3/23/2008	Y	280	5
	4/17/2008	Y	278	12
	7/29/2008	N		
	8/23/2008	N		
	4/27/2009	Y	280	10
	6/23/2009	N		
	7/25/2009	N		

83) Descabezado Grande

1507-05	2/15/2003	N		
	5/6/2003	Y	278	8
	11/30/2003	Y	275	5
	2/9/2004	N		
	2/4/2005	N		
	2/11/2005	N		
	4/9/2005	N		
	7/5/2005	N		

	3/11/2006	Y		7
	10/21/2006	N		
	10/28/2006	N		
	4/6/2007	Y	280	10
	6/9/2007	Y	267	7
	2/4/2008	N		
	3/23/2008	Y	285	12
	4/17/2008	Y	278	10
	7/29/2008	Y	267	7
	8/23/2008	N		
	4/27/2009	Y	283	13
	6/23/2009	N		
	7/25/2009	N		

84) Cerro Azul

1507-06	2/15/2003	N		
	4/11/2003	N		
	11/30/2003	?	275	5
	2/9/2004	N		
	2/4/2005	N		
	2/11/2005	N		
	4/9/2005	Y	281	9
	7/5/2005	Y	262	12
	3/11/2006	?		4
	10/21/2006	N		
	10/28/2006	N		
	4/6/2007	N		
	6/9/2007	N		
	2/4/2008	N		
	3/23/2008	N		
	4/17/2008	N		
	7/29/2008	N		
	8/23/2008	N		
	4/27/2009	Y	275	10
	6/23/2009	N		
	7/25/2009	N		

85) San Pedro-Pellado

1507-062	4/11/2003	N		
	5/6/2003	N		
	11/30/2003	N		
	5/24/2004	?	275	10
	3/24/2005	N		
	11/3/2005	N		
	3/11/2006	N		
	6/9/2007	N		
	3/23/2008	N		

86) Laguna del Maule

1507-061	5/6/2003	N		
	11/30/2003	N		
	5/24/2004	N		
	3/24/2005	N		
	11/3/2005	N		
	3/11/2006	N		

	1/3/2008	N		
	2/4/2008	N		
	8/23/2008	N		
87) Nevado de Longavi				
1507-063	11/25/2002	?	275	4
88) Lomas Blancas				
1507-064	11/25/2002	N		
	10/9/2005	N		
	6/9/2007	N		
89) Resago				
1507-065	11/25/2002	N		
	7/23/2003	N		
	10/9/2005	N		
	6/9/2007	N		
90) Volcán Domuyo				
1507-067	5/6/2003	N		
	3/24/2005	N		
	11/3/2005	N		
	3/11/2006	N		
	2/4/2008	N		
	7/29/2008	N		
	8/23/2008	N		
91) Volcán Cochiquito				
1507-071	3/5/2004	N		
	8/31/2005	N		
	10/25/2005	N		
	3/11/2006	N		
	2/26/2007	N		
	2/4/2008	N		
	7/29/2008	N		
92) Nevados de Chillán				
1507-07	2/7/2001	Y	284	5
	12/17/2001	Y	293	13
	12/24/2001	Y	296	16
	12/11/2002	Y	283	11
	3/17/2003	Y	289	9
	7/23/2003	Y	270	10
	8/24/2003	Y	273	13
	1/17/2005	Y	287	7
	2/2/2005	Y	289	14
	2/18/2005	Y	288	10
	4/23/2005	Y	286	14
	8/6/2005	Y	266	4
	11/1/2005	Y	283	13
	1/29/2006	Y	294	14
	3/9/2006	Y	282	9
	4/10/2006	Y	288	12
	10/19/2006	Y	276	10
	12/6/2006	Y	287	13

	3/5/2007	N		
	4/13/2007	N		
	5/8/2007	Y	278	12
	8/12/2007	Y	274	9
	10/15/2007	Y	276	12
	3/14/2008	Y	308	28
	4/24/2008	Y	320	45
	6/18/2008	Y	312	47
	8/5/2008	Y	285	25
	8/21/2008	Y	292	33
	1/12/2009	Y	287	7
	3/26/2009	Y	281	9
	6/5/2009	Y	278	9
	8/8/2009	Y	270	9
	11/12/2009	Y	276	10
	3/13/2010	Y	285	7
	3/29/2010	Y	291	10

93) Tromen

1507-072	5/6/2003	N		
	3/5/2004	N		
	1/19/2005	N		
	3/24/2005	N		
	8/31/2005	N		
	3/11/2006	N		
	2/26/2007	N		
	1/3/2008	N		
	2/4/2008	N		
	8/23/2008	N		

94) Puesto Cortaderas

1507-073	3/5/2004	N		
	1/19/2005	N		
	2/26/2007	N		

95) Copahue

1507-09	3/17/2003	Y		40
	7/16/2003	Y	308	48
	8/8/2003	Y	292	30
	12/30/2003	Y	288	15
	10/29/2004	Y	292	28
	1/10/2005	Y		25
	1/17/2005	N		
	2/2/2005	Y	305	35
	2/18/2005	Y	315	35
	10/16/2005	Y	308	48
	3/2/2006	Y		25
	4/10/2006	Y	304	35
	10/19/2006	Y	300	30
	4/13/2007	Y	302	35
	8/19/2007	Y	298	38
	2/20/2008	Y	308	38
	8/21/2008	Y	298	38
	9/15/2008	Y	305	40
	10/17/2008	Y	310	40

	12/20/2008	Y	312	40
	1/12/2009	Y	310	35
	1/21/2009	Y	310	35
96) Caldera del Agrio				
-37.85S	3/17/2003	N		
-71.00W	2/18/2005	N		
	4/13/2007	N		
	8/21/2008	N		
97) Callaqui				
1507-091	2/3/2002	Y		8
	3/17/2003	Y		10
	7/16/2003	N		
	8/8/2003	Y	262	4
	12/30/2003	Y	278	7
	10/29/2004	N		
	1/10/2005	Y		5
	1/17/2005	Y		20
	10/16/2005	Y	268	12
	3/2/2006	Y		7
	4/10/2006	Y	288	7
	4/26/2006	Y	277	4
	10/19/2006	Y	272	7
	4/13/2007	Y	272	5
	7/27/2007	?	268	3
	8/19/2007	?	262	5
	2/20/2008	Y	282	7
	8/21/2008	N	262	5
	9/15/2008	Y	272	10
	10/17/2008	Y	272	10
	12/20/2008	Y	287	7
	1/12/2009	Y	280	8
	1/21/2009	Y	282	10
98) Laguna Marinaqui				
1507-092	12/24/2001	N		
	2/3/2002	N		
	12/2/2002	N		
	3/17/2003	N		
	3/22/2005	N		
	3/2/2006	N		
	4/10/2006	N		
	7/27/2007	N		
	3/14/2008	N		
	8/21/2008	N		
	9/15/2008	N		
	10/17/2008	N		
99) Tolhuaca				
1507-093	12/28/2000	N		
	12/24/2001	N		
	12/31/2001	N		
	2/3/2002	N		
	1/3/2003	N		

	3/8/2003	N		
	7/16/2003	N		
	4/27/2004	N		
	1/10/2005	N		
	2/25/2005	N		
	3/22/2005	?	285	10
	9/21/2005	N		
	1/27/2006	N		
	3/2/2006	N		
	11/11/2006	N		
	3/19/2007	N		
	4/13/2007	N		
	4/20/2007	N		
	7/27/2007	N		
	1/1/2008	N		
	2/20/2008	N		
	9/15/2008	N		
	10/17/2008	N		
	10/24/2008	N		
	10/31/2008	?	272	5
	12/11/2008	N		
	12/20/2008	N		
	1/19/2009	N		
	2/20/2009	N		
	4/9/2009	N		
100) Volcán Navidad				
-38.36S	12/24/2001	Y	292	7
-71.55	11/11/2006	Y	285	8
	4/13/2007	Y	280	8
	8/21/2008	Y	270	10
	10/24/2008	Y	280	10
	10/31/2008	Y	282	12
	12/11/2008	Y	288	10
101) Lonquimay				
1507-10	12/24/2001	N		
	12/31/2001	N		
	1/3/2003	N		
	3/8/2003	N		
	3/17/2003	N		
	4/27/2004	N		
	2/25/2005	N		
	3/22/2005	N		
	9/21/2005	N		
	1/27/2006	N		
	11/11/2006	N		
	3/19/2007	N		
	4/13/2007	N		
	4/20/2007	N		
	1/1/2008	N		
	8/21/2008	N		
	10/24/2008	N		
	10/31/2008	N		
	12/11/2008	N		

	1/19/2009	N		
	2/20/2009	N		
	4/9/2009	N		
102) Cerro Chapulul				
-38.37S	12/24/2001	N		
-71.08W	12/2/2002	N		
	3/17/2003	N		
	3/22/2005	N		
	4/10/2006	N		
	4/13/2007	N		
	3/14/2008	?	288	4
	8/21/2008	N		
103) Llaima				
1507-11	10/18/2000	Y	278	10
	3/27/2001	Y	282	12
	12/31/2001	N		
	7/4/2002	Y	272	10
	1/3/2003	Y	280	12
	2/13/2003	Y		15
	3/8/2003	Y		18
	1/15/2004	Y	278	5
	2/23/2004	Y		10
	3/10/2004	?		5
	3/13/2005	N		
	8/20/2005	Y	271	4
	9/21/2005	Y	270	5
	10/23/2005	Y	269	6
	1/27/2006	?		5 to 10
	3/19/2007	Y	278	5
	1/1/2008	Y	307	35
	1/26/2008	Y	382*	107
	2/11/2008	Y	368*	88
	2/27/2008	Y	309	29
	10/8/2008	Y	290	20
	10/24/2008	Y	298	20
	10/24/2008	Y	290	22
	11/25/2008	Y	295	20
	12/11/2008	Y	288	15
	12/11/2008	Y	290	15
	12/11/2008	Y	288	12
	12/18/2008	Y	290	20
	1/19/2009	Y	288	8
	2/20/2009	Y	275	8
	5/27/2009	Y	295	30
	6/12/2009	Y	300	32
	9/16/2009	Y	280	15
104) Sierra Nevada				
-38.58S	3/27/2001	N		
-71.60W	12/31/2001	N		
	1/3/2003	N		
	3/8/2003	N		
	1/15/2004	N		

	9/21/2005	N
	10/23/2005	N
	1/1/2008	N
	2/27/2008	N
	10/24/2008	N
	11/25/2008	N
	12/11/2008	N
	12/11/2008	N
	12/18/2008	N
	1/19/2009	N
	2/20/2009	N
	5/27/2009	N
	6/12/2009	N
	9/16/2009	N

105) Sollipulli

1507-111	10/18/2000	N
	12/31/2001	N
	7/4/2002	N
	1/3/2003	N
	2/13/2003	N
	3/8/2003	N
	3/8/2003	N
	1/15/2004	N
	2/23/2004	N
	3/10/2004	N
	3/13/2005	N
	8/20/2005	N
	9/21/2005	N
	10/23/2005	N
	1/27/2006	N
	1/27/2006	N
	3/19/2007	N
	1/1/2008	N
	2/20/2008	N
	2/27/2008	N
	9/15/2008	N
	10/8/2008	N
	10/24/2008	N
	11/25/2008	N
	12/11/2008	N
	12/11/2008	N
	12/18/2008	N
	1/19/2009	N
	1/21/2009	N
	2/20/2009	N
	5/27/2009	N
	6/12/2009	N
	9/16/2009	N

106) Caburgua

1507-112	10/18/2000	N
	1/3/2003	N
	3/8/2003	N
	1/15/2004	N

	2/23/2004	N			
	3/10/2004	N			
	3/26/2004	N			
	1/20/2006	N			
	1/27/2006	N			
	10/26/2006	N			
	11/27/2006	N			
	2/27/2008	N			
	10/8/2008	N			
	11/16/2008	N			
	11/25/2008	N			
	12/18/2008	N			
	1/3/2009	N			
	1/19/2009	N			
	2/20/2009	N			
	3/8/2009	N			
	3/24/2009	N			
	4/9/2009	N			
	6/12/2009	N			
	7/14/2009	N			
	9/16/2009	N			
107) Villaricca					
1507-12	12/2/2002	Y	312	42	
	1/3/2003	Y	292	22	
	3/8/2003	N			
	4/25/2003	Y	285	35	
	7/30/2003	Y	290	30	
	9/9/2003	Y	305	45	
	2/23/2004	Y		25	
	3/10/2004	Y		40	to 45
	3/26/2004	Y		35	
	9/14/2005	Y	300	38	
	9/21/2005	N			
	10/23/2005	Y	335	75	
	4/17/2006	Y	343	73	
	5/3/2006	Y	325	55	
	10/26/2006	Y	320	50	
	11/20/2006	Y	325	55	
	11/27/2006	Y	335	65	
	2/24/2007	Y	312	40	
	2/11/2008	Y	290	30	
	2/27/2008	Y	284	8	
	10/8/2008	Y	278	8	
	11/25/2008	Y	275	5	
	12/18/2008	Y	302	35	
	1/3/2009	Y	292	20	
	1/19/2009	Y	300	25	
	2/20/2009	Y	272	5	
	3/8/2009	Y	290	15	
	3/24/2009	Y	354	80	
	4/9/2009	Y	300	29	
	4/18/2009	Y	298	30	
	6/12/2009	Y	288	22	
	7/14/2009	N			

	9/16/2009	N
108) Quetrupilián		
1507-121	10/18/2000	N
	12/2/2002	N
	1/3/2003	N
	2/13/2003	N
	3/8/2003	N
	4/25/2003	N
	7/30/2003	N
	9/9/2003	N
	1/15/2004	N
	2/23/2004	N
	3/10/2004	N
	3/26/2004	N
	9/14/2005	N
	9/21/2005	N
	10/23/2005	N
	1/20/2006	N
	1/27/2006	N
	4/17/2006	N
	5/3/2006	N
	10/26/2006	N
	11/20/2006	N
	11/27/2006	N
	2/24/2007	N
	2/11/2008	N
	2/27/2008	N
	10/8/2008	N
	11/16/2008	N
	11/25/2008	N
	12/18/2008	N
	1/3/2009	N
	1/19/2009	N
	2/20/2009	N
	3/1/2009	N
	3/8/2009	N
	3/24/2009	N
	4/9/2009	N
	4/18/2009	N
	6/12/2009	N
	7/14/2009	N
	9/16/2009	N
109) Lanin		
1507-122	10/18/2000	N
	3/27/2001	N
	12/2/2002	N
	2/13/2003	N
	1/15/2004	N
	2/25/2005	N
	9/14/2005	N
	1/20/2006	N
	11/20/2006	N
	2/24/2007	N

	2/11/2008	N		
	2/27/2008	N		
	3/21/2008	N		
	10/8/2008	N		
	10/24/2008	N		
	11/16/2008	N		
	11/25/2008	N		
	12/18/2008	N		
	1/19/2009	N		
	3/8/2009	N		
	3/24/2009	N		
	4/9/2009	N		
	4/18/2009	N		
110) Huanquihue Group				
1507-123	12/2/2002	N		
	2/25/2005	N		
	5/3/2006	N		
	2/24/2007	N		
	2/11/2008	N		
	3/21/2008	N		
	10/8/2008	N		
	11/16/2008	N		
	11/25/2008	N		
	12/18/2008	N		
	1/3/2009	N		
	1/19/2009	N		
	3/8/2009	N		
	3/24/2009	N		
	4/9/2009	N		
	4/18/2009	N		
111) Mocho-Choshuenco				
1507-13	5/3/2006	?	275	5
	2/24/2007	N		
	3/21/2008	?	278	5
	1/3/2009	?	277	4
	4/18/2009	N		
112) Carran-Los Venados				
1507-14	3/5/2002	N		
113) Cordón Caulle				
1507-15	5/13/2004	Y	285	15
	4/29/2007	Y	295	22
	7/9/2007	Y	278	18
	8/3/2007	Y	285	25
	11/14/2007	Y	288	12
	4/22/2008	Y	290	15
114) Puyehue				
1507-15	3/5/2002	N		
	1/31/2004	N		
	5/13/2004	N		
	4/29/2007	Y	288	17

	7/9/2007	Y	272	12
	8/3/2007	Y	275	15
	11/14/2007	Y	278	10
	4/22/2008	Y	288	15
115) Cerro Pantoja				
1507-152	3/5/2002	N		
	1/31/2004	N		
	4/29/2007	N		
	5/6/2007	N		
	7/9/2007	N		
	8/3/2007	N		
116) Antillanca Group				
1507-153	3/5/2002	N		
	1/31/2004	N		
	3/3/2007	N		
	5/6/2007	N		
	8/3/2007	N		
	8/3/2007	N		
117) Volcán Sarnoso				
-40.83S	3/5/2002	N		
-72.32W	1/31/2004	N		
	3/3/2007	N		
	5/6/2007	N		
	7/9/2007	N		
	8/3/2007	N		
	1/24/2008	N		
	12/25/2008	N		
118) Puntiagudo-Cordón Cenizos				
1507-16	3/5/2002	N		
	1/31/2004	Y	279	5
	3/3/2007	N		
	5/6/2007	N		
	7/9/2007	N		
	8/3/2007	N		
	1/24/2008	Y	282	6
	7/2/2008	N		
	12/25/2008	N		
119) Volcán Pichihuinco				
-41.00S	1/29/2004	N		
-72.62W	4/21/2005	N		
	7/2/2008	N		
	10/15/2008	N		
120) Volcán la Picada				
-41.05S	1/31/2004	N		
-72.43W	3/3/2007	N		
	8/3/2007	N		
	7/2/2008	N		
	10/15/2008	N		
	12/25/2008	N		

121) Osorno

1508-01	1/31/2004	N
	3/3/2007	N
	8/3/2007	N
	1/24/2008	N
	7/2/2008	N
	10/15/2008	N
	12/25/2008	N
	12/25/2008	N

122) Volcanes el Negrillar de Ensenada

-41.13S	3/3/2007	N
-72.53W	10/15/2008	N
	12/25/2008	N

123) Volcan Tronador

1508-011	3/5/2002	N
	11/9/2002	N
	2/9/2005	N
	4/29/2007	N
	5/6/2007	N
	7/9/2007	N
	8/3/2007	N

124) Cayute(Cayutue)-La Vigueria

1508-012	11/9/2002	N
	5/2/2003	N
	2/9/2005	N
	4/21/2005	N
	8/3/2007	N
	1/24/2008	N
	7/2/2008	N
	12/25/2008	N

125) Cerro Volcánico

-41.26S	11/9/2002	N
-71.83W	4/29/2007	N
	8/3/2007	N

126) Calbuco

1508-02	12/22/2001	N
	3/12/2002	N
	4/13/2002	N
	10/22/2002	N
	5/2/2003	N
	1/22/2004	N
	4/21/2005	N
	12/1/2005	N
	3/3/2007	N
	1/24/2008	N
	7/2/2008	N
	10/15/2008	N
	12/9/2008	N
	12/25/2008	N

127) Cono Cabeza de Vaca

-41.33S	11/9/2002	N
-72.28W	2/9/2005	N
	4/21/2005	N
	10/10/2006	N
	3/3/2007	N
	8/3/2007	N
	1/24/2008	N
	7/2/2008	N
	12/25/2008	N

128) Cuernos del Diablo

1508-021	11/9/2002	N
	1/31/2004	N
	2/9/2005	N
	7/19/2005	N
	10/10/2006	N
	3/3/2007	N
	8/3/2007	N

129) Cono Rollizo

-41.43S	11/9/2002	N
-72.32W	4/21/2005	N
	3/3/2007	N
	8/3/2007	N
	1/24/2008	N
	7/2/2008	N

130) Cono Pocoihuen

-41.50S	11/9/2002	N
-72.33W	4/21/2005	N
	3/3/2007	N
	8/3/2007	N
	1/24/2008	N
	7/2/2008	N

131) Yate

1508-022	3/12/2002	N
	6/3/2003	N
	1/22/2004	N
	2/9/2005	N
	4/21/2005	N
	7/19/2005	N
	2/3/2006	N
	10/17/2006	N
	3/3/2007	N
	4/27/2007	N
	6/14/2007	N
	1/24/2008	N
	4/13/2008	N
	7/2/2008	N
	12/9/2008	N

132) Volcán Hornopiren

1508-023	10/16/2000	N
	12/22/2001	N
	3/12/2002	N
	7/2/2002	N
	10/22/2002	N
	2/11/2003	N
	6/3/2003	N
	1/22/2004	N
	4/21/2005	N
	7/19/2005	N
	2/3/2006	N
	10/17/2006	N
	3/3/2007	N
	4/27/2007	N
	6/14/2007	N
	1/24/2008	N
	4/13/2008	N
	7/2/2008	N
	12/9/2008	N

133) Volcán Apagado or Hualiaque

1508-024	10/16/2000	N
	12/22/2001	N
	3/12/2002	N
	7/2/2002	N
	10/22/2002	N
	6/3/2003	N
	1/22/2004	N
	4/21/2005	N
	2/3/2006	N
	10/17/2006	N
	4/27/2007	N
	6/14/2007	N
	1/24/2008	N
	4/13/2008	N
	7/2/2008	N
	12/9/2008	N

134) Huequi

1508-03	10/16/2000	N
	3/12/2002	N
	7/2/2002	N
	10/22/2002	N
	2/11/2003	N
	6/3/2003	N
	1/22/2004	N
	2/3/2006	N
	10/17/2006	N
	6/14/2007	N
	12/16/2007	N
	3/5/2008	N
	4/13/2008	N
	10/15/2008	N
	12/9/2008	N

135) Minchinmavida (Michinmahuida)

1508-04	10/22/2002	N		
	2/11/2003	N		
	1/22/2004	N		
	1/31/2005	N		
	10/30/2005	N		
	2/3/2006	N		
	12/16/2007	N		
	3/5/2008	N		
	4/13/2008	N		
	9/29/2008	N		
	10/15/2008	N		
	12/9/2008	N		

136) Chaitén

1508-041	10/22/2002	N		
	2/11/2003	?	285	4
	1/22/2004	?	288	7
	1/31/2005	?	284	12
	10/30/2005	?	277	4
	2/3/2006	?	289	22
	7/29/2006	?	274	4
	4/13/2008	?	278	5
	5/31/2008	Y	375*	100
	6/9/2008	Y	267	10
	8/19/2008	Y	343	71
	9/4/2008	Y	373*	100
	9/29/2008	Y	373*	95
	12/9/2008	Y	373*	100

137) Corcovado

1508-05	2/7/2004	N
	1/31/2005	N
	1/18/2006	N
	7/29/2006	N
	2/18/2008	N
	5/31/2008	N
	9/4/2008	N
	9/29/2008	N

138) Cerro Yanteles

1508-050	5/18/2003	N
	2/7/2004	N
	1/31/2005	N
	1/18/2006	N
	7/29/2006	N
	2/18/2008	N
	5/31/2008	N
	9/4/2008	N
	9/29/2008	N

139) Palena Volc Group

1508-051	1/31/2005	N
	1/18/2006	N
	7/29/2006	N

	2/18/2008	N
	5/31/2008	N
	9/4/2008	N
140) Melimoyu		
1508-052	10/11/2007	N
	2/18/2008	N
141) Puyuhuapi		
1508-053	7/29/2006	N
	4/4/2007	N
	2/18/2008	N
142) Mentolat		
1508-054	7/7/2007	N
	8/17/2007	N
143) Volcán Cay		
1508-055	7/7/2007	N
	8/17/2007	N
	10/11/2007	N
144) Maca		
1508-056	7/7/2007	N
145) Cerro Hudson		
1508-057	4/12/2005	N
	7/17/2005	N
	7/7/2007	N
	3/3/2008	N
146) Lautaro		
1508-06	1/22/2008	N
147) Volcán Viedma		
1508-061	5/29/2002	N
	5/2/2004	N
148) Aguilera		
1508-062	9/11/2002	N
	7/27/2006	N
149) Palei-Aike Volc Field		
1508-08	6/5/2007	N
150) Monte Burney		
1508-07	9/16/2007	N

A1.2 VOLCANOES WITH POTENTIAL HOTSPOTS

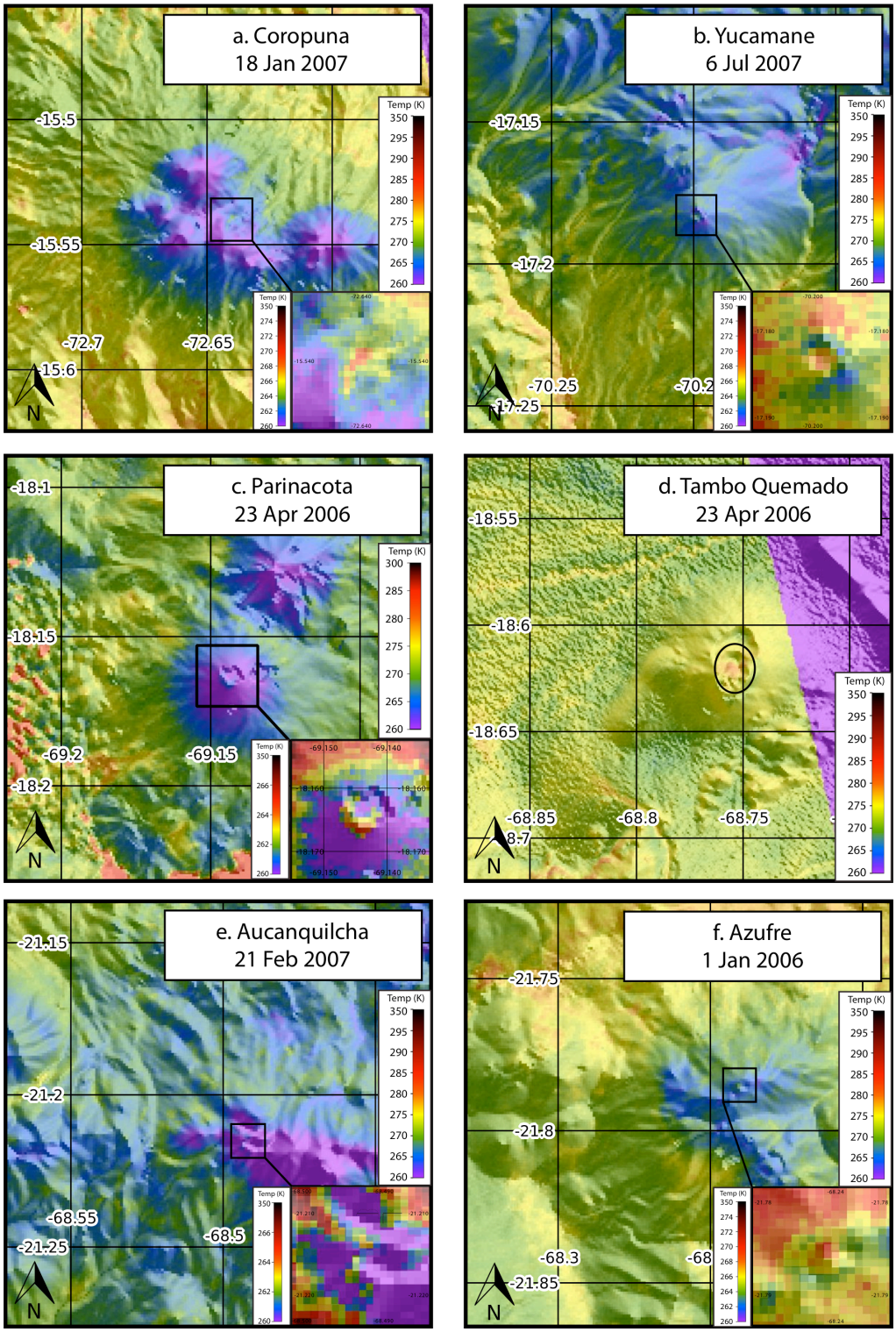

Figure A1.2.0.1 Close-up views of volcanoes with potential hotspots identified in ASTER Pixel integrated temperatures.

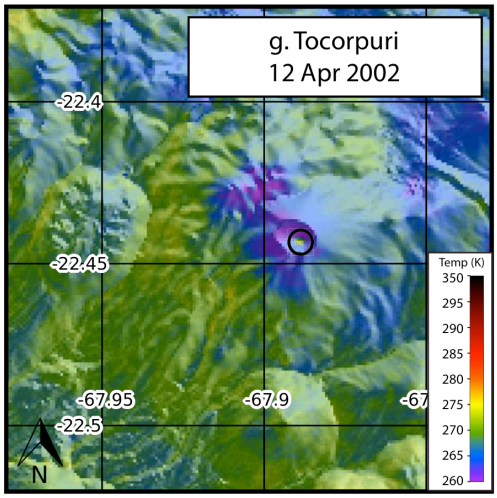
g. Tocorpuri
12 Apr 2002
-22.4
-22.45
-67.95
-67.9
-22.5
N
Temp (K)
350
295
290
285
280
275
270
265
260

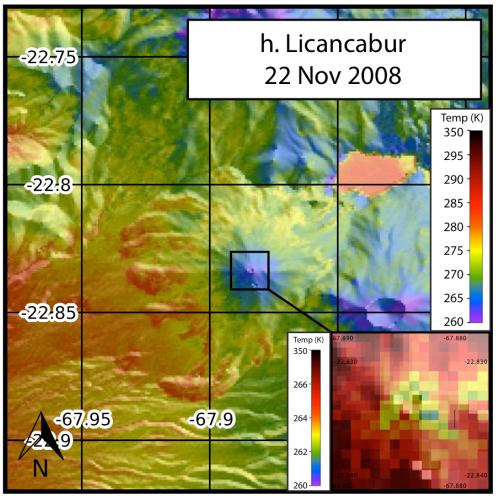
h. Licancabur
22 Nov 2008
-22.75
-22.8
-22.85
-67.95
-67.9
N
Temp (K)
350
295
290
285
280
275
270
265
260

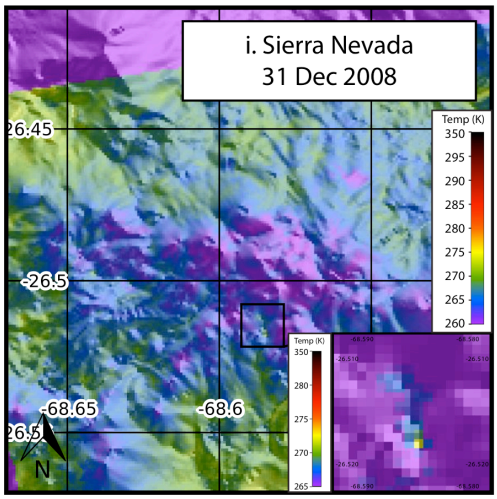
i. Sierra Nevada
31 Dec 2008
-26.5
-68.65
-68.6
N
Temp (K)
350
295
290
285
280
275
270
265
260

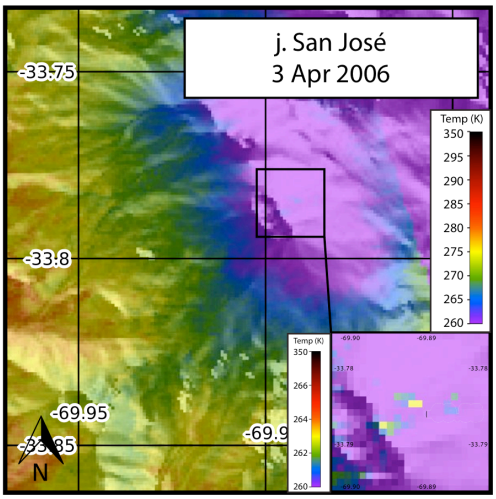
j. San José
3 Apr 2006
-33.75
-33.8
-69.95
-69.9
N
Temp (K)
350
295
290
285
280
275
270
265
260

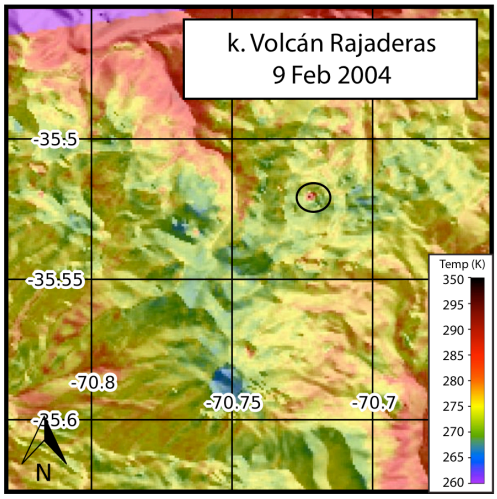
k. Volcán Rajaderas
9 Feb 2004
-35.5
-35.55
-70.8
-70.75
-70.7
N
Temp (K)
350
295
290
285
280
275
270
265
260

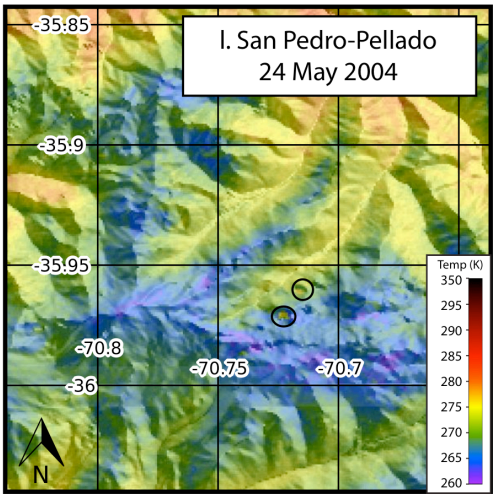
l. San Pedro-Pellado
24 May 2004
-35.85
-35.9
-35.95
-70.8
-70.75
-70.7
-36
N
Temp (K)
350
295
290
285
280
275
270
265
260

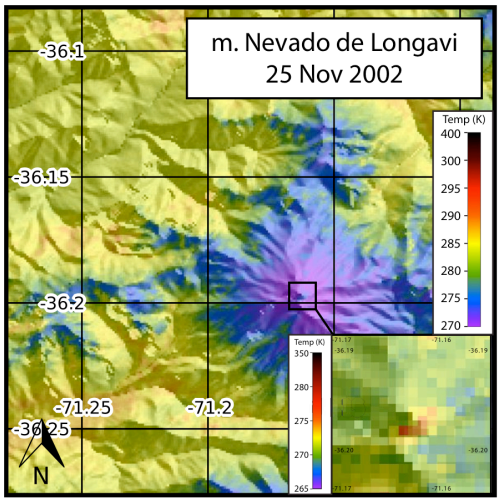
m. Nevado de Longavi
25 Nov 2002
-36.1
-36.15
-36.2
-36.25
-71.25
-71.2
N
Temp (K)
400
300
295
290
285
280
275
270

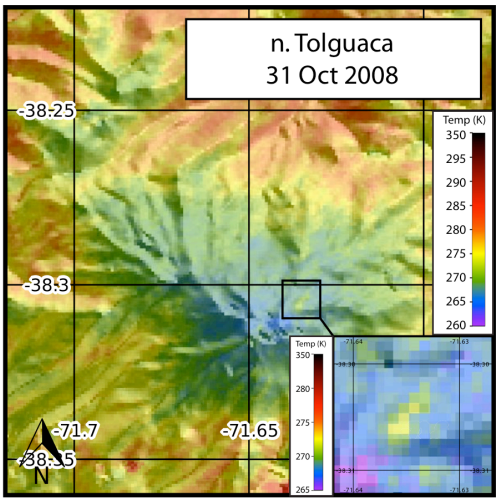
n. Tolguaca
31 Oct 2008
-38.25
-38.3
-38.35
-71.7
-71.65
N
Temp (K)
350
295
290
285
280
275
270
265
260

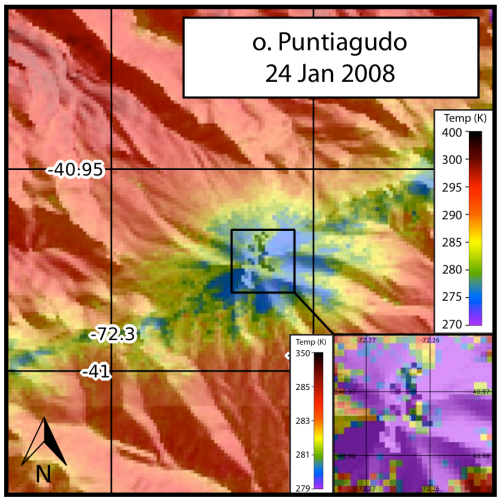
o. Puntiagudo
24 Jan 2008
-40.95
-72.3
-41
N
Temp (K)
400
300
295
290
285
280
275
270

APPENDIX A2

CORDÓN CAULLE SUPPLEMENTAL MATERIAL

A2.1 INSAR MODELING OF THE 2008-2009 DEFORMATION

We use two different inversion techniques to model the 2008-2009 deformation episode using ALOS InSAR data from ascending and descending orbits. First, we employ a Levenberg-Marquardt algorithm. We attempt to model the deformation using the following source models: Mogi point source (Fig. A2.3), finite radius spherical source (Fig. A2.4), Yang-type spheroidal source (Fig. A2.5), Okada tensile opening, combined Okada tensile opening plus slip (Fig. A2.6), combined Mogi point source plus Okada opening/slip. Second, we employ the Neighborhood Algorithm (e.g., Sambridge 1999). Using this approach, we model the deformation using an Okada tensile opening (Fig. A2.7).

We find that none of the models adequately fit the ascending and descending data simultaneously. There is only one interferogram from the descending path (p417), and this interferogram displays a high magnitude of deformation that cannot be accounted for by any of the models attempted here. Since the timespan of the p118 stack completely encompasses the timespan of the p417 interferogram (see Fig. A2.1), we are confident that the issue is not related to a pulse of deformation that is only covered in the p417 interferogram. We offer three possible explanations for why our models do not fit the ascending and descending data: 1) the true source geometry is more complex than any of the modeled source geometries; 2) the heterogeneities and/or viscoelasticity of the subsurface play a significant role in altering the surface

deformation; 3) the p417 interferogram is contaminated by atmospheric signal and does not accurately represent the true surface deformation.

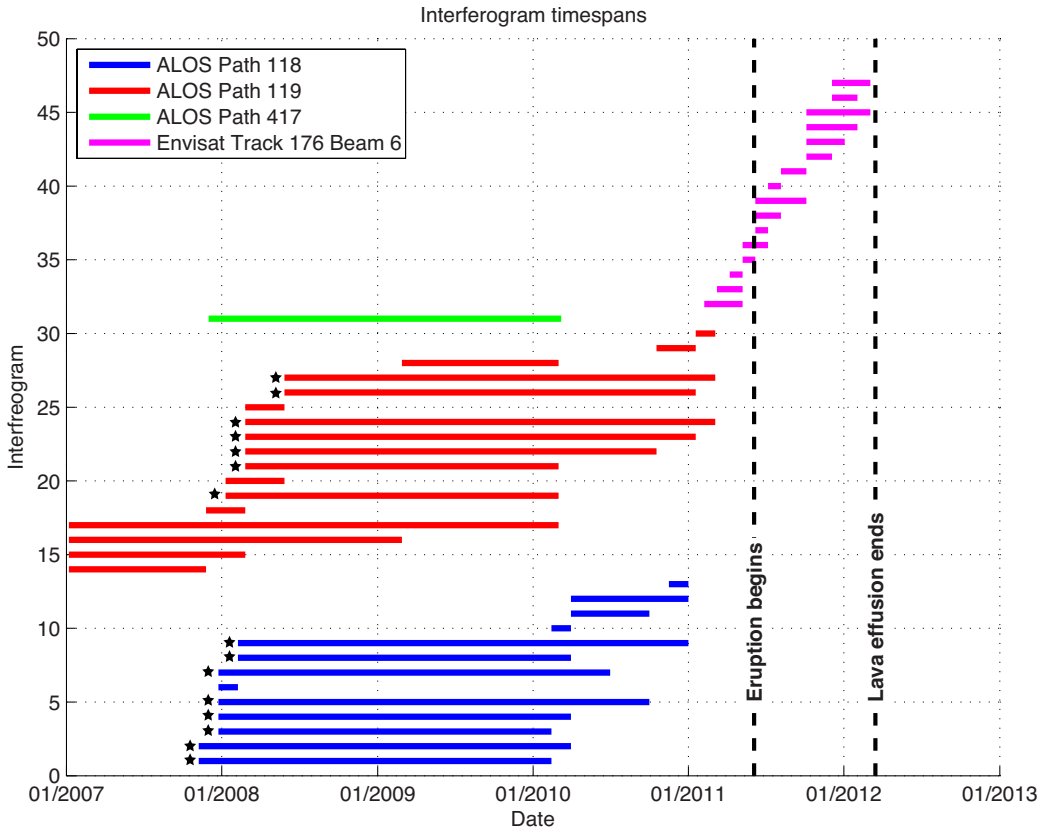

Figure A2.1 Plot showing timespans of every interferogram used in this study from both ALOS and Envisat satellites. Stars indicate interferograms that were used in the 2008-2009 stacks.

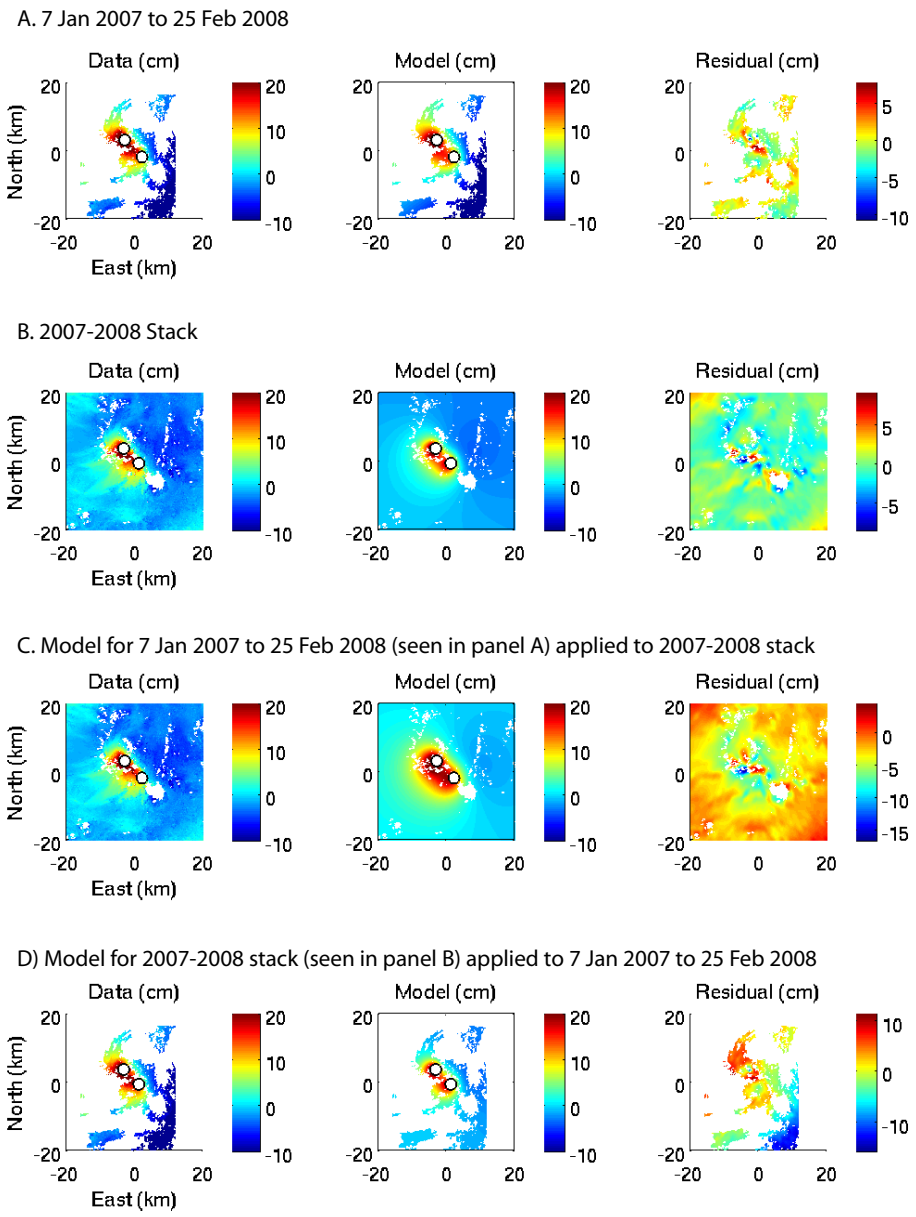

Figure A2.2 2007-2008 deformation episode. Pre-eruptive interferograms (data), modeled interferograms (model), and residuals for ALOS path 119 using the Levenberg-Marquardt algorithm. A) Inversion results using single interferogram 7 Jan 2007 to 25 Feb 2008 as input. Model is two Mogi point sources at 3.9 km depth with a volume change of 0.016 km^3 (NW source) and 5.3 km depth with a volume change of 0.025 km^3 (SE source). B) Inversion results using stack of two interferograms (7 Jan 2007 to 25 Feb 2008 and 7 Jan 2007 to 25 Nov 20078) as input. Model is two Mogi point sources at 2.5 km depth with a volume change of 0.008 km^3 (NW source) and 3.8 km depth with a volume change of 0.014 km^3 (SE source). C) Two Mogi model of (A) applied to interferogram stack in (B). D) Two Mogi model of (B) applied to interferogram in (A).

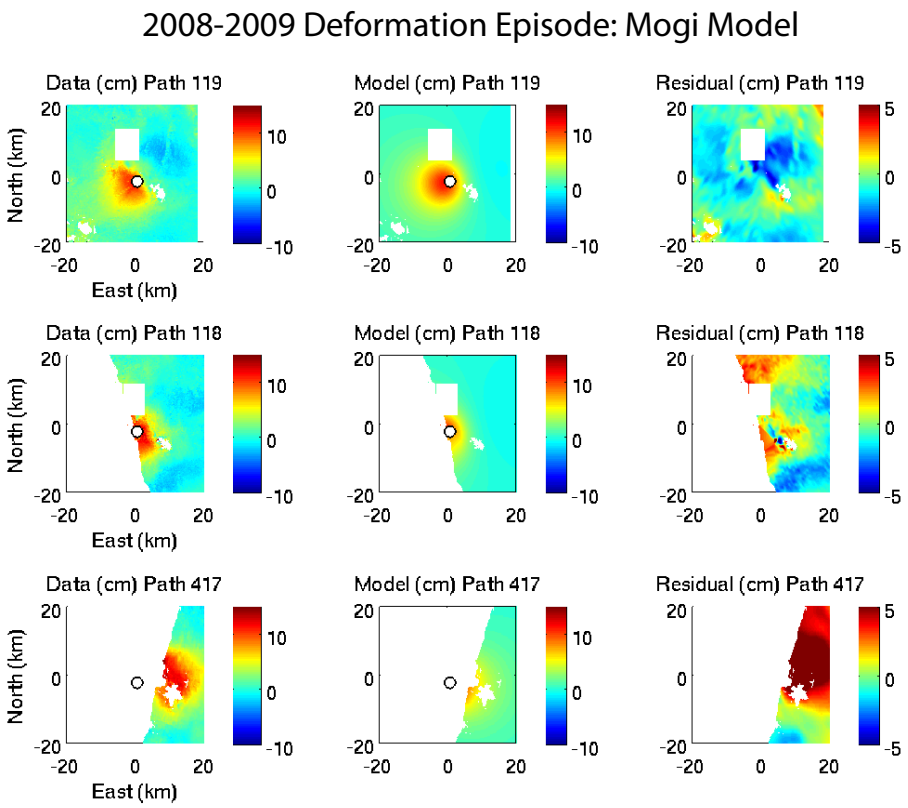

Figure A2.3 2008-2009 deformation episode. Pre-eruptive interferograms (data), modeled interferograms (model), and residuals for ALOS paths 118, 119, and 417 using the Levenberg-Marquardt algorithm. Paths 118 and 119 are interferogram stacks (see Fig. S1 for timespans) while path 417 is a single interferogram. The Cordillera Nevada deformation region is masked out during the inversion for the 2008-2009 deformation episode since it is temporally and spatially isolated. The model is a Mogi point source at 7.6 km depth with a volume change of 0.032 km^3. White circle shows location of point source.

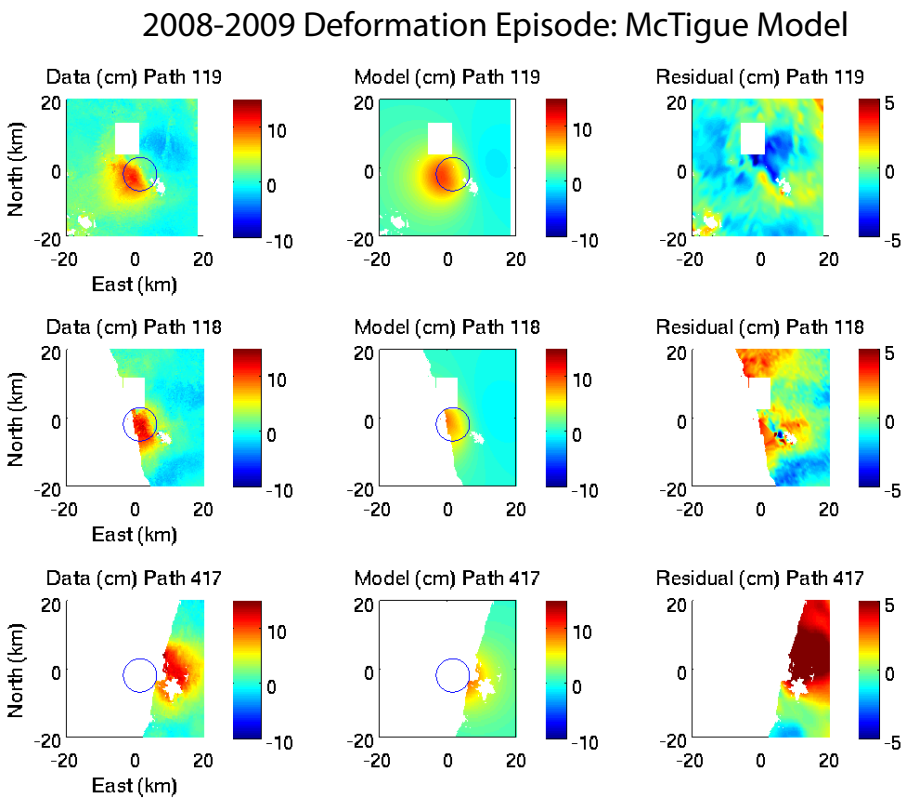

Figure A2.4 2008-2009 deformation episode. Pre-eruptive interferograms (data), modeled interferograms (model), and residuals for ALOS paths 118, 119, and 417 using the Levenberg-Marquardt algorithm. Paths 118 and 119 are interferogram stacks (see Fig. S1 for timespans) while path 417 is a single interferogram. The Cordillera Nevada deformation region is masked out during the inversion for the 2008-2009 deformation episode since it is temporally and spatially isolated. The model is a McTigue spherical source at 5.8 km depth with a radius of 4.9 km and a volume change of 0.036 km^3. Circle shows size and location of spherical source.

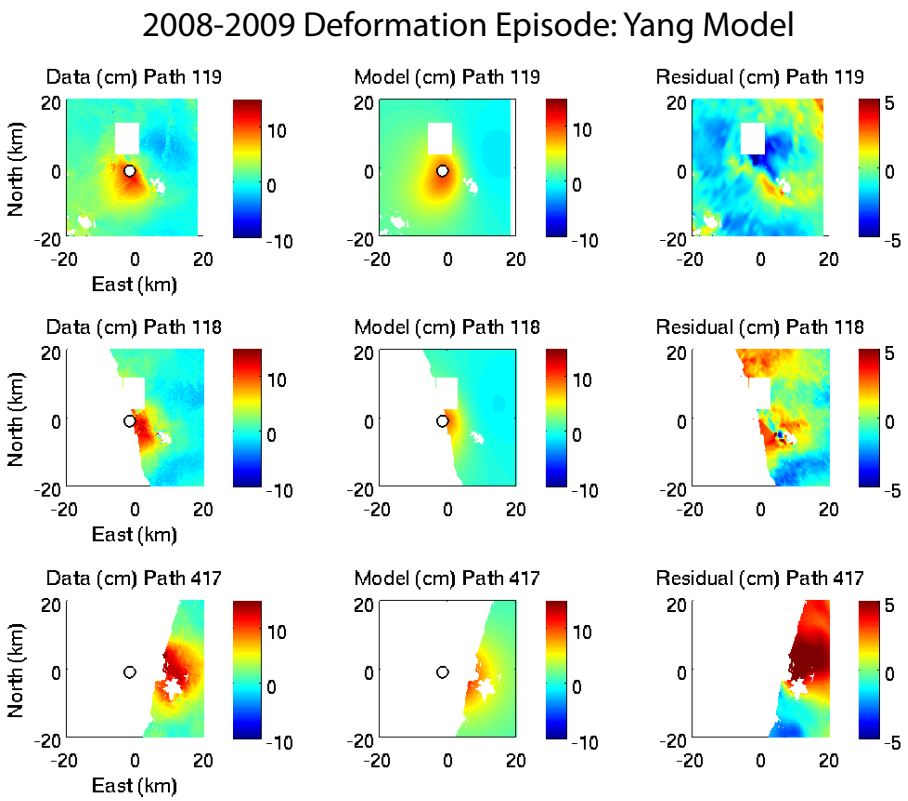

Figure A2.5 2008-2009 deformation episode. Pre-eruptive interferograms (data), modeled interferograms (model), and residuals for ALOS paths 118, 119, and 417 using the Levenberg-Marquardt algorithm. Paths 118 and 119 are interferogram stacks (see Fig. S1 for timespans) while path 417 is a single interferogram. The Cordillera Nevada deformation region is masked out during the inversion for the 2008-2009 deformation episode since it is temporally and spatially isolated. The model is a Yang spheroidal source at 8.7 km depth with a 250 m semi-major axis; 180 m semi-minor axis; 2 degree dip; 140 degree strike; and 30 MPa pressure change. White circle shows location of center of spheroidal source.

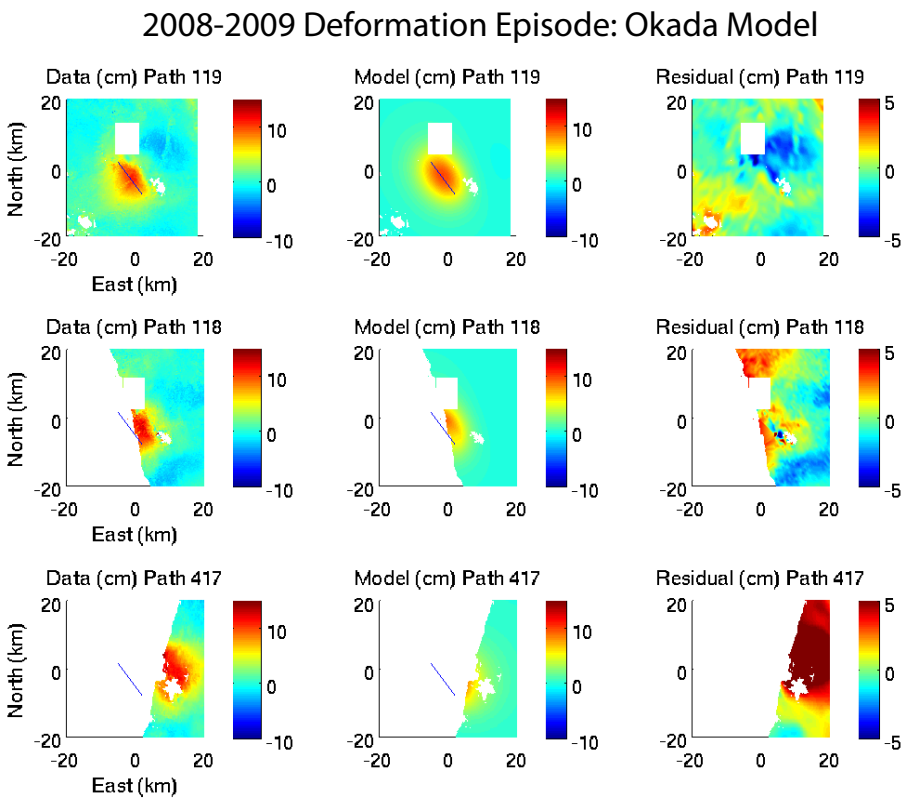

Figure A2.6 2008-2009 deformation episode. Pre-eruptive interferograms (data), modeled interferograms (model), and residuals for ALOS paths 118, 119, and 417 using the Levenberg-Marquardt algorithm. Paths 118 and 119 are interferogram stacks (see Fig. S1 for timespans) while path 417 is a single interferogram. The Cordillera Nevada deformation region is masked out during the inversion for the 2008-2009 deformation episode since it is temporally and spatially isolated. The model is an Okada dislocation source at 9.2 km depth with 12 km length; 2 km width; 0 degree dip; 143 degree strike; 0.4 m slip; and 1.2 m opening. Line shows strike, length, and location of dislocation plane.

A) Model 1: 27 May 2008 to 18 Jan 2011 (Ascending p119)

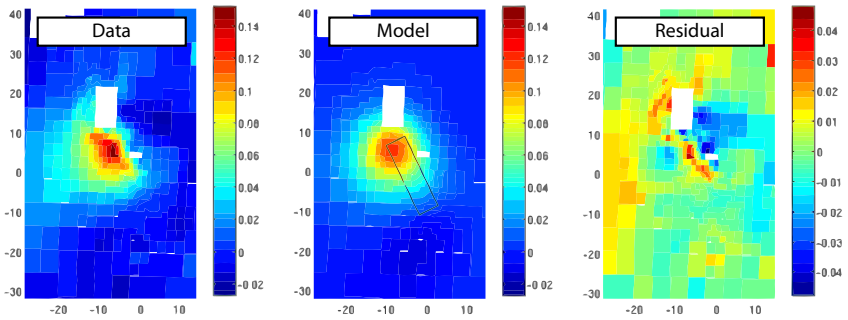

B) Model 1: 1 Dec 2007 to 8 Mar 2010 (Descending p417)

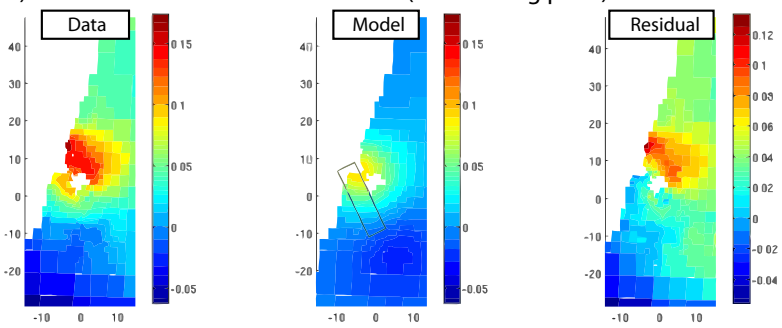

C) Model 2: 10 Jan 2008 to 2 Mar 2010 (Ascending p119)

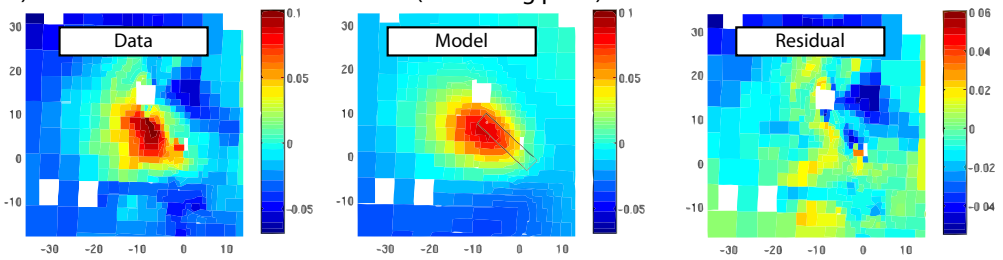

D) Model 2: 1 Dec 2007 to 8 Mar 2010 (Descending p417)

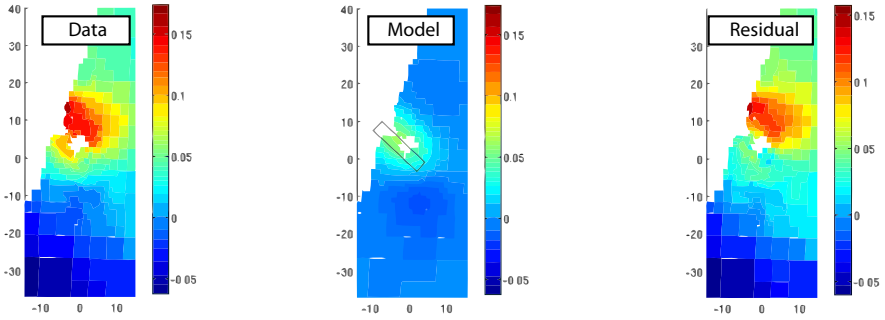

Figure A2.7 2008-2009 deformation episode. Pre-eruptive interferograms (data), modeled interferograms (model), and residuals for ALOS paths 118, 119, and 417 using the Neighborhood Algorithm. A) and B) Model results using input interferograms 27 May 2008 to 18 Jan 2011 from path 119 and 1 Dec 2007 to 8 Mar 2010 from path 417. C) and D) Model results using input interferograms 10 Jan 2008 to 2 Mar 2010 from path 119 and 1 Dec 2007 to 8 Mar 2010 from path 417.

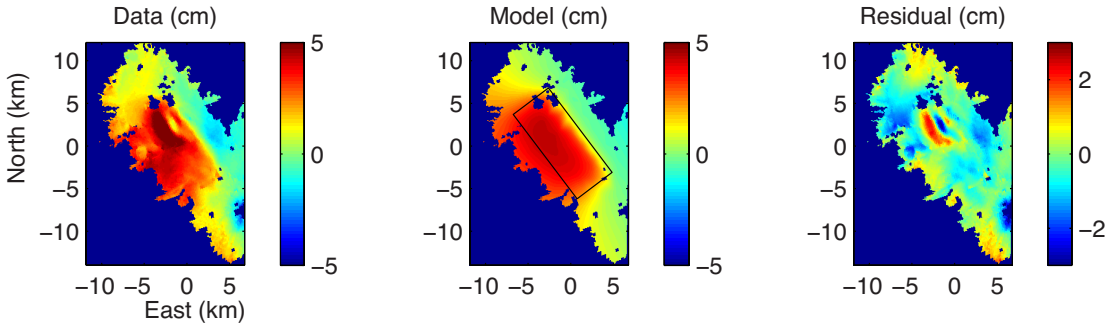

Figure A2.8 Data, model, and residual for the 9 March to 8 May 2011 deformation episode modeled with a rectangular sill with the following parameters: 12.4 km length, 6.1 km width, 4.2 km depth, 32 degrees dip, 143 degrees strike, 4.5 cm opening. The residual signal is probably related to the earthquake swarms that were occurring during this time interval.

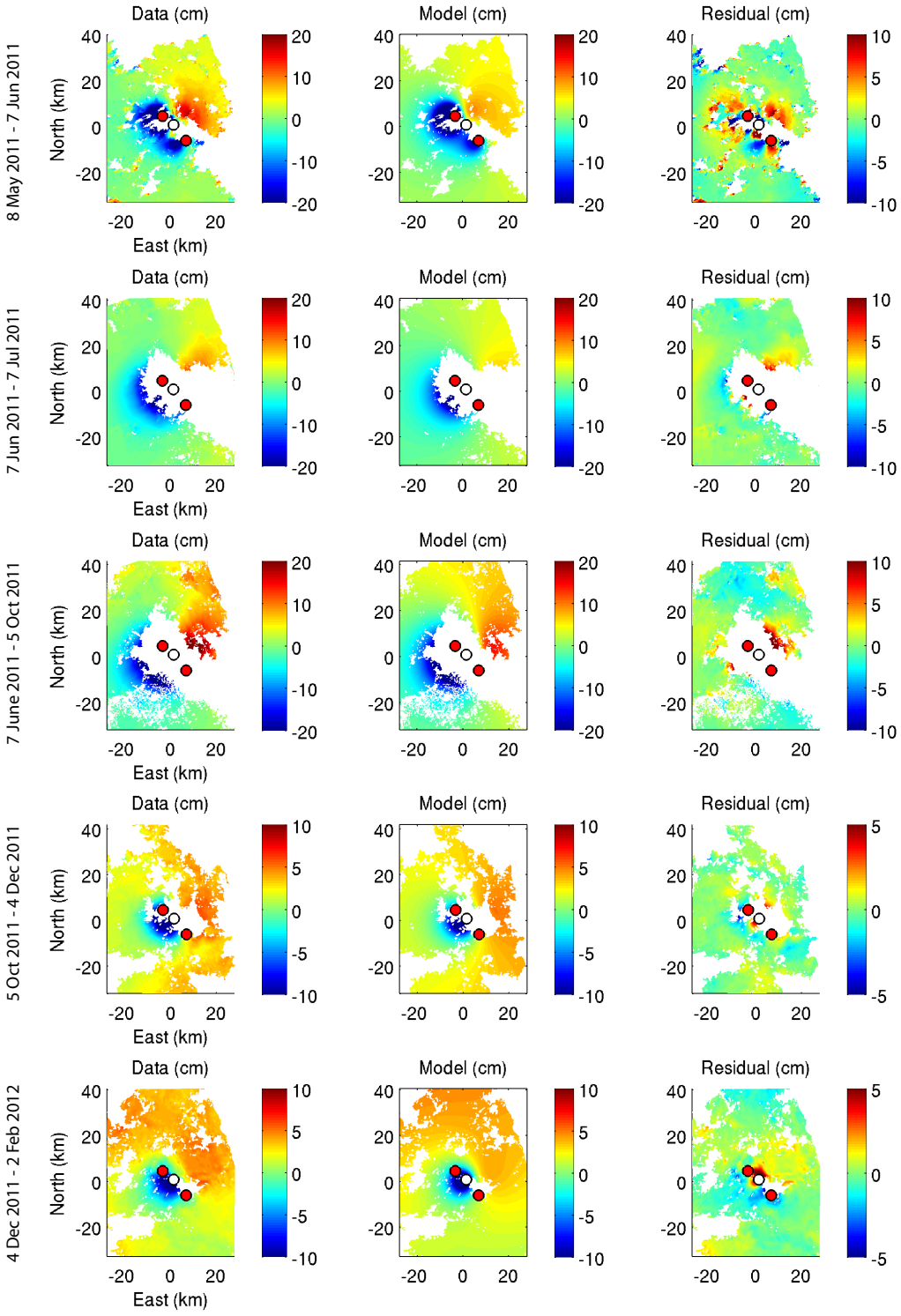

Figure A2.9 Data, models, and residuals for Envisat co-eruptive interferograms. The interferogram in the top row, 8 May 2011 to 7 June 2011, requires two deflating point sources (red circles); all others are modeled using one deflating source (white circle) at the same location and at 6 km depth (Table 1). Black star indicates 2011 eruptive vent.

A2.2 CALCULATION OF MAGMA COMPRESSIBILITY AND MASS BALANCE

We calculate the compressibility of the magma (beta) according to Huppert and Woods (2002), and related the volume changes derived from inversion of InSAR data with the observed extruded volume following the approach of Mastin et al. (2008) and Segall, (2010)

(1) $\beta = \frac{1}{\rho}\frac{\partial \rho}{\partial p}$

To calculate the magma density rho, we use the equation

(2) $\rho = \alpha\rho_g + (1-\alpha)\rho_m$

where alpha is the volume percent of exsolved volatiles and rho_g is the gas density calculated using the ideal gas law. Making use of the conservation of mass, it is possible to relate the dV derived from inversion of InSAR data with the observed extruded volume (e.g., Mastin et al., 2008; Segall, 2010) by

(3) $\Delta V_c \rho\left(1 + \frac{\beta}{\beta_r}\right) = \rho_e V_e$

where dVc is the magma volume change calculated from the inversion of InSAR data, rho is the magma density, beta is the compressibility of magma, beta_c is the compressibility of the wall rock, V_e is the erupted magma volume, and rho_e is the erupted magma density. Solving equation (3) for beta, we have

(4) $\beta = \beta_r\left(\frac{V_e\rho_e}{\Delta V_c \rho} - 1\right)$

Parameter values are shown in Table 3. Equating equations (1) and (4) and solving for alpha we are able to relate the compressibility with changes of volume from InSAR and erupted volumes.

A2.3 DETAILS OF THE PETROLOGICAL ANALYSES

For electron microprobe analyses an accelerating voltage of 15 kV, current of 15 nA, and spot size of about 1 μm was used for most mineral analyses. For glass, the current was 10 nA, and spot sizes were increased to 5 to 10 μm. To minimize the loss of alkalis, Na and K were always analyzed first. Counting times on peak positions were varied according to the concentration; from 10 s for major elements and up to 120 s for trace elements. Backgrounds on both sides of the peak were measured for half of the peak time. For Mg in plagioclase we used 50 nA and 60 s on the peak and backgrounds. More than xx analyses were done in pyroxenes, plagioclase, olivine, and Fe-Ti oxides.

Volatile contents (H, C, Li, B, Be, S, Cl, F, S) of 6 glass inclusions in pyroxene were obtained at the Stanford-USGS SHRIMP-RG ion microprobe using the same instrument conditions, standardization, and corrections as detailed in Wright et al. (2012). The reported CO_2 contents may be an overestimation of the real values because external contamination of C was found in other samples of the same session (J. Cabato, pers. comm.) although the values of the inclusions from Caulle show a very narrow variability.

APPENDIX A3

INTERFEROMETRIC SYNTHETIC APERTURE RADAR (INSAR) METHODOLOGY

A3.1 TECHNIQUE

InSAR is a radar remote sensing technique commonly used in geodesy to measure deformation of the Earth's surface through time. The technique requires the acquisition of two satellite radar images taken at different times but covering the same area on the Earth's surface. The location of the satellite at the time of the second pass must be close to the location of the satellite at the time of the first pass (~300 m for C-band and ~2 km for L-band); this spatial distance is called the baseline. The polar orbits of satellites carrying SAR instruments are carefully controlled so that the position of the satellite is known to within meters of accuracy; however the baseline is re-estimated during InSAR processing. The orbits generally have repeat cycles of tens of days (e.g., 11 days for TerraSAR-X and 46 days for ALOS).

A3.2 PROCESSING

The first step in producing an interferogram is to acquire two SAR images that have been acquired by the same satellite at different times and cover the same geographic region. The two images are then co-registered to each other by cross correlating the amplitude images and an affine transformation is applied to one image so that it matches the geometry of the other. The interferogram is then constructed by differencing the phase value of each pixel. Corrections for various factors such as the Earth's curvature and topography are made at this time. The resulting interferogram

can then be filtered using a power spectrum filtering algorithm to enhance the coherent phase information. At this stage, the interferogram is still "wrapped," meaning that the phase values vary from 0 to 2π, so that the deformation field appears as fringes. In order to calculate the absolute displacement at each pixel, the interferogram must be "unwrapped." Finally, the interferogram is geocoded, transforming the image from radar to geographic coordinates.

A3.3 LIMITATIONS

InSAR is an excellent tool for measuring surface deformation over large areas of land. However, there are a few limitations of the technique.

1. **Data availability.** SAR data is not always available to capture "before" and "after" scenes of processes of interest such as earthquakes and volcanic eruptions. The scarcity of data can lead to temporal aliasing of deformation signals. This issue will be addressed with the launch of more satellites in the near future that will acquire data more frequently over more regions of the Earth.
2. **Viewing geometry.** InSAR provides surface displacement in only one direction – the line-of-sight between the satellite and the ground. Given a single interferogram, calculating the north-south, east-west, and vertical components of displacement is impossible. However, if interferograms constructed from different satellite tracks with different viewing geometries are available, inversion for a three-dimensional displacement field becomes possible.

3. **Phase coherence.** Many factors contribute to the quality of an interferogram. In order for a pixel to be coherent, the scattering properties of the ground contained in that pixel must not have changed significantly between the first and second scenes. Factors that may cause incoherence include large baselines, long time spans, atmospheric path effects, steep topography, and snow cover.